THE DESIGN, DEVELOPMENT AND GENERAL APPLICATION OF AN INFRA RED RATIO PYROMETER, INTENDED PRIMARILY FOR SURFACE TEMPERATURE MEASUREMENT OF MAGNOX FUEL CANS

by

G. K. Caulton

SYNOPSIS

The development of magnox fuel cans at the Heston Laboratories of A.P.C. Ltd. required a non contact method of measuring fuel can temperature during heat transfer tests. Infra red techniques were examined and a two colour ratio pyrometer was selected as offering the greatest prospect of success. A design specification was compiled for an instrument having a lower temperature limit of 250°C with a target area of approximately 1 mm^2.

During heat transfer tests a pressurised rig is used and an observation window is necessary. This leads to some deterioration in performance which it is impracticable to remove by internal chopping and the pyrometer is designed for outside use. Operational wavebands around 1.8 and 2.3 microns are chosen and a lead sulphide infra red detector operating at room temperature is selected. The properties of the detector lead to a design where the signal is chopped at 900 cps and modulated at 30 cps by the energy in each waveband.

Conventional optical systems are considered and rejected in view of the large size of chopper wheel necessary. An alternative system is devised in which a commercially available pencil galvanometer is used to combine the function of chopping at both 900 cps and 30 cps. This enables an optical system to be designed which, because it employs reflecting optics, is compact and for the most part axially symmetric.

The signal ratio is extracted using an automatic gain control technique and a high signal to noise ratio is achieved with a phase sensitive rectifier at the output. The pulses which activate the galvanometer chopper and phase sensitive circuits are derived from a master oscillator operating at 900 cps.

The performance of the system is assessed and it meets the specification in all respects except for a small surface geometry effect. The underlying cause for this is examined and a means for overcoming it is suggested. The performance when scanning a magnox can during bench tests is illustrated and it can be seen that although agreement to within 2°C is obtained with thermocouples placed at the fin roots, the geometry effect prevents the isolation of fin tip temperature.

During the development of the instrument the possibility of wider application was an important consideration. Some of the applications which have arisen are discussed briefly and an indication of the performance of the pyrometer is given. Furthermore the system is capable of easy modification for use with a cooled detector and other regions of the infra red spectrum.

ACKNOWLEDGEMENTS

I would like to thank the management of Atomic Power Constructions Limited for providing me with the opportunity to carry out the work described. In particular I am indebted to Dr. R. Berenbaum, Mr. J. A. Fryer and Mr. N. Miller as successive industrial tutors, under whose guidance the project has been brought to a successful conclusion and to Dr. J. W. Warren of Brunel University as College tutor, for his help in arranging suitable lectures and tutorials during the period of study.

I have also to thank employees of APC who have contributed in the manufacture of the infra red system and the Reactor Development Laboratory of the UKAEA and Berkeley Nuclear Laboratories of the CEGB for whom some of the results presented in Chapters 7 and 8 were obtained.

G.K. Caulton
30th April, 1966.

PREFACE

The application of infra red techniques to the surface temperature measurement of magnox fuel cans in heat transfer experiments has provided a basis for the design and development of the pyrometer described. It has been necessary to optimise the design so that the temperature of an area approximately 1 mm square at a distance of 60 cm can be measured down to a temperature of 250°C with a reasonable response time, using optical components of manageable size. A ratio pyrometer has been selected as the method likely to achieve the highest overall accuracy although the performance will be limited by the sensitivity at the bottom end of the temperature range where valuable energy is discarded in the waveband selection process.

In order to achieve maximum sensitivity within the required specification considerable emphasis has been placed on the optical modulation and electronic demodulation techniques, which reduce extraneous signals to a minimum in the output indication. Thus the system is noise-limited by the infra red detector itself rather than the signal processing system.

The optical system has been designed so that it may be readily modified for operation over the infra red spectrum from 1 micron to the long wavelength limit of infra red detectors and filters. This allows its extension as a temperature measuring instrument to ambient temperatures using cooled detectors.

The performance of the pyrometer from the instrument point of view has been examined using a stable emitter. It has not been possible, however, due to the continual development of power reactors, to complete the development along the lines originally intended. Thus the measurements on magnox which are described, have been restricted to an assessment of the pyrometer on the bench. The completely developed instrument is being made available commercially and a few of the applications envisaged and the results obtained have been discussed briefly.

The work described in this thesis appears as far as is practicable in chronological order with a few minor exceptions. Thus it has been necessary to adjust the position of the operational wavebands from those suggested in Chapter 2, in the light of experimental information obtained in appendix A at a later date. Also, although the description of the electronic system appears after that of the optical system, it was developed in practice while the optical system was being manufactured.

An apology is made for the use of mixed units in various sections of the work. The heat transfer calculations employ lb. ft. hr., which are most commonly used in this field, and the remainder of the work is carried out in the decimal system.

CONTENTS

Chapter 2 - Temperature measurement using infra red radiation

Introduction:

2.1 The nature of infra red radiation

2.1 Planck's radiation law

2.3 Emission from non-ideal surfaces

2.4 Emission from re-entrant surfaces

2.5 Measuring techniques available

2.6 Comparison of performance of various types of instrument

2.7 Feasibility study using ratio pyrometer

2.8 The spectral emissivity of clean and oxidised magnox

2.9 Spectral response of infra red detectors

2.10 Upper wavelength limit for pyrometer

2.11 Absorption bands of carbon dioxide and water vapour

2.12 Upper wavelength limit imposed by window material

2.13 Effect of window on pyrometer calibration

2.14 Conclusion

2.15 References

Chapter 3 - The infra red detector and its influence on the design of the optical and electronic systems

Introduction:

3.1 Types of detector

3.2 Spectral response

3.3 Sensitivity

3.4 Response time

3.5 Operational factors

NOTATION

English Letters

A = area; amplitude coefficient, amplifier gain

A_H = heat transfer free flow area

a = distance; amplitude coefficient

B = amplitude coefficient, amplifier gain

b = distance; amplitude coefficient

C = capacitor; $^{\circ}C$ = degrees centigrade

$C_1 = \frac{ch}{k}$ $(cm\,^{\circ}K)$

$C_2 = \frac{\varepsilon_1}{\varepsilon_2}\left(\frac{\lambda_2}{\lambda_1}\right)^5$

$C_3 = C_1\left(\frac{1}{\lambda_1} - \frac{1}{\lambda_2}\right)$ $(cm.\,^{\circ}K.microns^{-1})$

c = velocity of light wave in vacuum (3×10^{10} $cm.sec^{-1}$)

c_p = specific heat at constant pressure ($chu.lb^{-1}.\,^{\circ}C^{-1}$)

D = diameter

D^* = specific detectivity ($cm^2.\,watts^{-1}$)

d = diameter

E = energy level

e = exponential series

e_o = dielectric constant

F = focal ratio (f.no.); filter; noise figure = $\frac{\text{signal to noise power at input}}{\text{signal to noise power at output}}$

δf = system bandwidth

f = focal length; frequency of alternating current

fn = function

f_t = gap between fins at tips

f_r = gap between fins at roots

f_h = fin height

G = stage power gain; galvanometer coil

G_r = Grashof number defined as $G_r = \frac{\alpha g \Delta T l^3 \rho^2}{\eta^2}$

g = acceleration due to gravity $ft.hr^{-2}$

H = heat transfer coefficient; quarter wave layer (high refractive index)

h = Planck's constant (6.63×10^{-27} erg.sec.); distance

I = radiant intensity into hemisphere; radiation field ($watts.cm^{-2}$)

I_b = radiant intensity into hemisphere of black body ($watts.cm^{-2}$)

I_n = radiant intensity normal to surface ($watts.cm^{-2}$)

i = current

J = mechanical equivalent of heat ($ft.lb.chu^{-1}$)

$j = \sqrt{-1}$

K = constant; kilo-; kilohm; ^oK = degrees absolute ($chu.ft^{-1}.hr^{-1}.{}^oC^{-1}$)

k = Boltzmann's constant (1.38×10^{-16} erg.^oK); thermal conductivity

L = length; inductance; quarter wave layer (low refractive index)

l = length

M = mirror

m = mirror width; milli-

N = number of fins on can; number of interference layers in filter

Nu = Nusselt number defined as $Nu = \frac{\theta l}{k_c \Delta T}$

n = number; turns ratio in transformer

P = pressure; power

P_H = heat transfer perimeter

P_r = Prandtl number defined as $P_r = \frac{c_p \eta}{k_c}$

p = position factor; probability

Q = heat transfer (chu $ft^{-2} \cdot hr^{-1}$); quality of tuned circuit

q = shape factor; electronic charge (1.6×10^{-19} coulumbs)

R = signal ratio; resistance; revolutions per second

R_e = Reynold's number defined as $R_e = \frac{v_b \rho l}{\eta} = \frac{Wl}{A\eta}$

r = radius of curvature, resistance, reflectivity

S = signal to noise ratio

S_t = Stanton number defined as $S_t = \frac{N_u}{R_e P_r}$

s = aperture stop diameter, image diameter

T = temperature, transistor

TT = transformer

ΔT = temperature difference

t = time; thickness

U = complex index

u = object distance

V = potential difference; volume

V_R = reference voltage; variable resistor

v = image distance; velocity

v_b = bulk velocity

W = mass flow ($lb.hr^{-1}$)

w_r = width of fin at root

w_t = width of fin at tip

x = variable parameter

y = variable parameter

Z = impedance

Z_d = zener diode

Greek Letters

α = coefficient of volumetric expansion; current ratio $\frac{i_c}{i_e}$; angle

α_c = size of comatic image

β = current gain defined as $\frac{\alpha}{1-\alpha}$

γ = angle

δ = phase difference

ε = emissivity

ε_n = emissivity at wavelength λ_n

η = viscosity ($lb.ft^{-1}.hr^{-1}$)

θ = angle

λ = wavelength (microns)

λ_m = wavelength at which maximum energy is radiated

μ = refractive index

ν = frequency of electromagnetic wave defined as $\nu\lambda = c$

$\bar{\nu}$ = wave number of electromagnetic wave defined as $\frac{1}{\lambda}$

ρ = density

ρ_r = resistivity (ohms.metres)

σ = electrical conductivity ($ohms^{-1}.metre^{-1}$)

τ = periodic time

ϕ = angle

Ω = ohms; solid angle

$d\Omega$ = element of solid angle

ω = angular frequency

Suffices - unless defined otherwise

b = transistor base; black body

c = coolant gas; cut off; transistor collector; conduction band

D = dynamic

d = diode; difference

dc = direct current

e = transistor emitter

F = Fermi

f = feedback

g = gap

H = heater

i = input; i^{th} term

j = j^{th} term

L = load

l = leakage

m = marginal; magnox

n = noise

o = atmosphere; output; rejection; resonant

p = pressure; peak; cell bias; primary; paraxial

pp = peak to peak

q = quiescent

R = reference

r = root; reflection

s = signal; source; secondary; series; surface

t = transmission, transconductance; transistor

v = voltage

w = window material

λ = wavelength

Miscellaneous

NEP = noise equivalent power level (watts)

chu = centigrade heat unit defined as the amount of heat required to raise the temperature of 1 pound of water through 1 degree centigrade at 20 degrees centigrade

CHAPTER 1 - THE APPLICATION OF PYROMETRY IN HEAT TRANSFER MEASUREMENTS

Introduction

Economic considerations in the magnox power reactor have emphasised the importance of the magnox fuel element and its heat transfer characteristics. The measurement of the heat transfer coefficient is described and the disadvantages of surface temperature measurement using conventional thermocoupling techniques are discussed. The need for a pyrometric method becomes apparent, and, taking into account various necessary precautions, a specification for a pyrometer is compiled. The special features in the design peculiar to temperature measurement through the channel wall of a heat transfer rig are then considered and the window temperature is calculated for a typical set of conditions.

1.1 The magnox reactor

The economics of nuclear power generation differ from those of conventional methods in that the capital costs are higher and the running costs lower (1). To secure low total generation cost, therefore, considerable emphasis is placed on running the capital plant as efficiently as possible within its natural limitations.

In a power reactor heat is generated by nuclear reactions inside the fuel elements. The heat is extracted by forced convection of a coolant fluid through the fuel element channels and the coolant fluid is pumped through heat exchangers where the heat is used to raise steam for conventional steam generating plant.

The thermal efficiency (2) of the power station depends ultimately on the reactor coolant fluid outlet temperature and since this is maintained by the nuclear reactions inside the fuel elements, the operating temperature of the fuel elements becomes an important factor. In a magnox reactor (3), where a gas coolant is used (4) the operating temperature is limited by possible fault conditions in the gas circuit and by considerations of material damage to the fuel element. Considerable research and development effort is directed towards setting the limit as high as possible without leaving the structural integrity of the fuel element in doubt. If the coolant gas is also to approach the temperature limit, the heat transfer coefficient of the fuel element should be as high as possible. Thus once the operating temperature of the fuel element has been limited, it becomes necessary to ensure that as many elements as possible are at the limit and that they are maintained uniformly at the limit with a high heat transfer coefficient.

In practice the temperature pattern over the fuel element will be influenced by the presence of various protuberances such as temperature sensing devices and structural members such as W-braces, which cause local variations in the gas flow pattern. It is found that protuberances tend to increase the heat transfer coefficient while W-braces tend to decrease it because they prevent coolant gas from entering the fins. In addition the element itself will exhibit large variations in heat transfer coefficient due to its helical formation, which causes a cyclic flow pattern to develop. In the event of a hot region occuring on an element under reactor conditions it becomes necessary to derate that particular element and as a result all the elements in the same channel. If this were to apply to many elements a significant derating of the reactor would be necessary. Thus apart from establishing the heat transfer coefficient for a particular can design, it is necessary to search out any hot regions or hot spots in the early stages of design. These are the functions of heat transfer experiments.

1.2 Heat transfer measurements

The heat transfer coefficient is established for a particular fuel element design in extensive laboratory tests.

Heat transfer measurements are carried out at Heston in a pressurised carbon dioxide rig (5). The nuclear reaction heat is simulated by direct current resistance heating of a stainless steel tube which replaces the uranium fuel rod in the fuel can. The carbon dioxide is blown over a string of three or more such cans in a horizontal metal channel which simulates the reactor graphite channel. During a test the measurements required are basically the inlet temperature and mass flow of gas, the electrical power input to the heater tubes and a series of surface temperatures on any but the upstream can. The mass flow is measured by means of a calibrated orifice plate, the electrical power input with precision ammeters and voltmeters, and the temperature with fine wire thermocouples. The measurement of the first two quantities has a negligible perturbing effect on the experiment but the measurement of the fuel element surface temperature disturbs the quantity being measured due to the presence of the temperature sensors and is subject to certain errors.

A portion of a typical fuel can is shown in Fig. 1.1. It consists of a magnox cylinder 30 in. long with 48 helical fins along its length. The can circumference is divided into four quadrants for heat transfer purposes by four full length splitters. The splitters are located by longitudinal slots cut in the fins and rigidly fixed by W-braces which join adjacent splitters. During a heat transfer measurement it is necessary to build up an accurate temperature pattern over the can and it is customary to employ up to 40 thermocouples. The errors introduced by the thermocouples may be divided into two categories:-

(i) errors associated with the attachment of thermocouples to the can

(ii) errors arising due to disturbance to the gas flow pattern by the thermocouple leads.

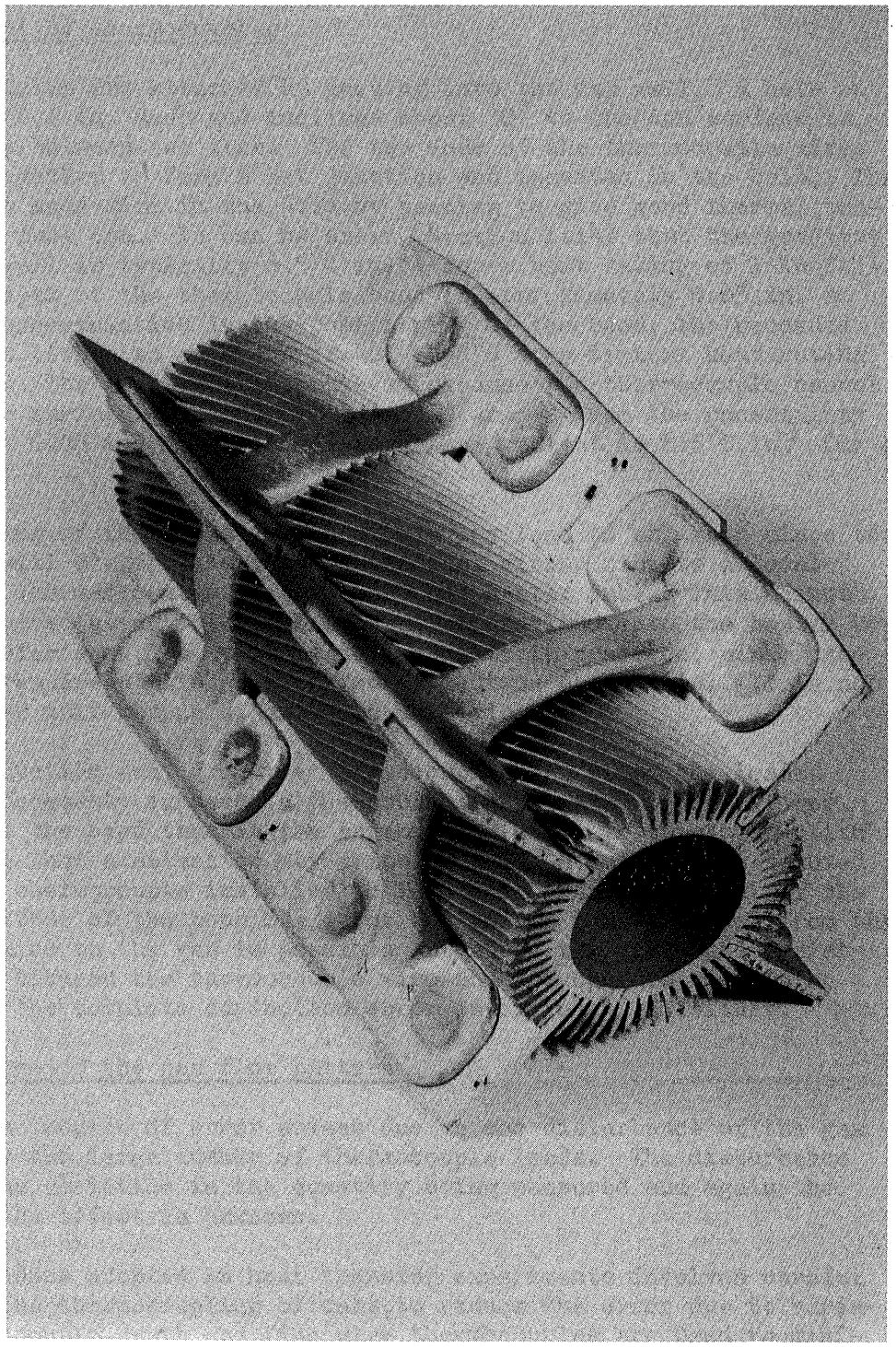

Fig. 1.1 Portion of a typical fuel can

1.3 Attachment of thermocouples

Thermocouples are attached by peening into the can wall. A hole approximately 0.1 in. deep and inclined about 30° to the can surface is drilled midway between two fins. The two ends of the thermocouple wires are twisted together to form a hot junction and inserted in the hole. The wires are then made firm in the hole by peening to give good thermal contact with the fuel can. It can be shown (Section 1.14) that the gradient across a can wall is typically $6.5^{\circ}C.in.^{-1}$ for a heat rating of 1 $kW.ft^{-1}$. The maximum depth of the thermocouple bead is approximately 0.05 in. so that, due to uncertainties in the positioning of the bead, the recorded temperature is liable to an error of $-0^{\circ} + 3\frac{1}{2}^{\circ}C$ at a typical heat rating of 10 $kW.ft^{-1}$. The limit -0° is achieved because the thermocouple cannot be outside the surface, while the limit $+ 3\frac{1}{2}^{\circ}C$ arises from the uncertainty in position of 0.05 in. in a region where the gradient is $6.5^{\circ}C.in^{-1}$ for each $kw.ft^{-1}$.

The peening of the wires into the hole may lead to an error since too heavy a blow will distort the base of the can, giving rise to a local change in the thermal contact between can and heater tube. This effect could be minimised using thick walled cans pressurised onto the heater bar for heat transfer work, but this is not possible in practice, since production cans require a thin wall to reduce neutron absorption. It is not certain whether this source of error is negligible.

Heat conduction away from the thermocouple bead along the leads, which are of necessity exposed to the coolant gas, may produce a lower temperature at the bead than in the surrounding can. In this connection it is possible that a situation may arise in which a hot spot is removed by the actual thermocouple installed to locate it. An assessment of the order of magnitude of the possible error due to the heat transfer from the thermocouple wire to the gas is possible but since the interface resistance and area between the thermocouple wire and the can are unknown, an estimation of the complete conduction error is extremely difficult.

1.4 Disturbance to the gas flow pattern

The second source of error arises due to the disturbance of the gas flow caused by the large number of thermocouple leads. The disturbance must cause some variation in the quantity being measured and again the magnitude of the effect is unknown.

The procedure adopted in heat transfer experiments involves careful attention to the thermocoupling of cans, to reduce the error due to variation in thermocouple depth and fine wire thermocouples are used to minimise conduction and disturbance to the gas flow pattern. With these precautions being taken, the errors discussed above are assumed to be small and the inaccuracy of temperature measurement is taken to be due to the

uncertainty in position of the thermocouple bead only. This provides an uncertainty of $-0^{\circ} + 1\frac{1}{2}$ to $3\frac{1}{4}^{\circ}C$ for a gradient of $6.5\,^{\circ}C.in.^{-1}$ for every $kW.ft^{-1}$ if the uncertainty in position is 0.05 in. and the heat ratings are in the typical range 4.5 to 10 $kW.ft^{-1}$, with an additional error due to inaccuracies of thermocouple calibration.

1.5 Possible improvements in temperature measurement

It may be possible to reduce the variation in depth of the thermocouple beads by using a fine wire welding technique (6). Even if this method were developed to the stage where it could replace peening for the large scale attachment of thermocouples, however, the unknown factors discussed in the preceding sections would still remain. It would be possible in principle to devise experiments to estimate the magnitude of the errors introduced in temperature measurement, but both the time and expense involved are prohibitive. For this reason an entirely independent method of can temperature measurement was suggested which would have ideally, a negligible influence on the experimental conditions.

Infra red methods of temperature measurement do not in general perturb appreciably the object under investigation, and for this reason such techniques were investigated with a view to developing an accurate instrument for measuring can surface temperatures under experimental rig conditions. The intention was that such an instrument would be used to supplement thermocouples which would be relied upon to provide the absolute temperature measurement. The instrument would be calibrated at a thermocouple and then used to scan the can surface, thus providing a far more comprehensive measurement of can surface temperature distribution than would be possible with thermocouples alone.

1.6 Discrimination between temperature changes

The calibration of thermocouples is normally carried out to $\pm\,\frac{1}{4}^{\circ}C$ and this represents the smallest possible error in temperature measurement at present. The deterioration due to other factors already discussed is uncertain and errors may well be significantly greater than this. If an infra red instrument is to make a useful contribution to heat transfer work at the present stage of development it should approach the discrimination of a thermocouple, namely $\pm\,\frac{1}{4}^{\circ}C$. This is likely to be difficult to achieve in practice especially at the lower temperatures in view of the small amount of energy available. (See 1.10) A discrimination of $\pm\,1^{\circ}C$ is an acceptable figure.

1.7 Absolute accuracy of pyrometer

The absolute accuracy of an infra red pyrometer is governed by many factors. These will be dealt with later in detail and they are mentioned briefly here:-

(i) departure of all materials from predictable radiative properties

(ii) variation of radiative properties with temperature and surface condition of the specimen

(iii) absorption of specimen radiation by the intervening media between specimen and pyrometer which may be a function of temperature

(iv) absorption of specimen radiation by optical components in the pyrometer

(v) addition of background radiation to the specimen radiation

(vi) instrumental errors introduced before final indication of temperature is obtained.

These factors inevitably limit the absolute accuracy of a pyrometer, and if high absolute accuracy were necessary then an infra red technique would probably be unsuccessful. However, in heat transfer measurements on fuel cans the requirement is to measure temperature variation over the can surface. If the temperature of a few points is known then the temperature pattern of the can may be referred to these. The absolute temperature of the fuel can may be defined by thermocouples within the errors already discussed. In this way the need for absolute accuracy in the pyrometer is removed since it will be possible to calibrate it at the surface close to a thermocouple and refer all other measurements to this point. The absolute temperature could be corrected if the thermocouple was seen to depress the temperature locally due to conduction errors or on the other hand the calibration could be performed under conditions of no gas flow when conduction errors would be reduced to a minimum. It is sufficient to say at this stage that the absolute accuracy required is not a limiting factor in the design but naturally it should be made as high as circumstances will allow.

1.8 Target area

From Fig. 1.1 it can be seen that the can is covered with thin fins to provide efficient heat transfer. During heat transfer measurements the heat flows from the axial heater bar through the can wall to the coolant gas via the fins and the regions between fins. It has been suggested that the temperature gradient from fin root to tip is 30°C, the root being hotter than the tip. It is the temperature of the fin roots which is mainly of interest in heat transfer measurements since it is of necessity the highest. To distinguish the fin root temperature from that of the surrounding fins will require a small target area for the pyrometer. The gap between fins at the roots for a typical can (7) is 0.033 in. This represents the maximum allowable target width. The length of the target area can be larger, but if a hot region is to be located the target area should not be so large as to average out the temperature of the hot spot. The size of target area to be aimed at is therefore about 1 mm square.

1.9 Response time

During a heat transfer experiment it is difficult to maintain very stable conditions. The gas mass flow will fluctuate due to variation in blower speed and mains supply voltage and frequency. Although voltage stabilisation is employed, the temperature can be maintained within $\pm \frac{1}{4}$°C for only a few minutes.

For this reason and also to reduce operator fatigue, automatic reading of thermocouples has been introduced enabling a complete set of readings of 100 thermocouples to be taken in a few minutes. This relaxes the need for continuous monitoring of the absolute temperature since it can be assumed that the absolute temperature of the fuel can remains constant throughout a set of readings. If the same is to apply to the pyrometer then a complete temperature pattern of the fuel can must be obtained in about five minutes. This demands a fast response for the pyrometer and is a function of target area and rate of scan. If the pyrometer is to complete a single scan of the fuel can inside five minutes and yet locate hot spots as small as 1 mm square then a response time to 90% given by (target length/fuel can length) x time for single scan, is required. For a 30" can the value obtained is 0.4 seconds for a scan time of five minutes.

1.10 Temperature range

In a magnox reactor the operating temperature of the fuel elements is typically (7) 450°C. In heat transfer experiments this represents the maximum temperature of operation and most work is done at lower temperatures. The pyrometer will therefore be required to operate up to 450°C. The lower limit required is ideally about 150°C and in this connection it should be realised that the lower temperature limit of the pyrometer is

influenced by the sensitivity, target area and response time discussed above. Since the pyrometer relies for its operation on receiving infra red radiation, its performance is bound to deteriorate as the available energy decreases, which occurs when the specimen temperature is lowered. This means that a compromise always exists between target area, response time, discrimination and lowest measurable temperature. If a large target area can be tolerated then either better discrimination or response time is achieved or on the other hand the instrument will measure lower temperatures. In this application the target area and temperature discrimination are most important and as a result the minimum operating temperature is not as low and response time not as fast as a different application might allow.

Thus it has been decided to maintain a small target area and achieve as low a limit in operating temperature as the other factors will allow. It will be shown that a lower limit of about 250°C should be attainable. This is acceptable in the heat transfer experiments considered.

1.11 Effect of surface geometry

The fuel can has a peculiar surface geometry brought about by the requirement of efficient heat transfer. Variations in surface geometry have the effect of altering the radiating characteristics of the surface or effective surface and this introduces a particular requirement; the pyrometer should be able to measure the temperature at the bottom of the cavity formed by adjacent fins without being influenced by the temperature of the fin walls. This is a very real problem in temperature measurement by infra red means and is dealt with more fully in Chapter 2 when the various types of infra red temperature measuring instruments are examined.

1.12 Effect of coolant gas and window material

The carbon dioxide coolant gas influences the infra red radiation from the can surface in two ways, both of which must be ignored by the pyrometer if accurate temperature measurement is to be ensured. The gas will absorb to some extent the radiation from the can and because it is itself at an elevated temperature due to the heat transfer from the can, it will also emit radiation above the normal background level.

The same is true of the window material, which must be used in place of a section of the metal channel to enclose the pressurised carbon dioxide. To estimate the effect of the heated carbon dioxide and the window material requires a knowledge of their individual temperatures. These are now calculated for future reference.

The heat transfer parameters used in forced convection analysis are the Nusselt, Reynolds and Prandtl numbers all of which are dimensionless (8).

$$Nu = \frac{Q l}{k_c \Delta T}$$

$$Pr = \frac{c_p \eta}{k_c}$$

$$Re = \frac{v_b \rho l}{\eta} = \frac{W l}{A \eta}$$

Q = rate of heat transfer per unit area (chu.ft^{-2}.hr^{-1})

k_c = thermal conductivity of fluid (chu.ft^{-1}.hr^{-1})

ΔT = temperature difference (^{o}C)

c_p = specific heat of fluid at constant pressure (chu.lb^{-1}.^{o}C^{-1})

η = viscosity of fluid (lb.ft^{-1}.hr^{-1})

W = mass flow (lb.hr^{-1})

l = characteristic length (ft)

A = area (ft^{2})

1.13 Calculation of can and coolant gas temperature

In the case of heat transfer from a fuel can it is more convenient to use the Stanton number (9) defined as

$$St = \frac{Nu}{Re\ Pr} = \frac{Q}{c_p v_b \rho \Delta T} \qquad (1\text{-}1)$$

v_b = coolant fluid bulk velocity (ft.hr^{-1})

ρ = coolant fluid density (lb.ft^{-3})

$W = \rho v_b A$ (lb.hr^{-1})

If this expression is used to compare the performance of two fuel cans under similar conditions and we assume that the can heater bar generates heat uniformly along its length, the heat transfer coefficient of the can is given by:-

$$H = \frac{Q P_H}{\Delta T} = \frac{V_i}{J} \frac{I}{L \Delta T} \qquad (1\text{-}2)$$

being the heat lost per unit length per unit time divided by the excess temperature

where V = voltage drop over heater bar

i = heater bar current

L = heater bar length

J = mechanical equivalent of heat

P_H = heat transfer perimeter (given by perimeter of fuel can cross section in Fig.1.1)

ΔT = temperature difference between fuel can surface and bulk gas.

We have further for the continuous flow of coolant in the channel

$$W = \rho v_b A_H \qquad (1\text{-}3)$$

where A_H = free flow area

substitution of H & ρv_b in (1-1) gives:-

$$\frac{St.\ P_H}{A_H} = \frac{Vi}{JLWC_p\Delta T}$$

The bulk rise in temperature of the coolant gas to any point in the channel is calculated from the heat release up to that point assuming no heat loss through the channel walls.

$$\therefore T = T_{inlet} + \frac{Vi}{JWC_p} \times \frac{x}{L} \qquad (1\text{-}4)$$

where x is the distance along the fuel cans at which the temperature T is required

$$\therefore \frac{St P_H}{A_H} = \frac{Vi}{JWC_pL} \left\{ \frac{1}{T_{can} - T_{inlet} - \frac{JVi\,x}{WC_pL}} \right\} \qquad (1\text{-}5)$$

The gas temperature may now be calculated at the centre of the central can and also the temperature of the can itself using the following data for carbon dioxide.

x = distance from end of cans = 3¾ feet (Ref.11)

J = 1900 joules.chu^{-1} (Ref.12)

$\frac{Vi}{L}$ = 10 kW ft^{-1}

P_H = 3.63 ft for typical can (Ref.11)

A_H = 0.06 ft^2 for typical can (Ref.11)

W = 3 lb.sec^{-1} (10800lb.hr^{-1}) (Ref.11)

C_p = 0.26 chu at 275°C and 180 psi (Ref.12)

T_{inlet} = 275°C

∴ gas temperature at centre of central can is, using (1-4)

$$T_{gas} = 275 + \frac{10^4 \times 3.75}{1900 \times 3 \times .26} = 300°C$$

and the can temperature is

$$T_{can} = \frac{Vi}{JLWC_p} \cdot \frac{A_H}{St\, P_H} + T_{inlet} + \frac{Vi\, x}{JWC_p L}$$

$$\therefore T_{can} = \frac{10^4 \times .061}{1900 \times 3 \times .26 \times .0017 \times 3.63} + 275 + \frac{10^4 \times 3.75}{3 \times .26 \times 1900}$$

$$= 367.3°C$$

where the Stanton number is 1.7×10^{-3} which is the value obtained by measurement for a typical fuel can.(9)

1.14 Calculation of window temperature

The window temperature may now be calculated. The calculation is much simplified if emission from the window is neglected initially. In this case a pessimistically high value will be obtained.

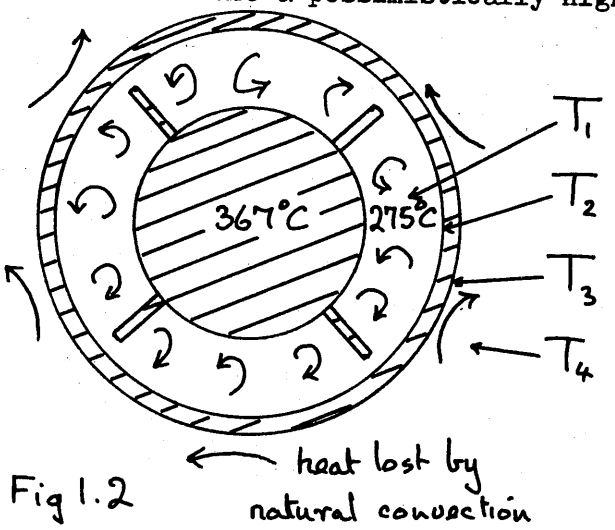

Fig 1.2

Fig. 1.2 shows the situation

T_1 = bulk gas temperature

T_2 = inner wall temperature

T_3 = outer wall temperature

T_4 = air temperature

$\Delta T_1 = T_1 - T_2$

$\Delta T_2 = T_2 - T_3$

$\Delta T_3 = T_3 - T_4$

The inner wall of the channel window is heated by the turbulent coolant gas. The relation between Nu, Pr and Re for fluid flowing in a cylindrical channel (13) is given by:- $\log \frac{Nu}{P_r^{0.4}} = fn(\log R_e)$

An experimental curve describing this function has been obtained (8) and if the following values for carbon dioxide are used the inner wall temperature may be deduced.

l = characteristic length ⅓ ft

η = 0.64 lb.ft^{-1}. hr^{-1} } for CO_2 at 180 psi and 300°C

P_r = 0.71 }

k_c = 0.019 chu.ft^{-1}. hr^{-1}. °C } (Ref. 12)

$$\therefore \log R_e = 5.96$$

$$\therefore \log \frac{Nu}{P_r^{0.4}} = 3.2 \quad \text{using curves given in Ref. 8.}$$

$$\therefore \quad Nu = \frac{Q l}{k_c \Delta T_1}$$

$$= 1600\, P_r^{0.4}$$

$$= 1400$$

whence:-

$$Q = 96.8\, \Delta T_1$$

The flow through the channel wall is given by the conduction equation

$$Q = -k_w A \frac{dT}{dr}$$

$$= -k_w 2\pi r l \frac{dT}{dr}$$

the negative sign is required since heat flows in the direction of decreasing temperature

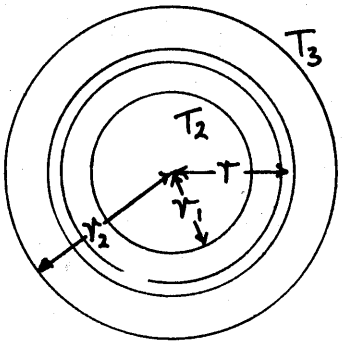

$$\int \frac{dr}{r} = \frac{-2\pi k_w l}{Q} \int dT$$

where k_w = thermal conductivity of window material

$$\therefore \log \frac{r_2}{r_1} = \frac{2\pi k_w l}{Q} (T_2 - T_3)$$

the heat flow/unit area at radius r is

$$Q = \frac{k_w \Delta T_2}{r \log r_2/r_1} \quad (1\text{-}7)$$

k_w = 0.023 chu.ft.$^{-1}$ hr.$^{-1}$ ^{o}C^{-1} (Ref. 10)

$\Delta T_2 = T_2 - T_3$

r = mean radius of annulus 0.156 ft

r_1 = inner radius 0.146 ft

r_2 = outer radius 0.167 ft

$$\therefore Q = 39.2 \Delta T_2 \quad (1\text{-}8)$$

The outer channel wall is cooled by the natural convection of air. In addition to the Nusselt and Prandtl numbers, the Grashof number is used in natural convection analysis.

$$Gr = \frac{\alpha g \Delta T l^3 \rho^2}{\eta^2}$$

α = coefficient of volumetric expansion

g = acceleration due to gravity

The relation between Nu and Gr.Pr has been investigated for horizontal cylinders for which the ratio of length to diameter is large. Experimental curves relating log Nu to log Gr.Pr have been obtained (8) and using the following data for air we have

$$\log Nu = fn(\log Gr.Pr)$$

$$\frac{g c_p \rho^2}{k_c \eta} = 24.5.10^7 \text{ ft.}^{-3}$$

$$\alpha = \frac{1}{423}$$

$$l = \frac{1}{3} \text{ foot.}$$

the parameters used for the circulating air are those at the mean temperature between channel and ambient temperature (150^{o}C)

$$Gr.\,Pr = 24{\cdot}5.10^{7}\,\frac{\Delta T_3}{423\times 27}$$

$$= 21{\cdot}4.10^{3}\,\Delta T_3$$

$$Nu = \frac{Ql}{k_c \Delta T_3} = 17{\cdot}5\,\frac{Q}{T_3}$$

$$\log 17{\cdot}5\,\frac{Q}{\Delta T_3} = fn\left(\log 24{\cdot}5.10^{7}\,\frac{\Delta T_3}{423\times 27}\right) \qquad (1\text{-}9)$$

summing the temperature difference from channel coolant to ambient gives

$$\Delta T_1 + \Delta T_2 + \Delta T_3 = 280^{\circ}C \qquad (1\text{-}10)$$

$$\text{for } T_{ambient} = 20^{\circ}C$$

combining (1-6) and (1-8)

$$Q = 96{\cdot}8\,\Delta T_1 = 39{\cdot}2\,\Delta T_2 \quad \therefore \frac{\Delta T_2}{\Delta T_1} = 2{\cdot}46$$

substituting in (1-10) and using (1-6)

$$\Delta T_3 = 280 - \Delta T_1 - \Delta T_2 = 280 - 3{\cdot}46\,\Delta T_1$$

$$= 280 - \frac{3{\cdot}46\,Q}{96{\cdot}8}$$

$$= 280 - {\cdot}036\,Q$$

substituting in (1-9)

$$\log 17{\cdot}5\left(\frac{Q}{280-{\cdot}036Q}\right) = fn\left[\log 21{\cdot}4.10^{3}(280-{\cdot}036Q)\right] \qquad (1\text{-}11)$$

With the aid of the experimental curve of Ref. 8 a value of Q is obtained:-

$$Q = 358 \text{ chu. ft}^{2}.\text{hr}^{-1}$$

$$\therefore \Delta T_1 = 3{\cdot}7^{\circ}C. \text{ and } T_2 = 271{\cdot}3^{\circ}C$$

$$\Delta T_2 = 9{\cdot}1^{\circ}C. \qquad T_3 = 262{\cdot}3^{\circ}C$$

$$\Delta T_3 = 267{\cdot}2^{\circ}C.$$

The additional cooling due to emission from the quartz may now be estimated. The emissivity of quartz is very nearly unity (i.e. approaching a black body) at wavelengths greater than four microns and very nearly zero at wavelengths less than four microns. Thus at 262°C quartz will radiate 75% of the energy radiated by a black body.

Emission from a black body at 262°C is 0.46 watts cm^{-2}. sec^{-1}

∴ Emission from quartz at 262°C is approximately 0.34 watts cm^{-2}. sec^{-1}

= 617 chu.ft^{-2}. hr^{-1}

The emission suggests that the heat flow is $\frac{617 + 358}{358}$

= 2.72 times as great as calculated from convection effects alone. Thus the temperature gradients across the carbon dioxide quartz interface and the quartz wall can be adjusted by the same factor:-

$\Delta T_1 = 10.1°C$ $\quad\therefore\quad T_2 = 265°C$

$\Delta T_2 = 25°C$ $\quad\quad T_3 = 240°C$

and ΔT_3 is adjusted with a small effect on the convective heat transfer:-

$\Delta T_3 = 220°C$

Equation (1-9) is now modified to :-

$$\log 0.0795Q = fn\left[\log 4.7 \cdot 10^6\right]$$

and using the experimental curve of ref. 8 we have: $Q = 282$ chu.ft^{-1}. hr^{-1} showing that the modification of the original calculation of convective heat transfer is not changed appreciably by the introduction of the emission term.

1.15 Temperature gradient across can wall

The temperature gradient across the can wall may be estimated using equation (1-7) and the dimensions of a typical can.

$$Q = \frac{k_m \Delta T}{r \log r_2/r_1}$$

Q = heat flow/unit area/unit time

$$Q_l = \frac{2\pi k_m \Delta T}{\log r_2/r_1}$$

Q_l = heat flow/unit length/unit time

$$\Delta T = \frac{Q_l \log r_2/r_1}{2\pi k_m}$$

$= 6.5°C\ kW.^{-1} ft^{-1}.\ inches^{-1}$

Q_l = 1kW per foot

r_2 = 0.6 in.

r_1 = 0.5 in.

k_m = 84.3 chu.ft^{-1}. hr^{-1}. $°C^{-1}$

Thus for a typical heat flow of 10 KW.ft^{-1} the gradient over the can wall is 6.5°C for a wall thickness of 1/10 in.

The values ΔT_2 = 9.1 and 25°C represent the limits for the temperature gradient over the window. ΔT_2 = 9.1°C is very pessimistic and ΔT_2 = 25°C is slightly optimistic. Thus with the can at 367°C a temperature difference of about 110° to 120°C exists between the can and the outer wall of the channel for the typical coolant flow of 3lb.sec^{-1}.

1.16 Summary of Specification

Discrimination between temperatures ± 1°C.

Absolute accuracy - not critical - factors affecting it require further assessment

Response time - faster than 1 second to 90% of a step input

Target area - 1 mm square

Temperature range - 250 to 450°C

Surface geometry - indication of temperature independent of geometry of fuel can surface

Coolant gas - indication of temperature to be unaffected by absorption and emission of coolant gas.

Observation window - indication of temperature to be unaffected by absorption and emission of observation window.

1.17 Conclusion

It has been shown that a pyrometric method of temperature measurement could prove useful in heat transfer measurements. The specification for a pyrometric system has been compiled and the conditions under which it would be required to operate have been considered. It has been shown in particular that the pyrometer should be capable of measuring the temperature of an area of approximately 1 mm square of can with a sensitivity of 1°C at typical test temperatures of 300°C. Furthermore its performance should be unaffected by the peculiar reentrant geometry of the fuel can, and the measurement should be made through a suitable window, which will be 100°C lower than the fuel can under typical conditions in a heat transfer rig.

1.18 References

1. M. Goldring. J. Brit. Nuclear Energy Soc.,1964,3,(1),p.11. Discussion (3),p.222

2. J.K. Roberts and A.R. Miller. Heat and Thermodynamics,5th Edition. London,Blackie,1960,p.319

3. Calder Symposium. J. Brit. Nuclear Energy Conf.,1957,2

4. H.H. Gott et al. Symposium on the Use of Secondary Surfaces for Heat Transfer with Clean Gases. Paper 1. Inst. Mech. Eng.,Nov.1960

5. B.E. Boyce. APC Internal document

6. Nuclear Eng.,1964,9,(96),p. 185

7. APC Internal document

8. M. Fishenden and O.A. Saunders. An Introduction to Heat Transfer. Oxford,Clarendon Press,1957,p.71, p.110

9. M.R. Slack and C. Cunningham. Symposium on the Use of Secondary Surfaces for Heat Transfer with Clean Gases. Paper 10. Inst. Mech. Eng.,Nov.1960

10. G.N.C. Kaye and T.H. Laby. Physical and Chemical Constants, 12th Edition. London,Longmans Green & Co.,1959,p.53

11. J.A. Lang. APC Internal document

12. D. Slater. UPC Internal document

13. W.H. McAdams. Heat Transmission,3rd Edition. New York, McGraw-Hill,1954,p.219

CHAPTER 2 - TEMPERATURE MEASUREMENT USING INFRA RED RADIATION

Introduction

The origin of infra red radiation is considered with particular reference to emission from heated metals and reentrant surfaces. The various types of instrument which measure temperature by infra red means are compared and the most suitable system for the application is selected. A feasibility study is carried out using the selected system in a suitable region of the infra red spectrum decided upon in the light of information available on the spectral emissivity of magnox, the spectral response of infra red detectors, the radiation laws, the absorption bands of gases in the radiation path and the window material of a heat transfer loop. Theoretical calibration curves are calculated for various possible operational wavebands in this region and the level of radiated energy at these wavelengths is estimated. It becomes apparent that information on the spectral emissivity of magnox must be obtained to enable the design to proceed.

2.1 The nature of infra red radiation

All matter emits and absorbs a continuous band of electromagnetic radiation which is the result of the thermal motion of the elementary charged particles. The intensity of the radiation increases with temperature due to the increased thermal agitation, and it is distributed throughout the spectrum in a manner which is dependent upon the temperature. It is found that as the temperature is increased the maximum intensity moves to shorter wavelengths. In addition to the continuous spectrum there exists selective sources of radiation where the emission is concentrated around preferred modes of vibration or when an electron makes a transition between two quantum states.

Although electromagnetic waves are radiated at all wavelengths by these processes we shall confine our attention to the near infra red region of the spectrum where the maximum radiated energy is available from bodies in the temperature range 200 to 500°C. This region extends from about 1 to 20 microns and the radiation originates during molecular vibration and rotation in gases, molecular vibrations in liquids and molecular vibrations in solids.

The absorption of electromagnetic radiation takes place when the processes described above operate in reverse. Thus the absorption of continuous radiation produces increased thermal agitation and hence an increase in temperature while selective absorption causes increased vibration in the preferred modes. No material can absorb all the energy incident upon it however, but in practice a close approximation to a perfect absorber or black body exists in the form of a small opening in a large enclosure (1). Radiation at any wavelength entering the enclosure will undergo multiple reflections inside the enclosure until virtually all the original energy has been absorbed and a negligible amount reflected back out through the opening. It can be shown that a good absorber is also a good radiator (2) from which it follows that a black body will radiate more energy at a given temperature than any other material.

Thus the radiant emissivity of a surface is defined as

$$\varepsilon = \frac{I}{I_b} \tag{2-1}$$

Where I_b is the total radiant power per unit area emitted from a black body at the same temperature. The radiant emissivity cannot exceed unity which is the value for a black body.

In the same manner the spectral radiant emissivity of a surface is defined as

$$\varepsilon_\lambda = \frac{I_\lambda}{I_{b\lambda}} \tag{2-2}$$

Where I_λ is the spectral radiant power per unit area emitted from the surface and $I_{b\lambda}$ is that for a black body at the same temperature.

2.2. Planck's Radiation Law

Since the radiant emission from any material can be expressed by the product emissivity times radiant emission from a black body, the theoretical prediction of the distribution of energy emitted by a black body throughout the spectrum as a function of temperature has been established. This prediction, Planck's Radiation Law (3) can be obtained by considering all the possible modes of oscillation for electromagnetic waves inside a cavity. The result is an expression for the energy density of radiation in a black body enclosure.

$$\rho_\nu \, d\nu = \frac{8\pi\nu^2}{c^3} \cdot \frac{h\nu}{e^{\frac{-h\nu}{kT}} - 1} \, d\nu$$

It is more convenient for our purposes to convert this to an expression for the energy density as a function of wavelength.

We have: $\rho_\lambda = \frac{E}{\lambda}$; $\rho_{\bar\nu} = \frac{E}{\bar\nu}$; $\bar\nu = \frac{1}{\lambda}$

$$\therefore \frac{d\bar\nu}{d\lambda} = -\frac{1}{\lambda^2} = -\frac{\bar\nu}{\lambda}$$

$$\therefore \frac{\rho_\lambda}{\rho_\nu} = \frac{\bar\nu}{\lambda} = -\frac{d\bar\nu}{d\lambda}$$

$$\therefore \frac{d\nu}{d\lambda} = -\frac{c}{\lambda^2} \qquad \text{since } \nu\lambda = c$$

$$\therefore \rho_\lambda \, d\lambda = \frac{8\pi c h}{\lambda^5} \cdot \frac{1}{e^{\frac{ch}{k\lambda T}} - 1} \cdot d\lambda \tag{2-3}$$

by considering the portion of this energy which leaves unit area in unit time we have (4)

$$I_\lambda d\lambda = \frac{2\pi c^2 h}{\lambda^5} \cdot \frac{d\lambda}{e^{\frac{ch}{k\lambda T}} - 1} \qquad (2\text{-}4)$$

$$\text{where } \frac{ch}{k} = 1.438 \text{ cm}^\circ K = C_1$$

This is the spectral radiant emittance of a black body into a hemisphere in the wavelength range λ to $\lambda + d\lambda$.

The spectral radiant emission for a black body at temperatures in the range of interest is shown in Fig. 2.1 using logrithmic scales. The emission at any value always increases with temperature and the wavelength at which maximum radiation λ_m occurs, decreases as the temperature increases. This wavelength is determined by setting the derivative with respect to λ in (2-4) equal to zero. The resulting expression can be reduced to

$$\left[1 - \frac{C_1}{5\lambda_m T}\right] e^{\frac{C_1}{\lambda_m T}} = 1 \qquad (2\text{-}5)$$

The solution to this equation with the value for C_2 substituted gives Wien's displacement law

$$\lambda_m T = 2897 \text{ microns.}^\circ K \qquad (2\text{-}6)$$

Further development of these equations leads to the following results

(i) The radiant emission is proportional to the fifth power of the absolute temperature providing λT is maintained constant (i.e. emission at λ_m).

(ii) The radiant emission of a black body over all wavelengths, which is obtained by integration of (2-4) is proportional to the fourth power of the absolute temperature (Stefan's Law).

(iii) The radiant emission of a black body at wavelengths much smaller than λ_m falls off exponentially for a given temperature.

No departure has been found experimentally from Planck's radiation law and consequently it can be used as a reliable basis for the design of instruments employing infra red radiation.

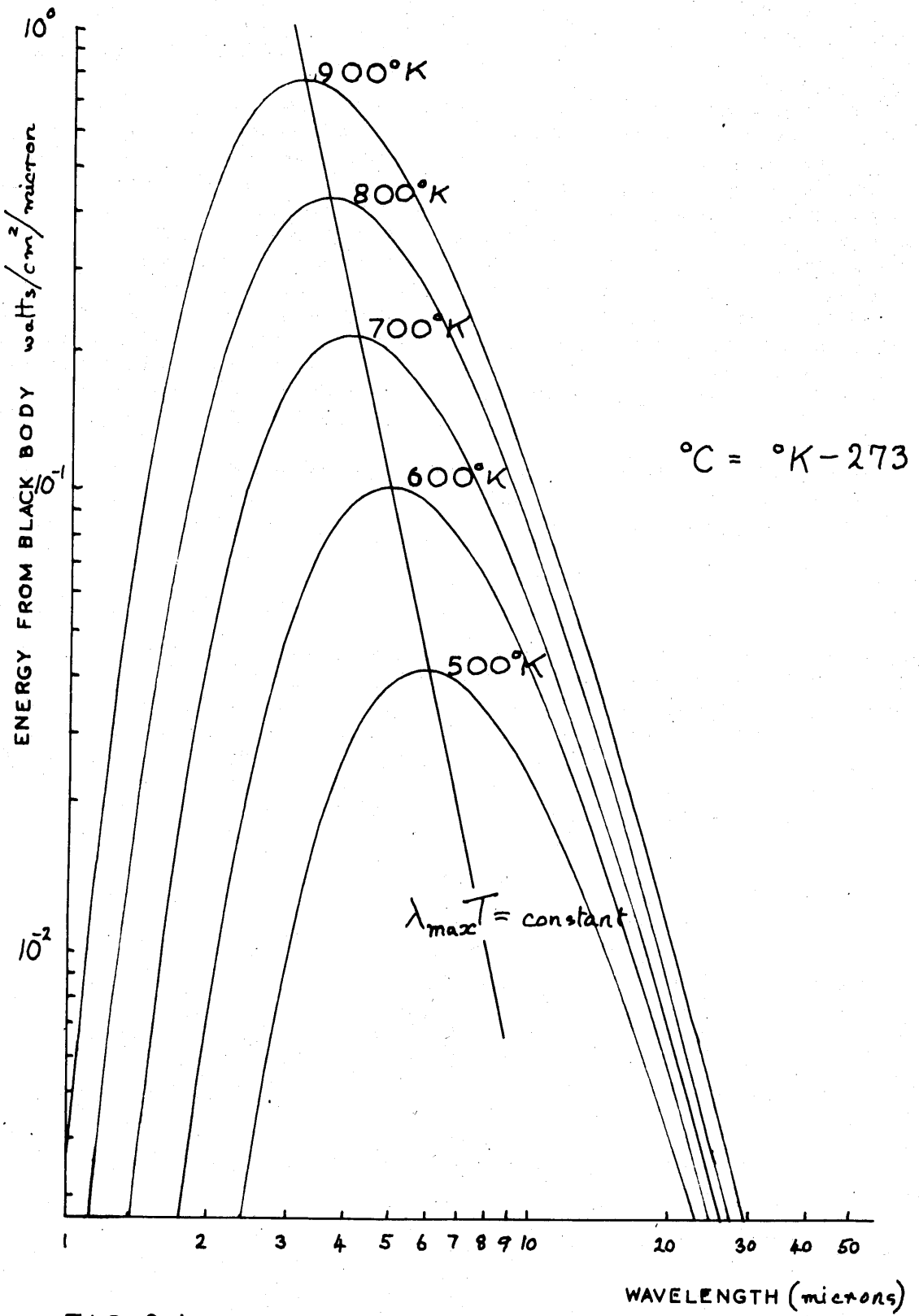

FIG 2.1. SPECTRAL EMISSION FROM BLACK BODY

2.3. Emission from non-ideal surfaces

In practice the emissivity of materials varies with wavelength, producing a departure from the black body curve shape for the energy radiated at a particular temperature. In the case of a clean metal, it is to be expected that the spectral emissivity curve will be smooth, the emissivity varying little with wavelength in the infra red region of the spectrum (See appendix A). The radiation from a metal is confined to emission from atoms in the surface layers of the lattice (5). Radiation from within the metal is suppressed due to the high electrical conductivity. In the case of semi-conductor material radiation is emitted selectively. Thus radiation leaving the material originates both beneath and at the surface over portions of the spectrum and from the surface only for the remainder (6). In insulators, the radiation originates below and at the surface over the entire spectrum.

It can be seen in general therefore that examination of the radiation leaving a surface gives an indication of the surface temperature in the case of a metal and in the other extreme the bulk temperature of an insulator.

2.4. Emission from re-entrant surfaces.

Although the emissivity of a metal is not expected to vary appreciably with wavelength (7), modifications occur in practice due to changes in surface geometry which are large compared with the wavelength of the energy emitted. Since this wavelength is in the micron range the effect of surface roughening must be considered. Consider radiation emitted from a region B into a hemisphere (Fig. 2.2).

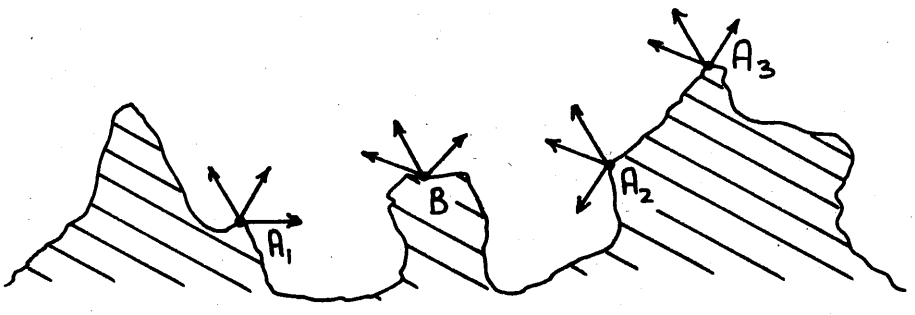

Fig 2.2 Emission from a practical surface.

This radiation will consist of radiation originating at B together with reflected radiation from surrounding regions A_1, A_2, A_3 etc. The radiant emissivity of the specimen at B has thus been changed to a higher value than the surface emissivity. This value, the "effective emissivity", increases with surface roughening until in the extreme case an approximation to a black body cavity is achieved. It is to be expected that surface roughening will produce a variation in spectral emissivity such that as the wavelength decreases the emissivity will increase. (i.e. as wavelength decreases surface geometry becomes relatively more pronounced).

On a larger scale the surface geometry will modify the shape of a spectral emissivity curve. It has been shown (8) that the effective emissivity of a re-entrant surface at uniform temperature is given to a first approximation by:-

$$\varepsilon_\lambda = 1 - r_\lambda \, d\Omega_b . \qquad (2\text{-}7)$$

where r_λ is the spectral reflectivity of a flat surface of the material and $d\Omega_b$ is the solid angle subtended by the back face of the re-entrant surface when viewed from outside the enclosure.

since for a metal $\quad r_\lambda \simeq 1 - \varepsilon_\lambda \sim 0.9$

then for spectral emissivities ε_1 at λ_1 and ε_2 at λ_2

and for spectral reflectivities r_1 at λ_1 and r_2 at λ_2

the ratio $\frac{\varepsilon_1}{\varepsilon_2}$ for a flat surface becomes $\frac{1 - r_1 d\Omega_b}{1 - r_2 d\Omega_b}$ for a re-entrant surface. In this case $r_1 d\Omega_b$ and $r_2 d\Omega_b \to 0$. Thus the ratio approaches unity as the approximation to a black body cavity improves and the spectral emissivity curve is modified as a result, Fig. 2.3. The only shape of the spectral emissivity which will remain unaffected by surface geometry is that which is flat. A material possessing such a spectral emissivity is commonly called a "grey body".

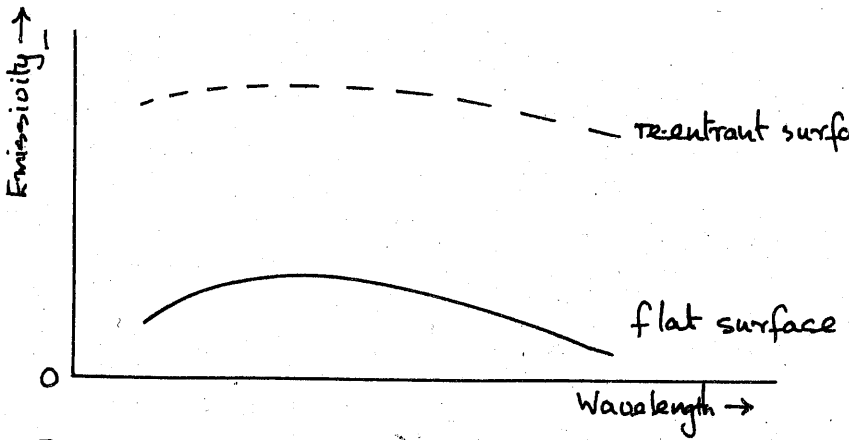

Fig 2.3 Effect of re-entrant surface on spectral emission.

2.5. Measuring techniques available

The limitations of infra red temperature measuring systems will now be considered in the light of the preceding discussion.

The available techniques can be conveniently divided into two groups designated active and inactive devices. The active device employs an infra red source of its own which it compares directly or indirectly with radiation from the specimen. The inactive device which is more common, utilises radiation from the specimen only to determine the temperature.

2.5.1 Total radiation pyrometer

The simplest instrument collects radiation over the whole specimen or over as large an area as can conveniently be observed. Thus by making use of Stefan's T^4 power law it is very sensitive to changes in temperature and can be used in principle to measure specimen temperatures down to ambient. It has the serious drawback that any change in signal reaching the output will be interpreted as a change in target temperature. Such changes in signal may readily be brought about by the following:-

(i) local or wide band variation of the spectral emissivity;

(ii) absorption of radiation between specimen and instrument;

(iii) change in gain of signal amplifying equipment;

(iv) reflection by the specimen of infra red radiation from the surroundings.

Some of these effects may be reduced by careful design and operation of the instrument but their presence inevitably restricts its application.

2.5.2 Selective radiation pyrometer

It follows from Planck's law that the radiant emission varies more rapidly with temperature as the wavelength is reduced (9). This can readily be deduced from Fig. 2.1. If an instrument utilises energy at short wavelengths only, therefore, it becomes more sensitive to changes in temperature. In addition inaccuracies introduced by inappropriate signal changes brought about by (i) to (iv) above will be reduced since such changes represent a smaller temperature change than previously. In general the reduction of the long wavelength limit in such an instrument improves the performance, providing an adequate signal to noise ratio at the detecting element is maintained. The disadvantage of interpreting all signal changes as temperature changes can only be reduced and not be removed, however, because the instrument is still unable to differentiate between changes in signal produced by a temperature change or by other means.

2.5.3 Internal standard pyrometer

The first means which may be adopted to reduce the specimen emissivity dependence of a total radiation pyrometer makes use of an internal standard (10). The standard is made from the same material as the specimen and radiations from standard and specimen are compared. The temperature of the standard is adjusted until zero output is obtained. Being a null device the system is independent of detector sensitivity and gain of the amplifying equipment. It relies however on close agreement being maintained between the spectral emissivity of specimen and standard. The examination of specimens with peculiar surface geometries exposed to uncertain surface treatments introduces serious difficulties in this respect and furthermore the instrument is still sensitive to possible absorption of specimen radiation.

2.5.4 Total or selective emissivity compensated radiation pyrometer

The use of an internal standard may be extended still further if an active system is used (11). This relies on the sum of reflectivity and emissivity of a surface being unity. Radiation from the surface under examination and radiation reflected at the surface from a reference heater is focussed on an infra red detecting element. The intensity of these combined radiations is compared with that from the back of the heater. By automatic adjustment of the heater temperatures they are made equal in intensity. Fig. 2.4 shows that when this condition is reached

$$I_H = r I_H + (1-r) I_b$$

$$\therefore I_H = I_b$$

where T_H = heater temperature

T_S = target surface temperature

r = target surface reflectivity

I_H = energy radiated by heater into optical system.

I_b = energy radiated by black body at same temperature as target surface

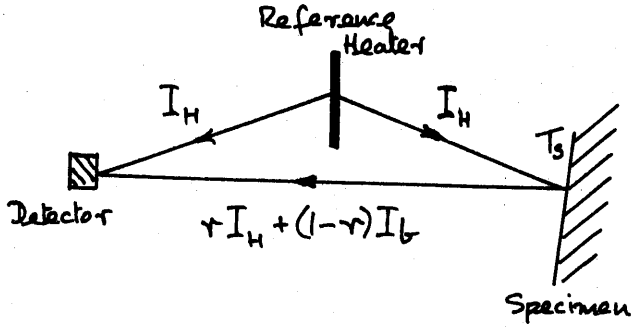

Fig 2.4 Emissivity compensation system

Thus the energy from the heater becomes the same as that from a black body at the temperature of the surface. If the emissivity of the heater were unity then the heater and target surface would be at the same temperature. In practice the heater emissivity is about 0.9 and the heater temperature becomes proportional to the target temperature on the absolute scale.

This system has the advantage that the emissivity of the surface is eliminated during measurement providing all the radiation from the heater, which is reflected by the surface, is collected by the instrument. This means that it will operate accurately only on specular surfaces at normal incidence. When a diffuse surface is examined reflected radiation is lost and inaccuracies are introduced. The performance on re-entrant surfaces is difficult to predict because of the diffusing effect a re-entrant surface introduces.

The response time of the device is determined by the heater performance which will be considerably slower in heating and cooling than the average infra red detector. Again the performance is affected by an absorbing atmosphere. The main advantage of the total radiation pyrometer, operation down to ambient, is maintained; also it is a null device calling for less stringent stability in gain of the supporting circuit.

2.5.5 The ratio pyrometer

The third technique (12-18) to be considered makes use of the change in shape of Planck's radiation curves with temperature. Consider Planck's radiation law applied to the energy radiated by a hot body with spectral emissivity ε_λ. From equation (2-4) it can be seen that the energy radiated in the wavelength range λ_1 to λ_1' is

$$I_1 = 2\pi \varepsilon_1 \times hc^2 \int_{\lambda_1}^{\lambda_1'} \frac{d\lambda}{\lambda^5 \left(e^{\frac{ch}{k\lambda T}} - 1 \right)}$$

providing ε_1 is constant in range λ_1 to λ_1'

and the wavelength range λ_2 to λ_2'

$$I_2 = 2\pi \varepsilon_2 \times hc^2 \int_{\lambda_2}^{\lambda_2'} \frac{d\lambda}{\lambda^5 \left(e^{\frac{ch}{k\lambda T}} - 1 \right)}$$

providing ε_2 is constant in range λ_2 to λ_2'

The assumptions ε_1 constant, ε_2 constant are applicable in this case where a metal is being considered and the wavelength ranges λ_1 to λ_1' and λ_2 to λ_2' are small.

The ratio of these two quantities is

$$R = \frac{\varepsilon_1 \int_{\lambda_1}^{\lambda_1'} \frac{d\lambda}{\lambda^5 (e^{\frac{ch}{k\lambda T}} - 1)}}{\varepsilon_2 \int_{\lambda_2}^{\lambda_2'} \frac{d\lambda}{\lambda^5 (e^{\frac{ch}{k\lambda T}} - 1)}} \qquad (2\text{-}8)$$

Thus if the object is a grey body ($\varepsilon_1 = \varepsilon_2$) or the ratio of the emissivities remains constant in the two wavebands then the ratio R is a function of temperature only. This is the basis of the ratio pyrometer. The system has the following advantages providing the spectral emissivity relation is of the form ($\frac{\varepsilon_1}{\varepsilon_2}$ = constant) and suitable choice of the working wavebands is possible.

(i) the effect of absorption between target and instrument may be eliminated if it is temperature independent.

(ii) variations between diffuse and specular targets may be overcome

(iii) short response times are possible since no internal standard is employed

(iv) change in gain of the amplifying equipment will not affect the signal ratio

(v) If the condition $\frac{\varepsilon_1}{\varepsilon_2} = 1$ can be satisfied then accurate performance is obtained on re-entrant surfaces.

When the instrument is required to read the temperature at the root of a fin it will, in practice, measure a weighted average of the fin root and wall temperature of the cavity produced by adjacent fins, biassed in favour of the fin root temperature. This means that it will detect hot spots or reflections of hot spots. It should be noted that a single channel instrument would misinterpret an increase in emission due to the cavity effect, as an increase in temperature.

The only obvious disadvantage is the lower limit of temperature of operation. This is due to filtering of the available energy to provide the two wavebands, which causes a reduction in the signal to noise ratio.

A further extension of the ratio principle to three wavebands has been reported. In this case two ratio measurements of the energy radiated in three wavebands are required. Such an instrument is able to measure temperature providing the emissivity varies linearly with wavelength (14). It has the disadvantage of much reduced sensitivity to temperature changes (15) since it relies basically on the change in ratio of two quantities which are themselves ratios.

The many advantages inherent to the ratio system can only be realised on certain types of target as the previous discussion shows. Before a decision was made to proceed further, an estimate of the improvement in performance of a ratio pyrometer over the other types of instrument was made for the particular application envisaged; namely that of accurate measurement of the surface temperature of magnox fuel elements under experimental rig conditions.

The first important factor to be investigated was the available sensitivity of a typical instrument. This can be determined if an expression for the rate of change of R with temperature is obtained. If the wavebands are sufficiently narrow for emission over them to be assumed constant, it follows from equation (2-8) that the ratio of energy in the wavebands is

$$\frac{I_1}{I_2} = \frac{\varepsilon_1}{\varepsilon_2}\cdot\left(\frac{\lambda_2}{\lambda_1}\right)^5 \cdot \frac{\left(e^{\frac{c_1}{\lambda_2 T}} - 1\right)}{\left(e^{\frac{c_2}{\lambda_1 T}} - 1\right)} \qquad (2\text{-}9)$$

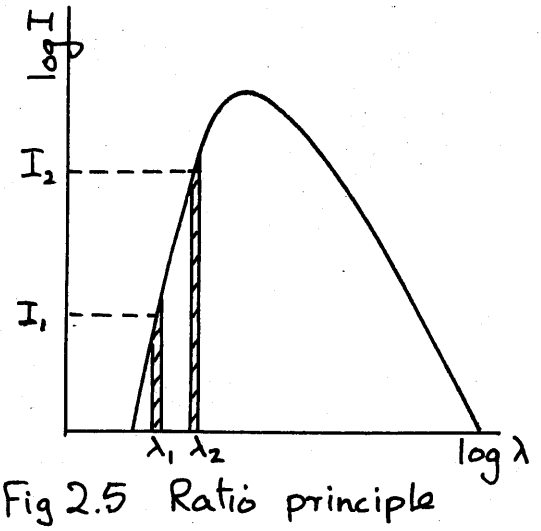

Fig 2.5 Ratio principle

Planck's radiation law has two limiting cases given by the two approximations $e^{\frac{c_1}{\lambda T}} \gg 1$ and $e^{\frac{c_1}{\lambda T}} \ll 1$. The first of these occurs on the low wavelength side of the peak in which case the expression for R reduces to

$$R = \frac{\varepsilon_1}{\varepsilon_2}\cdot\left(\frac{\lambda_2}{\lambda_1}\right)^5 \cdot e^{\frac{c_1}{T}\left(\frac{1}{\lambda_2} - \frac{1}{\lambda_1}\right)} \qquad \text{where } \lambda_1 < \lambda_2$$

If the ratio $\frac{\varepsilon_1}{\varepsilon_2}$ does not change then $R = C_2 e^{\frac{-C_3}{T}}$ where C_2 and C_3 are positive constants chosen to comply with the working wavelengths λ_1 and λ_2.

Thus

$$\log_e \frac{C_2}{R} = \frac{C_3}{T} \qquad (2\text{-}10)$$

The second approximation occurs on the high wavelength side of the peak. In this case R reduces to $R = \left(\frac{\lambda_2}{\lambda_1}\right)^5$ and is independent of temperature.

The initial requirement then, is that the working wavelengths be on the left hand side of the peak radiation over the working temperature range. Consider further (2-10). Fig. 2.6. shows how R/C_2 varies with $1/C_3$ plotted from the values of Table I. It is fortuitous that there exists an approximately linear portion of this curve and by choosing suitable values for C_2 and C_3 the centre of the working temperature range of the instrument can be made to coincide with the point of inflexion of the curve. C_3 is related to the working wavelengths by $C_3 = C_1 \left(\frac{1}{\lambda_1} - \frac{1}{\lambda_2}\right)$ see (2-10) and thus in principle it is possible to choose two wavelengths which will give rise to a linear sensitivity curve for any predetermined temperature range. In practice it may be difficult to achieve this condition since many factors play their part in the choice of wavelengths, but the advantages of a linear relation are considerable in a general purpose instrument and for the present we shall assume that this ideal relationship applies.

2.6. Comparison of performance of various types of instrument

It has already been shown that providing the ratio of emissivities does not vary with temperature then a ratio pyrometer reads accurately on a flat surface. Errors will occur on a re-entrant surface if $\frac{\varepsilon_1}{\varepsilon_2} = 1$. Figs. 2.7 to 2.11 compare the theoretical performance of a total radiation pyrometer, a pyrometer employing a selective detector and a ratio pyrometer on re-entrant surfaces. The assumed characteristics of these pyrometers were

(i) total pyrometer obeying T^4 law calibrated on flat surface of given emissivity (thermopile detector)

(ii) selective pyrometer obeying T^{10} law calibrated on flat surface of given emissivity. Energy radiated in the range 1 to 3 microns from bodies of the temperature of interest (250 to 450°C) obeys a T^{10} law approximately. 1-3 microns is the spectral range of the lead sulphide detector.

(iii) ratio pyrometer obeying linear law with values for $\frac{\varepsilon_1}{\varepsilon_2}$ in the range 1.0 to 2.0 calibrated on a flat surface of given emissivity.

All the figures give the errors introduced by these instruments when measuring on a re-entrant surface at a temperature of 300°C. The variation of the errors with the effective emissivity of the re-entrant surface over the range 0.1-1.0 is shown.

The hypothetical re-entrant surfaces considered for the purpose of these calculations had a reflectivity r_λ where $r_\lambda + \varepsilon_\lambda = 1$ and its effective emissivity was given to a first approximation by

$$\varepsilon_\lambda = 1 - r_\lambda d\beta.$$

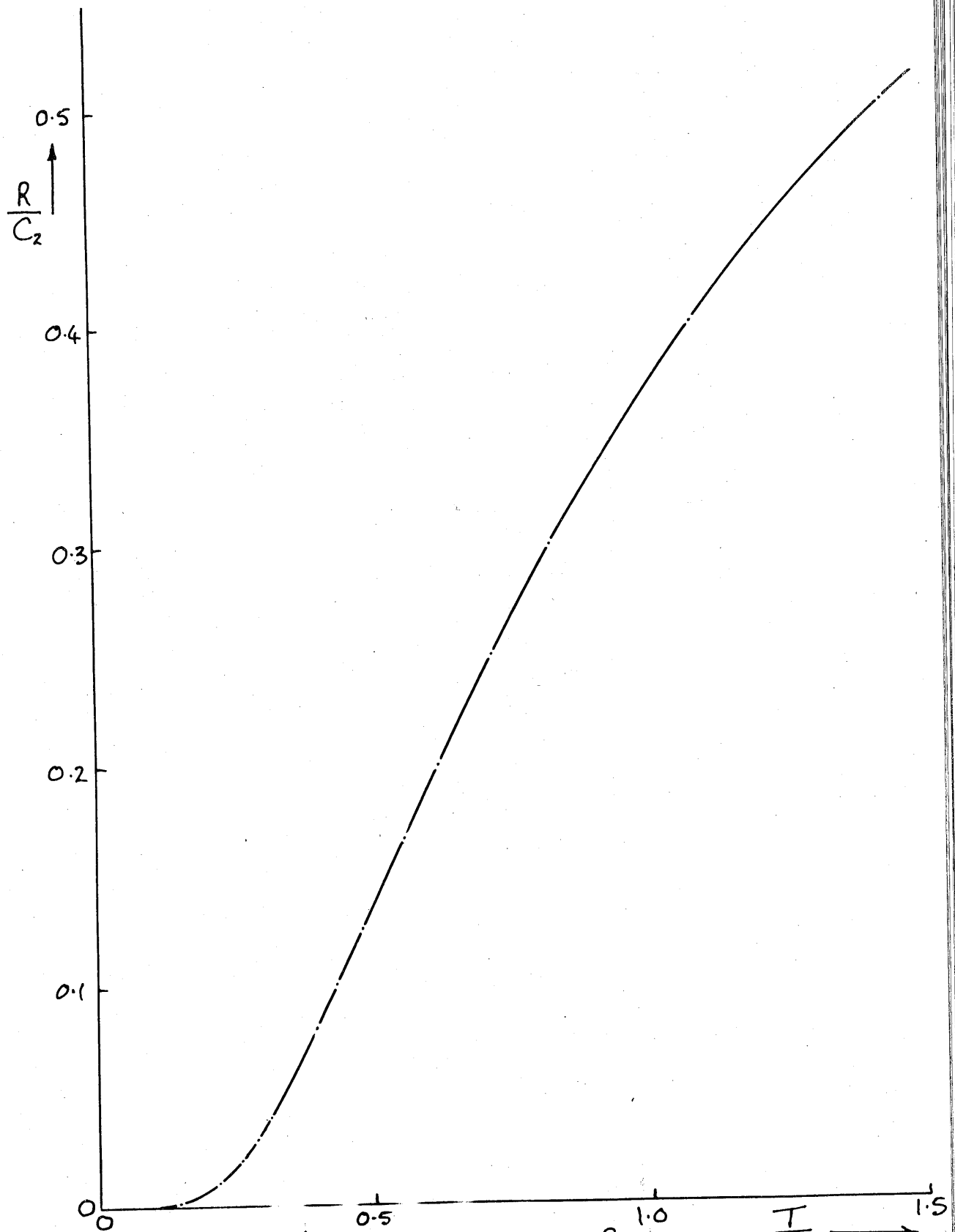

Fig 2.6 General sensitivity curve for a ratio pyrometer.

TABLE I

Values for general sensitivity curve.

$$\log_2 \frac{C_2}{R} = \frac{C_3}{T}$$

$\frac{R}{C_2}$	$\frac{T}{C_3}$
0.001	0.145
0.01	0.217
0.02	0.256
0.03	0.285
0.04	0.311
0.05	0.334
0.08	0.396
0.10	0.434
0.125	0.481
0.16	0.558
0.20	0.622
0.25	0.721
0.30	0.830
0.40	1.092
0.50	1.443

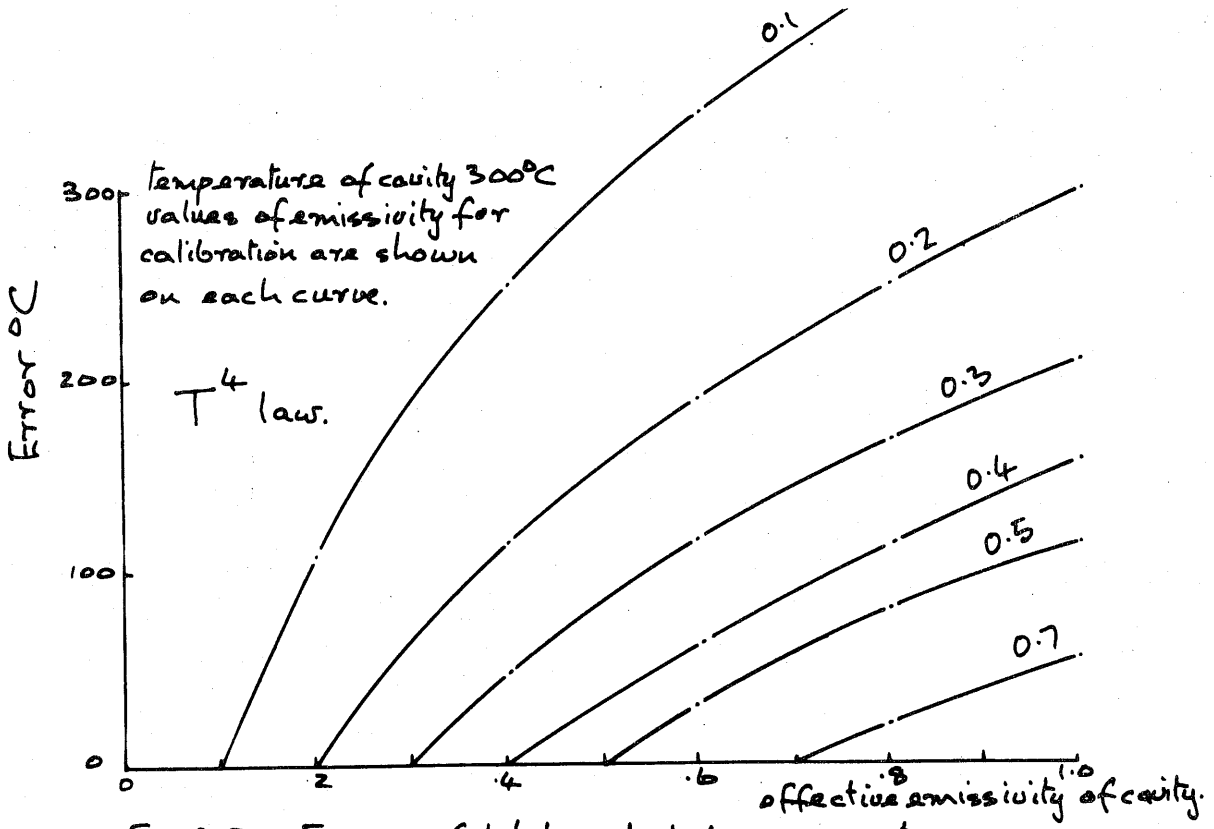

Fig 2.7 Error of total radiation pyrometer on re-entrant surface.

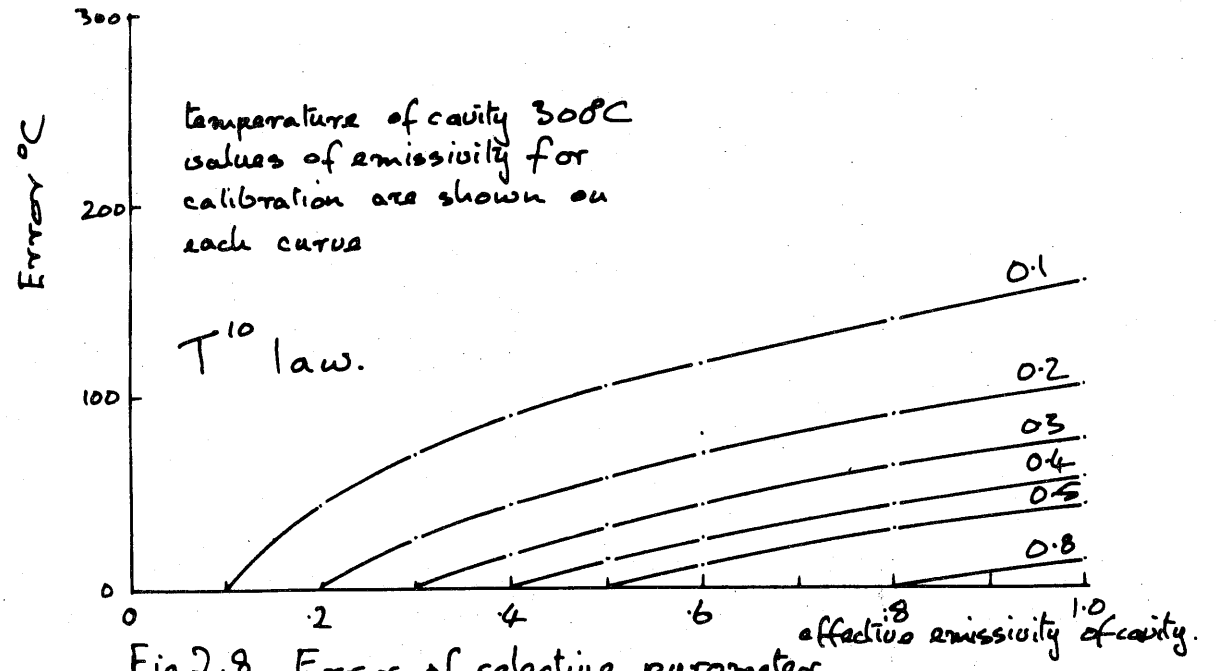

Fig 2.8 Error of selective pyrometer on re-entrant surface.

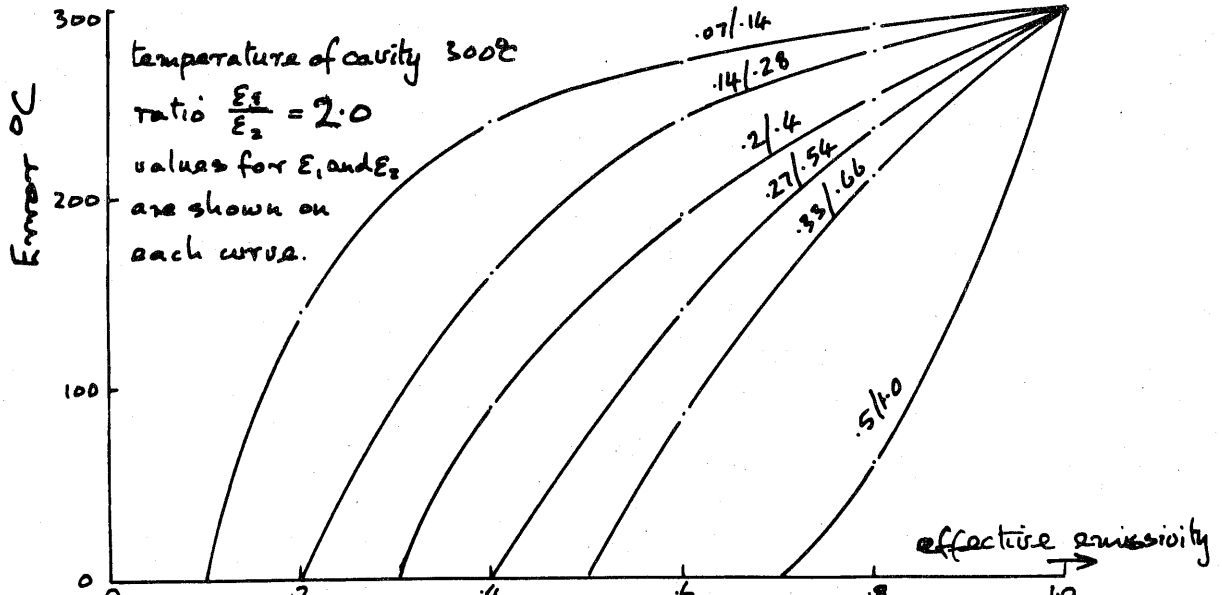

Fig 2.9 Error of ratio pyrometer on re-entrant surface if $\frac{\varepsilon_1}{\varepsilon_2} = 2$

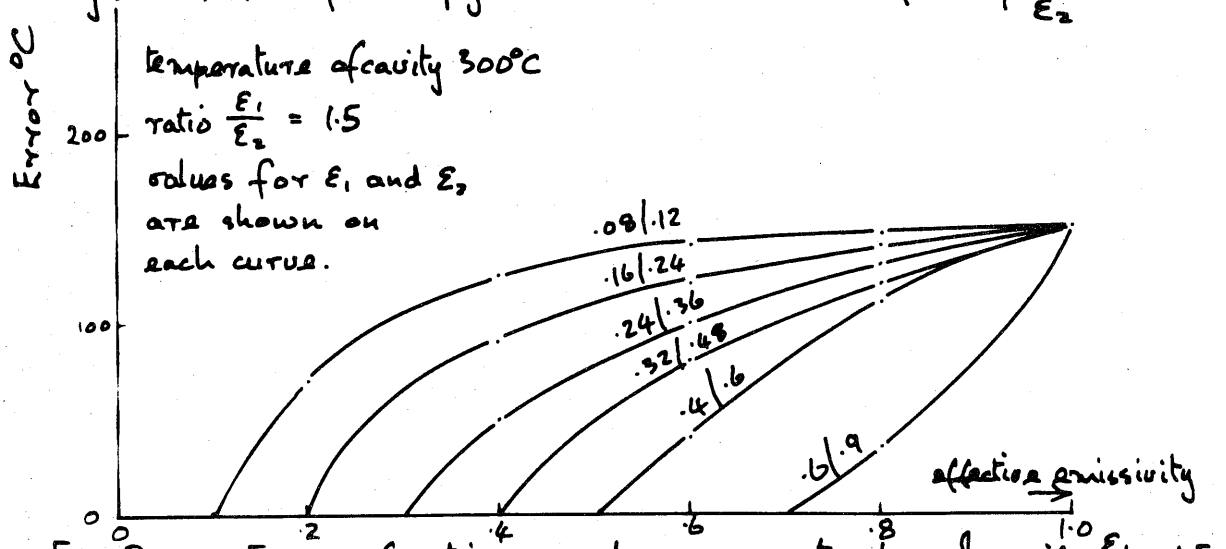

Fig 2.10 Error of ratio pyrometer on re-entrant surface if $\frac{\varepsilon_1}{\varepsilon_2} = 1.5$

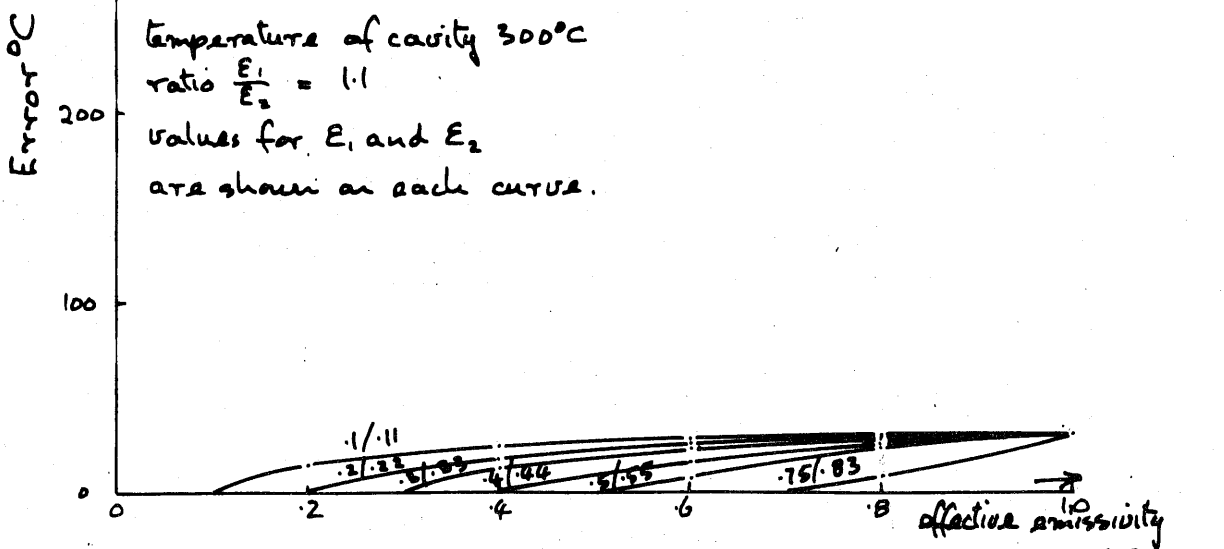

Fig 2.11 Error of ratio pyrometer on re-entrant surface if $\frac{\varepsilon_1}{\varepsilon_2} = 1.1$

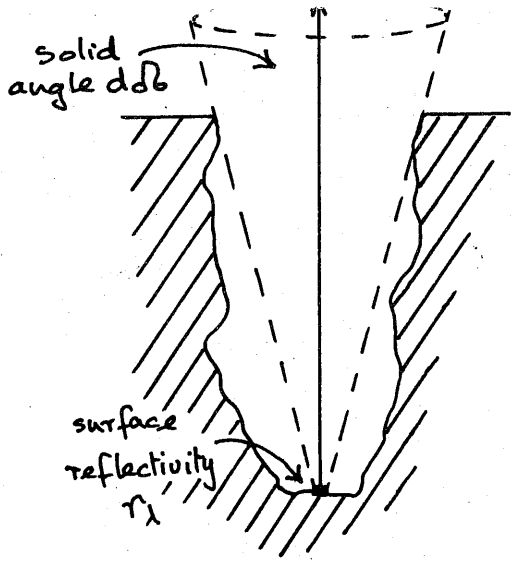

From these figures it can be seen that the performance of a ratio pyrometer on surfaces of low emissivity is better than the performance of a selective pyrometer operating on a T^{10}_4 law providing $\frac{\varepsilon_1}{\varepsilon_2} < 1{\cdot}3$. If a selective pyrometer operating on a T^4 law is used then for equivalent accuracy $\frac{\varepsilon_1}{\varepsilon_2} < 2$ for a ratio pyrometer. The very nature of the infra red emissivity of metals implies that $\frac{\varepsilon_1}{\varepsilon_2} \sim 1$ will be the case. (Appendix A).

All the advantages and disadvantages of the various types of instrument have been summarised below. The ratio pyrometer was chosen as the type of instrument best suited to the particular application envisaged.

Type	Advantages	Disadvantages
T^4 Law Pyrometer	Sensitive to target temperature changes down to ambient	Very emissivity dependent and usually requires temperature control of detector.
		- typical error of 60° occurs at 300°C for a 50% change in emissivity
T^{10} Law Pyrometer	Sensitive to target temperature changes down to about 100°C with reduced emissivity dependence	Requires temperature control of detector - typical error of 30° occurs at 300°C for a 50% change in emissivity.

Type	Advantages	Disadvantages
Internal Standard Pyrometer	Emissivity independent on specular reflectors.	Poor performance on diffuse reflectors of low emissivity (includes re-entrant surfaces). Sensitive to optical alignment.
Ratio Pyrometer	Emissivity independent on surfaces of any geometry providing $\frac{\varepsilon_1}{\varepsilon_2} = 1$ Emissivity independent on flat surfaces providing $\frac{\varepsilon_1}{\varepsilon_2}$ = constant Independent of ambient temperature variations and component ageing due to ratio principle.	Grey body approximation is important consideration and necessarily restricts the application. Nevertheless, providing oxidation effects are not an embarrassment the small dependence on surface geometry makes it ideal for the application envisaged.

2.7. Feasibility study using ratio pyrometer

Before proceeding with the detailed design of the system it was considered advisable to carry out a feasibility study. In this way any fundamental difficulties would be encountered in the early stages and crucial experiments could be designed to decide the best course of action. The feasibility study has been kept short and no attention has been paid to the mechanical execution of the ratio principle. The study is followed by a list of questions to which answers must be found if the required performance is to be obtained. The main function of the feasibility study is to discover whether sufficient sensitivity can be obtained with an economic instrument of reasonable dimensions.

2.7.1 Working wavebands

In this particular application the choice of wavebands is limited. The factors affecting the choice will be dealt with in considerable detail later and it is sufficient only to present them at this stage.

(i) the shape of the spectral emissivity curve of magnox and its dependence upon temperature and oxidation in carbon dioxide.

(ii) spectral response of detectors available.

(iii) the upper wavelength limit which is determined by the peak in the radiation curve at the highest measuring temperature of the instrument.

(iv) the wavelength limits imposed by the window required to contain the specimen in a pressurized system.

(v) absorption of radiation by the carbon dioxide coolant and by atmospheric water vapour.

When the feasibility study was carried out some information was available on all these factors except (i). Four suitable wavebands were found to exist at 1.1-1.3 microns; 1.6-1.9 microns; 2.1-2.5 microns; 3.3-3.7 microns. The first was discarded because insufficient energy is available in that region of the spectrum from surfaces at the lower limit of the desired temperature range. The remaining three wavebands form two near ideal waveband combinations as the following prediction shows.

Consider again the response curve for a ratio pyrometer (2-10)

$$\log_e \frac{C_2}{R} = \frac{C_3}{T}$$

$$\text{let } \frac{R}{C_2} = y \quad \text{and} \quad \frac{T}{C_3} = x$$

$$\therefore \log_e \frac{1}{y} = \frac{1}{x}$$

$$\therefore \log_e y = -\frac{1}{x}$$

The centre of the approximately linear region can be taken as the point of inflexion (x_i, y_i). At this point $\frac{d^2y}{dx^2} = 0$

Differentiating:-

$$\frac{1}{y} \cdot \frac{dy}{dx} = \frac{1}{x^2}$$

$$\frac{dy}{dx} \cdot \frac{dy}{dx}\left(\frac{-1}{y^2}\right) + \frac{1}{y} \cdot \frac{d^2y}{dx^2} = -\frac{2}{x^3}$$

$$\therefore \left(\frac{dy}{dx}\right)^2 \cdot \left(\frac{-1}{y^2}\right) = -\frac{2}{x_i^3} \qquad \text{since } \frac{d^2y}{dx^2} = 0$$

but $\frac{dy}{dx} = \frac{y_i}{x_i^2}$ at the point of inflexion

$$\therefore \frac{y_i^2}{x_i^4} \cdot \frac{1}{y_i^2} = \frac{2}{x_i^3}$$

$$\therefore x_i = 0.5$$

The centre of the linear portion is taken at $\frac{T}{C_3} = 0.5$

and $C_3 = C_1\left(\frac{1}{\lambda_1} - \frac{1}{\lambda_2}\right)$ see derivation of (2-10)
where C_1 appears in Wien's Displacement Law
($C_1 = 1.438 \times 10^4$ microns . ^oK)

For our purposes the centre of the temperature range is 650^oK (377^oC)

$$\therefore \left(\frac{1}{\lambda_1} - \frac{1}{\lambda_2}\right) = \frac{2T}{C_1} = 0.0904$$

λ_2 = 3.5 microns (i.e. centre of waveband 3.3 to 3.7)

$\therefore \lambda_1$ = 2.66 microns for linear calibration

λ_2 = 2.3 microns (i.e. centre of waveband 2.1 to 2.5)

$\therefore \lambda_1$ = 1.9 microns for linear calibration

Thus the wavebands with centres at 3.5 and 2.3 or 2.3 and 1.75 microns provide two near ideal possibilities for this particular application.

2.7.2 Calibration curve based on black body tables

Table II shows how the response curves are modified when true black body radiation functions are used and the finite width of the waveband is taken into account. For various temperatures in the range of interest the wavelength at which peak radiation occurs for a black body was deduced using Wien's displacement law (2-6). The product λT was then obtained for each possible waveband and using black body radiation functions, (19) with extrapolation where necessary, the ratios A, B and C were obtained. The ratios $\frac{A}{B}$ and $\frac{B}{C}$ give the estimated calibrationcurves. The absolute power available radiated into a hemisphere was then deduced from the tables for each waveband.

The energy radiated therefore into a hemisphere at 277^oC in the wavebands from a black body is:-

$$I_{1.75} = 1.67 \times 10^{-4} \text{ watts.cm.}^{-2} \text{ micron}^{-1}$$

$$I_{2.3} = 2.16 \times 10^{-3} \text{ watts.cm.}^{-2} \text{ micron}^{-1}$$

$$I_{3.5} = 1.93 \times 10^{-2} \text{ watts.cm.}^{-2} \text{ micron}^{-1}$$

which covers an energy range of over 100:1

TABLE II

Available energy for proposed pyrometer.

Temperature ^{o}K	400	450	500	550	600	650	700	750	800
Temperature ^{o}C	127	177	227	277	327	377	427	477	527
λ_{max} microns	7.24	6.44	5.80	5.29	4.84	4.47	4.15	3.88	3.63
$\lambda_{1.75}.T$ cm.^{o}K	7.00 10^{-2}	7.88 10^{-2}	8.75 10^{-2}	9.63 10^{-2}	1.05 10^{-1}	1.13 10^{-1}	1.22 10^{-1}	1.31 10^{-1}	1.40 10^{-1}
$\lambda_{2.3}.T$ cm.^{o}K	9.20 10^{-2}	1.03 10^{-1}	1.15 10^{-1}	1.26 10^{-1}	1.38 10^{-1}	1.50 10^{-1}	1.61 10^{-1}	1.73 10^{-1}	1.84 10^{-1}
$\lambda_{3.5}.T$ cm.^{o}K	1.40 10^{-1}	1.58 10^{-1}	1.75 10^{-1}	1.93 10^{-1}	2.10 10^{-1}	2.28 10^{-1}	2.45 10^{-1}	2.63 10^{-1}	2.80 10^{-1}
$A=\frac{I\lambda_{1.75}}{I\lambda_{max}}$	2.07 10^{-4}	1.12 10^{-3}	4.13 10^{-3}	1.14 10^{-2}	2.56 10^{-2}	4.95 10^{-2}	8.43 10^{-2}	1.31 10^{-1}	1.87 10^{-1}
$B=\frac{I\lambda_{2.3}}{I\lambda_{max}}$	7.17 10^{-3}	2.29 10^{-2}	5.35 10^{-2}	1.03 10^{-1}	1.73 10^{-1}	2.58 10^{-1}	3.54 10^{-1}	4.55 10^{-1}	5.55 10^{-1}
$C=\frac{I\lambda_{3.5}}{I\lambda_{max}}$	1.87 10^{-1}	3.25 10^{-1}	4.77 10^{-1}	6.25 10^{-1}	7.50 10^{-1}	8.52 10^{-1}	9.27 10^{-1}	9.75 10^{-1}	9.97 10^{-1}
A/B	2.88 10^{-2}	4.91 10^{-2}	7.71 10^{-2}	1.10 10^{-1}	1.48 10^{-1}	1.91 10^{-1}	2.37 10^{-1}	2.87 10^{-1}	3.37 10^{-1}
B/C	3.84 10^{-2}	7.05 10^{-2}	1.12 10^{-1}	1.66 10^{-1}	2.31 10^{-1}	3.03 10^{-1}	3.82 10^{-1}	4.67 10^{-1}	5.56 10^{-1}
$I\lambda_{1.75}$ watts.cm.$^{-2}$microns^{-1} (for black body)	2.73 10^{-6}	2.68 10^{-5}	1.67 10^{-4}	7.44 10^{-4}	2.57 10^{-3}	7.43 10^{-3}	1.83 10^{-2}	4.02 10^{-2}	7.90 10^{-2}
$I\lambda_{2.3}$ watts.cm.$^{-2}$microns^{-1} (for black body)	9.48 10^{-5}	5.44 10^{-4}	2.16 10^{-3}	6.77 10^{-3}	1.74 10^{-2}	3.88 10^{-2}	7.70 10^{-2}	1.40 10^{-1}	2.35 10^{-1}
$I\lambda_{3.5}$ watts.cm.$^{-2}$microns^{-1} (for black body)	2.47 10^{-3}	7.73 10^{-3}	1.93 10^{-2}	4.09 10^{-2}	7.53 10^{-2}	1.28 10^{-1}	2.01 10^{-1}	3.00 10^{-1}	4.23 10^{-1}

The ratio values show that in both cases departure from linearity occurs causing cramping of the scale at the lower temperatures for each set of wavebands. This is because in each case the lower waveband is taken at a smaller wavelength than that predicted for the centre of the linear portion of the calibration curve to coincide with 377°C. The last three rows of figures show how the absolute power in the waveband changes with temperature.

The calculation so far takes no account of noise effects. If we now assume that the observation area is 0.01 cm^2, the entrance aperture is f/4 (solid angle $\frac{\pi}{64}$), the emissivity 0.1 and a reasonable system transmission of 50%, then the energy falling on the dectector from the sample at 227°C will be:-

$$2 \times \frac{\pi}{64} \times 0.1 \times 0.01 \times 0.5 \times \frac{I_{b\lambda}}{2\pi} \qquad (2\text{-}11)$$

(solid angle)(magnox emissivity)(observation area)(transmission)

$$= 7.81.10^{-6}.I_{b\lambda}$$

$= 3.9 \times 10^{-4}$ micro watts at 1.6-1.9 microns

$= 6.8 \times 10^{-3}$ micro watts at 2.1-2.5 microns

$= 6.05 \times 10^{-2}$ micro watts at 3.3-3.7 microns

The factor 2 in this expression is introduced because radiation from a finite surface falls off with the cosine of the angle of emission (See Appendix B).

The infra red detector will introduce some random fluctuations into the signal. The magnitude of this noise will be the limiting factor to the temperature discrimination of the instrument. Fig. 2.12, 2.13 show the two calibration curves calculated in Table II where the ordinate is a percentage of the ratio at 800°K. Superimposed on these curves is the permissible random noise band for a discrimination of $\pm$ 10°C. Detectors are available which contribute noise equivalent to 10^{-5} μwatts of signal in a 1 cycle band width. Thus a discrimination well within the above can be achieved in principle. The choice of a suitable detector will be discussed in detail later.

Out of this brief estimate of the performance of a ratio pyrometer examining magnox fuel elements the following questions have arisen

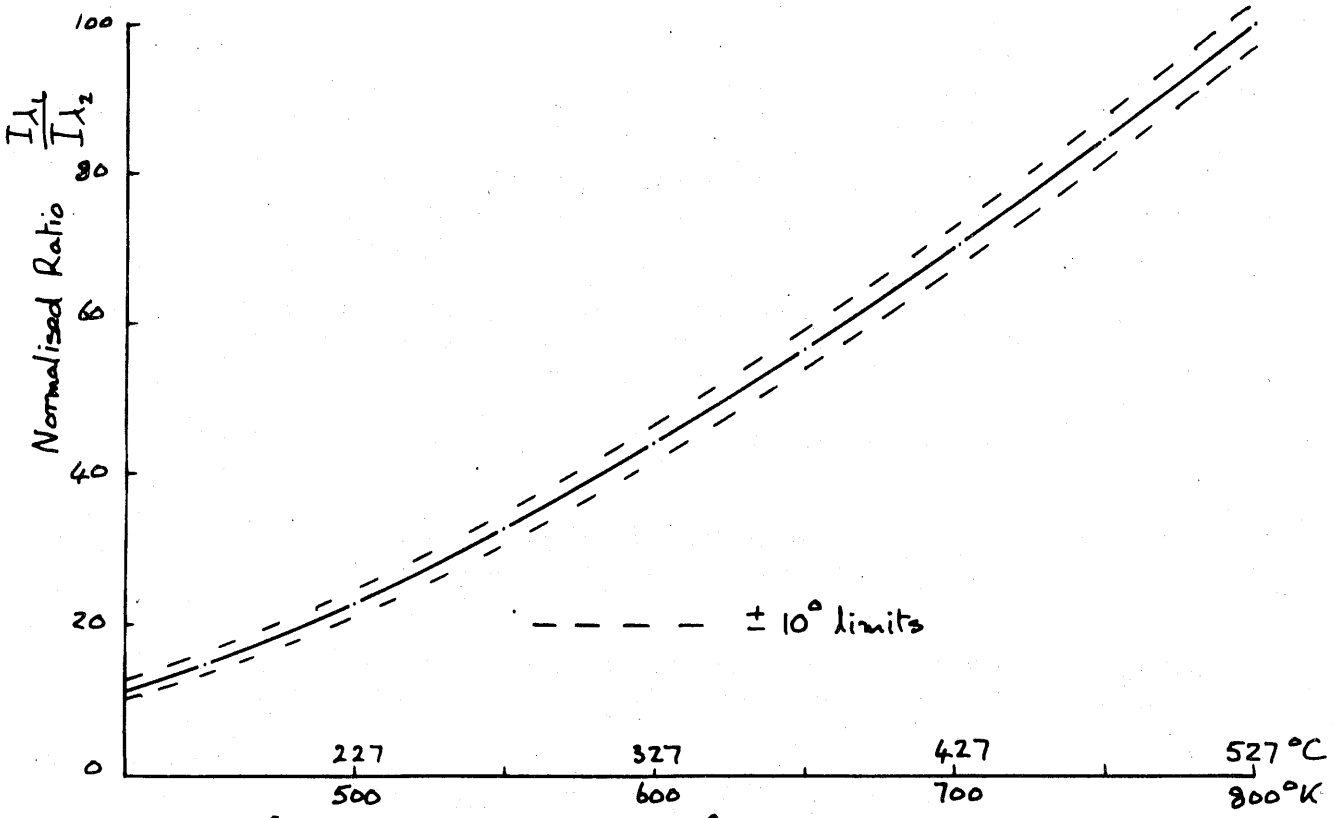

Fig 2.12 Theoretical calibration curve for 1·75 and 2·3 microns.

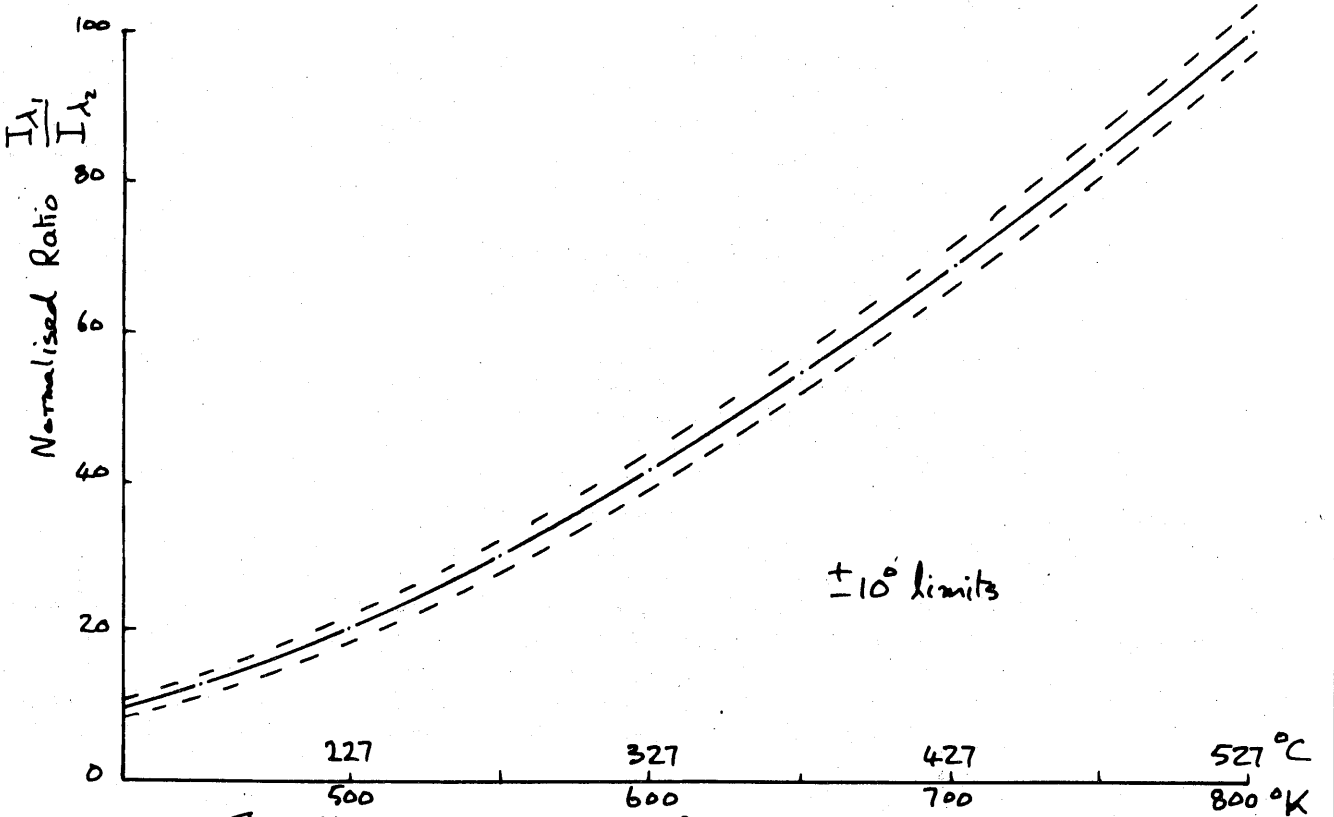

Fig 2.13. Theoretical calibration curve for 2·3 and 3·5 microns

(1) is the spectral emissivity curve of magnox of such a shape that two wavebands may be selected with the same emissivity?

(2) does the emissivity at these two wavebands change in a similar manner with temperature and with surface oxidation by carbon dioxide?

(3) will the wavebands selected, if different from those already mentioned, be sufficiently removed from the absorption bands of carbon dioxide and water vapour?

(4) what are the exact wavelength limits imposed by the window material?

(5) as the energy available in the two wavebands is different, would it be advantageous to sample the two signals for different periods?

These questions are now examined further. When the information could not be obtained from the literature suitable experiments were carried out to establish it.

2.8. The spectral emissivity of clean and oxidised magnox

In earlier sections the limitations of two colour pyrometry have been discussed. One of the deciding factors in choosing a two colour pyrometer is the likely grey nature of magnox in the near infra red. This assumption is based however on theoretical predictions which take no account of surface oxidisation. (Appendix A). While it is to be expected that a small amount of magnesium oxide will not affect greatly the spectral emissivity in the near infra red since it does not absorb or emit appreciably below about 10 microns, it has been suggested that the increase in total emissivity of magnox, when oxidised in carbon dioxide, is not entirely due to the formation of magnesium oxide but rather due to free carbon formed under the reducing action of magnox on carbon dioxide (20)

Since no spectral emissivity information was available it was decided to construct apparatus to measure the spectral emissivity of both clean and oxidised magnox. This apparatus and the results obtained are described in Appendix A and a summary of the results is now given.

The spectral emissivity does not follow as flat a curve as theoretical considerations suggest. The variation of the shape of the curve with oxidation in the presence of carbon dioxide at atmospheric pressure is small, however, and two suitable working wavebands for a two colour pyrometer exist at 1.8 and 2.6 microns where the emissivity is the same. It would be possible to use other wavebands for flat or slightly curved magnox specimens where the emissivities are not the same but the error discussed in section 2.6 would be introduced on re-entrant surfaces.

The spectral emissivity measurements show a reasonable approximation of magnox to a grey body in the region of interest and it was decided to proceed with the design of a two colour instrument on this basis.

2.9. Spectral response of infra red detectors

The range of infra red detectors available is extremely varied and no difficulty should arise in selecting one suitable for use in the spectral region of interest. The choice of the detector is discussed in Chapter 3

2.10 Upper wavelength limit for pyrometer

The upper wavelength limit brought about by the peak in the radiation curve for the highest operating temperature is not well defined. It represents a limit in as much as it causes the calibration curve to depart from linearity but this is fairly arbitrary since the shape of the calibration curve is very dependent upon the exact transmitting characteristics of the waveband selection components. The limit can be fixed at the wavelength at which peak emission occurs at the highest operating temperature. The wavelength is determined from equation (2-6) with a maximum operating temperature of 800°K.

2.11 Absorption bands of carbon dioxide and water vapour

The working wavebands must be outside the absorption bands of carbon dioxide because of its function as coolant in the heat transfer channel. Similarily, the absorption bands of water vapour are to be avoided due to its presence in the atmosphere. The other atmospheric constituents, which absorb infra red radiation and impurities such as carbon monoxide in the coolant gas, are not considered because they are only effective over long path lengths and will have a negligible effect over the two foot path length with which we are concerned. For the same reason scattering by atmospheric dust has also been neglected.

The absorption spectrum of water vapour and carbon dioxide consists of a large number of spectral lines which are arranged in bands. Although the absorption is strongest at the regions at which the bands are said to be located, a small amount of absorption occurs in almost any region of the spectrum. Again because of the short path length with which we are concerned, only the absorption in the main bands need be considered. Water vapour and carbon dioxide are triatomic molecules. Each has three normal modes of vibration which are illustrated in Fig. 2.14.

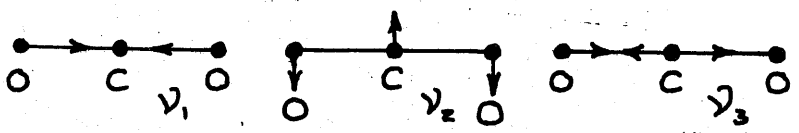

Fig 2.14a Normal modes for carbon dioxide

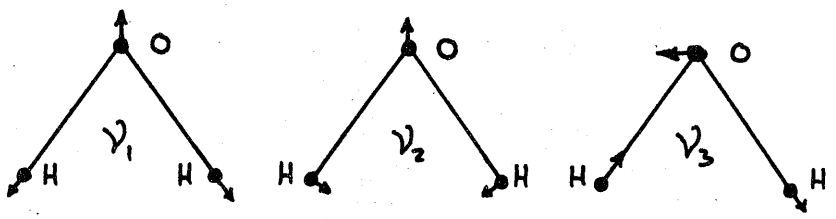

Fig 2.14b Normal modes for water vapour.

Carbon dioxide forms a linear molecule. Of the three normal modes of vibration only ν_2 and ν_3 absorb in the infra red at 15 and 4.3 microns respectively In the case of water the molecule forms an isosceles triangle. The fundamental vibrations ν_1 and ν_3 give two bands which are close together at 2.7 microns and ν_2 is associated with a band at 6.3 microns. In addition to the main absorption there are others which are due to a combination of the normal modes of vibration and the bands of interest lie in the spectral region 1.5 to 4 microns. Theoretical absorption tables have been compiled(21) from various sources(22) and these have been used to obtain the absorption curves illustrated in Fig. 2.15-16. The derivation of these curves for water vapour and carbon dioxide is now explained.

2.11.1 Absorption curve for water vapour

The absorption curves shown in Fig. 2.16 correspond to water vapour concentrations which if fully precipitated would form a film either 0.1 cm or 0.005 cm thick. The latter figure corresponds to a typical path length for the radiation received by the pyrometer under the atmospheric condition of 100% saturation at 30°C which represents an extreme case. The precipitable film thickness was determined as follows.

Consider the paths taken by radiation from the target area on its way to the pyrometer. The path forms a cone (see section 4.4) which is approximately 60 cm long and 15 cm in diameter at its widest point, Fig. 2.17

If the cone is divided into a number of discs of thickness δx then the water vapour contained in the volume of each disc can be represented by a thin film at the centre of the disc. The thickness of the film will be

$$t = \frac{\text{volume of disc x density of water vapour}}{\text{cross sectional area of disc}} = \frac{\pi \frac{d^2}{4} \delta x \times \rho}{\pi \frac{d^2}{4}}$$

$= \rho \delta x$ where ρ = density of water vapour Integrating over the entire cone gives

$$t = \int_0^{60} \rho \, dx = 60\rho$$

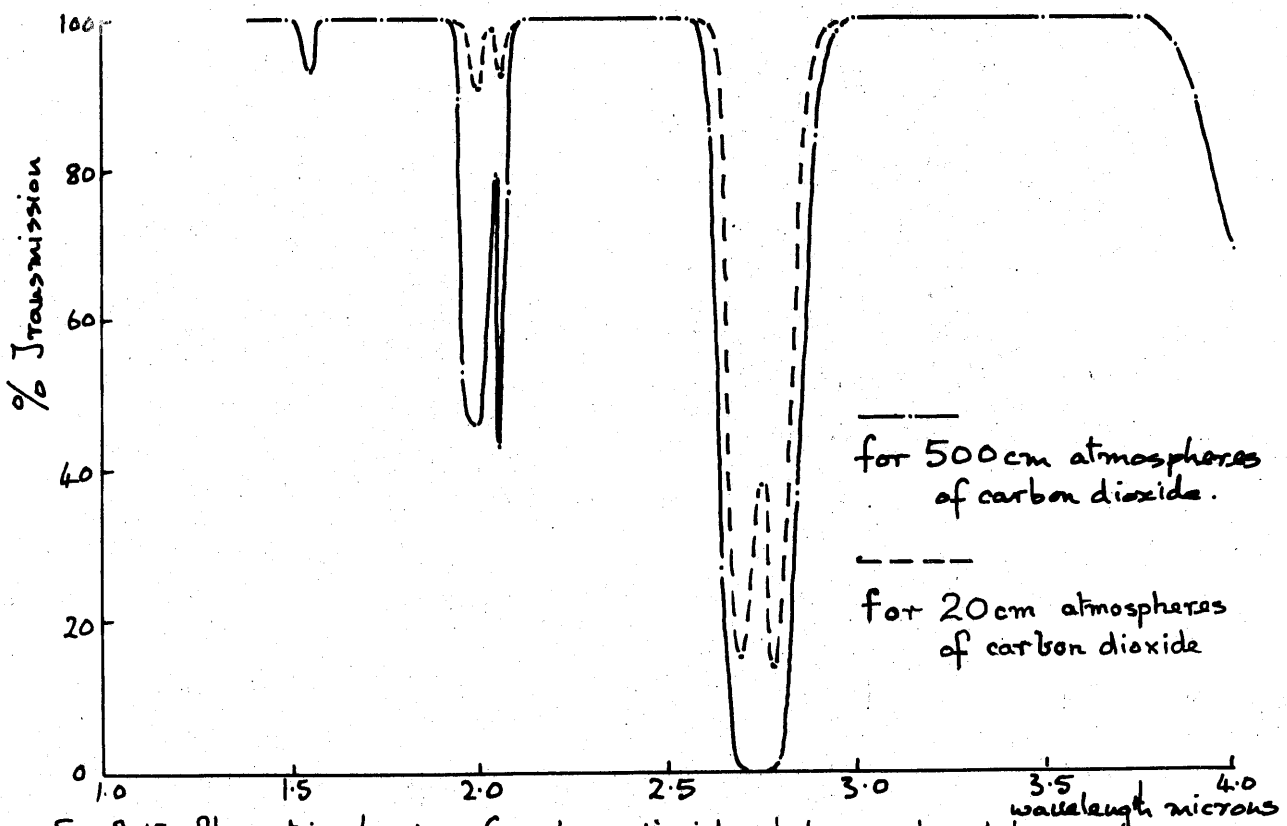

Fig 2.15 Absorption bands of carbon dioxide between 1 and 4 microns.

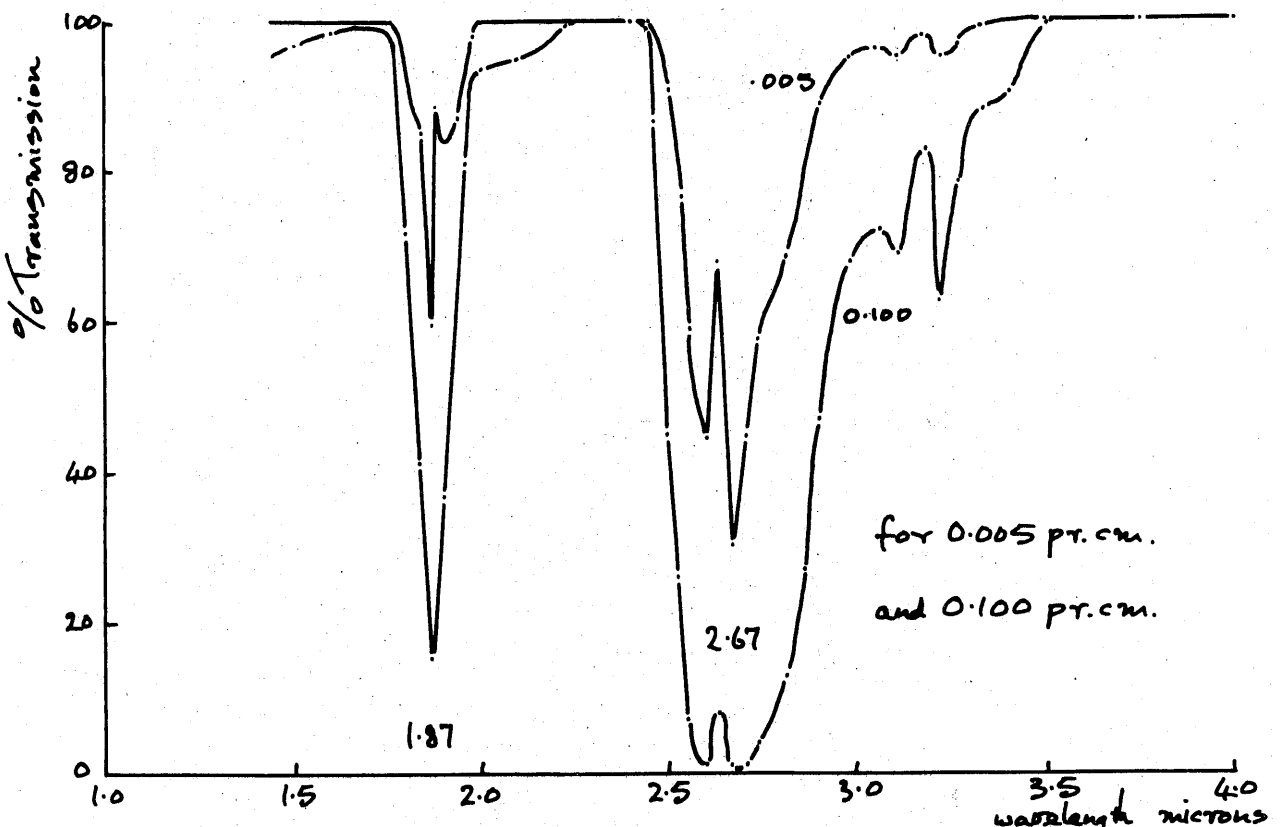

Fig 2.16 Absorption bands of water between 1·5 and 4 microns.

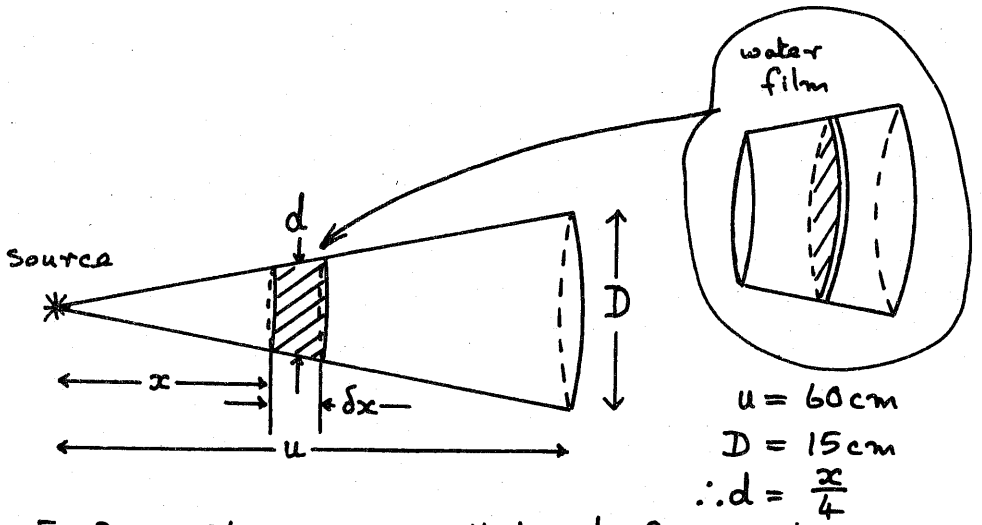

Fig 2.17 Absorption in optical path of pyrometer

An atmospheric condition of 100% saturation at 30°C gives a water vapour concentration of 30×10^{-6} gm.cm^{-3}(23). Thus the water vapour corresponds to a film of thickness

$$t = 0.0018 \text{ cm}.$$

This figure is multiplied by a factor of three to allow for additional absorption in the optical system giving approximately .005 precipitable cm of water vapour.

From Fig. 2.16 it can be seen that the absorption will be less than 1% in the regions 1.5 - 1.8; 2-2.45 and 3.4 - 4 microns.

2.11.2 Absorption curve for carbon dioxide

In order to estimate the absorption of carbon dioxide in the fuel element channel it is necessary to take into account the temperature and pressure of the gas. The highest temperature which is likely to be encountered (see Chapter 1) is 300°C at a can temperature of 450°C and the maximum pressure is 12.7 kg.cm^{-2}

The width of a spectral line is modified by collision processes. The number of molecular collisions increases as the pressure is raised and consequently each spectral line will broaden. When the path length is small the absorption varies linearly with the amount of absorbing gas and is independent of pressure because each molecule is able to absorb to its full extent. At larger path lengths the absorption increases as the square root of the pressure and amount of absorbing gas. In this case the absorption is complete over a band which covers several half line widths on both sides of the line centre. Thus as the number of molecules increases further absorption can only take place at the edges of the band where the molecules do not absorb so well.

The absorption is a function of pressure because as the pressure increases the spectral line broadens and the absorption by individual molecules decreases. On the other hand each one is able to contribute to the absorption now because it is not so well shielded by those preceding it.

The width of a line is modified by the thermal motion of molecules. If the temperature is increased then broadening will occur due to the increase in the probability of finding molecules with higher velocities. The broadening is brought about by the large variation in the frequency of the spectral line as seen by an observer due to the Doppler effect. The half width of the line is proportional to the square root of the absolute temperature. The overall effect of increasing temperature therefore, is for the line broadening to increase the absorption in a similar way to increase of pressure.

The above arguments apply only to absorption by a single spectral line which does not overlap its neighbours which is the case when both pressure and path length are small. When overlapping occurs the absorption is less than that predicted by the single line analysis at longer path lengths.

In order to determine whether the absorption was following a linear or square root law with pressure and temperature the absorption against path length for the carbon dioxide band at atmospheric pressure and 300°K was studied using a table of computed data(21). It was found that the absorption follows a square root law. The absorption has therefore been assumed to be a square root function of pressure and temperature also. The equivalent path length at atmospheric pressure of the carbon dioxide in the channel is obtained as follows.

A cross section of the fuel element channel is shown in Fig. 2.18. The annulus formed by the carbon dioxide coolant is approximately 3.5 cm thick. The maximum pressure used is 12.7kgcm^{-2} and the highest temperature is 300°C corresponding to a fuel element temperature of 450°C.

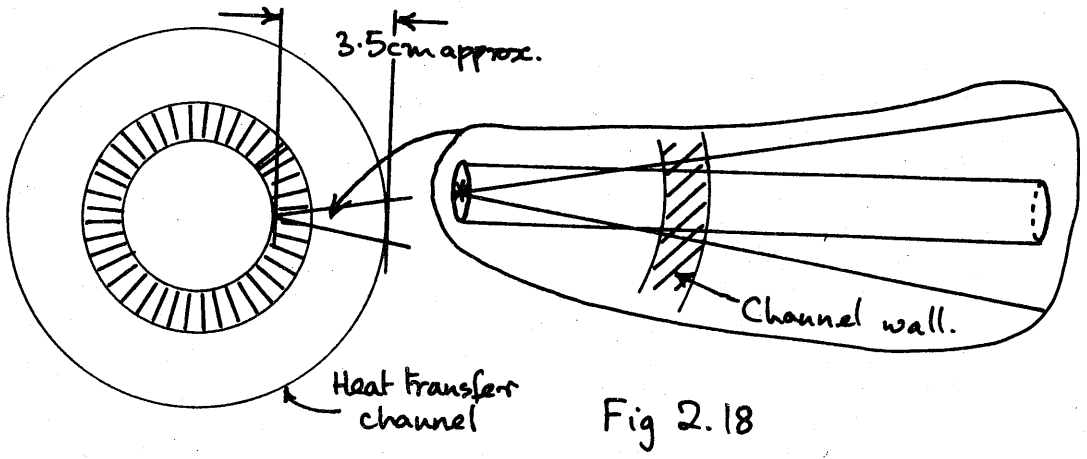

Fig 2.18

The carbon dioxide gas in the conical zone has been replaced by a cylinder with a diameter corresponding to that of the cone half way along its length. The cylinder has been extended to 20 cm using the scaling factor:-

$$\sqrt{\frac{P_c \cdot T_c}{P_o \cdot T_o}}$$

T_c = channel pressure ($12.7 kg.cm^{-2}$)

T_o = atmospheric pressure ($1.06 kg.cm^{-2}$)

P_c = channel temperature ($600^{\circ}K$)

P_o = atmospheric temperature ($300^{\circ}K$)

which corresponds to the path length of the carbon dioxide reduced to atmospheric pressure. The absorption for this length which is referred to in atmosphere centimetres has been obtained from the computed tables (21) for various wavelengths.

The absorption curves are shown in Fig. 2.15. The upper curve estimates the absorption under normal operating conditions and the lower curve is representative of 25 times as much carbon dioxide to emphasise the regions of the spectrum which should be avoided. It can be seen that the absorption is less than 1% in the regions 1.6 - 1.9; 2.1 - 2.55 and 3.0 to 3.75 microns.

The absorption of water and carbon dioxide combined thus limits the choice of wavebands to 1.6 - 1.8; 2.1 - 2.45 and 3.4 to 3.75 microns. These wavebands have been used in the feasibility study described in section 2.7

2.12 Upper wavelength limit imposed by window material

In addition to the transmission of infra red radiation in the required region of the spectrum the window material must be strong to withstand rig pressure and capable of operation at temperatures up to $450^{\circ}C$. It should be chemically inert for the sake of safety when operating at elevated pressure and for convenience in rig design.

The transmission of the window should be as high as possible at the working wavebands and the relative absorption of each waveband should not vary with operating temperature. This means that there should be no absorption bands in the region of interest and the absorption edge should be well outside it. Furthermore the wavelength at which the absorption edge occurs should not decrease appreciably when the window is raised in temperature. All these requirements make fused quartz the obvious choice for the window material. It is chemically and thermally stable and can be worked by cutting, grinding and polishing with ordinary techniques. It transmits from 0.3 to 3.5 microns in practicable thicknesses. Its softening point is $1500^{\circ}C$ and it is as strong as the average glass. The shift of the absorption edge with temperature is not appreciable. Measurements have shown that the shift takes place in the direction of decreasing wavelength as the temperature is raised and a typical amount is 0.4 microns for a $600^{\circ}C$ rise in temperature.(24)

Commercial fused quartz has the disadvantage that absorption occurs at 2.75 microns due to trapped water vapour. Special infra red quality quartz is now available however in which this effect has almost been eliminated.

2.13 Effect of window on pyrometer calibration

In spite of its high transmission characteristics in the infra red the emission from a fused quartz window cannot be ignored, especially when the heat transfer rig conditions are such that the gas temperature and consequently the window temperature approach that of the can.

No information has been found on the direct measurement of the spectral emissivity of fused quartz in the two micron region, probably due to its high transparency, which makes measurements difficult. However, the emissivity may be inferred from the absorption characteristics using an extension of Kirchoff's law to a partially transmitting body. (25) Extensive measurements by Drummond (26) have shown that the absorption coefficient of fused quartz at 2 microns is likely to be less than 0.001 mm^{-1} at room temperature, giving rise to an emissivity of 0.0064 for a thickness of 6.3 mm. It is reported (27) although no figures are given, that the absorption of fused quartz shows little change in the near infra red as the temperature is increased. This suggests that an emissivity of .0064 for a thickness of 6.3 mm may be used for the window at elevated temperature. However, measurements of transmission of heated quartz (24) indicate an emissivity of about .03 at 600°C for a thickness of 2 mm.

In order to estimate the effect of the window the data of Table II have been used with a window emissivity of .033 and a magnox emissivity of 0.1. In this calculation reflection losses have been neglected since they do not affect the result by more than a few percent.

The results are illustrated in Fig.2.19 for various assumed can and window temperatures in the range of interest. It can be seen that the calibration becomes most sensitive to changes in window temperature when the can to window temperature difference is less than 100°C. At larger temperature differences the effect of changes in window temperature is small, amounting to about 5°C change in calibration for a change in window temperature of 50°C.

A more serious effect introduced by the hot window is that it will cause the pyrometer to interpret an effective emissivity change of the specimen as a rise in temperature. Thus, an effective emissivity change of the specimen from 0.1 to 0.2 will halve the error due to the window at a given temperature and may well be the limiting factor in the performance of the pyrometer.

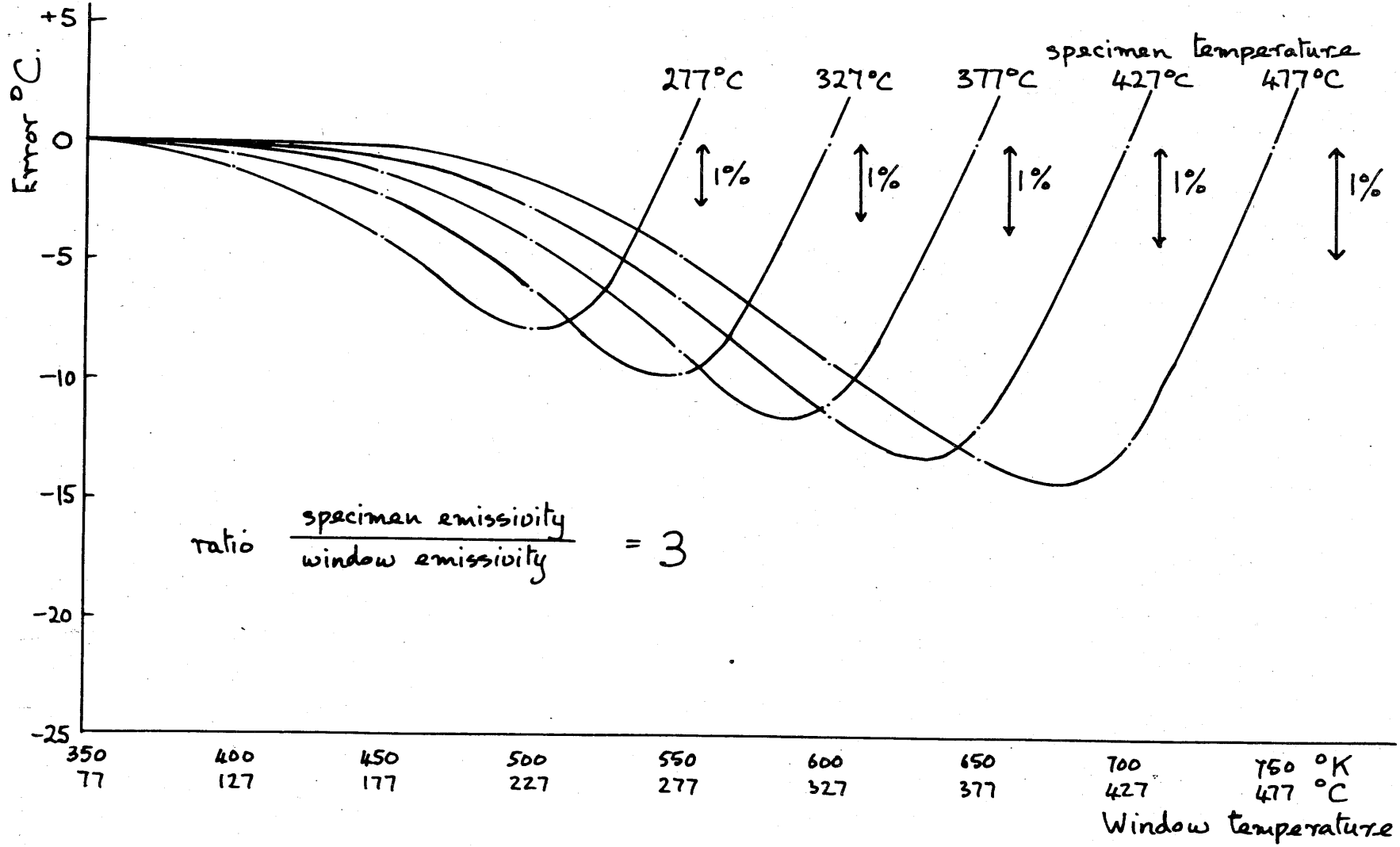

Fig. 2.19 Estimated error introduced by quartz window.

The above argument emphasises the need for a window, not only of the highest quality but also with minimum thickness. Thus, if a double window is used, the hotter portion can be made relatively thin (2 mm) and the cooler portion only needs to be sufficiently thick (6 mm), to withstand the gas pressure. In this case the effect of the window should be reduced by a factor of three: the thicker window will now be cool enough for emission to be neglected and the emission from the hotter window will have been reduced by a factor of three, since absorptivity and emissivity are proportional to thickness, if the absorption coefficient is small.(25)

2.14 Conclusion

It has been shown that provided the spectral emission of magnox does not depart significantly from that of a "grey" body, then a ratio pyrometer should be the most suitable infra red system for measuring the surface temperature of magnox fuel cans. Consideration of the energy level available and operational environment of the instrument have limited the operational region to wavebands in the range 1.5 to 4.0 microns and the required sensitivity of the infra red detector has been calculated. The absorption bands of carbon dioxide and water vapour in this region of the spectrum at 1.9, 2 and 2.7 microns have been examined and the upper wavelength limit imposed by the window has been fixed at 3.5 microns. The interference introduced by the window when heated, has been estimated and it has been shown that the magnitude of the interference could be the factor limiting the performance of the pyrometer.

2.15 References

1. J.K. Roberts and A.R. Miller. Heat and Thermodynamics, 5th Edition. London, Blackie, 1960, p.493

2. Ibid., p.490

3. A. Sommerfeld. Thermodynamics and Statistical Mechanics. New York, Academic Press, 1956, p.150

4. F.K. Richtmyer et al. Introduction to Modern Physics, 5th Edition. New York, McGraw-Hill, 1955, p.123

5. R.W. Wood. Physical Optics. London, MacMillan, 1934

6. T. Land. Glass Industry, May 1962, p.244

7. H. Rubens and E. Hagen. Ann.der Phys., 1903, 11, p.873

8. J.C. de Vos. Physica, 1954, 20, p.669

9. G.K.T. Conn and D.G. Avery. Infrared Methods. New York, Academic Press, 1960, p.186

10. H.L. Hackforth. Infrared Radiation. New York, McGraw-Hill, 1960, p.203

11. D. Kelsall. BSIRA Report R298

12. A.F. Gibson. J.Sci.Instruments, 1951, 28, (5), p.153

13. E.C. Pyatt. Brit.J.Appl.Physics, 1954, 5, (7), p.264

14. T.P. Murray and V.G. Shaw. Instrument Soc.America J. 1958, 5, (12), p.36

15. P.M. Reynolds. Brit.J.Appl.Physics, 1964, 15, p.579

16. H. Herne. Brit.J.Appl.Physics, 1953, 4, p.374

17. G.J. Hecht. Automatic Control, 1962, 16, (3), p.51

18. R.E. Leckenby. Reactor, 1962, 2, (2), p.6

19. American Inst.of Physics Handbook. New York, McGraw-Hill, 1957, p.6-65

20. L.A. Popple. J.Nuclear Mat., 1963, 8, (1), p.60

21. J.A. Jamieson et al. Infrared Physics and Engineering. New York, McGraw-Hill, 1963, p.81

22. P.J. Wyatt et al. Report 1717 & 1718. Aeronautic Division, Ford Motor Co. California

23. O.T. Zimmerman and I. Lavine. Psychrometric Tables and Charts. Dover U.S.A., Industrial Research Service, 1945, p.25

24. D.W. Lee and W.D. Kingery. J.Amer.Ceramics Soc., 1960, 43, (11), p.594

25. H.O. McMahon. J.Opt.Soc.America, 1950, 40, (6), p.376

26. D.G. Drummond. Proc.Roy.Soc., Series A, 1936, 153, p.318

27. T. Wentink and W.G. Planet. J.Opt.Soc.America, 1961, 51, (6), p.595

CHAPTER 3 - THE INFRA RED DETECTOR AND ITS INFLUENCE ON THE DESIGN OF THE SYSTEM.

Introduction

The infra red detectors which are available commercially for use in the infra red region of interest, are discussed. The limitations already introduced in the preceding chapters narrow the choice to a few types in the semi-conductor range. Of these few types, those which require cooling are eliminated, because of the continual maintenance they require. Lead sulphide is chosen and its properties are examined in detail so that its influence on the design of the pyrometer system may be anticipated. A suitable input stage is designed so that the optimum performance of the detector at low signal levels may be realised.

3.1. Types of detector

The detector is usually the most important single component in an infra red system. In many cases it will limit the final performance of an instrument and both the electronic and optical systems are designed around it. For this reason it is fortunate that some degree of flexibility exists in the choice of an infra red detector for a particular application. Some limitations have already been imposed on the design of the optical system for the ratio pyrometer by the working wavebands and the further limitations imposed by the detector will now be discussed and a suitable type selected.

The types of infra red detector which have been reported are extremely varied.(1, 3, 4.) The physical phenomena upon which they depend for operation are numerous but two broad categories exist.

(i) thermal phenomena - heating of a device occurs due to absorption of infra red radiation.

(ii) photon effects - where direct interaction occurs between photons in the infra red radiation and bound electrons in the detector material lattice.

The thermal detector must change in temperature by a measureable amount due to absorption of the smallest amount of radiation to be detected. This means that the sensitive element must be in poor thermal contact, apart from radiative heat transfer facilities, with its surroundings. It should have a low thermal capacity to achieve a fast response time to incident radiation. Usually the temperature change is transduced to an electrical signal, although optical or mechanical outputs are used (2). The spectral response is usually flat since practically all incident energy is absorbed at all wavelengths.

In photon detectors it is the detailed structure of the crystal lattice which determines how energetic incident photons must be if absorption is to take place. Thus photon detectors have widely varying spectral responses depending upon the nature of the material used. Semiconductors provide the most important of this type of detector. The response time is considerably less than for thermal detectors because the interaction occurs at the subatomic level.

Many accounts of the nature of infra red detectors have been given (3). It is sufficient for our purposes to examine the properties of the various types which are sensitive in the range 1.5 to 4 microns and make our choice accordingly.

We shall reduce the possibilities in the light of the following parameters:

(i) Spectral response

(ii) Sensitivity

(iii) Response time

(iv) Operational temperature

(v) Physical size of detector

3.2. Spectral response

The required spectral response has already been defined by the choice of working wavebands. This limitation removes many of the recently developed detectors employing group III metals which have been used in the medium infra red region. Table III gives all the detectors which respond in the region of interest. Many of these have their best response at about 5 microns with considerable reduction at 1.5 microns. The thermal detectors have a flat response and the four basic types have been included in the table.

3.3. Sensitivity

The sensitivity of a detector is defined at a given operating frequency and bandwidth. The standard used is 1 cycle/second. In addition, the detector area, the wavelength at which the sensitivity applies and/or the response to radiation from a black body at a given temperature are given. The quantity noise equivalent power is used (NEP) and is defined as NEP = that amount of radiant power falling on the detector which gives rise to a root mean square electrical signal equal in magnitude to the root mean square noise level introduced by the detector itself.

TABLE III

Detectors with suitable wavelength response.

Detector type	Area (approx) mm^2	Resistance (approx) ohms	Spectral response λ_p λ_c microns	Sensitivity D* $cm^2.watts^{-1}$	Time constant secs	Operation temperature ^oK
Thermistor bolometer	few	10^6	flat	8.10^9	few.10^{-3}	room temp
Bolometer	..	10-10^7	..	2.10^8	few.10^{-2}	..
Golay cell	..	—	..	2.10^9	..	..
Thermopile	..	30-300	..	3.10^9	..	..
Super-conducting bolometer	..	1	..	4.10^{10}	few.10^{-3}	2^o–15^o
Photo-transistor	1	10^3-10^6	5.6 5.8	3.10^9	10^{-4}	90
Ge/Au	few	10^6	5.3 8.0	3.10^{10}	5.10^{-8}	60
Ge/Au:Sb	..	10^6	2.0 3.0	2.10^{11}	10^{-4}	77
Tellurium	..	10^3	3.6 3.75	6.10^{10}	6.10^{-5}	77
InSb photo-conductor	1	10^4	5.1 6.4	10^{10}	2.10^{-7}	195
InSb photo-voltaic	..	10^2-10^4	5.0 5.6	5.10^{10}	2.10^{-7}	77
PbTe	..	10^7-10^8	4.1 5.4	7.10^9	2.10^{-5}	77
PbSe	few	10^7	4.7 5.6	6.10^9	10^{-4}	195
PbSe	..	10	5.2 6.3	$1.5.10^{10}$	4.10^{-5}	77
PbSe	..	10^7	2.7 3.3	3.10^{11}	2.10^{-3}	195
PbS	..	10^7	3.2 3.7	$1.2.10^{11}$	3.10^{-3}	77
InAs	1	10^4	3.2 3.55	10^{10}	2.10^{-6}	230
InAs	..	10^2	3.5 3.8	7.10^9	2.10^{-6}	room temp
InSb electromag.	..	10-10^2	6.3 7.6	3.10^8	2.10^{-7}	..
InSb photo-conductor		10^2	6.5 7.9	$3.5.10^9$	10^{-7}	..
PbS	few	10^6	2.5 2.8	10^{11}	2.10^{-4}	..
PbSe	..	10^6	3.9 4.6	$1.5.10^8$	5.10^{-6}	..

λ_c = wavelength cut off.

λ_p=wavelength for peak response.

Thus for a detector area A, in a uniform radiation field I watts.cm^{-2} and S = $\frac{\text{ratio signal generated}}{\text{r.m.s. noise}}$ we have:-

$$NEP = \frac{I.A}{S(\delta\nu)^{\frac{1}{2}}} \qquad \delta\nu = \text{bandwidth}$$

Detectors with different areas are more conveniently compared by using the quantity specific detectivity. This is related to the detector area and NEP by

$$\text{Specific detectivity } D^{*} = \frac{\text{detector area}}{NEP}$$

The specific detectivity is given for the various detectors in Table III

It has been shown in the feasibility study that to achieve the required temperature discrimination when the waveband 1.6 - 1.9 microns is used a signal to noise ratio is required at 227°C such that the rms noise level is equivalent to $\pm$ 1°C. From Fig. 2.12 it can be seen that $\pm$ 1°C is equivalent to an rms fluctuation of $\pm$ .2 in the ratio at 227°C. If the energies in the two working wavebands are $E_1 \pm \delta E_1$ and $E_2 \pm \delta E_2$ then the random error in the ratio is given by

$$\frac{\delta R}{R} = \sqrt{\left(\frac{\delta E_1}{E_1}\right)^2 + \left(\frac{\delta E_2}{E_2}\right)^2}$$

Since the energy in the 2.3 micron waveband is more than ten times greater than that at 1.75 microns and the noise is the same we have:-

$$\frac{\delta R}{R} = \sqrt{\left(\frac{\delta E_1}{E_1}\right)^2 + \left(\frac{\delta E_1}{10E_1}\right)^2} \qquad \text{where } E_2 = 10E_1, \quad \delta E_2 = \delta E_1$$

$$= \frac{\delta E_1}{E_1}\sqrt{\frac{100}{101}} \approx \frac{\delta E_1}{E_1}$$

Thus the signal in the 1.75 micron channel can be considered mainly responsible for the noise band. An rms fluctuation of .2 in 22.6 at 227°C results if the noise ratio is 113. A similar figure of 100 applies when the 2.3 and 3.5 wavebands are used. From equation (2-11) the maximum noise equivalent power level which can be tolerated is

1.75 & 2.3 wavebands (1 cps bandwidth) NEP = $\frac{3.9\times10^{-10}}{113} = 3.45\times10^{-12}$ watts

2.3 & 3.5 wavebands (1 cps bandwidth) NEP = $\frac{6.8\times10^{-9}}{100} = 6.8\times10^{-11}$ watts

This condition reduces the number of detectors which are suitable to those listed in Table IV

TABLE IV

Detectors with suitable wavelength response and sensitivity.

Waveband	Thermal types	Room temp semiconductors	Cooled semiconductors
1.75 & 2.3 microns	Superconducting bolometer $D^* = 4.3.10^{10}$	PbS $D^* = 10^{11}$	all except InSb photo-transistor PbSe PbTe
2.3 & 3.5 microns	all except bolometer	InAs $D^* = 7.10^9$ PbSe $D^* = 3.5.10^9$ PbS $D^* = 10^{11}$	all those listed

3.4. Response time

The third limitation is that of response time. The system measures the ratio of energies in two wavebands. Therefore, if the final response time of the system is to be 1 second then the rate at which the two signals are sampled must be considerably faster than this. The choice of sampling frequency and operation frequency are discussed in section 3.9.5. It calls for a response time of less than $\frac{1}{1000}$ second in the detector.

A second factor to be considered is the large degree of amplification necessary in a system of this kind. To avoid the necessity of using a direct current amplifier or a circuit with a good low frequency response, which entails large coupling condensers and transformers, the operation frequency should be made as high as possible. The thermal detectors were rejected for this reason since the best response time attainable with these amounted to tens of milliseconds.

3.5. Detectors operating under cooled conditions

Apart from the question of cost three important factors have to be considered when the use of a cooled detector is contemplated. These are instrument portability, ease of maintenance and general applicability. The requirements of the instrument for heat transfer work and other applications have already been discussed (chapter 1) and the limitations imposed on these by the use of a cooled detector are summarized below:-

(i) the detector must operate in a vertical position to prevent loss of coolant

(ii) the coolant jacket must be filled at frequent intervals (typically every 30 minutes). Such maintenance greatly reduces the applicability of the pyrometer to process control and would also prove inconvenient during experimental work.

(iii) cooled detectors are essentially fairly bulky because of the vacuum flask which contains the coolant. They do not lend themselves easily to miniaturisation and are more fragile than other types.

(iv) If Peltier cooling devices are used, instead of liquid nitrogen or a combination of the two, then the need for continual maintenance is overcome but the equipment is expensive and would probably rule out battery operation due to the high current required.

The whole field of cooled detectors remains untapped for uses of the instrument where further sensitivity is required, at the expense of its general application.

3.6. Detectors operating at room temperature

By far the most convenient detector to use is the room temperature semi-conductor. Only indium arsenide and lead sulphide have sufficient sensitivity if the 1.75 band is used and of these two, lead sulphide is by far the most sensitive. Its sensitivity is comparable with the best cooled detectors in its own particular spectral range. The long wavelength cut off, however, occurs at about 3 microns at room temperature which is a disadvantage in total radiation instruments since most of the energy from objects below 600°C is radiated at longer wavelengths than 3 microns Fig. 2.1. In the ratio pyrometer the wavebands have already been limited and the objection only arises if the 3.5 micron band is used.

There is still an appreciable response to energy at 3.5 microns and a lead sulphide cell can be used to detect energy in this region. For accurate work, however, this is undesirable because 3.5 microns lies on the absorption edge of the response curve. The reason is discussed in section 3.8. together with other properties of lead sulphide. Before proceeding with this discussion, it will be convenient to specify lead sulphide as the most suitable detector for the ratio pyrometer. This decision is based on the factors discussed above which are also used to eliminate the rest of the infra red detectors. The characteristics of lead sulphide are:-

(i) spectral response - sensitivity greater than 30% of the peak response (2.4 microns) over the range 1 to 3.2 microns

(ii) sensitivity - specific detectivity D^* is 10^{11} - linear response (9)

(iii) response time - 2×10^{-4} seconds.

(iv) operational factors - room temperature operation.

(v) physical size - various according to manufacturer and degree of protection against corrosion provided. Preferably not greater than 5 cm. long x 2 cm. diameter.

3.7. Characteristics of lead sulphide

Lead sulphide is by far the most widely used of the infra red detectors. It takes the form of a semi-conductor which exhibits photoconductivity at room temperature. The conduction band in lead sulphide, which is a result of the overlapping of atomic energy levels due to the proximity of the atoms in the crystal lattice, can be populated by electrons raised from the valence bands at room temperature. The electron transitions are brought about by the incident electro-magnetic radiation and it is the high sensitivity at which this occurs in lead sulphide that is responsible for its wide application. When an electron is excited it crosses the forbidden gap between valence and conduction

bands. The energy width of the gap determines the spectral response of the detector. If the incident radiation is of energy (E_i) greater than the forbidden gap energy then the photons will be absorbed producing electrons in the conduction band and holes left by the electrons in the valence bands. Photons of energy less than E_g will not be absorbed which gives rise to the long wavelength limit of the detector

$$\text{thus since } E_i = h\nu = \frac{hc}{\lambda}$$

the long wavelength limit is given by

$$\lambda_c = \frac{hc}{E_g} = \frac{1{\cdot}24}{E_g} \quad \text{for } \lambda_c \text{ in microns}$$

E_g energy gap in electron volts

The long wavelength cut off changes with temperature, due to a combination of the temperature variation of the forbidden gap (4) and the temperature variation of the dielectric constant (5). In lead sulphide the shift occurs towards longer wavelengths as the temperature is lowered (6).

If an electric field is applied to the crystal then the electrons, and holes left by them, move through the lattice in opposite directions. Thus the conductivity is a measure of the intensity of the incident radiation. The sensitivity is also temperature dependent due to the variation in conductivity with temperature. This is due to a reduction in the population of the conduction band by thermally excited electrons as the temperature is lowered, thus producing an increase in sensitivity (7).

In order to obtain uniformity of response over the detector surface it is necessary to achieve uniform density of the bias current throughout. This occurs when elements form a rectangle with the electrodes extending along one pair of opposite sides and the resistivity is constant throughout the element. In practice small variations in thickness arise during manufacture which lead to variations in resistivity and hence sensitivity across the element (8, 9). The same effect leads also to variations in sensitivity between individual detectors.

3.8. Influence of detector on design of optical system

In the ratio pyrometer the recorded output is proportional to the ratio of the energy in the working wavebands. Any change in the ratio is interpreted by the pyrometer as a change in the temperature of the specimen it is observing. Therefore it is essential that the optical system is designed in such a way that the signals corresponding to the energy in the two wavebands delivered by it to the electronics system remain in the same ratio. This design principle affects the detector installation because of the properties of the detector discussed above.

(i) The variation in sensitivity from one detector to another and the additional dependence of the sensitivity on the ambient temperature leads to the conclusion that only one detector should be employed in the system to detect both wavebands.

(ii) The variation in sensitivity over the detector surface leads to the conclusion that incident energy in both wavebands should fall on the same portion of the detector sensitive area, if it is not possible to utilise the whole area.

(iii) The wavelength shift of the absorption edge causes a rapid change in sensitivity to incident energy at wavelengths near the absorption edge which would alter the ratio of intensities at two wavelengths. Thus working wavebands near the absorption edge are to be avoided.

The first and second considerations above are dealt with in the design of the optical system (chapter 4). The third consideration is used to choose the final pair of wavebands for the pyrometer.

The wavelength shift and the general displacement of the sensitivity curve which result as the ambient temperature is varied combine to produce a change in shape of the spectral sensitivity curve with temperature. The sensitivity curve for a chemically deposited lead sulphide is shown for two widely differing temperatures in Fig. 3.1 (10). If one of the signal wavebands (e.g. 3.5 microns) were to lie on the absorption edge, then ambient temperature control or compensation of the detector would be necessary to prevent large errors arising in the signal ratio due to the differential sensitivity variations at the working wavebands. If both wavebands lie on the flatter portion of the sensitivity curve, however, the effect is much reduced and ambient temperature control is no longer necessary.

With this effect in mind it is now convenient to re-examine the suitability of the wavebands originally recommended. These are:-

(i)	1.6 to 1.8 microns	small amount of water vapour absorption
(ii)	2.0 to 2.45 microns	water vapour and carbon dioxide absorption negligible
(iii)	3.4 to 3.7 microns	water vapour and carbon dioxide absorption negligible

This leaves only the first two wavebands which can be used with a lead sulphide cell and intervening media of carbon dioxide/air containing water vapour. These wavebands are also suitable for measurements on magnox (see Appendix A).

The drift of calibration with ambient temperature has been estimated from the data in Fig. 3.1. which is based on the spectral sensitivity curves quoted by various manufacturers (9,10) for lead sulphide at different temperatures. It should be emphasised that the figures given are not very

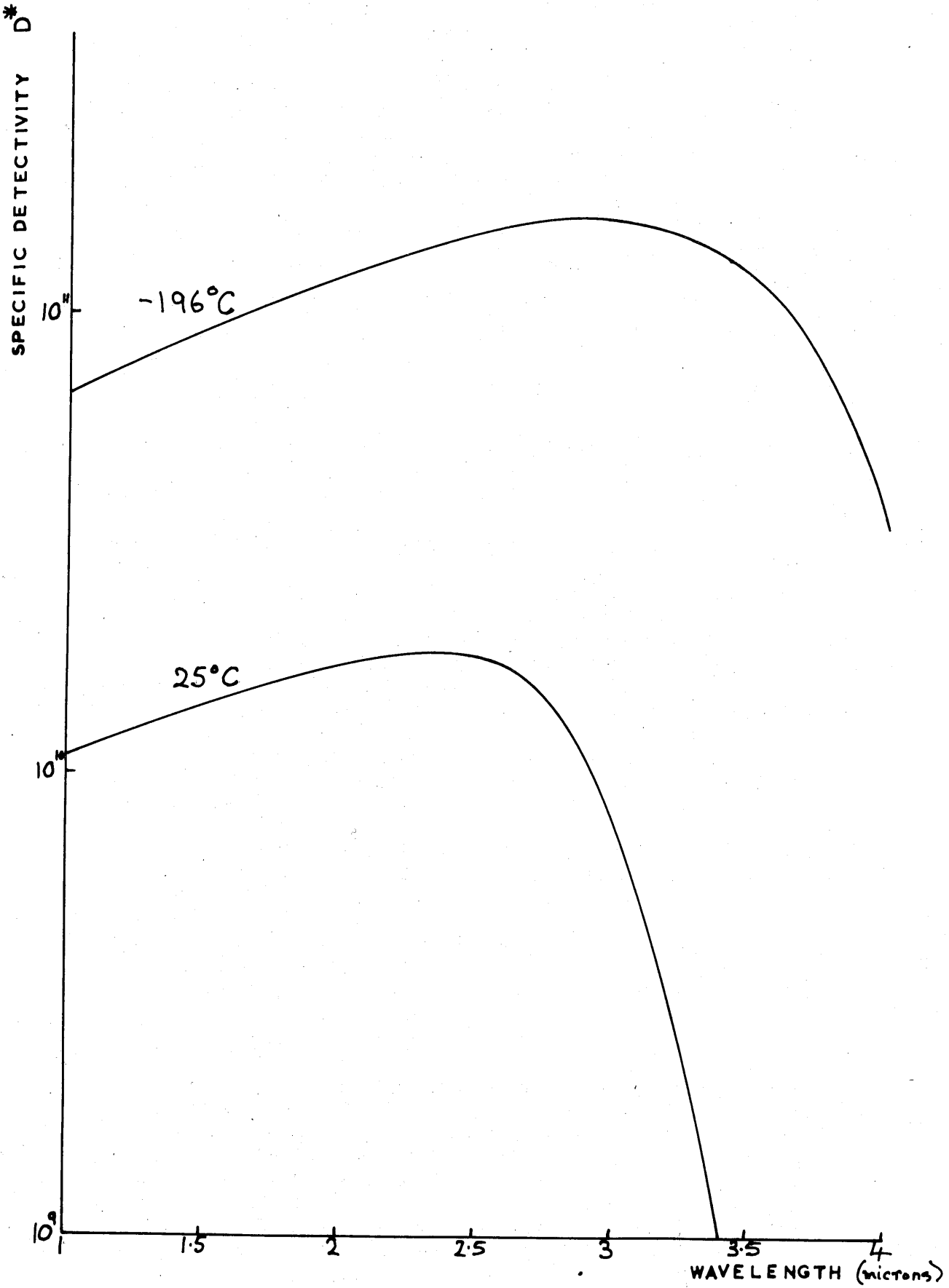

FIG 3.1. VARIATION OF RESPONSE OF PbS WITH TEMPERATURE

precise since they were obtained from general curves published by the manufacturers. Nevertheless the figures serve to indicate that the ratio of sensitivity at the working wavelengths is not sensitive to ambient temperature changes providing both wavelengths lie on the short wavelength side of the peak in the response curve of the cell.

Operation Temp.	D^*_1 1.75 microns	D^*_2 2.3 microns	D^*_3 3.5 microns	ratio $\frac{D^*_1}{D^*_2}$ %	ratio $\frac{D^*_2}{D^*_3}$ %
25°C	1.5×10^{10}	1.9×10^{10}	5×10^{8}	79	3800
-196°C	1.1×10^{11}	1.3×10^{11}	1.2×10^{11}	84.5	108

These considerations have lead to the choice of wavebands at 1.6 to 1.9 and 2.1 to 2.5 microns for the application to the temperature measurement of magnox.

3.9. Influence of detector on design of the electronic system

The performance of the ratio pyrometer will be noise limited at the lower end of the temperature range. The noise arising at the detector and input stage of the amplifier is responsible for the limit to the temperature range and the noise performance is closely associated with the electrical operation of the detector. Thus careful matching of the detector into the electronic system will be required. There are three basic factors which require consideration in this respect and they are all a result of the necessity to use a.c. amplification to remove drift in calibration arising from fluctuations in ambient temperature and ageing of components.

The first factor to be decided is the frequency of the carrier signal, which may be determined from a detailed study of the origins of noise in semi-conductors. The second consideration is the frequency at which the energy in the individual wavebands is to be sampled. This is a function of the required accuracy of the pyrometer and the bandwidth of the electronic system. The third consideration is that of matching the detector to the input stage of the signal amplifier.

3.9.1 The origins of noise in semi-conductors

Thermal noise - The thermal or Johnson noise (11,12) is due to the discrete particle nature of the current carriers (electrons and holes in the case of semi-conductors). Superimposed upon the drift motion of the particles, which is responsible for the current, is the random motion due to thermal excitation. This motion exists even in the absence of drift and being due to thermal excitation, it is temperature dependent. Nyquist (13) has derived the expression for the noise power P_n in a frequency interval δf as

$$P_n = \frac{\overline{V^2}}{R} = 4kT\,\delta f \cdot \frac{hf}{kT} \cdot \frac{1}{e^{\frac{hf}{kT}} - 1}$$

where P_n = noise power

k = Boltzmann constant

δf = bandwidth

h = Plank constant

f = centre frequency

$\overline{V^2}$ = is the mean square value of the instantaneous voltage

At normal ambient temperature and frequencies up to 30,000 Mc/s $\frac{hf}{kT} \ll 1$. Expansion of the above expression leads to

$$P_n = 4kT.\delta f \qquad (3\text{-}1)$$

which is independent of frequency and proportional to the frequency interval. Typically for a 1 MΩ resistor and 1 megacycle bandwidth we have:

$$\frac{\overline{V^2}}{R} = 4 \times 1{\cdot}4 \,.10^{-16} \times 300.10^{6} \,.\, 10^{-7} \text{ watts}$$

$$\therefore V = 130\mu V.$$

Thermal noise exists in all semi-conductors which means it is found in the other circuit components also and consideration must be given to this in the design of the input circuit.

Shot noise - In addition to the fluctuations in the motion of charge carriers there exists a fluctuation of the number of current carriers in various parts of a semi-conductor. The fluctuation in numbers gives rise to the shot noise. Thus, whenever a charge carrier moves across a junction of P type or N type material it will generate shot noise. It arises whether the crossing of a junction by the charge carrier is caused by the application of an external field (signal) or due to normal random migration. In the case of a diode operating at large collector voltages the expression for the mean square value $\overline{i^2}$ of the instantaneous current i is (14)

$$\overline{i^2} = 2q\, i_l\, \delta f \qquad (3\text{-}2)$$

where i_l = reverse saturation (leakage) current

q = electronic charge

and is proportional to the leakage current.

In the case of a photoconductor, fluctuations in the incident photon stream causes noise at the output terminals by causing fluctuations in the number of carriers present. An equivalent amount of noise is also

introduced when the recombination of the electron and hole carriers occurs. The noise level can only be reduced in practice by cooling in which case the number of thermally generated carriers present to fluctuate will decrease and be more dependent on the signal radiation and the number of recombinations due to thermally generated carriers will decrease. The generation recombination noise is twice the shot noise of the average current (4). (equation 3-2).

Current noise - when a semi-conductor carries a steady current another source of noise exists which is not fundamental like thermal and shot noise. It is generally larger than these and may be expressed in transistors by

$$\bar{i}^2 = \frac{K\, i_{dc}^{a}}{f^{b}}\, \delta f$$

where i_{dc} is dc current in transistor

In particular it has been shown that K is constant
in lead sulphide cells:- a & b are experimental indices
i_p is the cell bias current

$$i^2 = \frac{K\, i_p^2}{f} \qquad (3\text{-}3)$$

It has been suggested (14) that the noise arises in the surface layers of the semi-conductor where a small number of charge carriers become trapped. The number is dependent on the surface layer electrical and thermal gradients and the times involved for the release and capture of carriers are relatively long. The resultant fluctuations in surface charge influence the generation and recombination of electrons and holes in the vicinity causing a surface noise component. The time variation of this component is decided by the trapped carriers and follows the well known $\frac{1}{f}$ law. The effect can be reduced by special manufacturing techniques which are designed to reduce surface current (e.g. planar transistors)

The above are the main sources of noise in semi-conductors. Other noise sources arise in the associated circuit and may be reduced by careful choice of components.

3.9.2 The effect of detector area on noise performance

When an amount of radiation I is incident on a photoconductive detector a number of carriers proportional to I will be released. The carriers will flow under the influence of the polarising field giving rise to a current Fig. 3.2.

The number of carriers per unit volume is $\frac{KI}{abl}$. K is constant
The average speed at which they move is v

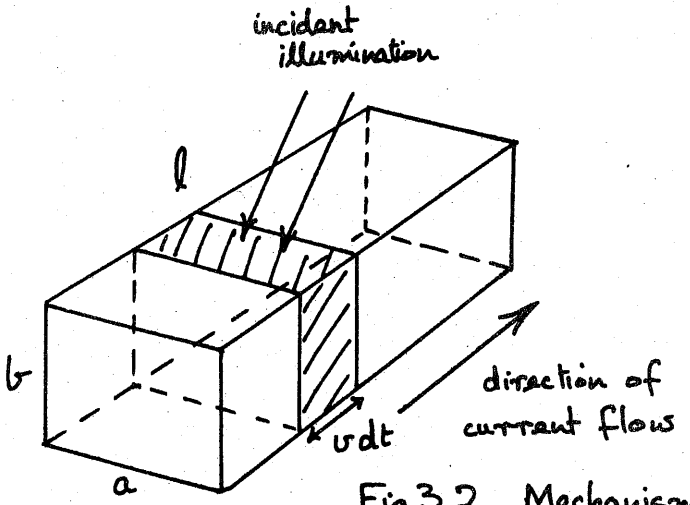

Fig 3.2 Mechanism of photoconduction

Thus in a time dt the charge dq passing through a cross section is

$$dq = \frac{KI}{abl} \cdot ab.\upsilon dt.q$$

q = charge per carrier

υ = speed of progression

ab = detector cross sectional area

$\therefore$ current is

$$\frac{dq}{dt} = \frac{KI\upsilon q}{l}$$

the resistance of the element is $\frac{\rho_r l}{ab}$

$\therefore$ the current will give rise to a signal power P_s

ρ_r = resistivity

$$P_s = \left(\frac{KI\upsilon q}{l}\right)^2 \frac{\rho_r l}{ab}$$

Consider now the effect of thermal noise. The thermal noise power is given by:

$$P_n = 4kT.\delta f$$

$$\therefore \frac{P_s}{P_n} = K' \frac{I^2}{la} \quad \text{for } b \text{ constant and } K' = \frac{(Kq\upsilon)^2 \rho_r}{4bkT\delta f}$$

Thus the signal to noise power ratio is seen to be inversely proportional to the area of the detector for the same quantity of incident radiation and a given bandwidth.

It has been shown (4,15) that this is a general rule applying to all sources of noise providing each element of the detector contributes signal and internal noise the same as do all other elements of the detector.

The area dependence of the performance of the detector introduces the further requirement into the optical system that the final image should be is small as possible enabling a small detector to be used.

3.9.3 Concept of noise figure

Before proceeding to the discussion of the amplifying circuit associated with the detector it will be convenient to consider the effect of noise introduced between stages of amplification. We are interested in the ratio of signal power to noise power (the signal to noise ratio) existing at the output of the system. The noise performance can be specified in terms of the noise figure F which is defined as:

$$F = \frac{\text{signal to noise power ratio at the input}}{\text{signal to noise power ratio at the output}}$$

which may be expressed as a fraction or logarithmically in the decimal form

If this is now extended to a number of stages each with its own noise figure it can be shown(14) that the overall performance is given by

$$F = F_1 + \frac{F_2 - 1}{G_1} + \frac{F_3 - 1}{G_1 G_2} + \cdots \text{etc} \qquad (3\text{-}4)$$

where G = stage power gain

It can be seen that the noise figure of successive stages is reduced by approximately the product of the gains of the preceding stages which means that it is only necessary to design the first stage for low noise performance if it is given a high power gain.

3.9.4 Effect of noise characteristics on operating conditions

The combined effect of the various noise components in a lead sulphide photoconductor produces a variation of noise with frequency in the range 0 - 10 Kc/s in the manner shown in Fig. 3.3. (4). The noise spectrum for a transistor follows a similar curve. Current noise is dominant in the range 0 - 1Kc/s and from 1Kc/s upwards the combined effects of thermal and shot noise, which are both independent of frequency, are present. To obtain the best noise performance both at the detector and input stage, therefore, requires an operation frequency greater than 1Kc/s. It cannot be much higher than this because of the frequency cut off of the lead sulphide cell (few thousand cycles per second), and limitations imposed by the chopping arrangement.

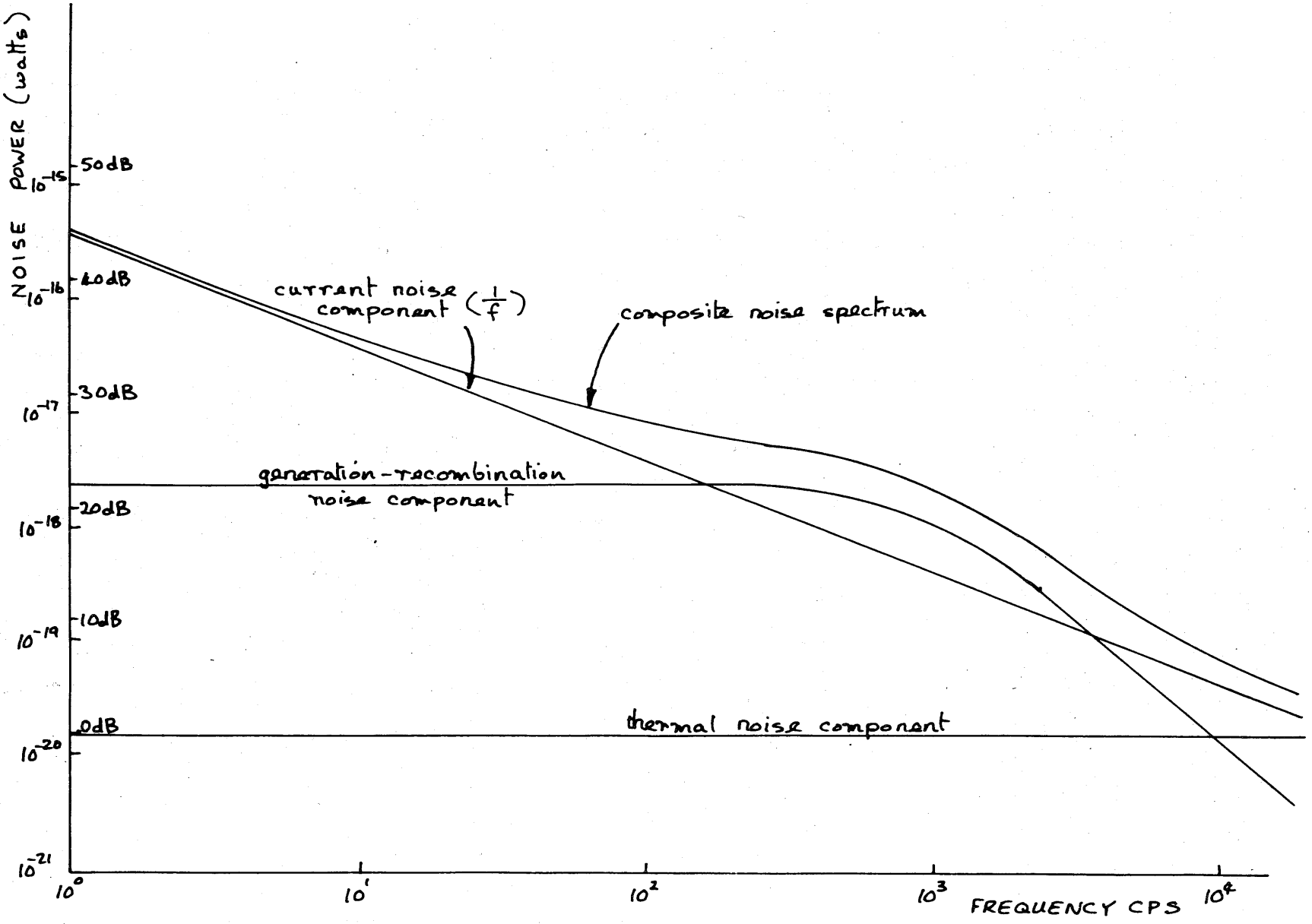

FIG 3.3 NOISE FREQUENCY SPECTRUM OF A TYPICAL LEAD SULPHIDE DETECTOR ($R = 2\,M\Omega$. $\delta f = 1$ cps).

The noise performance of a transistor is nearly independent of the mode of connection below the cut off frequency(12) and it will be convenient therefore to use a common emitter amplifying stage at the input because it has the highest power gain of all connections and reduces the effect of noise in later stages according to equation (3-4)

The ideal source impedance for operational frequencies in excess of 1000c/second may be deduced if the equivalent circuit for thermal and shot noise(4) for the common emitter input stage is considered Fig. 3.4. The operation frequency is high enough for the effect of current noise to be neglected if a transistor is used in which the surface leakage is small.

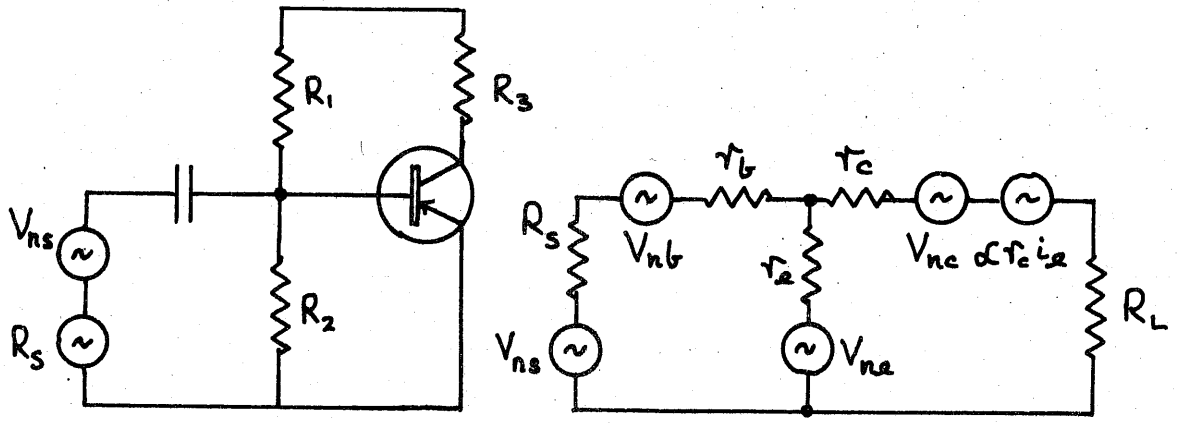

Fig 3.4 Common emitter stage aquivalent circuit.

where V_{ns} is the source thermal noise voltage of the form $\sqrt{4kT R_s \delta f}$ (3-1)

V_{nb} is the thermal noise voltage generated in the equivalent base resistance r_b and takes the form $\sqrt{4kT r_{bb} \delta f}$ see (3-1)

V_{ne} is the shot noise generated in the emitter region of the form $\sqrt{2q i \delta f r_e}$ see (3-2)

V_{nc} is the shot noise generated in the collector region of the form $2q\alpha(1-\alpha) i_e r_c^2 \delta f$

where $i = i_e + 2I_+$

r_{bb} = thermal noise resistance of base region

R_s = source resistance

If the Kirchhoff loop equations are written for this circuit then an expression is obtained for the noise figure of the stage

$$F = 1 + \frac{r_{bb}}{R_s} + \frac{q}{2kT} \cdot i_e \frac{(r_e + r_b + R_s)^2}{\beta R_s} + \ldots \qquad (3\text{-}5)$$

neglecting higher terms. where β = current gain $\frac{\alpha}{1-\alpha}$

TABLE V

Parameters of germanium and silicon transistors.

Parameter	Germanium	Silicon
r_b	1000 Ω	7000 Ω
r_{bb}	100 Ω	700 Ω
r_e	25-50 Ω	100-300 Ω
r_c	2-3 MΩ	30-50 MΩ
$\beta = \frac{\alpha}{1-\alpha}$	50-100	100-150
i_e	0.1-0.5 mA	30-300 μA
i_{ee}	1-5 μA	0.01 μA

These figures have been used in conjunction with (3-5) to obtain the curves of Fig. 3.5

Typical values for the parameters occuring in (3-5) are given in Table V for both germanium and silicon transistors . These values have been used to plot the curves in Fig. 3.5. for various values of the emitter current i_e . It can be seen that:

as $R_s \to 0$ $F \to \infty$ under the influence of the 2nd term (3-5)
as $R_s \to \infty$ $F \to \infty$ under the influence of the 3rd term (3-5)

An optimum source impedance occurs for each value of the emitter current and is approximately 2.5 KΩ in germanium and 10 KΩ in silicon transistors.

If the lead sulphide is used to current drive a common emitter stage it can be seen that poor noise performance will result because of the inherent high resistance of lead sulphide. A typical resistance is 2 MΩ and substitution of this value in (3-5) gives:-

F = 15 to 20dB for a low noise germanium transistor

F = 10 to 15dB for a low noise silicon transistor

To overcome this an impedance matching device is required so that the reflected impedance of the detector is of the right order of magnitude. From the theoretical point of view a transformer is the obvious choice since it performs impedance transformation with a negligible addition of noise. The equivalent circuit looking into the transformer is shown in Fig. 3.6.

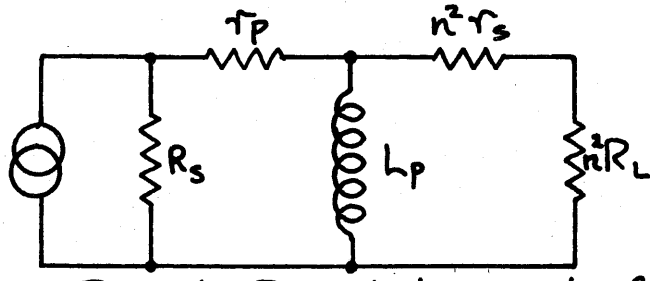

Fig 3.6 Equivalent circuit of input transformer

where r_p = Primary winding resistance
r_s = Secondary winding resistance
L_p = Primary inductance
n = Turns ratio
R_L = Load resistance (typically 1000 Ω)

The turns ratio is chosen so that the detector presents a reflected source impedance of a few.thousand ohms to the input stage (i.e. $n \sim 30$) for low noise performance.

The detector is represented by a current generator in parallel with the detector resistance R_s. In order to drive maximum current into the

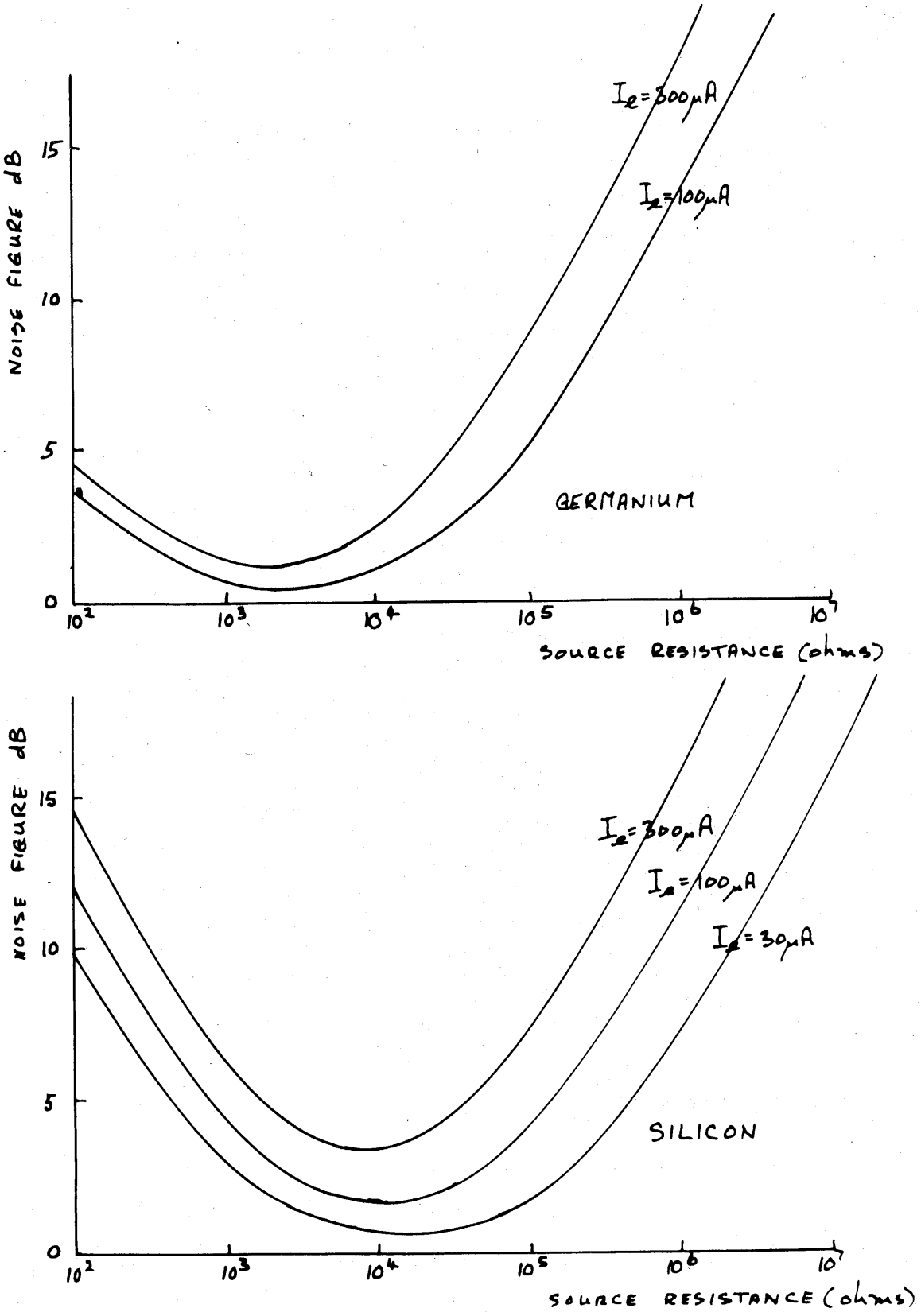

FIG 3.5. BROAD BAND NOISE FIGURE FOR SILICON AND GERMANIUM TRANSISTORS.

load the reactance of the primary winding should be large compared with the reflected load impedance, which will be typically a few thousand ohms. Therefore, a primary inductance of $\omega L_p \gg n^2(R_L + r_s)$ is required. This leads to a large number of turns and a large cross sectional area in the primary winding, however, and subsequent practical difficulties arise. The transformer becomes very susceptible to stray magnetic fields and induced signals in a vibrational environment.

An alternative approach is to use a semi-conductor which will operate from a high source impedance with good noise performance. Such a device is the field effect transistor which is used in the low noise input stage described in Appendix C.

3.9.5 Channel selection frequency

The final influence the detector has on the design of the electronics system is to decide the system bandwidth and channel selection frequency. The choice of these is not affected by the detector directly but rather because the system is noise limited by the detector.

It was shown in section 3.3 that the signal to noise voltage ratio expected at the lowest operating temperature (227°C) is 113 and that this is achieved only if the specified performance of the detector can be fully realised. Since the figure 113 is based on a 1 cps bandwidth at the output the signal to noise ratio in the amplifier will be considerably worse than this due to the necessarily wider bandwidth. In order to prevent continued overloading of the signal amplifier by noise pulses when a temperature of 227°C is being measured, it will be necessary either to limit its bandwidth or provide a signal handling capacity far greater than that required by the genuine signal. In practice both of these precautions will be taken. The voltage handling capacity will be made twice that required by the signal and the bandwidth will be limited to provide a signal to noise ratio of 2.5 when measuring at 227°C. This will allow peak noise voltage pulses a factor of seven times the rms noise level to be handled without overloading. The amplifier bandwidth required is given by

$$\delta f = \left[\frac{\text{signal to noise voltage ratio at output}}{\text{signal to noise voltage ratio at input}}\right]^2 \times \text{output bandwidth}$$

since the noise power level is a function of bandwidth

$$\therefore \delta f = \left(\frac{113}{2.5}\right)^2 \times 1 \simeq 2000 \text{ cycles.}$$

The bandwidth of the system is the criterion on which the choice of the channel selection frequency is based. Since we are using a carrier

frequency of about 1000 cps and a bandwidth of 2000 cycles it is to be expected that when the alternate channels are selected a time of approximately $\frac{1}{2}$ x .5 millisecs will elapse before the amplifier responds to the change. In the extreme case of measurement at the low end of the temperature range, when the signal in the 2.3 micron channel is 13 times greater than that in the 1.75 micron channel (see section 2.7), the overshoot will be interpreted by the ratio circuit as signal in the lower level channel with a resultant error in the temperature recorded. To overcome this the waveband selection frequency should be made as low as possible so that the overshoot is short compared with the sampling time for each channel. This leads to the choice of 30 cps as the selection frequency which is the lowest frequency that the electronics system will be able to handle conveniently.

Before the signal can be processed to produce the small bandwidth at the output it requires amplification in its original form. It is shown in Appendix D by Fourier analysis that the effect of low frequency attenuation is to adjust the waveform so that both signals are placed symmetrically about a centre line and the effect of high frequency attenuation is to cause each signal to overshoot into the other channel Fig. 3.7. The first of these effects is desirable since it simplifies the signal processing at the output, but the second effect is undesirable in that it will produce an inaccurate reading of the signal ratio.

The low frequency response is designed to be 3dB down at 550 cps and can be governed by a single time constant in the first stage of the amplifier. The high frequency response is controlled by one or more time constants in the early stages of the amplifier and the analysis shows that for the cut off value of 2000 cps, which is decided by the noise performance, terms which are less than 1% of the fundamental are removed from the signal waveform.

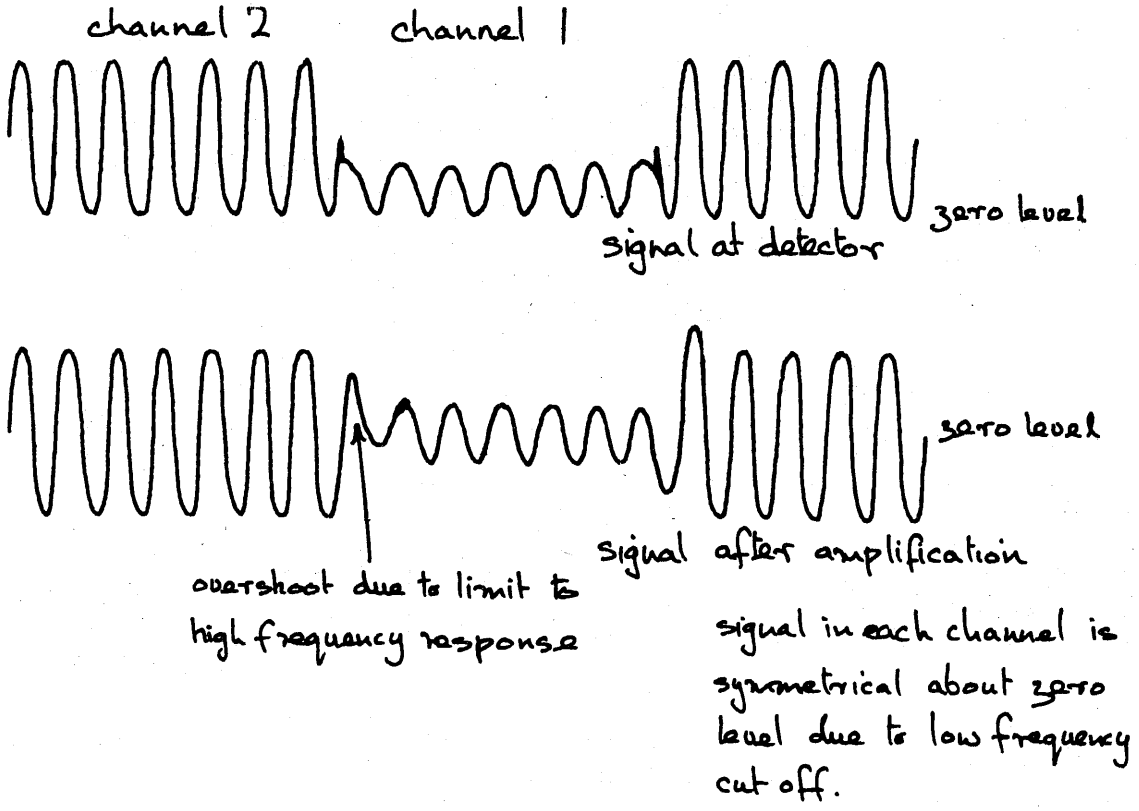

Fig 3.7 Effect of low frequency attenuation of input signal

3.10 Signal waveform shape and channel sampling time

These two factors require consideration before proceeding to the design of the optical and electronic systems since they may effect the general chopping arrangement as well as the detailed design of both systems.

The maximum signal to noise ratio is obtained when a dc signal is available providing the superimposed noise is frequency independent. The reasons for rejecting a dc system have already been discussed but nevertheless it is convenient to measure the performance of any system in terms of the performance of a dc system (16). In such a system the energy is being received continuously and since the noise is associated with it the noise factor of the dc system may be defined as unity.

When an ac system is employed the signal to noise performance deteriorates because the energy is received for part of the time only while the noise is always present. If the ac signal takes the form of a square wave produced by chopping a dc signal of amplitude unity (see Fig. 3.8) then the noise factor increases to 2. In practice,

however, to obtain the best performance it is necessary to restrict the bandwidth of a noise limited system at the output (see previous section) and the amplitude of the resultant first harmonic of the square wave may be shown by Fourier analysis to be $\frac{2}{\pi}$, and the energy content $\frac{2}{\pi^2}$ being one half the square of the amplitude. The square root of this quantity represents the mean amplitude of the first harmonic and a noise factor of 2.2 is obtained when compared with the dc system.

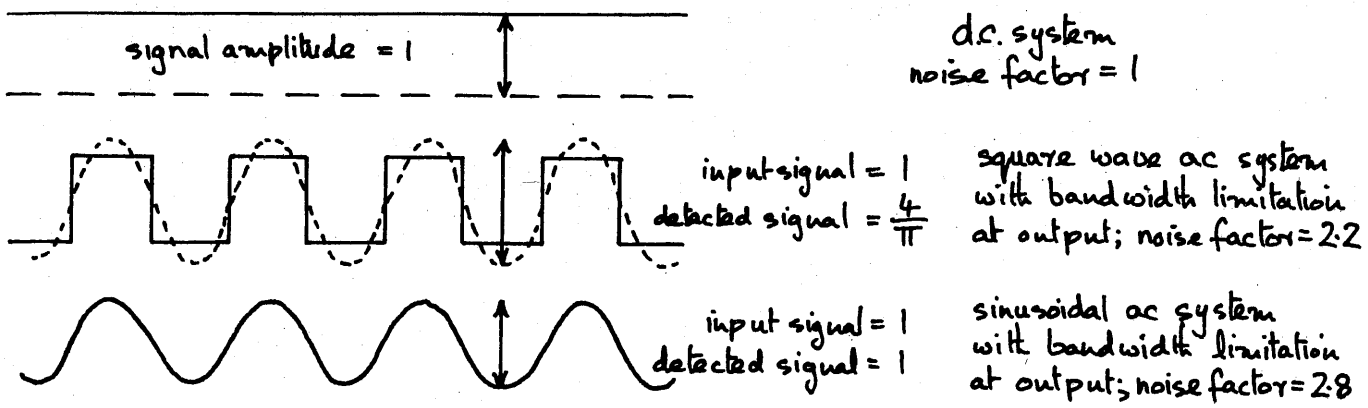

Fig.3.8 Effect of signal chopping on noise factor.

A further deterioration in signal to noise performance will result if sinusoidal chopping of the received energy is employed. In this case the amplitude is ½, the energy content is ⅛ and the mean amplitude is $\frac{1}{2\sqrt{2}}$ giving a noise factor of 2.8.

In view of this argument the best possible performance is obtained if square wave chopping is used. The optical system will be designed as far as possible to comply with this condition.

At first sight it might appear advantageous to sample the signal in the noisier of the two channels for a longer period than the other but the preceding argument shows that this will only be the case if noise is present during the off period. Since it will be straightforward to remove noise during the off period of each channel in the output circuit, equal sampling times can be used. (see Fig. 3.9)

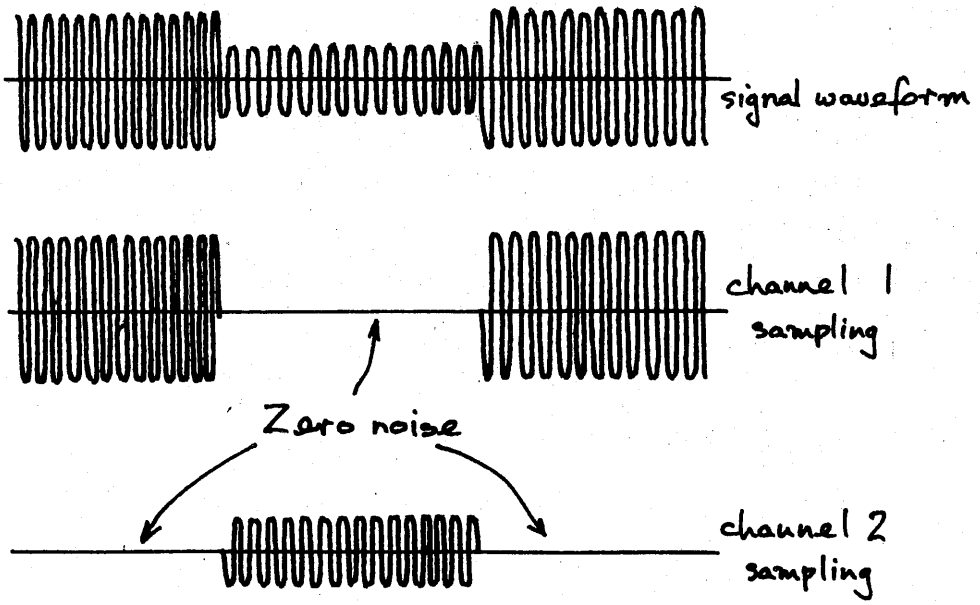

Fig 3.9 Channel sampling times.

3.11 Conclusion

The reasons for choosing lead sulphide as the detecting element have been outlined. Its spectral response has reduced the available operational wavebands to 1.6 to 1.9 microns and 2.1 to 2.5 microns. Consideration of the properties of lead sulphide has shown that it is essential to utilise the same portion of the sensitive area for each channel. Furthermore, for optimum sensitivity, a signal frequency of 1000cps has been chosen with modulation at 30cps corresponding to the energy in each channel. An input stage employing a field effect transistor has been designed to provide minimum noise contribution in the early stages of signal amplification.

3.12 References

1. H. Koenig. Rev.Opt.,1950,29,p.439

2. M.J.E. Golay. Rev.Sci.Instruments,1947,18,p.357

3. R.A. Smith et al. Detection and Measurement of Infrared Radiation. Oxford,Clarendon Press,1957,Chapters 3 and 4

4. J.A. Jamieson et al. Infrared Physics and Engineering. New York,McGraw-Hill,1963,p.136,p.162,p.422

5. T.S. Moss. Proc.Phys.Soc.,Series B,1950,63,p.167

6. T.S. Moss. Proc.Inst.Radio Eng.,1955,43,p.1869

7. B.N. Watts. Proc.Phys.Soc.,Series A,1949,62,p.456

8. G.K.T. Conn and D.G. Avery. Infrared Methods. New York, Academic Press,1960,p.98

9. Mullard Technical Data Sheets, Photoelectric Devices 1963/4

10. Kodak Electron Data Sheets, Ektron Detectors for the Infrared,1962

11. J.B. Johnson. Phys.Rev.,1928,32,p.97

12. J.H. Simpson and R.S. Richards. Physical Principles and Applications of Junction Transistors. Oxford,Clarendon Press,1962,p.222

13. H. Nyquist. Phys.Rev.,1928,32,p.110

14. A. van der Ziel. Noise. London,Chapman and Hall,1954,p.38

15. R Clark Jones. Advances in Electronics,1953,5,p.1. Edited by L. Marton. New York,Academic Press

16. M.J.E. Golay. J.Opt.Soc.America,1956,46,(6),p.422

CHAPTER 4 - THE OPTICAL SYSTEM

Introduction

The general principles of infra red optical system design are outlined and reflecting components are shown to be more suitable. Three types of optical system are described in which the waveband selection is performed by focal isolation, by interference filters using a rotating chopper and by interference filters using a reflecting switch. The systems employing interference filters and their construction is discussed. The chopper wheel system is rejected in favour of that which uses the reflecting switch and the latter is described in detail, with particular reference to the reduction of spherical aberration and the technique used for signal modulation.

4.1. General principles

The design of an infra red optical system is similar in many ways to conventional design in the visible region. This is because the wavelength of the radiation used, although an order of magnitude larger than visible radiation is still small in comparison with the gross dimensions of the system. The difference in wavelength is responsible, however, for the two chief differences which do occur between the visible and the infra red. Firstly the different photon energies associated with infra red radiation cause interaction with many of the materials which transmit visible radiation. This means that, in general, different sets of materials are used in the infra red and the visible to achieve the same result. Secondly the difference is due to the magnitude of the wavelength of the infra red radiation. Diffraction effects are a function of this wavelength, and consequential limitations occur in the imaging characteristics of infra red systems. By the same token however, the restrictions on the surface roughness of any reflecting or refracting elements used are less severe since scattering of radiation at an optical surface occurs when wavelength and surface roughness have similar dimensions.(1)

A choice exists in the image formation, as in the visible region, between reflecting or refracting elements or combinations of both and the problem of selecting the energy in the working wavebands from the incident energy may be approached in a variety of ways.

If lenses are used than the severe transmission and reflection losses which will occur in the infra red(2) when several components are employed, must be considered since they produce a further deterioration in performance of the system which is already noise limited. Thin film surface coatings(3) may be used to enhance transmission by means of constructive interference but such coatings will only improve transmission over limited bandwidths and will increase the cost of components which are already fairly expensive. If compound lenses are used then it will

be necessary to construct them from separate elements since suitable cementing materials are practically non existent in the infra red(2).

On the other hand if mirrors are used the system transmission will decrease with time as the highly reflecting surface coatings deteriorate. The transmission is also reduced by partial blocking of the object space which is usually necessary if aberrations are to be kept to a minimum. Apart from the general principles outlined above additional considerations were taken into account in the choice of a suitable optical system for this instrument. The need to maintain the correct ratio between energies in the working wavebands is of paramount importance. Thus the same components should be used as far as possible for both energy bands to avoid the introduction of errors due to variations in optical properties from one optical element to another. This consideration inevitably leads to a symmetrical design which has the further advantage that it is possible to arrange for certain aberrations introduced into the system to be cancelled.

Since the instrument will be required for more general applications a convenient means of sighting at a known position on the specimen is required. To avoid confusion, this should be built into the instrument in such a way that no misalignment can occur without being obvious to the operator. Also there is the need for portability. No special recommendation can be made at this stage in this respect and like the need for cheapness and robustness it was often a decisive factor when two equally attractive possibilities presented themselves.

The need to keep the cost of the instrument to a minimum emphasises the great advantage of simplicity of fabrication of spherical and plane surfaces, which should be used wherever possible.

Three possible optical systems are now considered. These are described in considerable detail because the study of each one led to the design of the final system. This method is discussed last.

4.2. A system employing focal isolation(4)

The variation of refractive index with wavelength which occurs in optical components provides the basis for this system. A waveband selection mechanism is built into it in such a way that the optical component which performs the imaging function also selects the required wavebands. If an objective lens is chosen whose refractive index varies rapidly with wavelength in the spectral region of interest then it will form images for each of the proposed wavebands at different points on the optical axis. Conversely, if the objective is moved along the optical axis a suitable amount it will image each waveband at the same point alternately. An aperture stop of suitable size placed at this point would be followed immediately by a chopper wheel to provide the signal carrier frequency and behind this would be placed the infra red detector.

A system is described fully in appendix E. The dimensions of optical components are deduced and the attainable spectral selectivity is given. The reason for rejecting the technique lies in the need to produce aberration free images and the inconvenient length of the system. This is unfortunate since the technique offers the distinct advantage of a mechanical means for continuously selecting wavebands and band pass characteristics.

4.3. Systems employing a rotating chopper and interference filters

4.3.1 An optical system employing reflecting components has certain advantages over a lens system. These are chromatic independence and compact construction. The absence of chromatic aberration means that the energy paths for all wavelengths are brought to the same focus even in the far infra red where the choice of suitable refractive materials is limited. The image produced by a reflecting system may be examined visually which is often very desirable when aligning the components. The compact construction arises out of the coincidence of both image and object spaces for a mirror at the expense of transmission efficiency of the system. Although the supports for reflecting systems are generally more complex than for refractive systems the mirror itself is considerably less expensive than the corresponding lens.

The system which was next considered, employed multilayer interference filters and a rotating chopper. Various arrangements of the components were considered but before these are discussed, the characteristics of the multi layer interference filter are discussed and the limitations they impose on the optical system defined.

4.3.2 Characteristics of filters

The working wavebands have been fixed at 1.6 to 1.9 microns for channel 1 and 2.1 to 2.5 microns for channel 2. Although the width of each waveband is not critical since it will be taken into account by the calibration of the instrument, the requirement of high background rejection is still an important one. This stems from the fact that the instrument temperature discrimination relies on the change in ratio of energy in each channel. Table II chapter 2 shows that a change of 3:1 in ratio is to be expected in the temperature range 550°K to 800°K for the above wavebands and this implies a change of only ¼% full scale deflection for a discrimination of 1°C if a linear calibration is assumed. Such discrimination cannot be maintained in the presence of signal due to energy outside the wavebands because it will add to the signal in each channel and reduce the change in ratio.

4.3.3 Background rejection

The background rejection is more important on the high wavelength side of each filter because of the increase in energy with wavelength in the design temperature range (see Fig. 2.1). This is illustrated in

Table II chapter 2 from which it can be seen that a background rejection of approximately 99.9% at 2.3 microns represents 1% of the energy at 1.75 microns in channel 1 when the waveband energy ratio is 0.1, which occurs at 550°K. Similarily a background rejection of approximately 99.9% at 3.5 microns represents 1% of the energy at 2.3 microns in Channel 2 when the energy ratio is 0.1, which occurs at 500°K. Over the response range of the detector 1 to 3.3 microns, the total signal due to background radiation may be significant therefore. The level of the background signal has been estimated from black body curves (Fig. 2.1) assuming a flat detector response for a specimen temperature of 500°K and 0.1% transmission outside the passbands. The figures obtained are presented in Table VI for the case of radiation from a black body at 500°K.

The addition of background radiation to the signal increases as the temperature decreases because of the shift of the radiation curves towards the infra red. Thus the figures in Table VI represent the worst case in the operating temperature range and are quite acceptable since the effect on the ratio is small.

A further consideration is the rejection of energy in the visible region from indoor lighting reflected in the specimen. Such energy is emitted from a source which is typically at 2200°K and consequently radiating with maximum intensity at 1.2 microns. Thus although no background energy at wavelengths below the working wavebands is emitted from the specimen efficient rejection at lower wavelengths is still desirable to prevent the instrument recording the temperature of reflected light sources. Thus the 99.9% rejection should be retained on either side of each waveband or care should be taken to prevent artificial illumination of the specimen.

The characterisation of the filters can now be clearly defined.

Channel 1 — peak transmission at 1.75 microns; width of pass band not less than 0.3 microns. Background rejection 99.9% on either side of pass band; transmission - as high as possible in pass band.

Channel 2 — peak transmission at 2.3 microns; width of passband 0.4 microns. Background rejection 99.9% on either side of passband; transmission - as high as possible in passband

The width of the passbands given is referred to 10% of the peak transmission, which means that immediately outside the passbands the background level will be high compared with 0.1% of the peak transmission. The edge of the response curve must therefore be fairly steep for the transmission to drop quickly to 0.1% outside the passband.

TABLE VI

Background rejection of filters.

Energy from black body at 500°K in range 1.6 to 1.9 microns:	$5.3.10^{-5}$ watts.cm^{-2}
Background energy from black body at 500°K in range 1.9 to 3.3 microns assuming 0.1% transmission:	$1.1.10^{-6}$ watts.cm^{-2}
Background level relative to signal:	2% (approx)
Energy from black body at 500°K in range 2.1 to 2.5 microns:	$9.0.10^{-4}$ watts.cm^{-2}
Background energy from black body at 500°K in range 2.5 to 3.3 microns assuming 0.1% transmission:	$9.6.10^{-6}$ watts.cm^{-2}
Background level relative to signal:	1% (approx)

4.3.4 Interference filters

Of all the filter types those which make use of the interference properties of electromagnetic radiation are the most commercially available. The reason for this is that they may be tailored to a considerable extent to achieve a desired filter characteristic with high transmission in the passbands, good rejection in the stop bands and a steep transition between the two. The detailed design of the filters used in the instrument has been left to the manufacturer who has already established a manufacturing technique. The filters supplied were mainly ex stock although a special filter was prepared to pass the 2.3 micron band. The theory of interference filters is rather involved and the prediction from first principles of transmission curves for a particular design is a lengthy procedure. This is outlined below.

If a ray of light from a source S (Fig 4.1) is incident on the surface of a plane thin film of refractive index μ then multiple reflection occuring at the two faces of the film will produce the reflected rays 1, 2 , 3 etc. and the transmitted rays X, Y, Z etc. Each ray will have travelled a different distance and because of the wave nature of the energy the different phase relations between rays will produce constructive or destructive interference according to the thickness of the film, the angle of incidence and the wavelength of the incident energy. It can be shown(3) that if the refractive index of the film is greater than the medium which contains the source S, a phase change of π occurs for the reflected waves. The intensity of the amplitude decreases rapidly with successive reflections and the rays from the first and second reflections dominate in the interference produced. If the thickness of the film is t and the angle of incidence is θ then the optical path difference between 1 and 2 is Δ

where:-

$$\Delta = \mu(AFB) - AD$$

but optical path AD = optical path μ(BC)

$$\therefore \Delta = \mu(AFB) - \mu(BC)$$

$$= \mu(AFC)$$

$$= 2t\mu\cos\phi$$

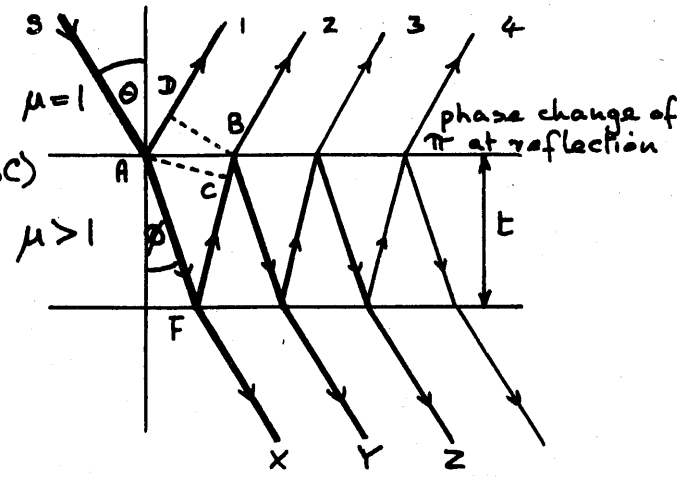

Fig 4.1 Interference in a thin film.

If the optical path difference is a whole number of wavelengths then the rays 1 and 2 would be in phase if it were not for the phase change of π occuring at the first reflection. Thus the relation $n\lambda = 2\mu t \cos\phi$ is the condition for destructive interference of rays 1 and 2 producing a minimum in intensity. (4-1)

If the argument is extended to rays 3, 4, 5 etc. then since reflection is taking place at the interface with a less dense medium no phase changes will occur. This leads to the conclusion that rays 1 and 2 are out of phase with each other and rays 2, 3, 4, 5 etc. are in phase.

If the condition: $$n + \frac{\lambda}{2} = 2\mu t \cos\phi \qquad (4\text{-}2)$$

prevails then the maximum of intensity will occur in the reflected light since rays 1 and 2 will be in phase but rays 2, 3, 4, 5 etc. will be out of phase with each other.

Rays emerging from the far side of the film will also undergo interference. Since there are no reflections at a more dense medium for any of these rays equation (4-1) becomes the condition for maximum intensity and equation (4-2) the condition for minimum intensity of the transmitted energy. The intensity of energy at the minima is controlled by the intensity of the ray X. The intensity of this ray can be reduced if a film with high reflecting power ($\mu \gg 1$) is used. In this case a lower minimum is achieved.

If the amplitudes of the transmitted rays are summed to infinity(5) then an expression is obtained for the intensity of the transmitted energy:-

$$I_t = \frac{1}{1 + \frac{4r \cdot \sin^2 \delta/2}{(1-r^2)^2}}$$

where r is the amplitude reflection coefficient at a single interface

r^2 is the intensity reflection coefficient at a single interface.

δ is the phase difference between successive rays.

This expression which is commonly called the Airey sum is the fundamental equation of the interference filter. It can be seen that for values of $\delta = 0, 2\pi, 4\pi$ etc. the intensity is unity and is independent of the value of r. For the minima however, when $\delta = \pi, 3\pi$ etc. the intensity is very dependent upon r and falls off rapidly as r increases.
i.e. for r approaching unity and $\delta = \pi, 3\pi, 5\pi$ etc.

$$I_t \to \frac{1-r^2}{4r^2} \quad \therefore I_t \to 0 \text{ as } r \to 1$$

The intensity of the reflected energy may be deduced from the law of conservation of energy. If absorption in the film is neglected then:-

$$I_r + I_t = 1$$

Consequently the reflected energy is the exact complement of the transmitted energy. Thus while zero intensity occurs at the minima for reflection the intensity of the maxima is low for small values of τ.

4.3.5 A quarter wave stack

To obtain improved rejection of energy with destructive interference in transmission, or to increase the energy with constructive interference in reflection requires therefore, a high reflection coefficient. This may be achieved by a thin metallic surface coating on the film as in the case of the Fabrey Perot etalon. The use of a metallic coating introduces absorption however, and improved performance is obtained if further films are deposited instead on the initial film. To achieve high reflection the condition of equation (4-2) must be satisfied and this is found to be the case if layers of alternately high and low refractive indices are deposited (Fig. 4-2 a & b)

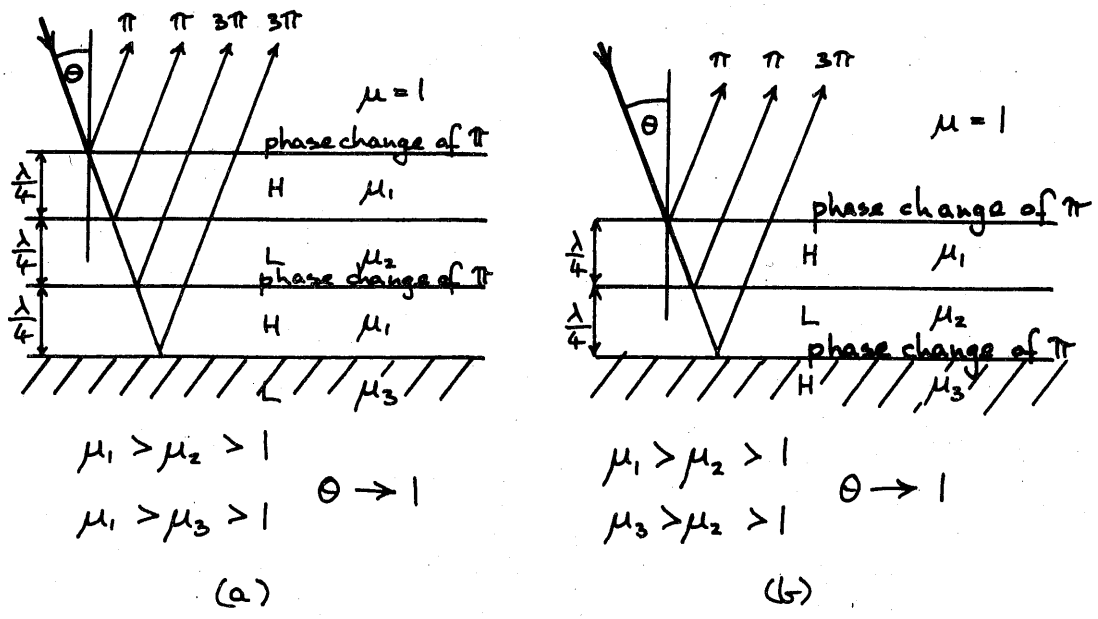

Fig 4.2 Interference in a quarter wave stack.

4.3.6 quarter wave stack with spacers

If a set of these layers, known as a quarter wave stack, with such a thickness that the condition of equation (4-2) is fulfilled, is deposited on either side of a film whose thickness satisfies equation (4-1) then the overall effect is a filter with high transmission at the required wavelength with good rejection at neighbouring wavelengths, due to the high reflectance of the quarter wave stack. If the stack employed is of the type illustrated in Fig. 4.2 a, then a filter of the form shown in Fig. 4.4 is obtained. In this filter an H layer is one of high refractive index and an L layer has low refractive index. The filter is referred to as HLHLLHLH the double LL at the centre implying half wave thickness.

It can be shown(6) for a quarter wave stack consisting of N+1 layers with refractive index μ_1 separated by N layers of refractive index μ_2 surrounded by thick media of refractive index μ on one side and μ_3 on the other side (see Fig. 4.2 a) that the reflectance is given by:-

$$\tau_{2N+1} = \left[\frac{1 - \left(\frac{\mu_1}{\mu}\right)\cdot\left(\frac{\mu_1}{\mu_3}\right)\cdot\left(\frac{\mu_1}{\mu_2}\right)^{2N}}{1 + \left(\frac{\mu_1}{\mu}\right)\cdot\left(\frac{\mu_1}{\mu_3}\right)\cdot\left(\frac{\mu_1}{\mu_2}\right)^{2N}}\right]^2$$

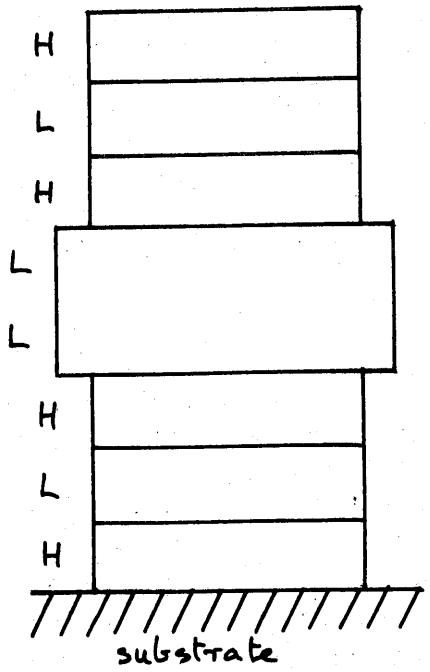

Fig 4.3 Typical multilayer filter

For R to be high $\left(\frac{\mu_1}{\mu_2}\right)^{2N}$ term is governed by $\left(\frac{\mu_1}{\mu}\right)\left(\frac{\mu_1}{\mu_3}\right)\left(\frac{\mu_1}{\mu_2}\right)^{2N}$ should be small and since this the relation $\mu_1 \ll \mu_2$ is desireable. In the infra red the most suitable materials are germanium (μ= 4.03), and silicon (μ= 3.5) for the H layers and silicon monoxide (μ= 1.32) for the L layers. The substrate material which is also an L layer is usually quartz (μ= 1.43) or mica (μ= 1.61).

A filter of the type shown in Fig. 4.3 will exhibit a single narrow passband at the desired wavelength. The technique may be further extended if the number of half wavelength layers, known as spacers, is increased. In an analysis carried out by Smith[7] the filter is replaced by two effective interfaces only and the properties of filter systems containing one or two half wavelength spacers is discussed. It is shown that the double half wavelength system has the advantage of increased peak transmission with improved band shape. It is shown that systems of the form HLLHLHLLH, where the half wavelength spacers are formed of low refractive index material, are superior to the form HLHHLHHLH where the half wavelength spacer has a high refractive index. The improvement is one of band pass shape, the superior filter producing two transmission peaks close enough together to form a good approximation to a square band pass.

All interference filters exhibit unwanted regions of transmittance on either side of the chosen band of transmittance. At shorter wavelengths transmittance occurs because the half wavelength spacers are used at high orders of interference and at larger wavelengths the transmittance improves when the thickness of the quarter wavelength stacks becomes a multiple of half a wavelength.

4.3.7 Filter performance

The filters supplied for the pyrometer were made up as follows.

Channel 1

An interference filter of the form H L H L H L H on a mica substrate designed to reject 2.48 microns has a side band transmission from 1.1 to 2.2 microns. No further rejection below this is required since the filter already has a transmission of only 0.1 - 1% below 1 micron. No rejection above 2.2 microns is required either since the filters natural rejection past 2.5 microns is adequate.

The transmission of this filter combined with the lead sulphide detector spectral response curve of Fig. 3.1 is shown in Fig. 4.4. It can be seen that the transmission is greater than 50% of the peak in the region 1.6 to 2.15 and below 0.25% below 1.0 and above 2.4 microns.

Channel 2

An interference filter of the form H L L H L H L L H L H L L H on a mica substrate is designed to produce three transmission peaks close together at 2.2, 2.3 and 2.4 microns. A sideband occuring below 1.8 microns is removed by a germanium filter bloomed for maximum transmission at 3 microns with a quarter wavelength surface layer.

Rejection above 2.5 microns is provided by a 1mm glass disc. The transmission of the filter system combined with the lead sulphide detector response of Fig. 3.1. is also shown in Fig. 4.4. The transmission is greater than 50% of the peak in the region 2.15 - 2.45 and less than 0.1% below 1.6 and above 2.7 microns.

The curves of Fig. 4.4 were drawn using data supplied in the form of transmission curves. These have been tabulated in Table VII and the combined response of filters and detector obtained by multiplying filter transmission and detector response figures.

4.3.8 Wavefront shape incident upon filters

The previous discussion has been based upon energy which is incident normally upon the filters. Since the transmission characteristics of the filters which rely upon interference for their correct function, are dependent on the thickness of the deposited films the characteristics must change with the angle of inclination. The magnitude of this effect has been discussed by Lissberger and Wilcock[8]. They show that for a parallel wavefront incident at an angle θ on an interference filter of the type discussed in the previous sections a shift towards shorter wavelengths occurs which is proportional to θ^2 and is also an increasing function of the refractive index of the spacer material. The magnitude of the shift is suprisingly small and is very nearly independent of the number of layers in the quarter wavelength stack. Typically a wavelength shift of 0.2% is obtained for an angle of incidence of 0.1 radians with a refractive index of 1.34 for the spacer material. The analysis is also extended to filters in convergent beams. It is shown that for a filter in a convergent beam of semi-angle ϕ the wavelength displacement from the passband is one half the displacement when the filter is in a parallel beam and tilted through an angle ϕ from the normal. The effect of a converging beam on the filter passband is to increase its width. The magnitude of the increase is again small, however, providing the passband is not a very narrow one.

Thus although oblique angles of incidence and convergent beams produce a deterioration in filter performance the effect is small and may be neglected for practical purposes in this application.

It is evident that the effect will only be present in an instrument with variable focus any way when the angle of convergence of beams is variable. In a fixed focus instrument the deterioration in the design performance would be taken into account in the initial calibration.

4.3.9 Limitations imposed on optical system

The limitations imposed by the filters on the optical system are very few. Their performance is very dependent upon the dimensions of the deposited films and although these are controlled during manufacture variations in thickness over the filter surface inevitably exist.

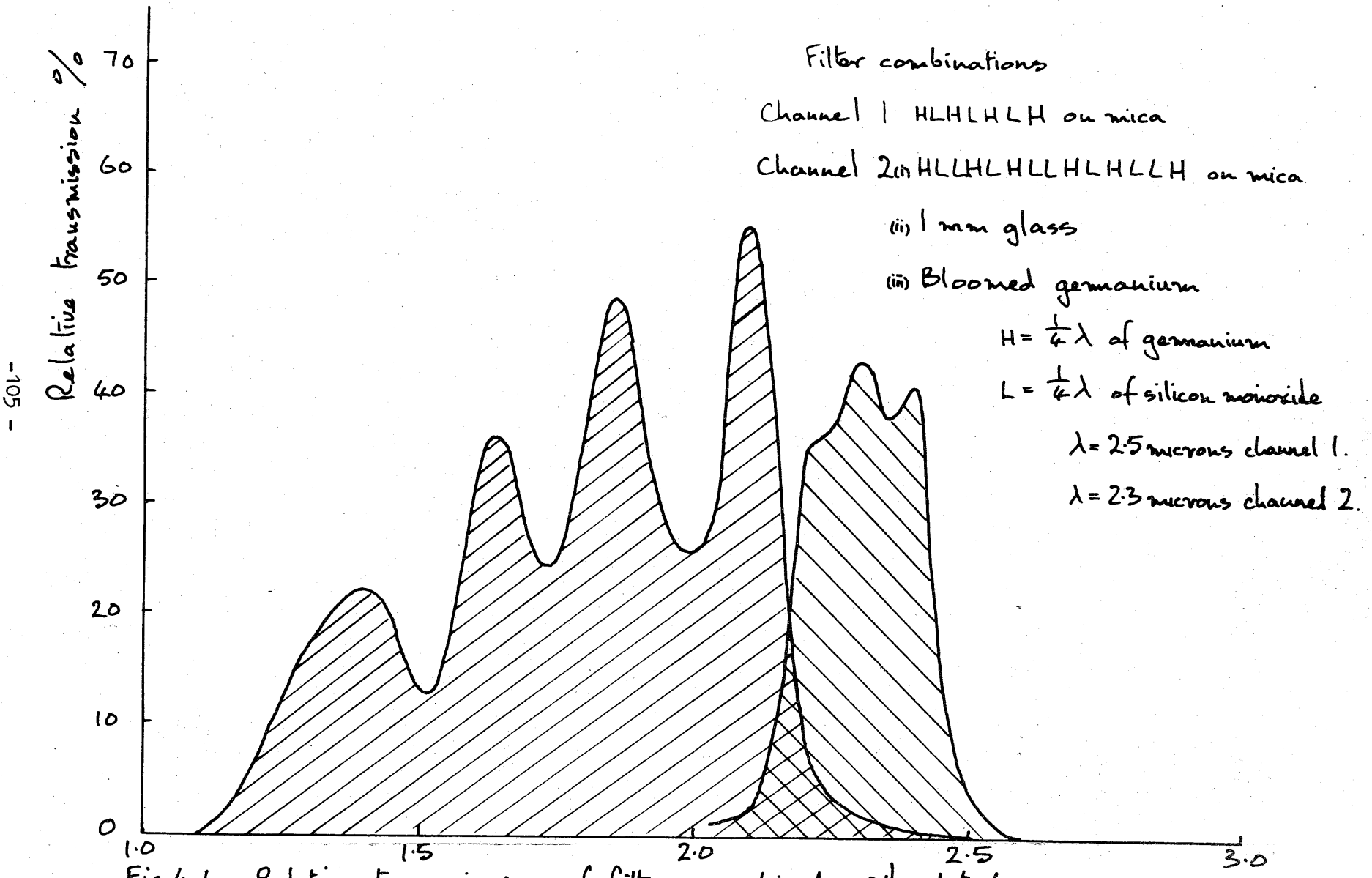

Fig 4.4 Relative transmission of filters combined with detector response.

TABLE VII

Filter characteristics and detector response

	Channel 1		Channel 2		
Wave length microns	Detector response %	Filter trans-mission %	Detector output	Filter trans-mission %	Detector output
1.1	35	-	-	-	-
1.2	40	17	6.8	-	-
1.3	45	37	16.7	-	-
1.4	50	44	22	-	-
1.5	55	24.5	13.5	-	-
1.55	57	30	17.1	-	-
1.6	60	53	31.8	-	-
1.65	62	58	36	-	-
1.7	65	41	26.7	-	-
1.75	68	38	25.9	-	-
1.8	71	51	36.3	-	-
1.85	74	66	49	-	-
1.9	78	49	38.3	-	-
1.95	81	34	27.6	-	-
2.0	84	31	26	-	-
2.05	87	42	36.6	1.7	1.5
2.1	90	62	55.8	2.74	2.47
2.15	93	31	28.9	12.2	11.2
2.2	96	8.8	8.5	35.7	34.3
2.25	97	3.5	3.4	38.5	37.2
2.3	98	1.8	1.8	44.4	43.5
2.35	99	1.0	1.0	38.6	38.0
2.4	100	0.8	0.8	41.3	41.2
2.45	99	-	-	13.8	13.5
2.5	98	-	-	3.2	3.1
2.55	96	-	-	0.7	0.7

The variation in thickness is averaged out if all of the filter is used during operation. In this case removal of the filters will not upset the instrument calibration. If only a portion of the filter is utilised, however the instrument may well require calibration each time filters are interchanged.

The filters impose a limit to the ambient operating temperature of the instrument due to the nature of the interference films. The limit in temperature due to damage of the layers is however, greater than that imposed by the lead sulphide detector and need not concern us. A more real limit may be imposed by the thermal expansion and temperature coefficient of refractive index of the layers which will produce a change in the transmission characteristics of the filter.

The fundamental interference equations (4-1) and (4-2) are linear in both the refractive index and thickness of the deposited layers. Thus, any wavelength shift due to ambient temperature will be linearly dependent on the changes in both μ and t. Thus, λ_1 will shift by $\partial\lambda_1$ and λ_2 will shift by $\partial\lambda_2$ due to the combined change in μ and t with temperature.

Returning to the derivation of equation (2-10) for the energy ratio at the operational wavelengths, we have:-

$$R = \frac{\varepsilon_1}{\varepsilon_2}\left(\frac{\lambda_2}{\lambda_1}\right)^5 \rho^{\frac{C_1}{T}\left(\frac{1}{\lambda_2}-\frac{1}{\lambda_1}\right)}$$

If we assume $\frac{\varepsilon_1}{\varepsilon_2}$ = constant, then differentiating R with respect to λ_1 and λ_2 we obtain:-

$$\left(\frac{\partial R}{\partial \lambda_1}\right)_{\lambda_2} = -R\,\frac{1}{\lambda_1}\left(\frac{C_1}{T}\cdot\frac{1}{\lambda_1}+5\right); \quad \left(\frac{\partial R}{\partial \lambda_2}\right)_{\lambda_1} = +R\,\frac{1}{\lambda_2}\left(5-\frac{C_1}{T}\cdot\frac{1}{\lambda_2}\right)$$

for λ_1 = 1.9 microns; λ_2 = 2.3 microns. T = 650°K

C_1 = 14380 microns.°K

$$\left(\frac{\partial R}{R}\right)_{\lambda_2} = -6.16\left(\frac{\partial \lambda_1}{\lambda_1}\right)_{\lambda_2}; \quad \left(\frac{\partial R}{R}\right)_{\lambda_1} = +4.08\left(\frac{\partial \lambda_2}{\lambda_2}\right)_{\lambda_1}$$

The temperature coefficient of the interference layers is, according to the manufacturer, less than 5.10^{-3} microns/micron/°C, which is likely to be due mainly to the temperature coefficient of the refractive index.

Substitution of the above equations gives a ratio temperature coefficient of approximately 10^{-4} parts/°C, since the effects are opposite in each filter.

4.3.10 Rotating chopper wheel system

In the chopper systems to be considered the energy is collected using a Cassegrainian type mirror system. This arrangement presents a primary image at the chopper blades. This was considered necessary because in the extended application of the instrument operation down to as low a temperature as possible is desired. By chopping the signal energy where it enters the optical system it may be separated from the steady background falling on the detector. In this way the detector sees the difference between the signal entering the system and energy leaving the chopper blades when the signal is blocked. This energy is a combination of that emitted by the chopper blades and a reflection of the background. Thus in the off position the detector will see black body radiation effectively from an ambient temperature source.

In the first arrangement to be considered fig. 4.5 the energy is chopped at 900cps by circumferential teeth on the chopper wheel. It is then rendered into a parallel wavefront by M_3 and M_4 and deflected alternately through filters F_1 and F_2 by the chopper. It is then reconstructed and focussed on the detector. In order to achieve a good approximation to a step change of energy falling on the detector (see section 3.10) the edge of a tooth should cross the primary image in a time which is short compared with the on or off period. Since an interuption frequency of 1000cps is required the primary image should be as small as possible. A magnification of unity in the Cassegrainian system was decided upon, being a compromise between small image size and the blocking of energy by M_2. Thus for a primary image width **S** and a rise time **t** the tooth speed is given by

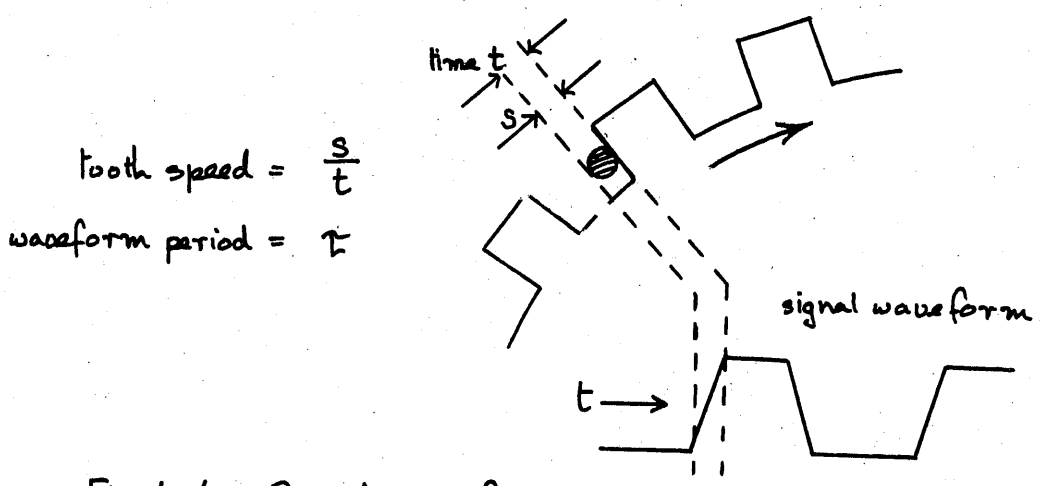

Fig 4.6 Signal waveform produced by chopper wheel.

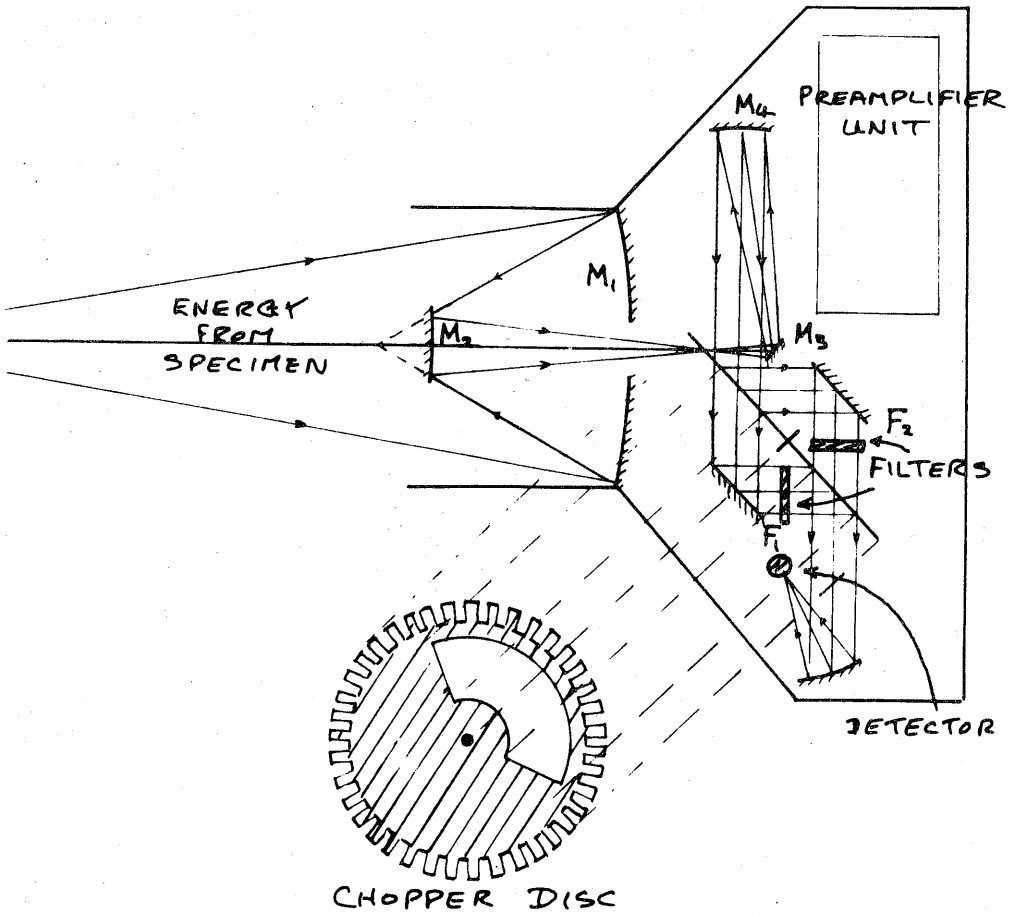

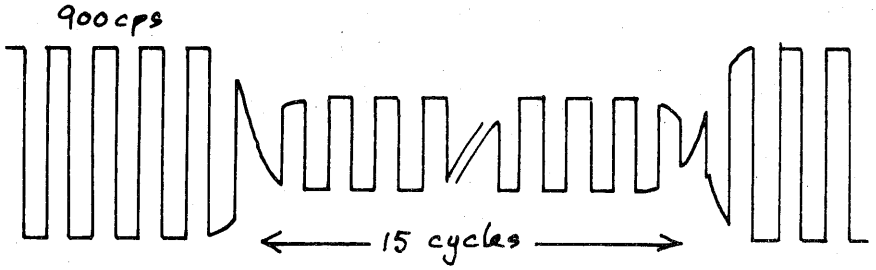

Signal waveform

FIG 4.5 OPTICAL SYSTEM EMPLOYING CHOPPER WHEEL

Furthermore the chopper wheel reflects the energy alternately through the two filters at a frequency of 30cps. Thus there must be 30 teeth (or in any case a multiple of 30) around the chopper circumference to achieve this.

The width of a tooth is given in terms of s, t, and τ by

$$\text{width} = \frac{s}{t} \times \frac{\tau}{2}$$

Thus the chopper diameter is $\frac{s}{t} \cdot \frac{\tau}{2} \cdot \frac{1800}{\pi R}$ for a signal frequency of 900cps where R = revolutions per second.

Since a constant speed is required the chopper should be driven from a synchronous motor. The maximum speed attainable is 1500 rpm assuming 4 poles which gives 25 cycles per second.

For a rise time of $\frac{1}{10}$ cycle $\frac{t}{\tau} = \frac{1}{10}$ and an image size S = 0.1 cm
$\therefore$ chopper diameter = 11.5 cm

The chopper geometry is shown in Fig. 4.5 and it is necessary that it be optically flat and highly reflecting on both faces. The width should be maintained constant to within a thousandth cm to prevent any significant addition of noise to the signal. A reference signal for the electronic system is obtained from a light and photocell working at the chopper periphery.

The system is partially folded for compactness and since it employs mirrors it is necessary to form both primary and secondary images away from the optical axis because of the coincidence of object and image space. This necessarily reduces the quality of the final image because all the Seidel aberrations are introduced. These are listed below together with the parameters which govern their magnitude (9, 10.)

	parameters determining magnitude
spherical aberration	F^3 present on axis
comatic aberation	$F^2 b$ present for small field of view
astigmatism aberration	$F b^2$ small if field of view is small
curvature of field	$F b^2$ small if field of view is small
distortion	b^3 small if field of view is small

By arranging the detector as shown, on the opposite side of the optical axis, cancelling of coma and distortion in the plane of the system cross section shown in Fig. 4.5 is possible (see 4.4). In this event the secondary image will be a line if the primary image is a point source. The effects due curvature of field and astigmatism will be small because the field of view is small ($b \to 0$).

where F = focal ratio
b = distance of image from optical axis

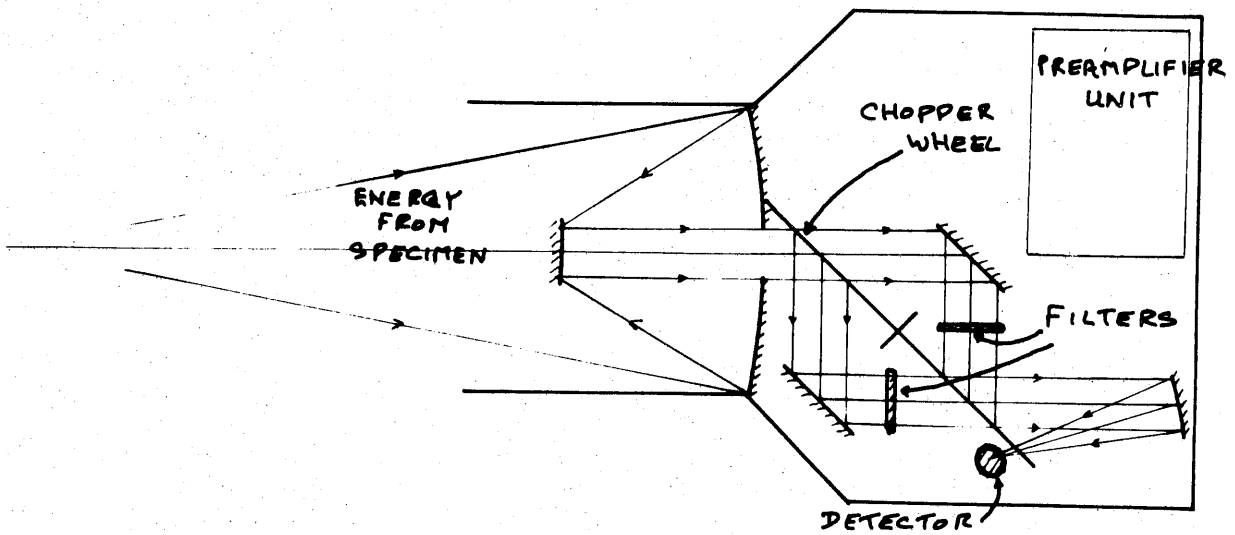

FIG 4.7 ALTERNATIVE OPTICAL SYSTEM EMPLOYING CHOPPER WHEEL

The system employs 7 surface aluminised glass reflecting surfaces and filters with 50% transmission. Assuming a reflectivity better than 95%(11)the system transmission will be better than $(.95)^7 \times \frac{1}{2} \times 100\% = 35\%$ deteriorating to 16% for a reflectivity after ageing, of 85%.

The second system shown, Fig. 4.7, reduces the number of reflecting surfaces to 5 but has the disadvantage that chopping is performed at the detector. This causes addition of any background radiation, entering the system, to the signal energy. Furthermore, partial cancellation of aberrations in this system is not straightforward and would require the inelegance of an object off the axis.

The transmission of the system would be $(.95)^5 \times \frac{1}{2} \times 100 = 39\%$ for a reflectivity of 95% reducing to 22% for a reflectivity after ageing, of 85% showing only an 11% improvement in transmission.

A further reduction in the number of reflecting surfaces is possible if the filters are carried on the chopper itself Fig. 4.8. Such a system is simple in construction and has the same disadvantage as the previous one since effectively only M_4 and M_5 have been dispensed with. Furthermore, any variation in transmission of the filter would produce a 30cps modulation on the signal providing one more factor to be removed during calibration. The transmission of this system would be $(.95)^3 \times \frac{1}{2} \times 100 = 43\%$.

The disadvantage of all the systems in this second category is the need for a chopper wheel which must be maintained in rotation at a constant speed. This calls ideally for a synchronous drive motor (already assumed in the deduction of chopper wheel diameter) and consequently the dependence of the instrument on an ac mains power supply. To drive the chopper wheel from a battery operated motor for any appreciable period would require heavy duty batteries.

4.4. System using optical modulator

4.4.1 The third and final system to be considered relies on optical chopping of the energy by changing its path with a moving mirror rather than a rotating wheel. In this manner the need for 30 identical teeth on a chopper wheel is removed and the opportunity arises to decrease size and mass of the moving parts of the optical modulator by an order of magnitude. The optical beam chopping can now be made independent of the ac mains, which reduces the precautions required to screen the system from troublesome 50 cycles pickup. The only moving part in the entire system is the suspension of the optical modulator. The optical system will now be described in principle and the particular arrangement employed in practice will be described in detail.

4.4.2 Reduction of aberrations

The aberrations which result from third order theoretical analysis are functions of either the field of view of the system or the relative aperture or a combination of both. In the present application the field

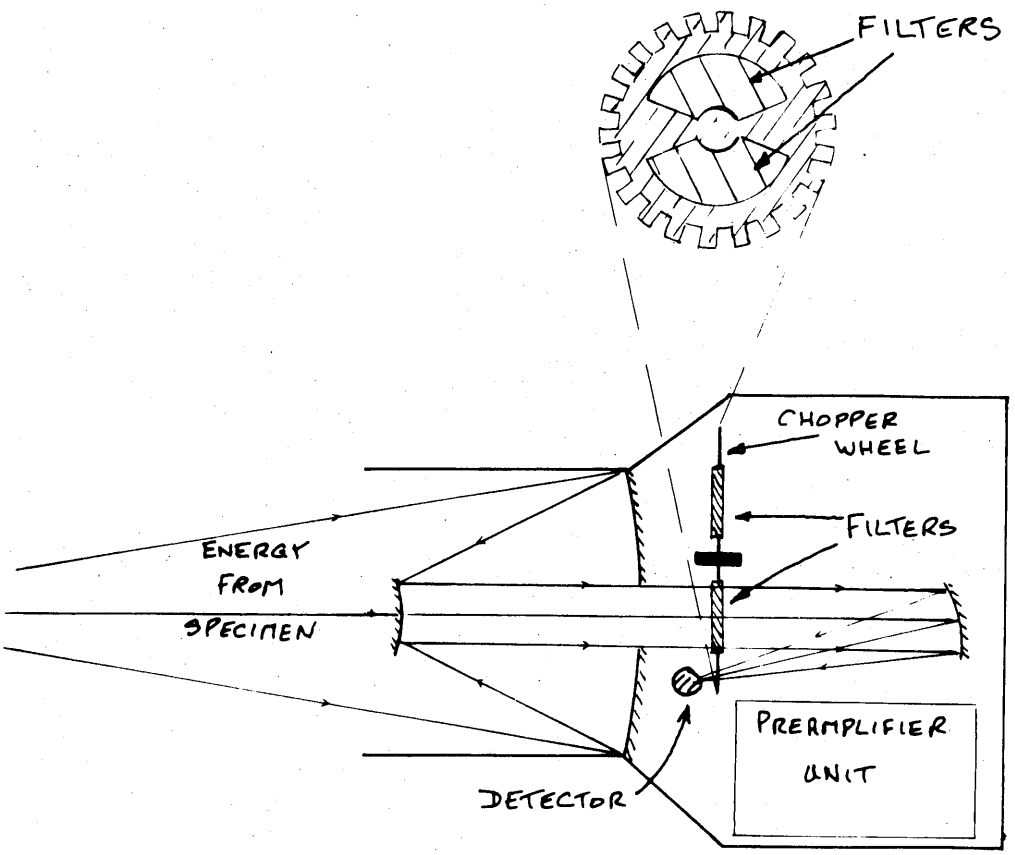

FIG 4.8 ALTERNATIVE OPTICAL SYSTEM EMPLOYING CHOPPER WHEEL

of view required is small and in order to gather sufficient energy to make a measurement the relative aperture is large. By forming all images on the optical axis and keeping the field of view small, astigmatism, field curvature and distortion are therefore small compared with the aberrations which are predominantly functions of aperture, namely coma and spherical aberration. The optical system has been designed with a view to reducing spherical aberration and coma as much as the other requirements of the instrument will allow.

The optical system is similar to an arrangement introduced by Littrow (12) in which cancellation of coma is achieved by forming the primary and secondary images with the same mirror working in opposite senses for each image. Fig. 4.9 a shows two spherical mirrors A and B each forming a point object from the same set of parallel rays. The parallel set of rays is inclined at an angle θ to each mirror axis. The rays C D E F and C D' E' F are marginal for each mirror while G H J K and G H' J' K are paraxial. The off axis images at CG and FK display comatic aberration and a three dimensional sketch Fig. 4.9 b shows that one image is the reverse and inverse of the other.

In particular, for this system the pencil of rays, which strike mirrors A and B inside the circles shown, produces the shaded portion of the images CG and FK in Fig. 4.9 b(9). If an object is now placed at CG which has this comatic shape then its image will be KF. If the object is reduced to a point source the image KF will reduce likewise and the comatic aberration is cancelled. The cancellation of comatic aberration is academic as far as the pyrometer is concerned since it is a small aberration in any case. The cancellation of comatic aberration is more important in the wider application of the system(13).

4.4.3 The Modulator System.

In the arrangement used for the pyrometer the system is folded one stage further combining mirrors A and B into one mirror M_4. The folding is achieved by two plane mirrors M_5, M_6 which cause a further inversion of the image in the vertical plane and have no effect in the horizontal plane. Fig. 4.10 shows this system. It is basically the same as Fig. 4.9 with B combined with A by turning it through 180° about a horizontal axis. The pencil of rays striking the mirror within the shaded circles only is shown.

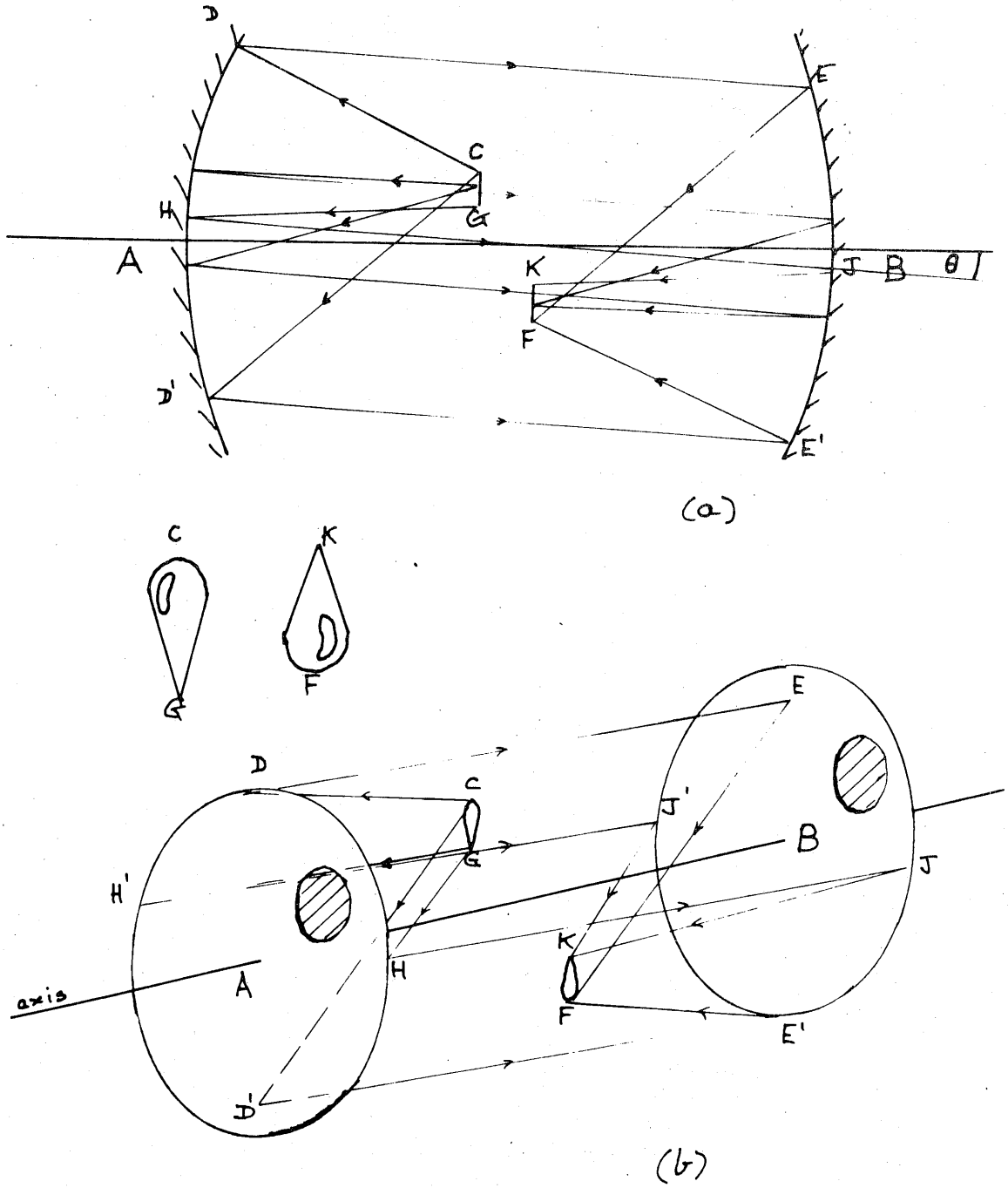

FIG 4.9 CANCELLATION OF COMATIC ABERRATION

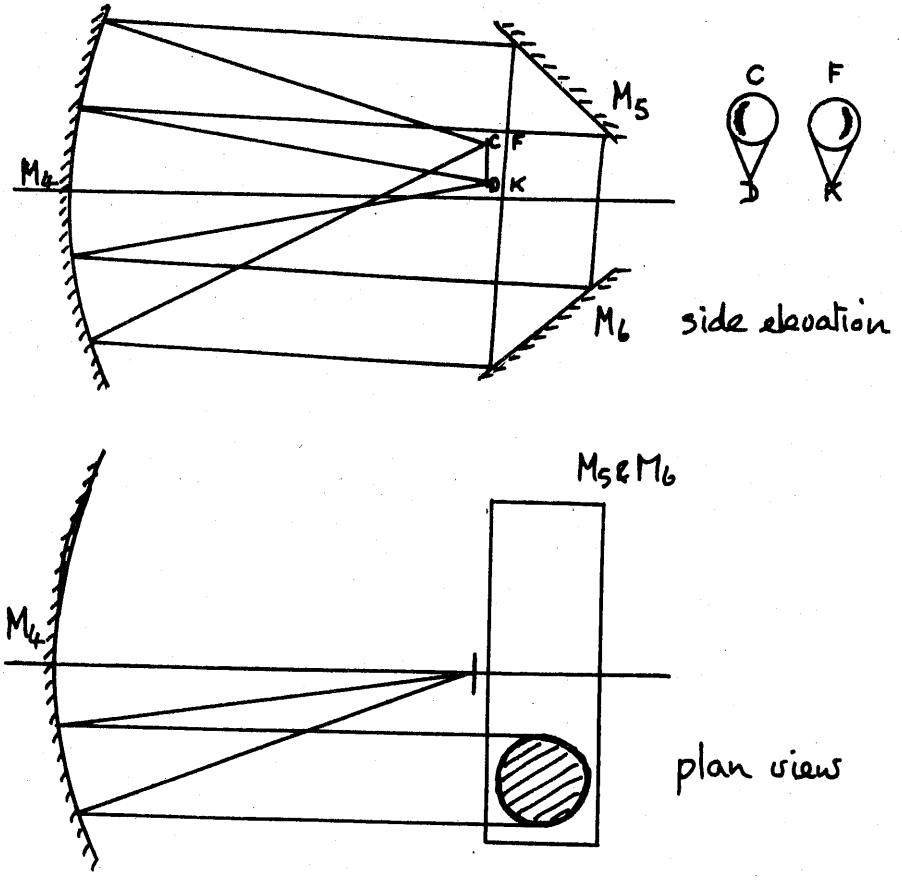

Fig 4.10 Single channel modulator system.

Again if C D is treated as an object then when it is reduced to a point source FK will reduce to point source also.

The spherical aberration of this system is examined later in conjunction with the collecting optics.

The arrangement shown in Fig. 4.10 uses half of the mirror M_4. If the object CD is made the primary image of the system which is formed by the collecting optics through a hole in the centre of M_4, then by introducing a small plane mirror M_3 coinciding with CD and inclined to the vertical, the image FK may be formed by a pencil of rays striking M_4 at any angle, which depends on the angle of inclination of the small mirror. In practice the small mirror may be driven from one side to the other diverting the incoming pencil of rays into two paths alternately see Fig. 4.11. The multilayer interference filters F_1 and F_2 can now be introduced into each path and the energy arriving at FK will be alternately that filtered by F_1 and F_2 respectively. FK becomes the secondary image of the system which should be focussed on the

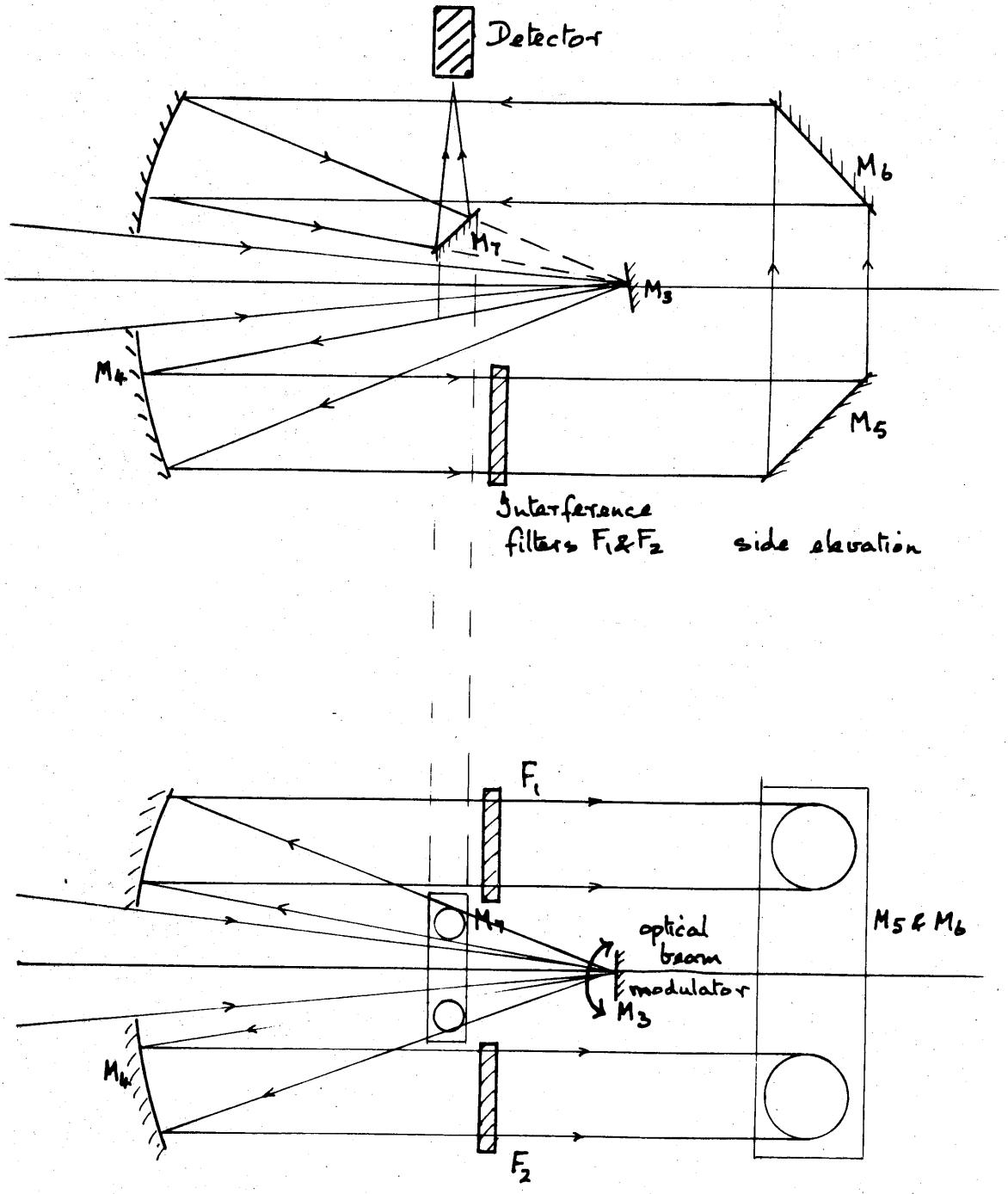

Fig 4.11 Practical two channel modulator system.

detector surface. This is achieved by intercepting the beam by another plane mirror M_7 to focus on the detector at the top of the system.

The system is now completely symmetrical about the optical axis and uses complementary zones of the spherical mirror M_4. The energy moves with a plane wavefront when it passes through the filters which is the ideal but not necessary requirement demanded by the filters (see section 4.3). Furthermore since it is folded twice its practical length is a quarter of the optical path length.

4.4.4 Modulation of the signal

Ideally a 30 cps modulation by the signal of a carrier frequency of 1000 cycles is required (see 3.9.4 to 3.9.6). The amplitude of the modulation represents the difference in energy in each channel and may be obtained in any desired form e.g. square wave or sinusoidal by driving the mirror M_3 from side to side in a suitable manner. The carrier frequency is obtained by driving M_3 in addition, to a central position at 1000 cps, where the energy it reflects cannot reach the detector. The ideal drive waveform is shown in Fig. 4.12 together with the resulting signal appearing from the detector.

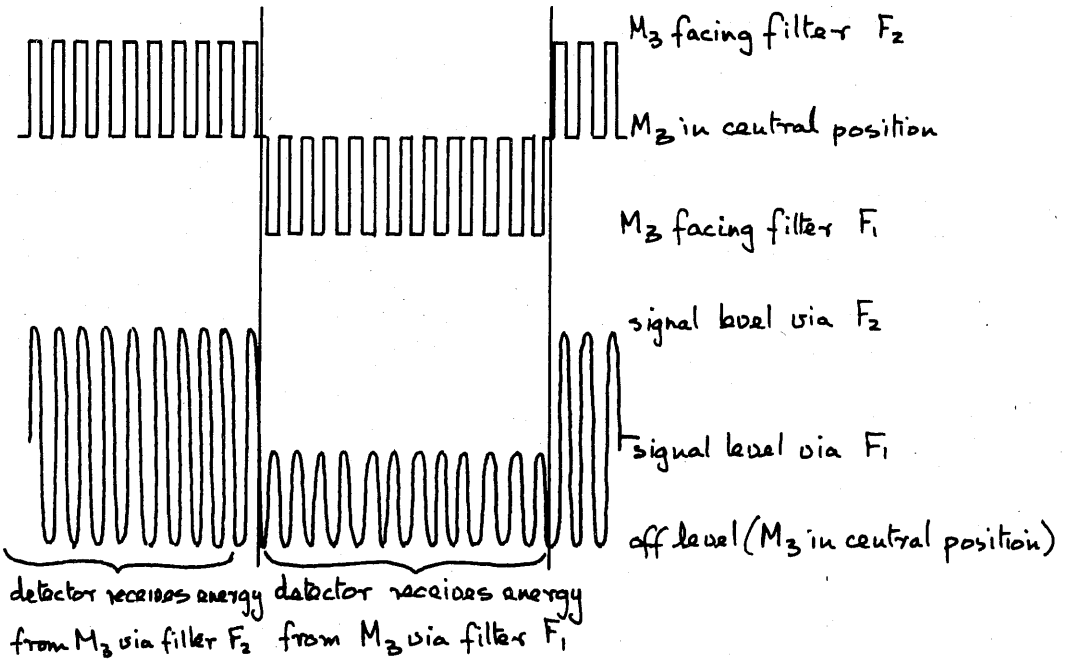

Fig 4.12 Galvanometer and signal waveforms.

This method of modulating the incoming energy and its use in the type of optical system shown is the subject of a British patent(13) claimed by United Power Company Ltd.. It is a complete unit in itself and is described in the patent for a wider application as a polychromator in which energy is diverted in sequence into a plurality of optical paths and combined on a single detector.

The beam splitting mirror M_3 is part of a pencil galvanometer as used in the commercially available ultra violet recorders. The size of such a mirror is limited by the required frequency response of the galvanometer and in this case, where ideally a 1000 cycles square wave is needed, a galvanometer operating to 1600 cycles has been used. The maximum mirror size available was .150 x .050 cm^2.

4.4.5 The collecting optics

To complete the general description of the optical system for the ratio pyrometer, the energy gathering components are now described. Again, reflecting optics were chosen for the reasons of long wavelength response, cheapness and chromatic independence discussed earlier. The requirements of the collecting system are given below.

(i) the primary image should not be formed too near the object to avoid blocking incoming energy.

(ii) the primary image should be formed on the system optical axis to comply with the minimum aberration conditions.

(iii) for the sake of compactness the optical axis should remain undeviated throughout the instrument.

These requirements narrow the choice of simple systems to the Cassegranian or the Gregorian arrangements, the difference being that folding occurs before the primary focus in the Cassegrainian system and after it in the Gregorian system.

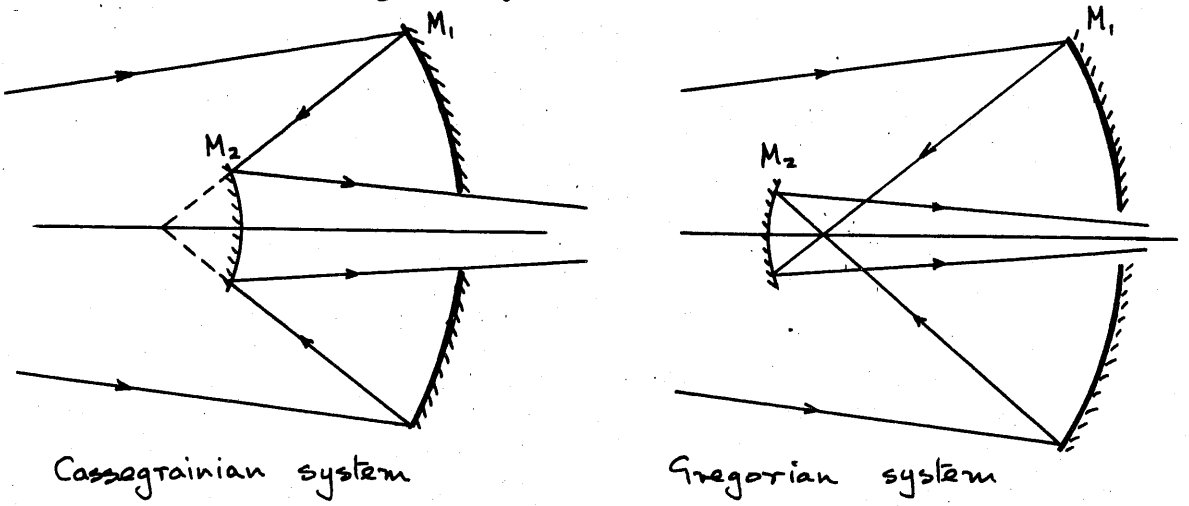

Fig 4.13 Energy collecting systems.

It is possible to remove spherical aberration completely in both these systems for one pair of object and image distances if suitably figured mirrors are used. The Gregorian system requires a concave elliptical primary M_1 with the object and image on axis at its two focii and a concave elliptical secondary M_2. The Cassegrainian system requires a similar primary mirror but a convex hyperbolic secondary is needed(5). In both cases the primaries would become paraboloidal for distant objects. These aspheric surfaces are costly however and could not be justified in this application.

It can be seen from Fig. 4.13 that the Gregorian system is longer than the Cassegrainian. This means that for the same magnification and primary mirror, the secondary mirror will be larger and, hence, more blocking of the incoming energy occurs. A more important consideration however lies with the opportunity of reducing spherical aberration in the Cassegrainian system, even when spherical mirrors are used for the typical dimensions and object and image distances involved.

If a parallel wavefront from a distant on axis object strikes a concave spherical mirror the marginal rays are brought to a shorter focus than the paraxial rays, causing spherical aberration. If the object is placed at the radius of curvature the spherical aberration reduces to zero. In the practical case the object distance must be greater than the radius of curvature so that a secondary mirror may be used to intercept the entire beam. Some degree of spherical aberration will therefore exist. When the secondary mirror is introduced the aberration is such that a point image formed at B, Fig. 4.14, would produce two virtual objects A' and A'' for paraxial and marginal rays. If these two systems are combined for the particular case when $v_{p_1} - v_{m_1} = u_{p_2} - u_{m_2}$ then for particular combinations a point image will be formed at B for a point source at A.

The complete optical system employing the Cassegrainian arrangement to collect the energy is a combination of the arrangements of Fig. 4.11 & 4.14. The system satisfies all the requirements already discussed under optical design namely:

(i) ideal condition of parallel wavefronts at filters

(ii) on axis images throughout and in line system apart from M_7

(iii) only reflecting surfaces are used

(iv) aberrations are reduced to a minimum

Furthermore, when the energy is separated into the wavebands each channel undergoes reflection symmetrically about the optical axis from the same set of mirrors. This reduces the possibility of drift of calibration with time since the whole of a single mirror surface is likely to deteriorate uniformly. Thus, when a reflecting component is replaced at any time it will have the same effect on both wavebands.

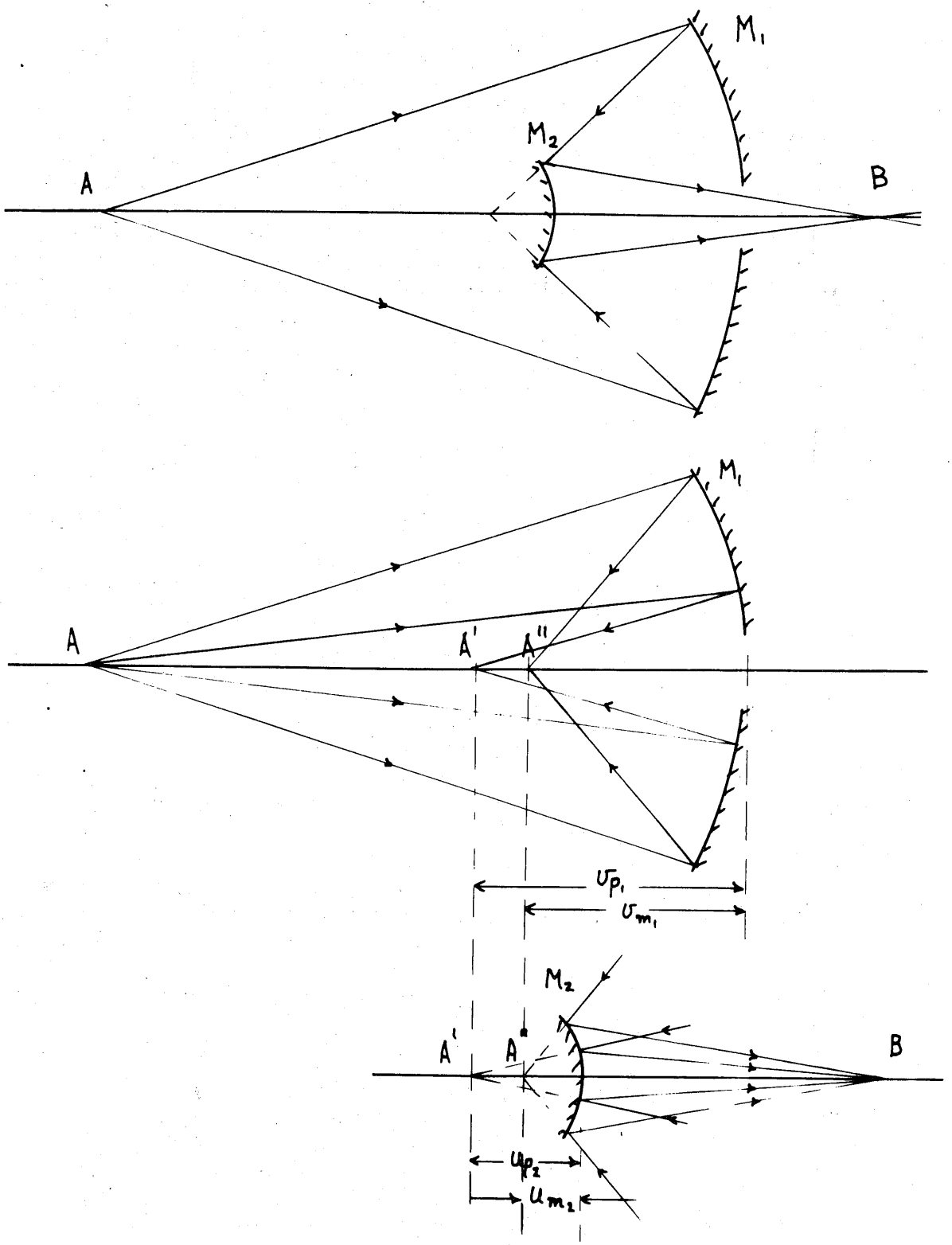

Fig 4.14 Reduction of spherical aberration in collecting system.

Before the detailed design of the system can proceed it is necessary to fix the primary object distance u_1 and the secondary image distance between M_3 and M_4. The object distance is calculated in conjunction with the F number of the system and the diameter of the primary mirror. In the feasibility study an f/4 entrance aperture was considered. The entrance aperture was chosen as large as possible to obtain sufficient energy. This aperture is limited, however, by the nature of the target. In chapter 1 the measurement of fin root temperature was stated as the objective and relevant dimensions are given in Fig. 4.15 for a Trawsfynydd fuel can.

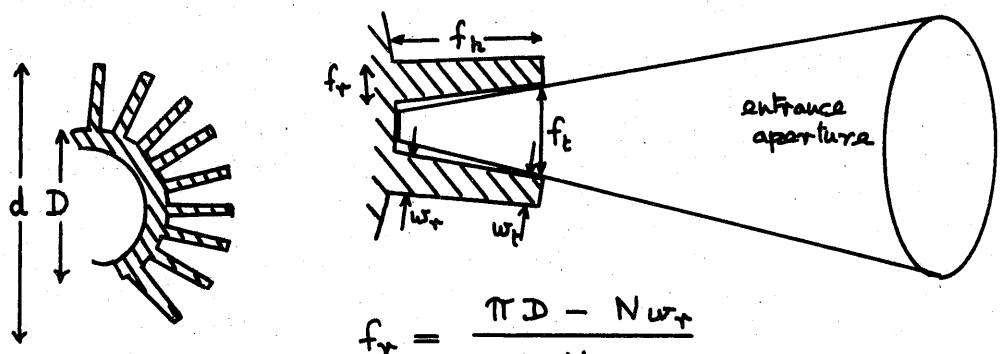

$$f_r = \frac{\pi D - N w_r}{N}$$

$$f_t = \frac{\pi d - N w_t}{N}$$

Fig 4.15 Determination of entrance aperture.

If the instrument is to accept energy from the fin root only, supplemented by energy from the fin wall reflected at the root and no energy from the fin tip, then we have:-

$$\text{Maximum entrance aperture} = \frac{f_h}{f_t - a} = \frac{f_h N}{\pi d - N(w_t + a)} \qquad (4\text{-}3)$$

where:- N = number of fins around circumference (48)
D = fin root diameter of can (3.25cm)
d = fin tip diameter of can (5.2cm)
w_r = fin root width (.113cm)
w_t = fin tip width (.055cm)
a = maximum width of target area (.050cm; see size of M_3)
f_t = gap at fin tips
f_r = gap at fin roots
f_h = fin height (0.98cm)

Substitution of these values in (4-3) leads to

Entrance aperture = 4.15 (Hence f/4 aperture used in section 2.7)

The fuel element is mounted centrally in a channel with an internal diameter of approximately 10cm. A minimum operating distance of 30cm is visualised to give sufficient clearance of rig supports.

Since the system is folded, approximately 15cm extra is required to reach the primary mirror. This gives a primary mirror diameter of 45/4.5 = 10cm. It was decided that a 15cm mirror would not be too inconvenient to handle in the system and this was decided upon to give a clearance of approximately 45cm between the instrument and the rig.

Thus the object distance was fixed at 60cm and the objective diameter at 15cm.

The distance between M_3 and M_4 is fixed by the useful diameter of the interference filters and the available amplitude of vibration of the mirror M_3. Reference to Fig. 4.11 shows that when the incoming beam is deflected by M_3 it achieves a diameter at mirror M_4 which it maintains through the filters. The standard filter diameter is 2.2cm but in practice less is available because a filter housing is required. A beam diameter of 1.9cm was used which allows for a small amount of divergence of the beam when passing from M_4 to the filters.

The amplitude of motion of the galvanometer mirror is limited by the current handling capacity of its coil and the strength of the magnetic field available. A 900 or 1600 cps movement can be used with a small horseshoe magnet supplying the field through suitably machined pole pieces. Measurements of amplitude for various driving currents were made (Appendix F) and an optimum working angular peak to peak amplitude of about 11° was decided upon. The filters are mounted on either side of the magnet block which is 1.9cm wide. It can be seen that a deflection of the beam at M_4 of 1.9cm is required to clear the mounting of the magnet. Combining this with a 11° deflection gives 1.9/2 tan 5.5° = 9.9cm.

It has already been shown that a target area width not exceeding .050cm must be used if no interference is to be allowed from the fin tips with an f/4 entrance aperture. The galvanometer mirror size must be chosen to accommodate this target area and to calculate its size the system magnification must be known. The magnification will be decided by the arrangement employed to reduce the spherical aberration and a suitable arrangement is now considered.

4.4.6 Aberration in the collecting optics

The spherical aberration was calculated for the system shown in Fig. 4.14 for various object distances u_1. The calculation (see appendix G) is in three parts, one part for each of the mirrors M_1, M_2 & M_4. The first part applies to the primary mirror M_1. It was carried out for three radii of curvature and four rays at h = 0, 2.5, 5, 7.5cm. The results of this calculation are plotted in Fig. G.5, 6 and 7

The second part was carried out for the secondary mirror M_2 again for suitable values of h and for six radii of curvature. The effect of varying the distance of the final image formed at M_3 was also included in this calculation. The results of this second part are plotted in Figs. G8 and 9.

Interpolation between the graphs led to an optimum arrangement. The calculation shows that to reduce spherical aberration it is necessary to increase r_2, increase v_1, and decrease v_2. This was done as far as possible and the last two graphs show the variation of spherical aberration with mirror radii for the image formed at M_3. See Figs. G 10 and G 11.

The third and final part of the calculation takes into account M_4. Energy is reflected twice by M_4 and since it forms an image to coincide with M_3 the spherical aberration is considered the same for each reflection and is additive. Due to the deflecting action of M_3 rays which were marginal for M_1 and M_2 became both paraxial or marginal for M_4 depending on whether the deflection is to the right or left. There is nothing which can be done to reduce spherical aberration at M_4 if spherical mirrors only are used. It is not possible to combine the spherical aberration of this section of the optics with that in the collecting optics to produce a minimum condition. However the aberration due to M_4 is small compared with that of M_1 and M_2 in the compromise arrangement. The final image is a circle of least confusion with the approximate diameter .075cm for a point source at u_1. The dimensions obtained for the system are

u_1 = 60cm
r_1 = 26.8cm
v_1 = 17.17cm
u_2 = 7.4cm

r_2 = 21.4cm
v_2 = 24.2cm
x = 10.43cm

$$\text{mag.} = \frac{24.2}{7.4} \times \frac{17.17}{60} = 0.94$$

required mirror size = .0063cm^2 for .01cm^2 object (1 sq. mm)

.01cm^2 object (1 sq. mm)

These dimensions are a compromise between those required and those readily available commercially.

The comatic aberration of the collecting optics will be small due to the on axis object and images and the small field of view and no attempt has been made to reduce it inthe collecting system.

4.4.7 Adjustments in optical system

In general the detecting element will not be uniform in sensitivity (section 3.8). This means that some adjustment is required so that the image may be directed onto the most sensitive region. This requirement necessitates adjustment of the final image position both laterally and longitudinally in the plan view of the system. Furthermore it is desirable, if the variation of sensitivity over the detector surface is to be removed, to combine the images in both channels at the detector. This is essentially at the final focus of the optical system. It would be possible to combine all these adjustments at the detector itself, but this leads to a complex mounting since adjustment in three perpendicular directions would be needed. It is preferable to incorporate only the focussing adjustment at the detector along its vertical axis. The other two adjustments can be most conveniently combined into the mounting of either of the plane mirrors which produce the folding at the rear end of the instrument.

An adjustment at M_3 may be convenient during the initial alignment of the optical system to take into account any small deviations of components from the design position due to machining tolerances. Such an adjustment is not essential because there is always a region in the object plane which will be imaged at M_3, but it does enable the object to be brought onto the axis of the system to satisfy the minimum aberration condition.

4.4.8 Alignment of the system . in general use

It is necessary to incorporate into the optical system some means for quick and accurate alignment of the instrument onto the target area during use. The obvious means is to use a sighting telescope which is aligned in parallel with the optical system. A more compact arrangement however, and one whose alignment is less likely to be disturbed consists of an eyepiece which uses the mirrors in the collecting optics. Such an eyepiece could be positioned either to intercept the energy after reflection from M_3 during the half periods when this mirror is at the centre of its travel or to intercept the incoming energy. The first arrangement allows alignment to proceed while the instrument is measuring, but suffers the disadvantage of having a very small field of view. This is brought about by the dimensions of M_3, which is the aperture stop for the system (Fig. 4.11), and it would mean that during alignment a magnified image of the target area only would be seen. Thus in the case of a polyzonal can it would be difficult to define the exact location of the target area in relation to the can as a whole.

The second arrangement has, as its aperture stop, the central hole in M_4. The hole can be made larger than required as far as energy from the target is concerned. In this way the field of view can be increased significantly beyond the target area.

The technique of employing a light beam which is focussed through the system in reverse lends itself ideally to the optical system. If a source of light the same size as the aperture stop is inserted into the system then a small patch of light identical in size to the target area is formed at the target area.

4.5 Conclusion

This concludes the discussion of the optical systems. A focal isolation technique, although it offers many advantages, has been rejected on account of its large size and inadequate performance caused by spherical aberration. A system employing a rotating chopper wheel, although conventional, has been rejected because of the large size of wheel required with its attendant drive motor. A system employing interference filters mounted on a chopper wheel has been rejected due to transmission variation over the filter which would have to be nonstandard in any case. The final system to be considered in which energy is switched by a vibrating mirror through two interference filters has been chosen. The operation of this system has been examined in detail and it has been shown that aberrations can be reduced to an acceptable level without the need for costly optical components.

The constructional details of the optical system are dealt with later in chapter 7 when the alignment is discussed and the performance is assessed.

4.6 References

1. R.W. Ditchburn. Light. London,Blackie,1958,p.68,p.234

2. J.A. Jamieson et al. Infrared Physics and Engineering. New York,McGraw-Hill,1963,p.193,p.199

3. F.A. Jenkins and H.E. White. Fundamentals of Optics,2nd Edition. New York,McGraw-Hill,1950,p.262

4. H. Rubens and R.W. Wood. Phil.Mag.,1911,21,p.294

5. R.W. Wood. Physical Optics. London,MacMillan,1934,p.45

6. M. Born and E. Wolf. Principles of Optics. Oxford,Pergamon Press,1959

7. S.D. Smith. J.Opt.Soc.America,1958,48,(1),p.43

8. P.H. Lissberger and W.L. Wilcox. J.Opt.Soc.America,1959, 49,(2),p.126

9. W.T. Welford. A Guide to Instrument Design. Chapter 4. S.I.M.A. and S.I.R.A.,London,Taylor and Francis,1963,p.108

10. H.J.J. Braddick. Physics of Experimental Method,2nd Edition. London,Chapman and Hall,1963,p.320

11. N.A.S.A. Report NASA sp-31,1963,p.139,p.176

12. G.K.T. Conn and D.G. Avery. Infrared Methods. New York, McGraw-Hill,1960,p.167

13. British Provisional Patent No.4333/64

CHAPTER 5 - THE ELECTRONIC SYSTEM

Introduction

Before proceeding with the design of the electronic system the reliability of components is examined and the transistor is selected as the active device. The precautions necessary in transistor circuit design are outlined and the principle of negative feedback is adopted to provide predictable circuit performance. The principle of negative feedback is extended further to the system as a whole and a particular ratio-ing method is adopted. A specification for the electronic system is compiled to suit the lead sulphide detector and the specification of Chapter 1. An analysis of the ratio circuit is carried out leading to the design of the signal circuit. A phase-sensitive rectification system enabling high rejection of noise to be achieved is discussed. The stability of the ratio circuit is examined and a suitable correcting network incorporated to provide the desired system response time.

5.1 The problem of reliability

5.1.1 An instrument of this type, could well be used in a process control loop. Such an application demands twenty four hours a day, seven days a week reliability. This is particularly important in the case of a temperature controlling instrument because plant operating temperature is usually a critical factor in determining the properties of the final product.

In the present application, operation in a hostile atmosphere is not required, but in the wider application the effects of heat, cold, shock, vibration, humidity, dust and corrosive atmosphere become important.

Table VIII (1) illustrates that capacitors and resistors, although the most reliable of circuit components, appear high on the order of failure lists simply because they are used in large numbers.

5.1.2 Valves

Valves appear at the top of the list in both the failure tables, being susceptible to shock and vibration because of their basic construction. Apart from this, their use is less desirable in this application than the transistor, because a portable instrument is required.

TABLE VIII

Order of failure total numbers	Order of failure proportional basis
1. Valves	1. Valves
2. Resistors	2. Meters
3. Capacitors	3. Relays
4. Transformers	4. Cables and connectors
5. Switches	5. Transformers
6. Relays	6. Switches
7. Meters	7. Plugs and sockets
8. Plugs and sockets	8. Capacitors
9. Cables and connectors	9. Resistors

5.1.3 Resistors

Because they are used in such large numbers the reliability of resistors has been made extremely high. In the case of carbon composition and cracked carbon resistors, faults are usually caused by overheating which produces changes in composition. In the larger rating wire-wound resistors, the failures are most likely with higher values where fine wire is used. At the expense of close tolerance, better protection against humidity and mechanical damage is available in vitreous enamelled resistors.

For the sake of cheapness carbon composition resistors are used where possible although the tolerance on value varies within wide limits ($\pm$ 5 to $\pm$ 20%). The temperature coefficient is $\pm$ .12% per ^{o}C and ageing effects on this type of resistor are the worst, variations of up to 25% are not uncommon during the working life. Thus when a resistor is performing an important function as far as its value is concerned, either a cracked carbon or a wire-wound type, even though more costly, should be used with 1 or 2% long term stability and $\pm$ .02% temperature coefficient. The circuit to be described uses carbon composition, cracked carbon and wire-wound resistors.

5.1.4 Capacitors

Capacitors are produced in a wide variety of forms as well as in large numbers. Those considered are paper, mica, ceramic and plastic dieletric types and electrolytics.

The paper capacitor is the capacity counterpart of the composition carbon resistor and is used as a coupling or decoupling element. It is susceptible to ingress of moisture and is encased in a protective coating to avoid breakdown at high working voltages.

The mica type is considerably more stable than the paper type and is used for higher working voltages. Selection and stability tolerance are 1 or 2%. Failure is usually caused by the slow accumulation of conducting material on the dielectric surface causing breakdown.

The silvered ceramic capacitor is particularly useful when temperature compensation is required since it is available with both positive and negative temperature coefficients.

The electrolytic capacitor has the particular advantage that its capactity to volume ratio is high. This characteristic makes its use in many applications virtually unavoidable which is unfortunate since it has many disadvantages, listed overleaf.

(i) capacity is very temperature dependent

(ii) performance is poor at low temperatures which affect the electrolyte

(iii) leakage current is large (with the exception of tantalum capacitors)

(iv) peak voltages must be carefully considered in relation to ratings, e.g. in smoothing applications the ripple voltage superimposed on the d.c.voltage must be considered

(v) the power factor is poor

(vi) bypassing is sometimes necessary at high frequencies.

In low level signal circuits the noise generated in capacitors can be troublesome. The source is due either to scintillation causing small random changes in capacity or internal discharge causing breakdown at local inhomogeneities in the dielectric (1).

The circuit employs paper, ceramic and electrolytic capacitors.

5.1.5 Transistors

Transistors have not been included in the reliability tables because they have not been in widespread use for long enough and the development in the methods of construction has been so rapid. The transistor appears, however, to be potentially a much more reliable component than the valve, since mechanical failure is far less likely.

Apart from the distinct advantages over the valve of compactness and low power consumption, there are a few inherent disadvantages which must be mentioned.

(i) The characteristics of germanium transistors are very temperature dependent and in high temperature or under widely varying ambient conditions silicon transistors may be required at consequently greater expense.

(ii) The tolerance range in transistor characteristics is appreciably greater than in valves.

(iii) Transistors are suceptible to damage by the application of excess voltage.

Since these disadvantages can be overcome by proper circuit design the transistor has been chosen as the active device for this application because of its compactness, low power requirement and potential reliability. The circuit techniques required to overcome the inherent disadvantages of the transistor will be dealt with in a later section. Both germanium and silicon transistors have been incorporated into the circuit.

5.1.6 Other components

The reliability of transformers is high if used within their power ratings. Ingress of moisture is again the usual cause of failure and progressive degrees of precautions are dictated by the nature of the environment. The reliability of the other components tested in the table has not been dealt with since the parameters to be considered are so varied. There is one further consideration, however, which arises in this particular system.

The use of plug in circuit boards should be approached with caution where there is insufficient voltage to breakdown and insufficient current to maintain breakdown of oxide films. This situation is likely to arise in low level signal circuits where transistors are used, when both low voltages and low currents will be encountered.

5.2 General design principle

5.2.1 The decision to use the transistor as the basic active component in the electronic system follows from the factors discussed in the previous section. No attempt is made to give a thorough account of the underlying principles of transistor operation but the effect upon the conduction process of changes in temperature and applied voltage are worthy of further consideration since it is these effects, together with lack of reproducibility of characteristics during manufacture, which determine the type of circuit to be used.

In both intrinsic and extrinsic semi-conductors the conduction processes are due to the combined effect of the drift of electrons and/or holes through the crystal under the influence of applied electric fields. Conduction can take place only if the probability of finding either an electron in the conduction band for N type material, or a hole in the valence band for a P type material is high. Statistical analysis (2) predicts that the population of the conduction band follows a Fermi distribution with respect to temperature and the population is expected to be proportional to

$$\frac{1}{1 + e^{\frac{(E_c - E_F)}{kT}}}$$

E_c = Energy level of conduction band

E_F = Fermi level

T = absolute temperature

k = Boltzmanns constant

assuming the width of the conduction band is small compared with the forbidden energy gap between conduction and valence bands.

This is an oversimplification of the problem, however, and the distribution is modified in practice due to the finite widths of valence and conduction energy bands leading to the relation for a given material (4)

$$\text{population} \propto T^3 e^{\frac{-E_g}{kT}}$$

where E_g = energy gap for semi-conductor in electron volts

T = absolute temperature in ^oK

The change in conduction band population with temperature is governed largely by the exponential term at ambient temperature. Thus for a temperature change of +9°C at normal ambient (9°C at 300°K is 3%) T^3 will change by approximately +9% and E_g/kT will change by -3%

$$\text{for } T = 300^oK \quad \frac{E_g}{kT} = \frac{\cdot 67 \times 1.6.10^{-12}}{1.4.10^{16} \times 300} = 25.5$$

and when T increases by 3%

$$\frac{E_g}{kT} = 24.75 \qquad \text{and} \qquad e^{-E_g/kT}$$

changes by a factor of 2 which means for a 9°C rise in temperature the population of the conduction band will double. This means that during normal operation of a transistor, when the collector base junction is reversed biassed, minority carriers will flow giving rise to leakage current. The leakage current will be dependent on the junction temperature and will cause drift in the operating point of the transistor unless taken into account.

5.2.2 Effect of applied voltage

In an extrinsic semiconductor when no external source of energy exists there is a potential barrier at the junction of N type and P type material. This barrier is in such a position as to encourage the flow of minority carriers only but the total amount is zero because some majority carriers will have sufficient energy to cross it. At room temperature the thermal energy of the majority carriers can be considered to follow a Boltzmann distribution (3). Thus if the potential barrier is decreased by the application of an external field, majority carrier current will increase exponentially. The resultant current will be the difference between the majority and minority carrier current and we have (4)

$$i = i_o\left(e^{qV/kT} - 1\right)$$

where i_o = minority current

V = applied voltage

q = electronic charge

This reduces to $i = 0$ when no bias is applied

During normal operation, therefore, when the emitter base junction of a transistor is forward biassed, the current flow will increase exponentially with applied voltage. In a typical transistor about 98% of this current is collected by the collector and the relation between input and output currents is linear. The relation between input voltage and output current will be exponential, however, and thus distortion will be introduced in large signal circuits if voltage amplification is used. For this reason current amplification is preferable whenever possible.

5.2.3 Spread in transistor characteristics

In addition to the variation in transistor characteristics with temperature there occurs a large spread in the parameters for transistors of the same type. This is due to the difficulties of controlling the composition of the semiconductor material and the dimensions of the emitter, base and collector during manufacture. Special selection can be carried out to produce smaller spreads for a given type of transistor or transistors developed more recently may be used at greater expense. It is more profitable, however, to design the circuit to be independent of transistor parameters wherever possible and this procedure has been adopted in this system. The most significant spread occurs in the current gain characteristics which may be given by the manufacturer as -50% +100%.

5.2.4 Feedback stabilisation

The temperature dependence and spread of characteristics in transistors has caused a particular type of circuit technique to be developed. Four important demands are made on circuits associated with the transistor. These demands apply to both the quiescent and the dynamic conditions.

(a) Quiescent condition

(i) the operating point of the transistor should be predictible even though spreads of 200 or 300% occur in the current gain.

(ii) the operating point of the transistor should not move outside the working range or introduce thermal runaway for the extremes of ambient temperature likely to be encountered during operation.

To satisfy the above requirements biassing circuits, which will define the operating current and hence the operating voltage, are required. Ideally the operating points can be specified in terms of the power supply and known resistors.

(b) Dynamic conditions

(i) the a.c. gain of a stage should be predictable and therefore independent of the transistor gain characteristics.

(ii) the loading exerted by one stage an another should be predictable either by defining input and output impedances by circuit resistors or introducing sufficient mismatch between stages so as to reduce the effect of variations in or uncertainty in the impedances.

The principle of negative feedback has been widely used in the system to be described both for defining quiescent and dynamic operating conditions. In many cases stages have been directly coupled with overall feedback combining both d.c. and a.c. predictability and stability. Also to reduce the effects of uncertain interaction between stages the technique of mismatch suggested by Cherry (5) has been employed where necessary.

(c) Effect on reliability

The reliability of a well designed system must depend ultimately on the number of components employed. The reliability may be expressed as the probability of survival of the system over a given period of time. If we define the individual survival probability of the nth component of a system containing n components as p_n then the overall survival probability is

$$p = p_1 p_2 p_3 \cdots\cdots\cdots p_n$$

For a system containing 100 components with $p_1 = p_2 = \cdots = p_n = 0.999$ for a given period of time the value of p is 91%. If the number is increased to 500 then the reliability reduces to 64% for the same period of time.

Reliability is improved if the number of components is kept to a minimum; but the use of negative feedback necessitates the use of additional components because valuable advantages are gained always at the expense of the stage gain. Yet negative feedback is required to achieve reliability in the form of predictability and stability. In this system where the ratio of two similar signals is required, the opportunity exists to relax the requirement of stability as far as a.c. gain is concerned. This reduces the number of feedback circuits required in the main amplifier and hence the overall number of components.

5.3 The null system

The relaxation in a.c. stability requirements can be tolerated if a null system is used. (Fig. 5.1). If the two signals from the detector, which represent the energies in the working wavebands, are processed through the same electronic system and a comb is driven to obstruct the energy in the waveband producing the larger signal then the direction of the drive

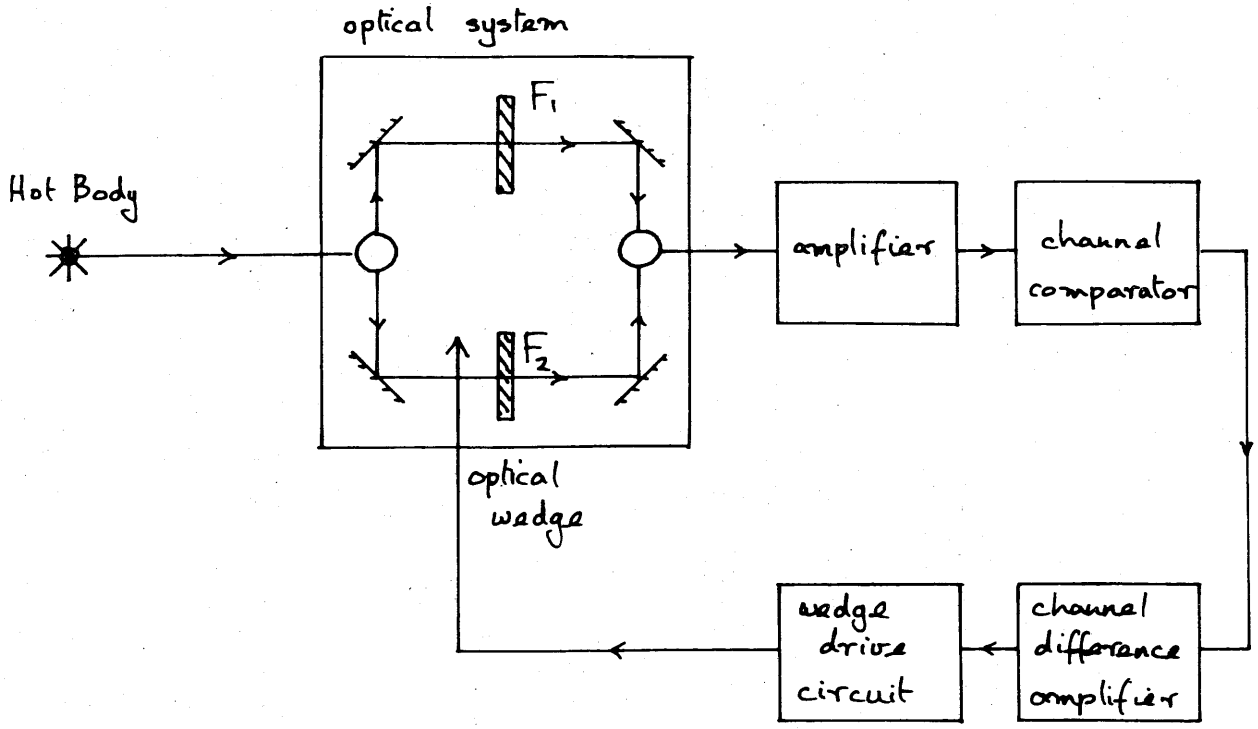

Fig 5.1 Schematic of Null System.

can be arranged to produce equal intensities from both wavebands at the detector. In such a system the ratio can be obtained from the setting of the comb position required to produce zero output from the channel comparator. At the balance condition which is the normal setting of the system the position of the comb will be independent of the gain of the detector and amplifiers. The accuracy of such a system is dependent upon the loop gain which is made large and the electro mechanical design of the comb drive mechanism.

5.4 The ratio system

One of the advantages of the optical system of the pyrometer described in Chapter 4 is the absence of moving parts other than the suspension of the beam channelling galvanometer. The null system described in the previous section calls for a moving comb or wedge, precisely engineered, and designed in such a way so as not to alter the shape of the signal waveform from the detector corresponding to that particular channel which it attenuates. Such an electro mechanical assembly can be dispensed with if a sytem is used where the ratio is taken with a commercial potentiometric recording instrument by applying the larger signal to the slide wire Fig. 5.2a. This reduces the general application of the instrument and reduces its portability, however, and a similar result can be achieved by using an automatic gain control system Fig. 5.2b, where the larger signal is compared with a stable reference voltage or current and the amplified difference used to control the gain of the main amplifier. The system has the additional advantage that the signal level following the gain controlled stages varies between narrow limits and the handling range of the output circuits is thereby reduced. This system forms the basis for the ratio circuit used in the instrument and is now described in detail. Its various advantages and disadvantages are summarised below.

(i) Both signals are processed through the same detector and amplifying equipment thus relaxing the requirement for stable gain in the main amplifier and removing the dependence on detector sensitivity (Chapter 3), which would be apparent if two detectors were used.

(ii) Providing the loop gain is high, the system will function reliably if the active components in the circuit remain within their operating range. Thus the system will fail if complete failure of a transistor or other circuit component occurs but it will operate satisfactorily even though the majority of the components drift or deteriorate within wide limits as a result of the effects discussed in preceding sections.

(iii) The system, although inferior to a null system, in that a stable reference voltage is required, is likely to be less costly, since the need for a precisely engineered optical attenuator and drive is removed.

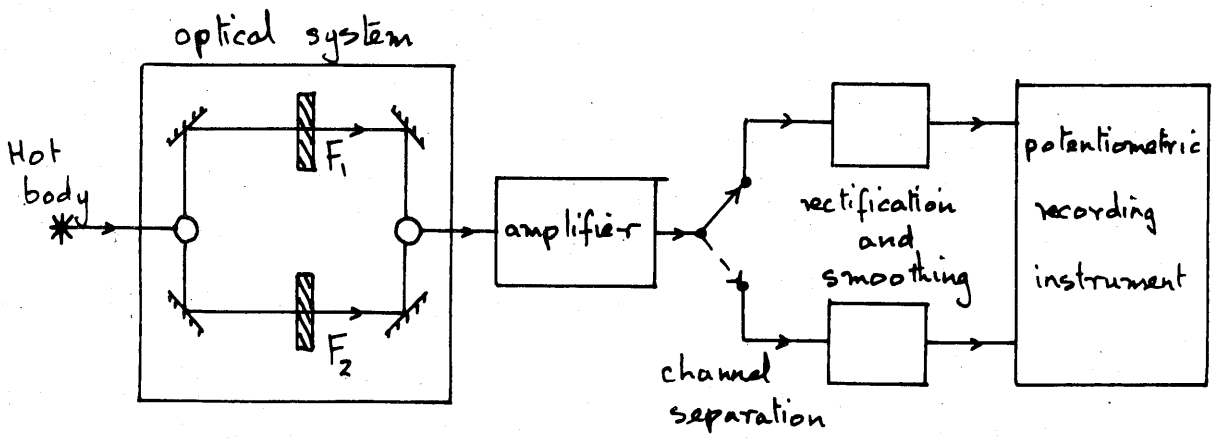

Fig 5.2a Ratio system employing potentiometric recorder.

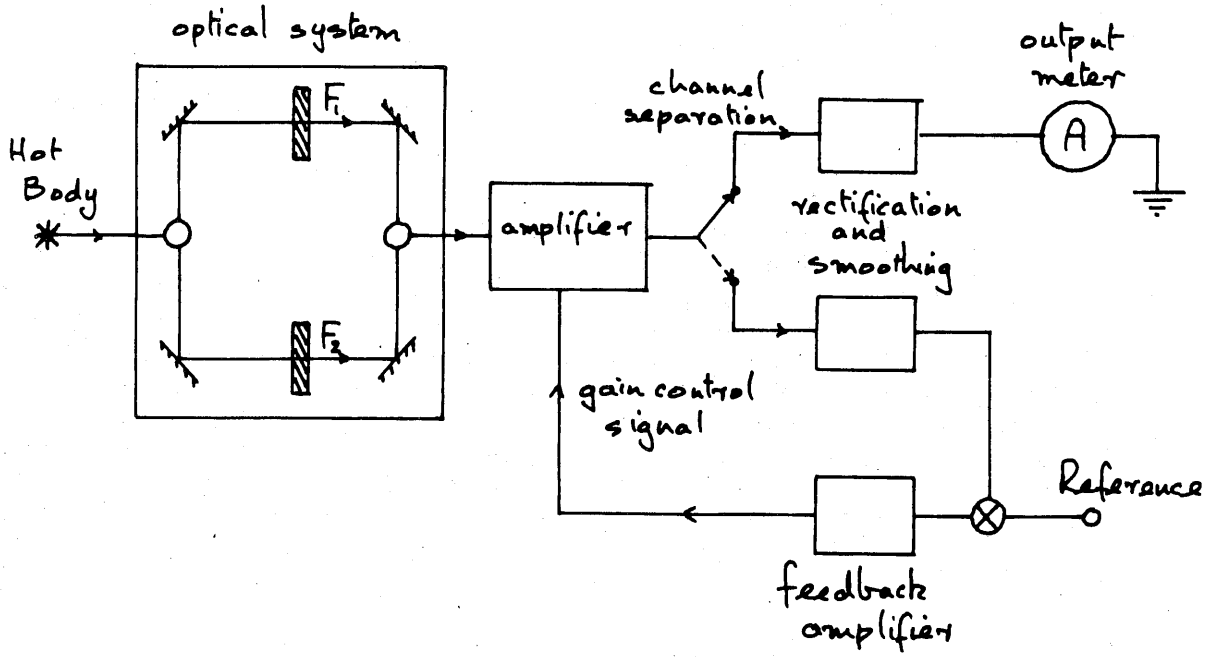

Fig 5.2b Ratio system employing automatic gain control.

(iv) The system, although inferior to a system utilising a ratio recorder because additional components are required for the feedback amplifier, does maintain the overall portability and general application possibilities of the pyrometer.

(v) The system suffers the disadvantage that the signals are separated for averaging at the output. Providing the properties of these circuits are defined in terms of high quality passive networks, this becomes a minor consideration.

5.5 Specification for the electronic system

5.5.1 The system specification which was presented in Chapter 1 called for a sensitivity which, combined with operating wavelength and other requirements discussed in Chaper 3, indicated that a lead sulphide cell would be the most suitable detector. The peculiar nature of the target material suggested that a ratio pyrometer was required and this determined the type of optical system to be employed. Thus the specification for the electronic system is governed in general by the system specification but depends in detail upon the detector and optical system in many respects. As a result we have an electronic system governed by:-

(i) the type and mode of operation of the infra red detector

(ii) the type of optical system employed

(iii) factors arising out of the system specification outlined in Chaper 1 not already introduced in (i) and (ii) above.

5.5.2 Input signal characteristics

(i) Handling range

The temperature range over which the instrument is designed to operate introduces the need for a large signal handling capacity in the electronic system. This is due to the energy radiated being a function of approximately the tenth power of the temperature over the spectral range of interest, (Chapter 2). The handling range may be estimated from Table II discussed in the feasibility study, (Section 2.7) The range of energy incident on the detector varies from a minimum of $2.5\ 10^{-3}\mu W$ in the 1.75 micron channel at $500^{o}K$, to a maximum of $3.52\mu W$ in the 2.3 micron channel at $800^{o}K$, for a target emissivity of 0.1. Further applications of the instrument, which are discussed in Chapter 8, introduce a range of target emissivities from 0.1 to unity over a temperature range of $500^{o}K$ to $1200^{o}K$.

(ii) Sensitivity

The above temperature range corresponds to a handling range of 20,000 in signal voltage levels from a minimum signal of 50 μV, assuming a typical cell responsivity of 20 $mV/\mu W$.

(iii) Input impedance

The input impedance of the system should be chosen for optimum noise performance since the sensitivity of the instrument is noise limited. The optimum input impedance will depend upon the particular transistors employed in the early stages of the amplifier and upon the detector matching circuit. (Chapter 3)

(iv) Signal frequency and band width

The signal frequency range has been discussed under optimisation of signal to noise ratio in Chapter 3. The chopping frequency of 1000 cps and the selection frequency of 30 cps, with sufficiently wide frequency response to prevent interference between channels, calls for a passband of few 100 to 2000 cps in the signal amplifier.

5.5.3 Output characteristics

(i) Presentation

In the portable instrument display on a meter, calibrated to read temperature, is required. In the light of the discussion in 5.2.2 this meter should be current driven. It will be convenient if zero supression facility is included in the output circuit to provide readability of the scale to $\pm$ 1°C at any temperature within the operating range.

In some applications the output presentation may be combined with a commercial potentiometric recorder as suggested in 5.4. This will provide a readily available means of obtaining an extremely accurate ratio measurement.

(ii) Output impedance

The output impedance should be high to conform with the current drive requirements. Thus if an ammeter is used for the display of temperature the associated range change and zero supression circuits can be expected to have little effect on the output current for a given signal ratio.

(iii) Time constant

In order to achieve the required discrimination of $\pm$ 1°C at 227°C an output time constant of about 1 second is required. This implies a system bandwidth of 1000 $\pm$ 1 cycle since the 30 cps selection frequency does not appear at the output. At higher temperatures in the operating range when considerably more energy is available, the time constant could be reduced. It must be noted, however, that the selection frequency of 30 cps provides a limit to the reduction in this particular system since the presence of 30 cps modulation in the output is highly undesirable.

5.5.4 Performance

(i) Accuracy

Many factors must be considered when the overall accuracy of the instrument is assessed on various target materials (see Chapter 2). Since in the present application measurement of temperature difference is required, the absolute accuracy of the instrument is not critical. The accuracy is best defined in relation to its performance on a black body radiator where the emitting characteristics are known. Reference to Fig. 2.13 which relates the signal ratio with temperature in ^{o}K shows that an instrument accuracy of $\pm$ 1% corresponds to $\pm$ 2^{o}C at 500^{o}K and $\pm$ 3$\frac{1}{2}^{o}C$ at 800^{o}K. A $\pm$ 1% accuracy should be attainable without the need for an elaborate circuit.

(ii) Repeatability

The instrument repeatability on a target of known emitting characteristics should be as good as the absolute accuracy of the calibration. This is important because the instrument is required to measure temperature differences rather than absolute values. Thus when the target emitting characteristics become uncertain and a departure from the original calibration occurs, the ability of the instrument to detect small changes in temperature is maintained. This applies also in the wider application of the instrument (see 8.1) since in many industrial applications day-to-day repeatability is more important than absolute accuracy. A repeatability of $\pm$ 1% of indiction is therefore desirable.

(iii) Stability

The conditions of use of the instrument described in Chapter 1, show that with a response time of 0.4 second, a target width of 1 mm and a can 75 cm long, a longitudinal scan will take approximately 5 minutes. The stability of the instrument over this period of time should be sufficiently high to render the instrument truly sensitive to target temperature changes of $\pm$ 1^{o}C. This requires a short term stability of $\pm$ 1^{o}C or $\pm$ $\frac{1}{2}$% full scale reading. (800^{o}K)

5.5.5 Supply requirements

(i) Detector supply

The detector functions at maximum sensitivity with a supply voltage far in excess of that required by the rest of the circuit. It will be convenient to combine the detector supply and the supply to the field effect transistor (see Appendix C) and since the consumption is low a battery will be most convenient. The recommended detector supply is 90-120 V.

(ii) Line voltage

The use of NPN and PNP transistors is anticipated both out of necessity in some cases and convenience in others. For the sake of symmetry a supply of $\pm$ 9 V centred around real earth has been used. If portability of the instrument is to be maintained battery operation will be required. This can be achieved by using rechargeable cells providing AC mains or battery operation.

(iii) Line voltage variations

A line voltage variation of about $\pm$ 10% is to be expected for rechargeable cells from the charged to the discharged conditions. This means that some stabilisation of the supply will be necessary if the required performance is to be achieved.

(iv) Power consumption

The power consumption will be limited by the capacity of the rechargeable cell. A reasonable maximum charging rate of a few hundred milliamps is typical and the circuit should be designed within this limit.

5.5.6 Operating temperature range

In some applications the pyrometer will be exposed to considerable radiation of heat. The operating temperature of the optical system is limited to 50°C by the mirror galvanometer (Appendix F) and the detector. In such applications if the electronics is used remotely from the optical system normal ambient temperature changes need only be encountered. The circuit should be capable of operating, therefore, remotely from the optical system over the temperature range 10°C-30°C.

General

In this application it is considered that vibration and corrosion will not be significant so that potting of the electronics is not justified. Also the instrument is being used for measuring purposes only and thus fail safe operation is not required at this stage.

5.5.7 Summary of design specification

Input signal characteristics

(i) handling range: 20,000:1

(ii) sensitivity: 50 μV peak to peak for full output

(iii) input impedance: chosen for optimum noise performance

(iv) band width 100-2000 cps reducing to 1000 $\pm$ 1 cycle at the output

Output characteristics

(i) presentation - ammeter calibrated to read a temperature in ^{o}C or a poteniometric recorder

(ii) output impedance - high enough to provide an approximation to current drive

(iii) reponse time - not more than 1 second

Performance

(i) accuracy $\pm$ 1% of indication on specified target material

(ii) repeatability $\pm$ 1% of indication

(iii) stability $\pm \frac{1}{3}$% full scale deflection for periods of 5 to 10 minutes depending on response time used

Size and weight

To be portable

Supply requirements

(i) detector and head amplifier supply; 90 V from battery

(ii) line voltage; $\pm$ 9 V supply from rechargeable cells

(iii) line voltage variation $\pm$ 10%

(iv) power consumption - few hundred milliamperes

Operating temperature range

Normal ambient conditions 10^{o}-$30^{o}C$

5.6 The block diagram

The block layout of the system is shown in Fig. 5.3. It is conveniently divided into three sections consisting of the signal, the feedback and the switching circuits.

The signal from the infra red detector, consisting of a 900 cps waveform in practice modulated by a 30 cps square wave, is amplified by A_1 and A_2 and separated into the two components corresponding to the energy in each waveband. The channel separation circuit obtains both 900 cps and 30 cps square waveforms, which are derived from the master oscillator.

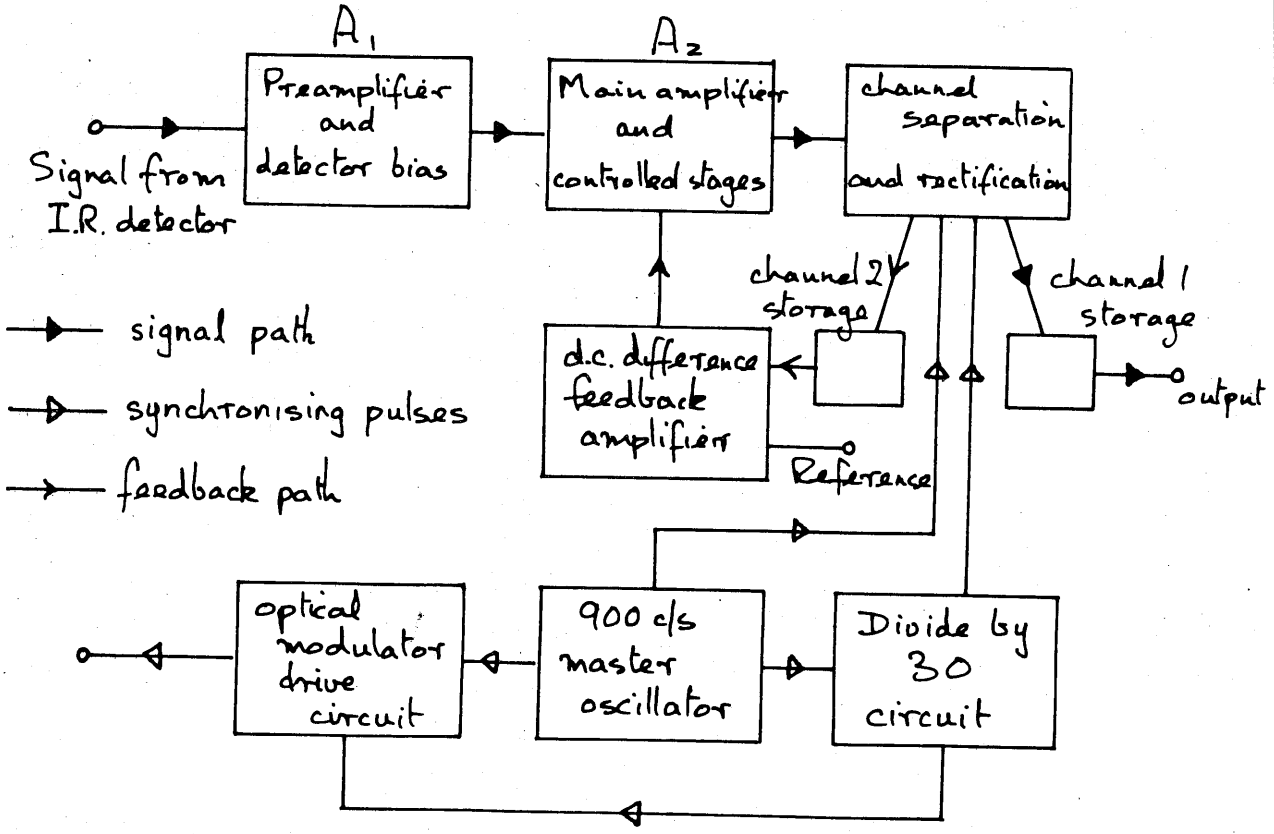

Fig 5.3 Electronics system block diagram.

The two signal components are stored after separation and the larger one (channel 2) is compared with a d.c. reference level and the difference amplified in a d.c. amplifier. The output of this amplifier is used to control the gain of the controlled stages in the main amplifier and this facility causes the level of the smaller signal component to be proportional to the ratio between them. The master oscillator also provides 900 cps and 30 cps square wave waveforms for the optical modulator drive circuit, which contains some phase adjustment so that synchronisation of the 900 cps and 30 cps pulses with the corresponding waveforms in the signal is possible.

5.7 The feedback loop

The signal and feedback circuits are now considered together, for the purpose of determining the parameters which decide the performance of the signal system. The control loop is an extension of the simple feedback loop illustrated in Fig. 5.4.

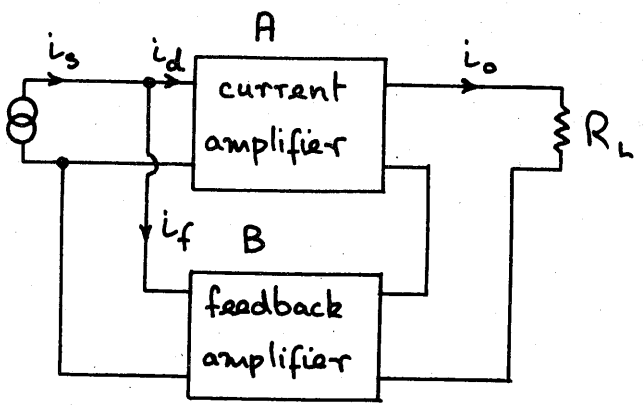

Fig. 5.4 Basic feedback loop.

In this type of circuit a signal which is proportional to the output current is fed back to the amplifier input with such phase that the input current is effectively shunted by the feedback amplifier. The shunt current i_f is therefore proportional to the output current i_o

$$i_o = A i_d \qquad \text{and} \quad i_s = i_d + i_f$$
$$= i_d + B i_o$$
$$= i_d + AB i_d$$

$$\frac{i_o}{i_s} = \frac{A i_d}{i_d + AB i_d} \qquad (5\text{-}1)$$

$$= \frac{1}{\frac{1}{A} + B}$$

where i_o = the output current in the load R_L

A = the gain of the current amplifier

i_d = the current seen by the current amplifier

B = the gain of the feedback amplifier

i_s = the input current

i_f = the shunt current

In such a system if $A \gg B$ then the gain approaches $\frac{1}{B}$. Thus if the gain of the feedback amplifier is defined in terms of reliable components such as resistors then the system gain is known to a close approximation. This principle is now extended so that the gain of the controlled stage K is proportional to the difference between the rectified component of i_o and a well defined standing current i_R, Fig. 5.5. The gain of the current amplifier is thus controlled in such a way that the output current i_o due to the signal component i_s is maintained equal to the reference current i_R In this case we have

$$i_o = A\, i_s \qquad (5\text{-}2)$$

$$i_o' = A\, i_s' \qquad (5\text{-}3)$$

$$A = KB(i_R - i_o)$$

$$\therefore i_o' = KB(i_R - i_o)\, i_s' \qquad (5\text{-}4)$$

$$i_o' = KB\left(i_R - \frac{i_o'}{R}\right) i_s R$$

$$i_o' = \frac{KB\, i_R\, i_s\, R}{1 + KB\, i_s} \qquad (5\text{-}5)$$

where i_s' = channel 1 signal current
i_s = channel 2 signal current
A' = gain of controlled amplifier
i_o' = channel 1 output current
i_o = channel 2 output current
i_R = reference current

If the term KBi_s is made large compared with unity then (5-5) reduces to $i_o' = R i_R$, in which case if i_R is constant a meter recording the output current i_o' can be calibrated to read the signal ratio or since this is proportional to temperature (see Chapter 2), the temperature directly. In order to maintain $\pm$ 1% accuracy in the ratio measurement for any input signal level we require

$$KB\, i_s \geq 100 \qquad (5\text{-}6)$$

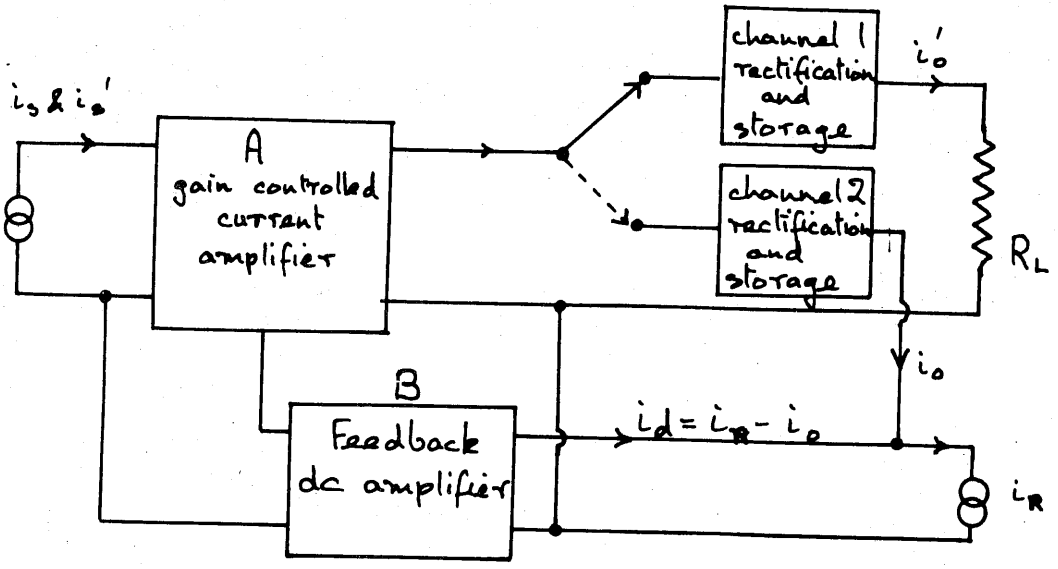

Fig 5.5 Gain controlled feedback loop.

The parameters in (5-6) require determination in a logical sequence. In order to reduce the number of components in the system to a minimum the loop gain of the system should be as small as possible. This calls for i_s to be as large as possible.

The parameter i_s, the larger signal current component, is derived from the detector via the pre-amplifier. Since i_s should be as large as possible, the limitation to its magnitude must first be examined. This current decides the operating level of the controlled stage of the amplifier and since the range of the control is very dependent upon the signal level it is required to handle, some preliminary investigation is necessary. This investigation is described in Appendix H and the results show that a control range of 100 to 1 in a single control stage appears feasible if i_s varies over the range 0.3 to 30μA rms. If we take the most pessimistic value of .3μA as representative then we have from (5-6)

$$KB \geq \frac{100}{0.3\times10^{-6}} = 3.3.10^{8} \text{ amps}^{-1}.$$

The treatment described in Appendix H also shows that if K is considered to be constant over the control range, a value for K based on measurement of 2630 volts^{-1} is obtained

$$\therefore \quad B \geq 1.25 \text{ volts} . \text{amps}^{-1}$$

The value of A depends on the maximum output current i_o' that is required. Since the current i_o is compared with the reference current, the larger it can be made, the greater is the signal available for recording purposes or controlling of external equipment. Furthermore, the gain of the feedback amplifier can be reduced if A is made large. There are many considerations which limit the available output current and these are presented now and are discussed in detail in the section describing the output circuit,

(i) limit to current set by resistances of 900 cps and 30 cps channel switches.

(ii) limit to current set by the output transformer winding resistances.

(iii) limit to current set by the maximum allowable voltage swing in the output stage.

(iv) limit to output swing set by the d.c. current in the low frequency output filter circuit, which is reflected back through the output transformer (see Section 5.12).

These combined considerations lead to a direct output current of about 1 mA being suitable. Thus when i_s is at the lower limit of the operating range (0.3μA) we have from (5-4)

$$i_R - i_o = \frac{10^{-3}}{3.10^{-7}} \cdot \frac{1}{3.3.10^{8}} = 10^{-5} \text{ amps}.$$

This leads to the simple conclusion that for 1% accuracy the error signal is 1% of the output signal.

5.8 The signal amplifier controlled stages

The required handling range of 20,000:1 can be achieved in two ways: more controlled stages can be introduced or a range change switch incorporated.

If more controlled stages are introduced then all stages prior to them must be capable of handling 20,000:1 signal range. The estimated detector output at the 227°C is 50 μV peak to peak and at the other end of the range this will increase to 1.0 V peak to peak. Before considering the best way to achieve this handling range it will be necessary to consider the other necessary functions of the signal circuit. Therefore, the circuit from the input up to and including the controlled stages and output stage is now considered in detail. The particular factors outlined in the specification which apply to this section have been re-arranged in the following order

(i) supply voltage −8 V

(ii) source and input impedance - chosen for optimum noise performance

(iii) bandwidth 100-2000 cps

(iv) sensitivity 50 μV for full output of 1 mA

(v) handling range 20,000:1

(i) Supply voltage

Because of the low signal present at the input of the signal circuit screening against external interference is a major consideration. Investigations with the cell used in conjunction with the impedance matching stage (see 6.8) showed that satisfactory performance was attainable if one side of the signal circuit was earthed. For this reason the signal circuit employs only the negative half of the available supply. The value of -8 V is used to allow for decoupling to isolate this section from the rest of the system as far as a.c. is concerned.

(ii) Input impedance and source impedance

The source and input impedances of the signal amplifier require careful consideration since they are closely associated with the noise performance. The optimum source impedance has already been discussed in Chapter 3 and is 2.5 KΩ for germanium transistors and 10 KΩ for silicon transistors. The impedance is provided by the field effect transistor which matches the detector impedance to the amplifier impedance. To achieve optimum performance power amplification is employed and the input impedance of the amplifier is approximately equal to the reflected source impedance. A value of 10 KΩ has been used with a silicon transistor in the first stage.

(iii) Amplifier bandwidth

In order to achieve acceptable performance of the instrument it is necessary to limit the system bandwidth. The factors affecting the choice of bandwidth have been dealt with in Chapter 3 and Appendix D. The recommended bandwith for the amplifier is 2000 cycles extending from about 100 cps to 2000 cps.

(iv) Input sensitivity and (v) handling range

The input signal for full output is 50 μV peak to peak or 18 μV rms. This is the minimum signal at the input which will operate the ratio circuit and therefore for this input signal the controlled stages will be turned fully on. This signal must be amplified to provide a current of 0.3 μA rms into the first controlled stage and a current at the output for control purposes of 1 m A d.c.

Thus the preamplifier gain is 17 μA/mV

The total gain is thus 55 m A/m V (this is separated into the gain of the controlled stage and amplifier 3,300 (see 5.7) and the preamplifier gain of 17.10^{-3} m A/m V).

The signal circuit has been designed according to the principles suggested by Cherry(5). The use of negative feedback is strongly recommended in order to achieve predictability in the design. The gain of each stage is defined usually by a single component and interaction between stages is reduced to a minimum. Table IX lists the maximum gains available for various types of connection with $\pm$ 10% uncertainty.

TABLE IX

Amplifer type	Theoretical limit	Gain for typical β		
		β= 30	β= 60	β= 100
Two series feedback stages	$(0.1\beta)^2$	9	36	100
Two shunt feedback stages	$(0.1\beta-1)^2$	4	25	81
Two alternate stages	$\beta(0.1\beta-1)$	60	300	900
Feedback pair	$0.1(\beta)^2$	90	360	1000

The terms 'series' and 'shunt' feedback refer to the type of feedback used. Four distinct types are possible(6) and these are given in Fig. 5.6. The two referred to in the table are series current feedback and shunt voltage feedback. In series current feedback a current proportional to the output current is fed back in series with the input. This has the effect of increasing both the input and output impedance. Conversely in the shunt feedback stage a voltage proportional to the output voltage is fed back in parallel with the input signal. This has the effect of reducing both input and output impedances.

Fig 5.6 Various feedback connections

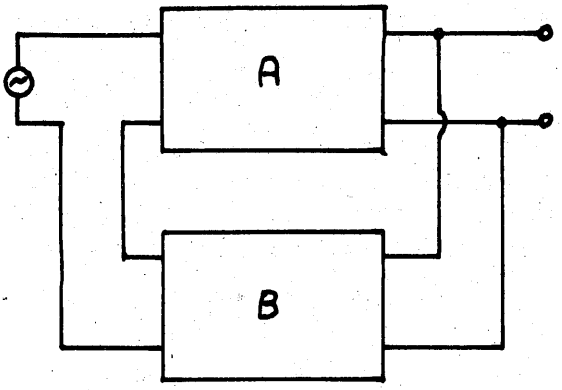

(a) Series voltage feedback

$$V_o = \frac{V_s}{B + \frac{1}{A}}$$

A is voltage amplifier
B is voltage amplifier

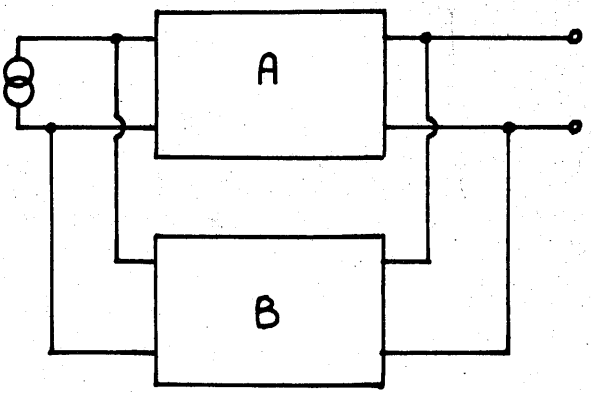

(b) Shunt voltage feedback

$$V_o = \frac{i_s}{B + \frac{1}{A}}$$

A is transresistance
B is transconductance

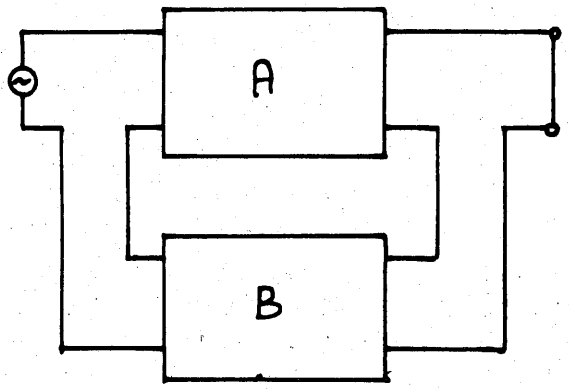

(c) Series current feedback

$$i_o = \frac{V_s}{B + \frac{1}{A}}$$

A is transconductance
B is transresistance

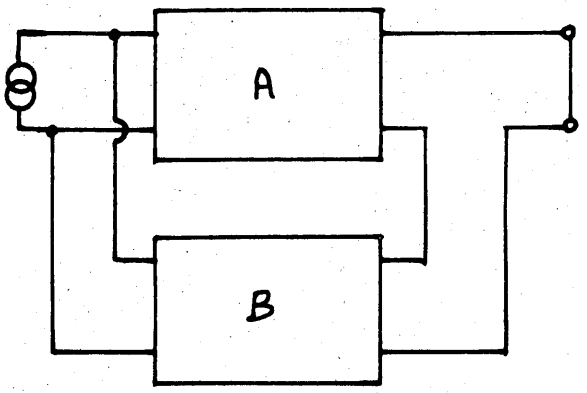

(d) Shunt current feedback

$$i_o = \frac{i_s}{B + \frac{1}{A}}$$

A is current amplifier
B is current amplifier

It can be seen from Table IX that the maximum gain with 10% uncertainty is available for the feedback pair, which consists of two directly coupled stages of alternate types.

5.9 The signal amplifier

5.9.1 The first stage of the signal amplifier Fig. 5.7 consists of a series current feedback stage (see Fig. 5.6c) driven from an ideal source impedence of few KΩ for low noise performance. According to Cherry(5) the maximum gain for ± 5% uncertainty is

$$A_v \leq 0.1\beta$$

if we assume $\beta = 60$ then $A_v = 6$ β = common emitter current gain

$$\text{but } A_v = G_t \times R_L \qquad G_t = \text{transconductance (amps/volt)}$$

$$\therefore G_t = \frac{6}{220} \qquad R_L = \text{load resistance (220Ω shunting 1st control stage)}$$

$$= 27\mu A/mV$$

for 5% predictability

This gain is defined by the uncoupled feedback resistor (R_e) in the emitter. The input and output impedances are high due to the nature of the feedback. Thus the stage is voltage driven by the field effect transistor T_1 and it current drives the following stage T_3.

we require $G_t \sim \frac{1}{R_e} = .0167$

$$\therefore R_e = 60\,\Omega$$

input impedance $\sim \beta(R_e + r_e) = 5.5\,K\Omega$

output impedance $\sim r_o\left(1 + \frac{R_e}{r_e}\right)$

$\sim 10^4\left(1 + \frac{60}{50}\right)$

$\sim 22\,K\Omega$

r_o = transistor internal output impedance (10 KΩ)

r_e = transistor internal emitter resistance

$= \frac{25}{I_c}$ for I_c in mA.

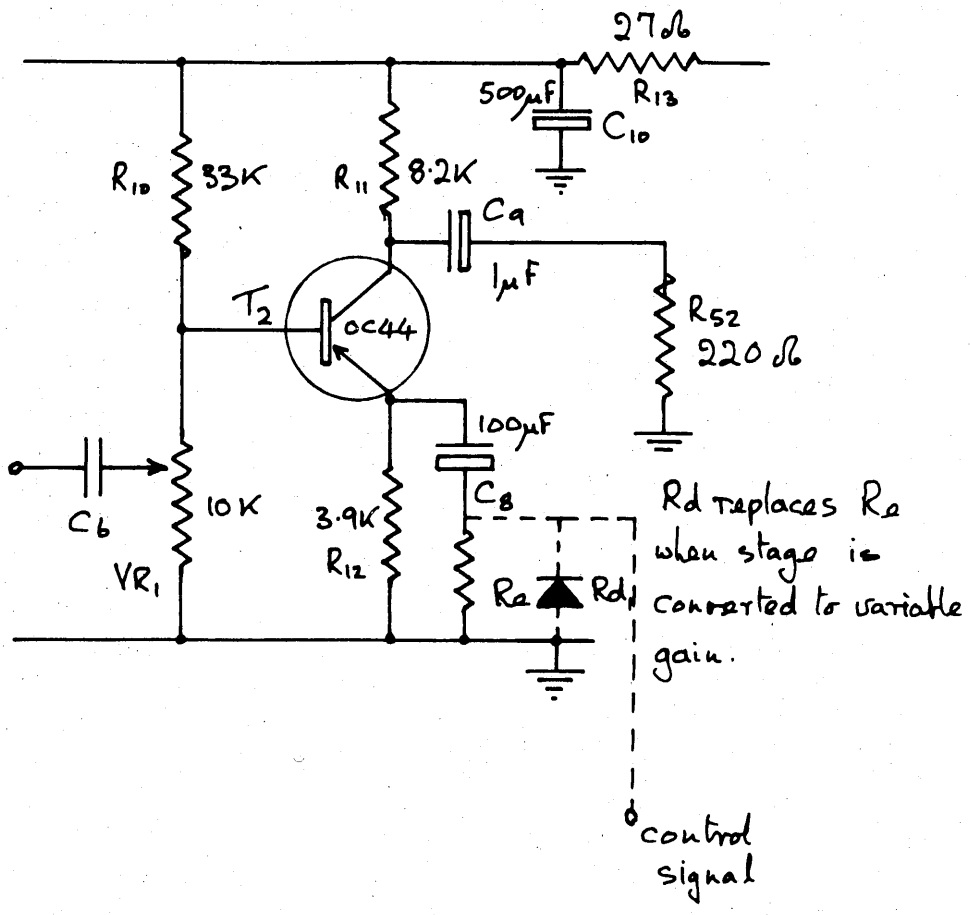

Fig 5.7 Signal amplifier – stage 1.

The coupling capacitors are chosen for adequate band pass beyond the frequency range 500 to 2000 cps to comply with the conditions discussed in Appendix D

Z_{C_6} at 500 cps $\ll 5.5K // V_{R_1}$ $\quad Z_{C_6} = 75\,\Omega$ if $C_6 = 4\mu F$

Z_{C_9} at 500 cps $\ll 8.2K$ $\quad Z_{C_9} = 300\,\Omega$ if $C_9 = 1\mu F$

The handling range of the stage is limited by the quiescent current of 0.5 m A. This will allow a maximum rms signal of .707 x 0.5 m A = .35 m A. The minimum signal is 0.3μA rms allowing a handling range of 1200 in signal level. The handling range could be improved by increasing the quiescent current but this produces a larger drain on the supply and is not justified until the ratio circuit is able to cope with a larger control range. This first stage forms the basis of the first control stage. The conversion is made when R_e is replaced by a diode.

Control is achieved by varying the amount of series feedback in the stage by controlling the resistance of the diode which together with C_8 bypasses the emitter resistor. The maximum gain is determined by the diode resistance R_{d_1} and the internal base-emitter resistance r_e when the diode is in a conducting state. The minimum gain occurs when the diode is in a conducting state being determined by Re (3.9KΩ). The control characteristics are discussed in Appendix H where it is shown that the voltage control range is 25:1 or 28dB. The coupling capacitor C_6 is designed to have an impedance at 500 cps much less than the input impedance at maximum gain and like C_9 it is unchanged by the conversion to a control stage.

The second control stage Fig. 5.8 is also discussed in Appendix H. It is a shunt voltage feedback stage (see Fig. 5.6b) with characteristically low input and output impedances. This enables it to be current driven from the previous stage and allows it to voltage drive the following stage with negligible interaction with either. Its gain is determined by R_{14} but when controlling begins the input impedance of the stage increases and the excess signal is bypassed by the 220Ω resistor R_{52} into the output stage of the d.c. feedback amplifier which has a very low output impedance. The stage will handle a signal input current from .3 to 30μA rms or 100:1 while maintaining a constant output, without distortion. The coupling capacitor C_{11} is designed to have an impedance less than the input impedance of the following stage at 500 cps.

The voltage handling range of these two stages is about 3000:1 or 70 dB in practice (see Appendix H). The signal input range for optimum control is 50μV to 200 m V and the output remains constant at about 3 m V peak to peak.

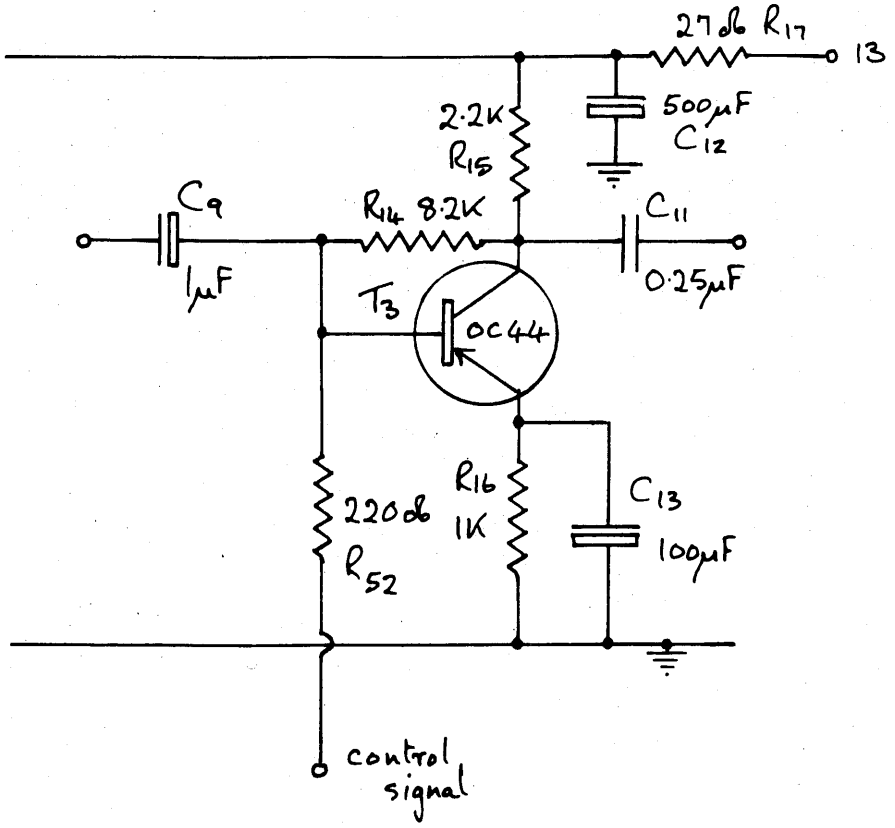

Fig 5.8 Signal amplifier - stage 2

5.9.2 The output stage

The remaining three stages (Fig. 5.9) are designed to provide sufficient amplification for a rectified and smoothed output current of 1 m A d.c. Allowing for losses in the output transformer TT_1 (see section 5.9.3) an output current of 1 m A calls for a peak to peak swing of 4 m A in the primary winding. The combined gain of the stages is therefore 1.33 m A/m V.

The first of these three stages again employs series current feedback (Fig. 5.6c). It is voltage driven by the second controlled stage and its gain is determined by the unbypassed emitter resistor R_{21}. A quiescent emitter voltage of -1.5 V is chosen to provide adequate thermal stability. The values of R_{22} and R_{20} are chosen to set the quiescent collector voltage at about -5 V and the biassing resistors R_{18} and R_{19} are sufficiently small to predict the operating point and yet not small enough to draw significant signal current from the previous stage.

The last two stages are combined to form a shunt current feedback pair (Fig. 5.6d). The operating level is determined by the bias resistors R_{23} and R_{25} and direct coupling is used within the pair. The first half consists of a high gain transistor which provides a predictable quiescent collector voltage, allowing a large voltage swing at the collector of the second transistor. The feedback is taken from the emitter of T_6 being proportional to the output current and fed back via R_{25} to shunt the input signal to T_5. The overall gain of the feedback pair is determined by the two resistors R_{25} and R_{28}. i.e. current gain is $\frac{6800}{22} \sim 300$

5.9.3 The output transformer

The output stage current drives the load due to its high output impedance. The transformer used is an interstage driver transformer of the type used in a typical battery driven transistor radio receiver. The parameters are listed below:

Output impedance(5) $= r_o\left(1 + \frac{R_e}{r_e}\right)$

$r_e = \frac{25}{I_c \text{ (in mA)}}$

$R_e = 22\,\Omega$

$r_o \sim 5$ to $10\,k\Omega$.

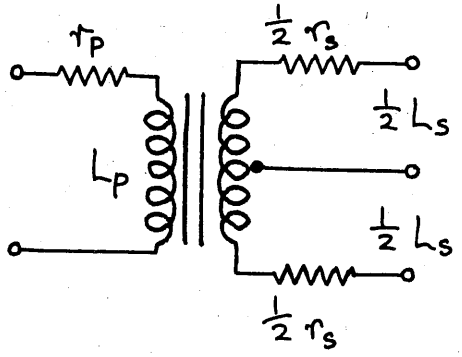

Turns ratio 2:1 + 1

$L_p = 2.2$ Henries $\quad r_p = 300\,\Omega$

$L_s = 2.4$ Henries $\quad r_s = 260\,\Omega$

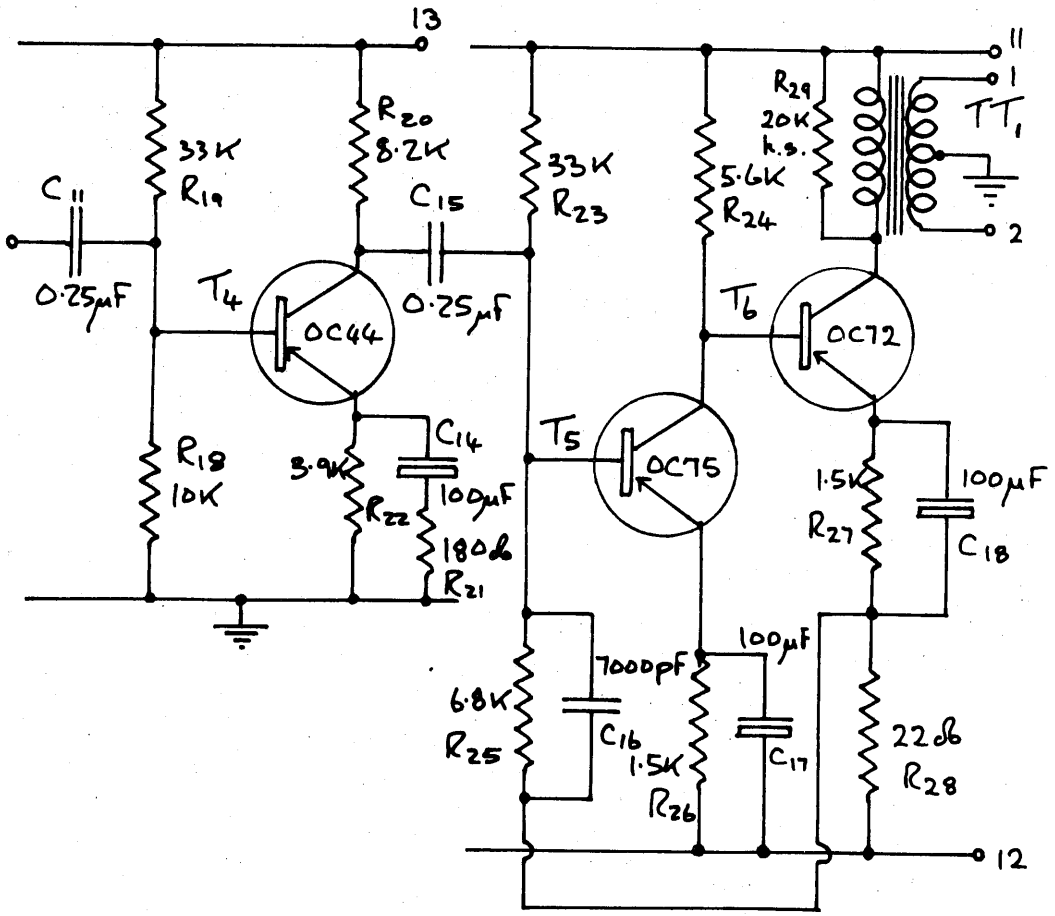

Fig 5.9 Signal amplifier – output stage.

In order to provide a current swing of 4 m A pp a quiescent level of at least 2 m A is required. This current is determined by R_{27} and is about 2.5 m A in practice. The available voltage swing at the primary is thus

2 x (Supply voltage - Vemitter - transistor bottoming voltage $- i_q r_p$)
= 17 V

assuming positive supply is + 8 V
negative supply is - 8 V
Vemitter is - 1.7 V
Transistor bottoms when V_{ce} is 0.5 V

Before discussing the rectifying and smoothing circuit in more detail the performance of the signal amplifier is summarised. The signal handling capacity is 70 dB. The gain when the controlled stages are at maximum gain, neglecting the shunting effect of R_{24}, is given by:-

$$\frac{i_o}{V_i} = \frac{R_{25}}{R_{28}} \times \frac{1}{R_{21}} \times R_{14} \times \frac{1}{R_{d_1} + r_e} = 140 \text{ mA/mV}$$

for $R_d + r_e = 100\,\Omega$

in practice $R_{24} \sim r_{in}$ for T_2 when at maximum gain

$$\therefore \frac{i_o}{V_i} = 70 \text{ mA/mV}$$

i.e. output current swing is 4.2 m A for an input swing of 50 μV

and when the stages are at minimum gain:-

$$\frac{i_o}{V_i} = \frac{R_{25}}{R_{28}} \times \frac{1}{R_{21}} \times \frac{R_{14}}{100} \times \frac{1}{R_{22}} = .035 \text{ mA/mV}$$

and again due to shunting effect of R_{24}, in practice the minimum gain is .018 m A/m V

5.10 The demodulation circuit

5.10.1 The phase sensitive rectifier

The specified performance of the system relies on a band width at the output meter of approximately 1 cps. This means that the 900 cps signal must be rectified and smoothed with the ultimate rejection of frequencies outside the band width 900 $\pm \frac{1}{2}$ cps. This condition is conveniently achieved with a phase sensitive rectifier operating at 900 cps. The output current signal from the signal amplifier is split in phase by the output transformer and the phase sensitive rectifier is synchronised to pass alternate half cycles from each half of the secondary, Fig. 5.10. The two sets of half wave rectified signals are combined to provide full wave rectification of the output signal. Before smoothing occurs the portions of the output wave train corresponding to the signals in the two channels are separated by a switch synchronised to the 30 cps channel selection frequency. Finally the signal corresponding to each waveband is smoothed by a low band pass filter designed to pass d.c. and only low frequencies sufficient to provide an output time constant of one second.

The rejection of frequencies outside the bandwidth 900 $\pm \frac{1}{2}$ cps is achieved by the action of the smoothing circuits. Consider the effect this system has on a signal at a lower frequency than 900 cps. Because the rectifier is not now synchronised the time average of the signal will be zero. The same argument applies to signals at higher frequencies, providing that these are not odd harmonics of the operation frequency of the rectifier. Waveforms for frequencies both higher and lower than the rectifier operating frequency are shown in Fig. 5.11. The effect on the 3rd and 5th harmonics is also illustrated, Fig. 5.12. It can be seen that the amplitude of the harmonics referred to the fundamental is

1st	3rd	5th	7th etc.
1	$\frac{1}{3}$	$\frac{1}{5}$	$\frac{1}{7}$

The bandwidth of the signal amplifier has already been fixed at 500 to 2000 cps so the effect of noise at the frequency of the third harmonic (2700 cps) is less than $\frac{1}{3}$ of the noise in a bandwith 900 $\pm \frac{1}{2}$ cps, or lower by more than 10 dB. The noise at higher harmonics is negligible because it is rejected in the signal amplifier.

The phase sensitive rectifier circuit is shown in Fig. 5.12. Each half of the phase sensitive rectifier consists of a transistor switch actuated by a square pulse from a secondary winding of the reference signal transformer TT_2. The switches are isolated from earth so that nothing is added to the signal by the reference pulse. In order to achieve a low forward resistance and a high reverse resistance the transistors are

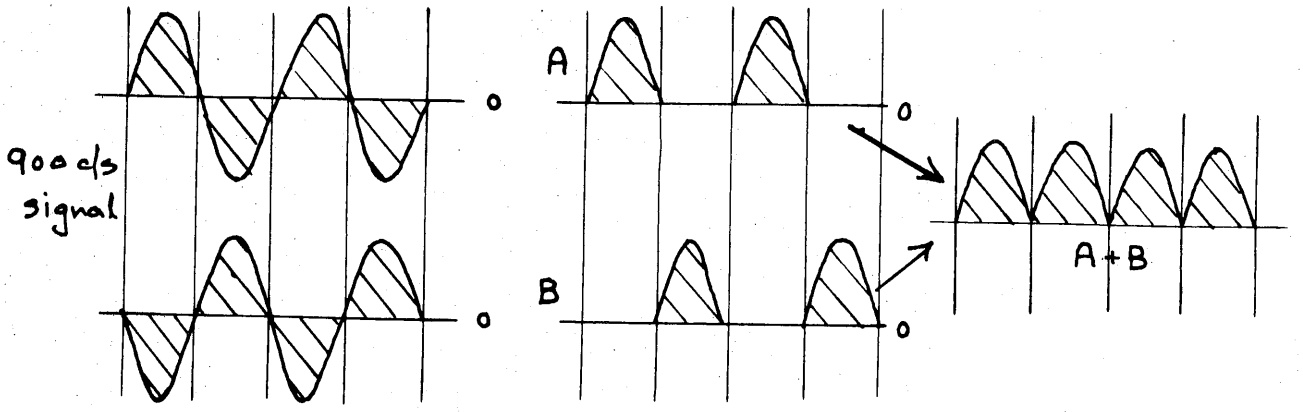

Fig 5.10a Phase sensitive rectification of signal.

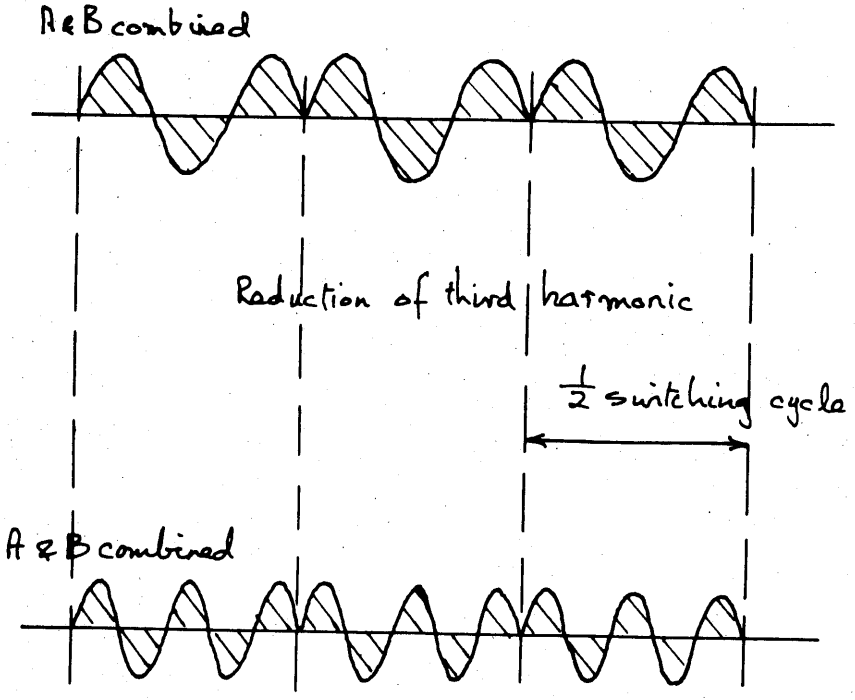

Reduction of fifth harmonic

Fig 5.10b Reduction of harmonics.

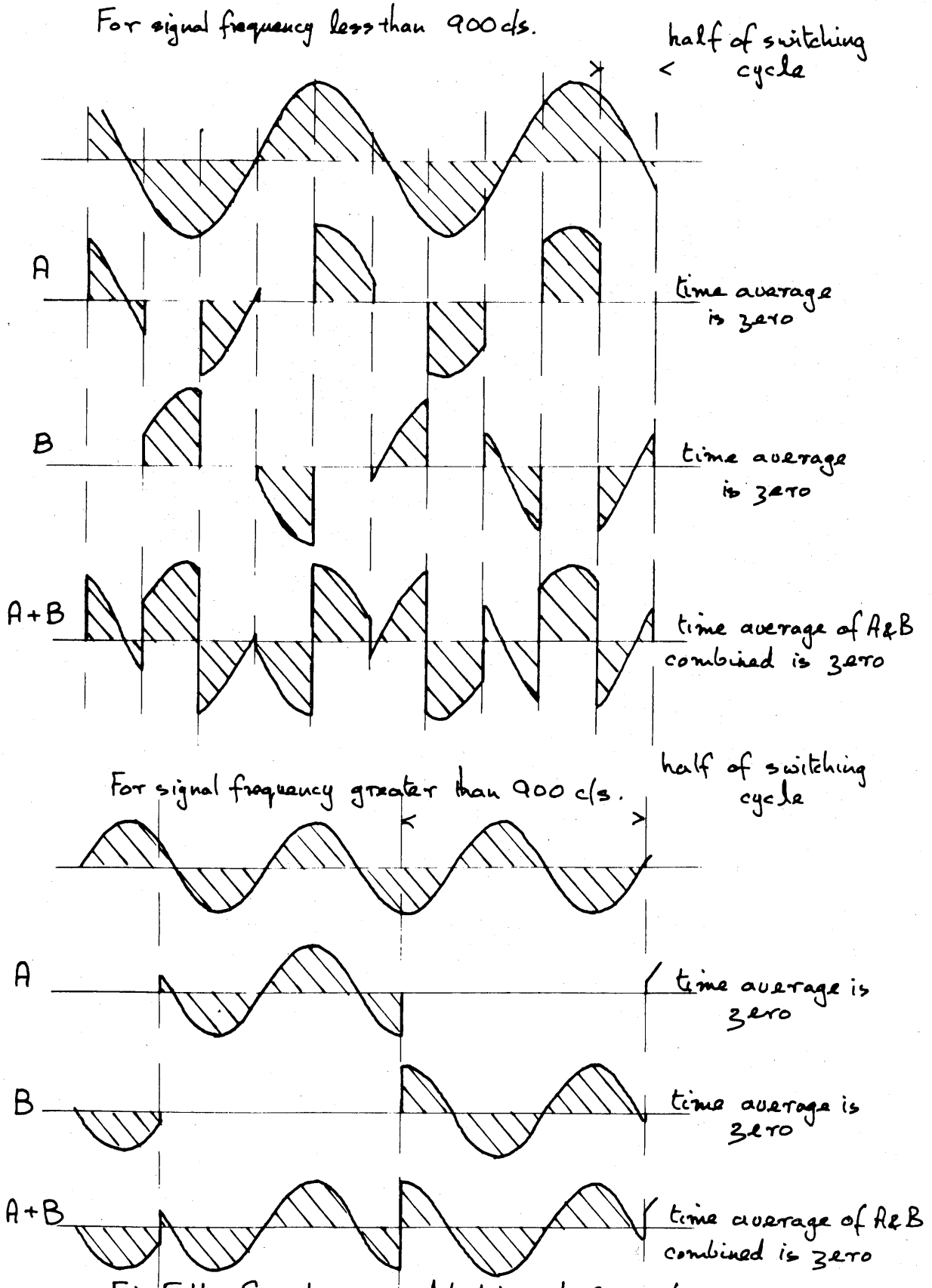

Fig 5.11 Synchronous detection at 900 c/s.

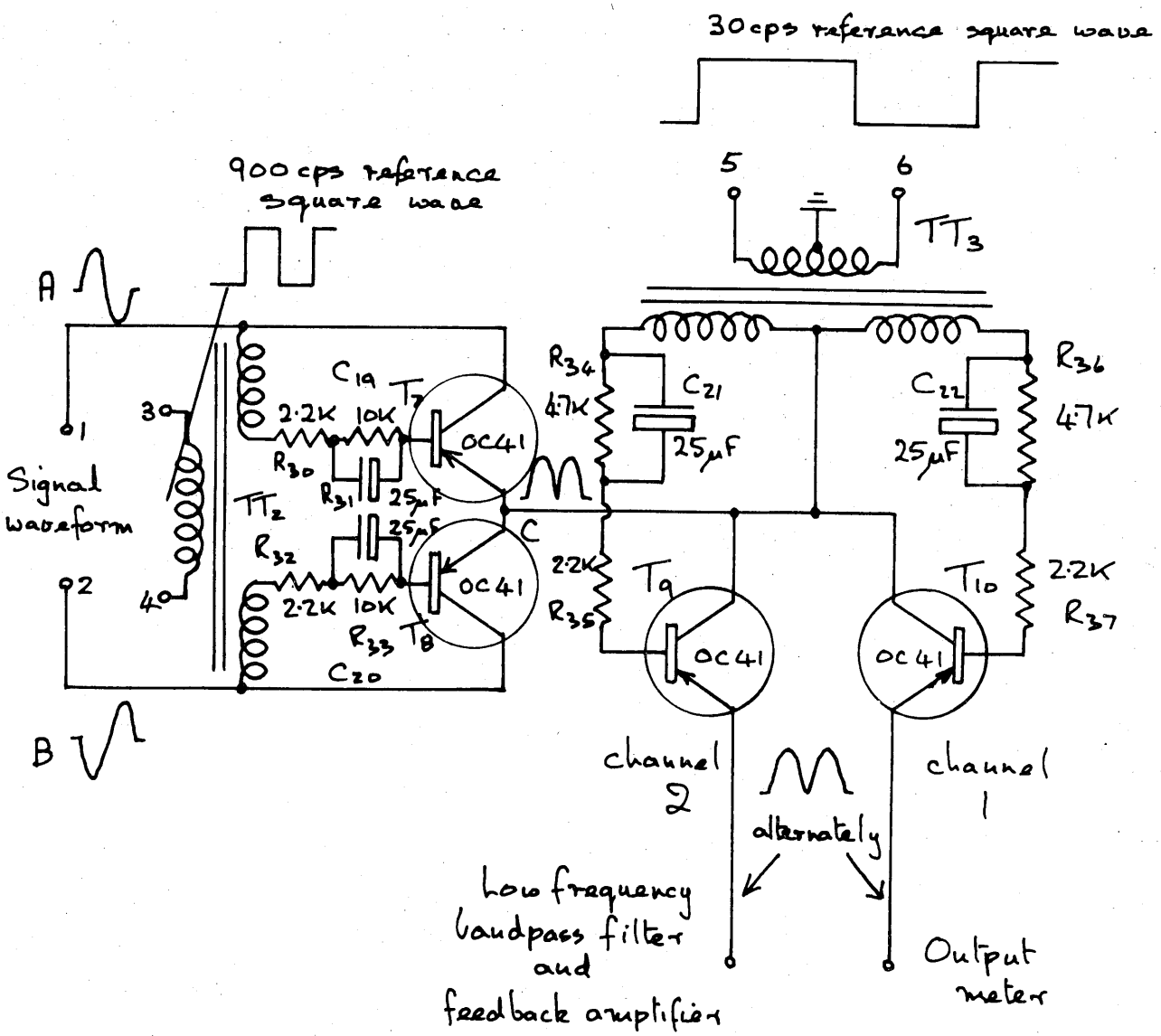

Fig 5.12 Phase sensitive rectifier and channel selection

operated in an inverted state (7, 8) by applying the switching pulse between collector and base. Thus in Fig. 5.12 the signal waveforms A and B with opposing phases are switched alternately to point C where they are combined in a rectified state. The transistor switches are voltage driven by the reference pulse firstly because they have a fairly high input resistance (few hundred ohms), and secondly because when they are not conducting, a large reverse bias voltage is essential. The large voltage is required to prevent the base of the reversed biassed transistor becoming negative with respect to the collector in the presence of noise pulses which would cause it to conduct. Fig. 5.13a shows the condition when the transistor (a PNP type) is reverse biassed in the inverted state. A negative signal is present at the emitter having come through the other half of the switch (T_8). At the collector is the corresponding positive signal from the other end of the output transformer secondary winding. The transistor is shown reverse biassed because the voltage at the base is positive with respect to its collector. If a noise pulse arrives with the signal then the transistor will conduct in the conventional direction if the noise pulse has a peak voltage V_n sufficient to bring the base voltage negative with respect to the emitter voltage. This will occur when

$$V_R + V_S - V_n < V_n - V_S$$

$$\text{i.e. } V_R < 2(V_n - V_S) \qquad (5\text{-}7)$$

where V_n = peak noise pulse

V_S = peak signal pulse

V_R = peak reference pulse

The handling range of the amplifier is limited to 15 volts peak-to-peak at the primary and therefore 7.5 peak-to-peak at each half of the secondary. The largest value for $V_n - V_S$ in (5-7) which can occur is therefore 3.75 V which corresponds to + 7.5 V for V_R.

A similar argument applies to a circuit which passes positive half cycles Fig. 5.13b. In this case the off transistor will be made to conduct when

$$V_R - V_n - V_S < V_n + V_S$$

$$\text{i.e. } V_R < 2(V_n + V_S) \qquad (5\text{-}8)$$

The largest value for $V_n + V_S$ in (5-8) which can occur is limited to 3.75 V which again corresponds to + 7.5 V for V_R. It can be seen therefore that there is little to choose between the positive going and

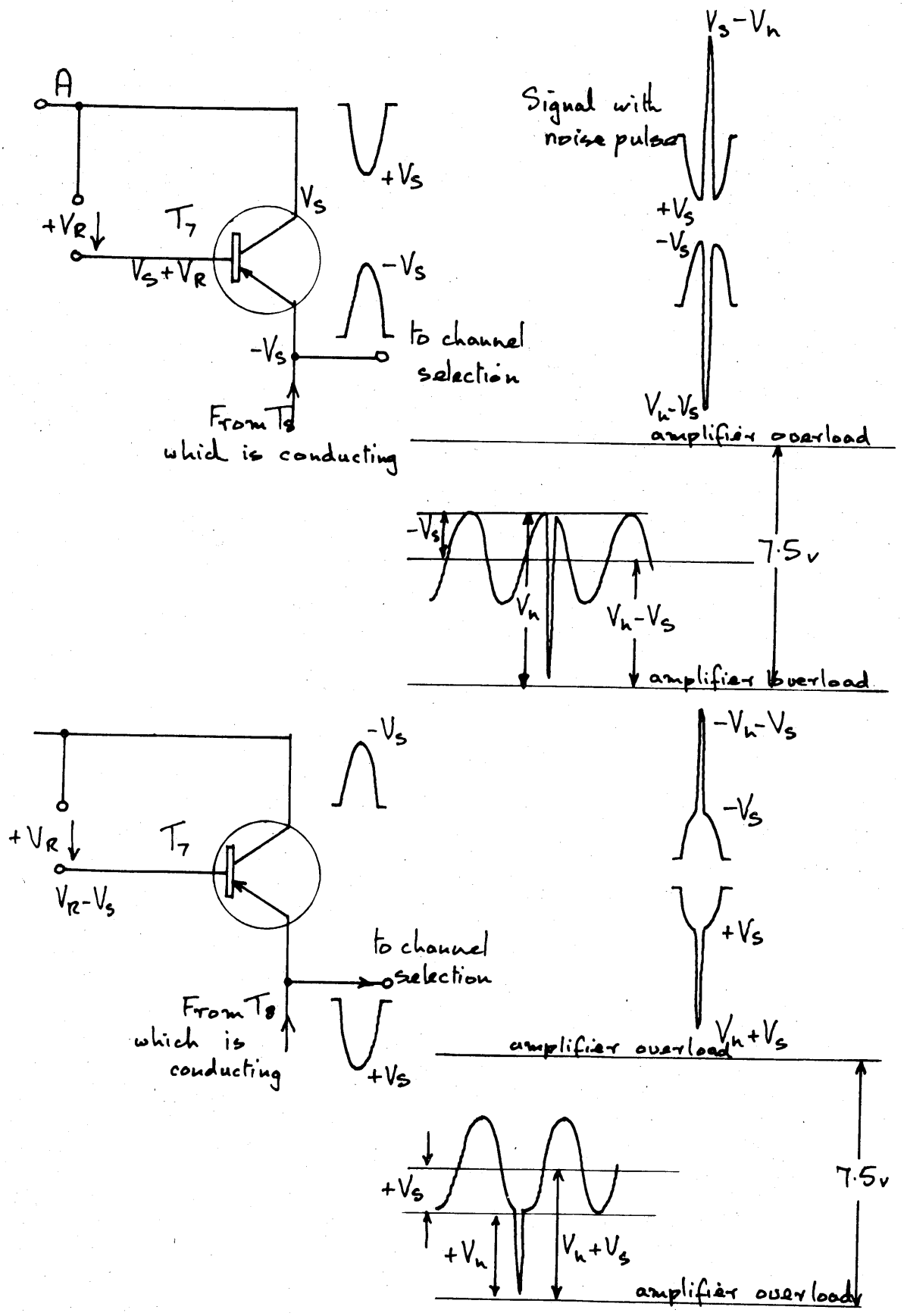

Fig 5.13 Handling of noise pulses in phase sensitive rectifier.

negative going circuits in practice. Since the signal amplifier uses a negative supply line, however, it is more convenient to use a negative going circuit as in Fig. 5.13a. The function of the components in the base leads of the transistor switches are to limit the base current and to provide restoration of the pulse so that it all appears over the collector base terminals in the reverse biassed condition.

5.10.2 The channel selection switch

The function of the channel selection switch is to separate the signals corresponding to the separate wavebands into two paths before smoothing takes place. The switch is very nearly identical with the phase sensitive rectifier except that it operates at 30 cycles per second and in reverse, separating instead of combining signals. Again, transistors operating in the inverted state have been used with restoration of the switching pulses at the base terminals. The required magnitude of the switching pulses at each half of the switch is less than for the phase sensitive rectifier since waveforms of opposite phase on each side of the reverse biassed transistor are no longer present. The situation is illustrated in Fig. 5.14 for the worst case when the larger signal (channel 2) is being fed through. To prevent conduction, the base of T_{10} must always be positive with respect to the emitter. Thus:

$$V_R - V_{s_2} - V_n > -\overline{V_{s_1}}$$

where $\overline{V_{s_1}}$ is the smoothed level of V_{s_1}

$$\text{ie.} \quad V_R > V_{s_2} - \overline{V_{s_1}} + V_n$$

When $V_s = 0$ and the noise pulse overloads the main amplifier, the required value for V_R is greatest

$$\therefore V_R > 3{\cdot}75 \text{ volts} \quad (5\text{-}9)$$

which is the size of the reference pulse required.

5.10.3 Signal smoothing

The signals corresponding to both wavebands require smoothing. It is convenient to make use of the damping in the output meter for the output signal. Thus if a moving coil meter is used it will automatically record the average level of the rectified signal. An elaborate filter will be required for the signal which is to be used for the automatic gain control of the signal amplifier since removal of 30 cps and 900 cps alternating current from the direct current feedback signal is essential. The signal current level from the output of the phase sensitive rectifier for channel 2 has a peak value of 4 m A.

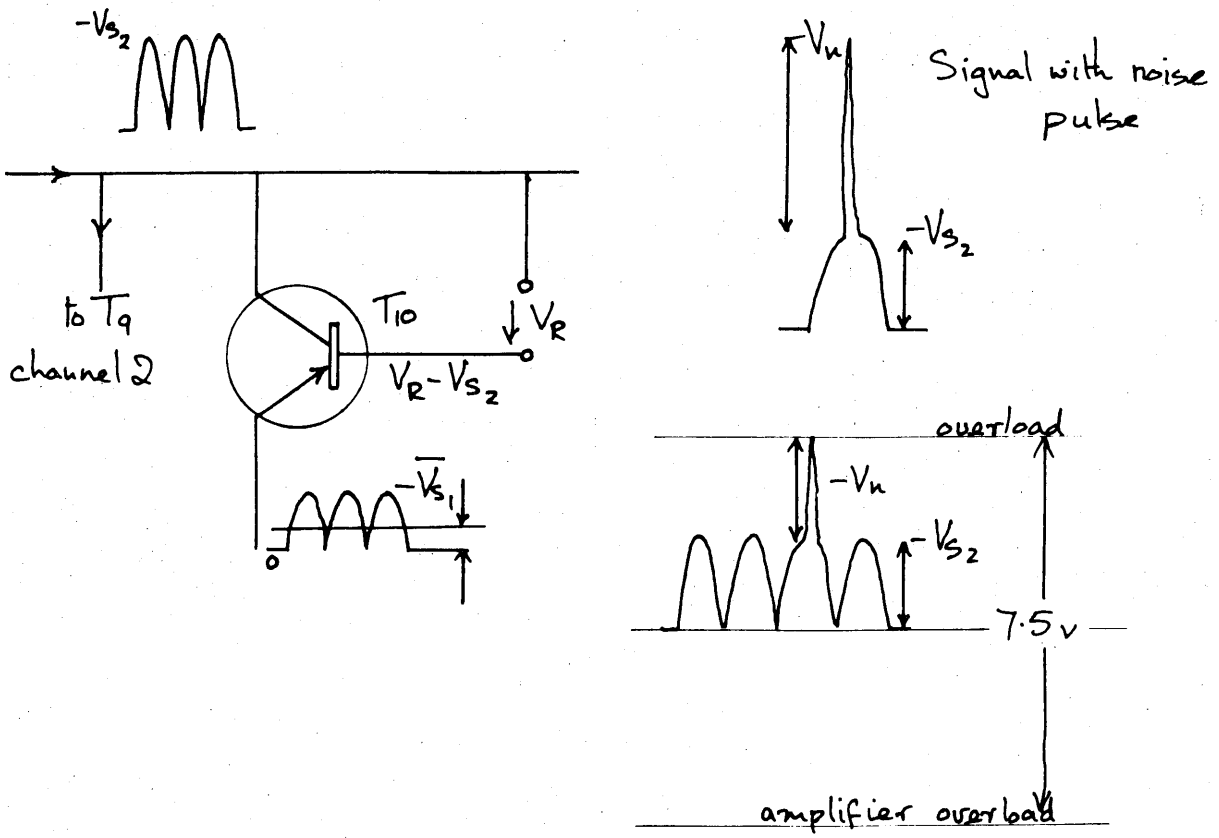

Fig 5.14 Handling of noise pulses in channel selection switch.

The smoothed level of this signal is given by

$$\frac{1}{2} \times \frac{4}{\pi} \int_0^{\pi} \sin\theta . d\theta = 1.27 \text{ m A d.c.}$$

the factor of $\frac{1}{2}$ is introduced because the switch is closed for half the time

A final value of 1 m A was attained in practice, the 20% reduction being due presumably to iron loss in the output transformer. The output of the channel switch is made up of an 1800 cps waveform due to the full wave rectification and a 30 cps fundamental waveform each with higher harmonics. The amplitudes of these are approximately 2 m A and 1.6 m A respectively using the argument outlined in 3.12 in the latter case.

These levels must be reduced by the filter so that they contribute a negligible amount when fedback with the d.c. control signal, to the signals passing through the controlled stages in the signal amplifier.

The minimum signal handling of the controlled stages is approximately 50 μV peak-to-peak at T_2 base and 50 μV peak-to-peak at T_3 base (see Appendix H). The series inductance L_1 in the control signal feed attenuates sufficiently to make the effect of 30 cps and 1800 cps waveforms at the junction of L_1 and R_{d_1} upon the signal at T_2 base, negligible compared with that at T_3 base. Thus the 1800 cps signal should be 1% of 50 μV for less than 1% error at the lowest signal level. The reduction of 30 cps is not so critical because it is removed by the phase sensitive rectifier if it adds to the signal. To prevent overloading of the signal amplifier by superimposed 30 cps, however, it should be lower than the signal level at the controlled stages. A level of 30 μV peak-to-peak should prove low enough. A specification for the filter circuit can now be written, a specification which is combined with that of the d.c. amplifier discussed earlier (section 5.7).

5.11 Specification for filter and feedback amplifier

The d.c. component of the signal entering the filter is 1 m A. This is required to provide -2 V at the output of the feedback amplifier to control the two stages (T_2 and T_3). In accordance with the 1% accuracy requirements discussed in section 5.7 an error signal of less than 10 μA must be used. This sets the gain of the feedback amplifier at 2 volts for 10 μA corresponding to a transresistance of 200 KΩ. Since current drive is employed in the signal amplifier output stage the input resistance of the d.c. amplifier should be as low as possible. It will also be convenient to have a low output impedance so that the working level of the second controlled stage (T_3) may be predicted.

(i) d.c. amplifier

input 0 to 10 μA for 0 to -2 V at output

a.c. attenuation as high as possible consistent with a one second time constant.

(ii) a.c. performance of amplifier and filter

for 2mA in $\frac{1}{2} r_{s_1}$

and 1μV over $R_{52} + r_L(T_5)$

reduction in level is $\frac{(.002)^2 \times 300 \times 280}{10^{-12}}$

$= 1.46.10^{11}$ ie. 112dB.

similarly for 30 cps, a reduction from 1.6 m A to 30μV is

$$\frac{(.0016)^2 \times 130 \times 280}{(30.10^{-6})^2}$$

$= 1.04.10^{8}$ ie. 80dB.

(iii) Phase characteristics

The feedback amplifier must provide a phase change of 180° for a d.c. signal to effect negative feedback control. Since the loop gain of the system is high oscillations are likely to occur around the entire loop. The design procedure adopted consists of the construction of a filter to provide the required a.c. attenuation, followed by the addition of an equalising circuit to provide adequate stability, at a later stage.

5.12 The filter and feedback amplifier circuits

5.12.1 The final circuit which is shown in Fig. 5.15 was developed through three distinct stages:

Stage (i) a circuit was developed which gave the required reduction of the 30 cps and 1800 cps signals. This circuit was used in the control loop with only one of the control stages operating. The circuit gave a prohibitively long response time of the control loop to input changes and because of large phase changes at low frequencies it was unstable at the higher end of the signal input range.

Stage (ii) additional circuits were added to provide better reduction of the a.c. signals with a corresponding improvement in response time. Instability was still troublesome at large signal input levels.

Stage (iii) a compensation circuit was introduced to remove the instability and the required response time and accuracy of control over the required range were achieved.

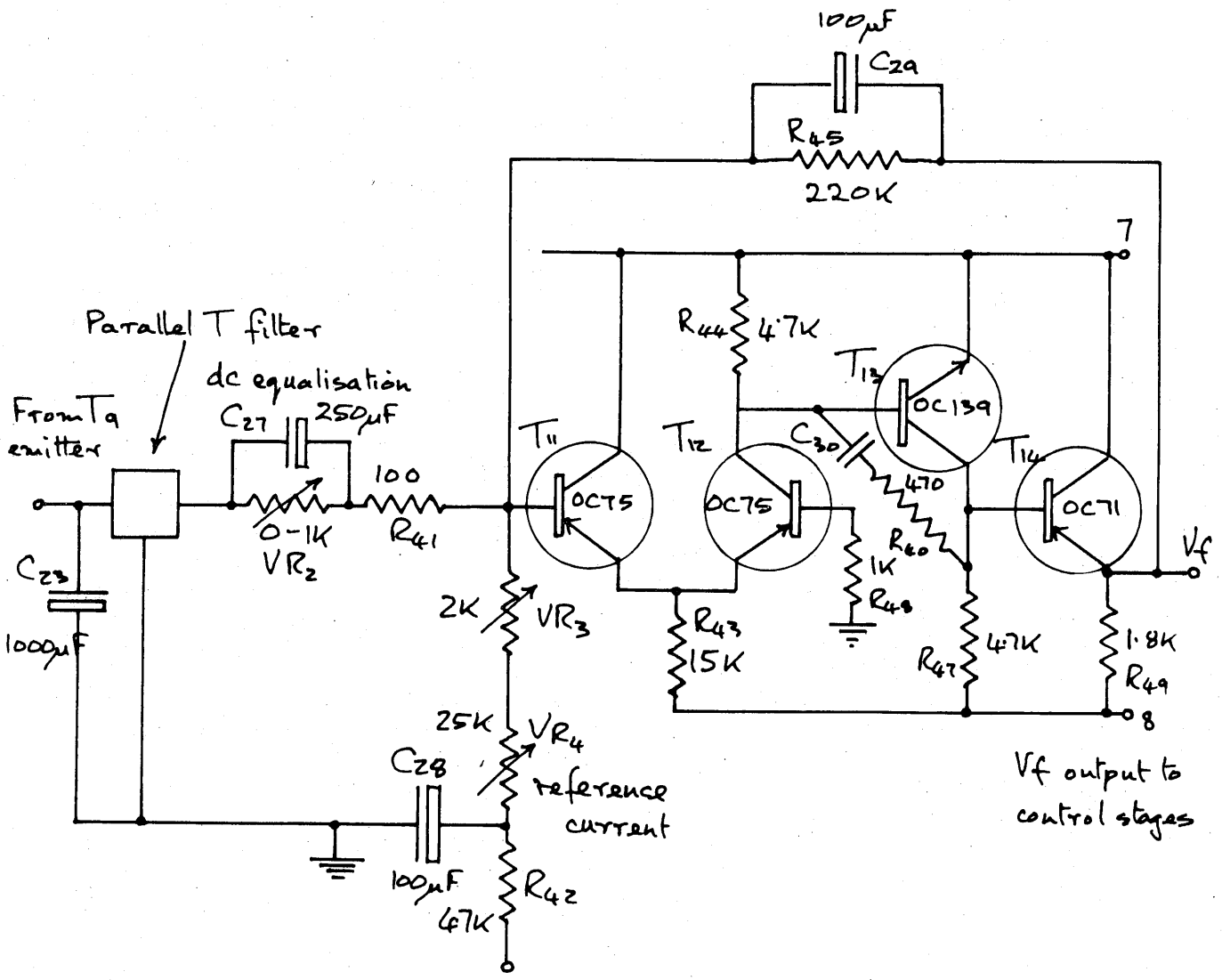

Fig 5.15 Filter and feedback amplifier.

5.12.2 Stage 1

The circuit used (Fig. 5.16) consists of a single lag filter followed by a d.c. amplifier which makes use of the Miller effect (9). The source impedance for this circuit is the impedance of the output transistor T_6 reflected through the output transformer TT_1. Initial smoothing of the signal occurs and the d.c. component, together with the superimposed ripple is compared with the reference current provided from the supply line through R_{42}. The difference is amplified by the d.c. amplifier to provide the feedback control voltage. The gain of the amplifier is such that as the error between signal and reference currents increases the output V_f goes negative to turn the control stage further on to decrease the error.

(a) d.c. performance

The d.c. amplifier employs shunt voltage feedback (Fig. 5.6b) from output to input giving low input and output impedances. The first stage consists of a balanced pair, in which temperature drift is cancelled to a large extent because of the large stability factor produced by the common emitter resistor (10,11). This is followed by a common emitter amplifier and emitter follower to provide a high open loop current gain of $\beta^3/2$ (approximately 50,000 for medium gain transistors). The open loop output resistance is given by R_{47}/β assuming β is the current gain of T_{14}. The open loop gain will therefore be:- $\beta^3/2 \times R_{47}/\beta = 5M\Omega$ or 5 volts/μA The gain with feedback is controlled by R_{45} at 220 KΩ and the output resistance is divided by the reduction in gain due to feedback (12).

i.e. closed loop gain to d.c. is 220 KΩ

closed loop output resistance $\frac{R_{47}}{\beta} \times \frac{220.10^3}{5.10^6} \simeq 4\Omega$

(b) a.c. performance

This is controlled by the feedback capacitor C_{29}. The transimpedance is thus very low and provides additional smoothing to the a.c. ripple. It should be noted, however, that the transimpedance cannot be reduced indefinitely by increasing the feedback capacitor C_{29} because eventually this will short circuit the output resistance at the operating frequency in which event the simple analysis breaks down (13). In practice it was found that the transimpedance could not be reduced below the open loop output resistance and the only advantage to be gained by increasing the feedback capacity was to reduce the transimpedance for increasingly lower frequencies to this limiting value.

Thus we have:-

(i) high open loop gain enabling predictable gain with feedback of 220 KΩ for d.c. signals.

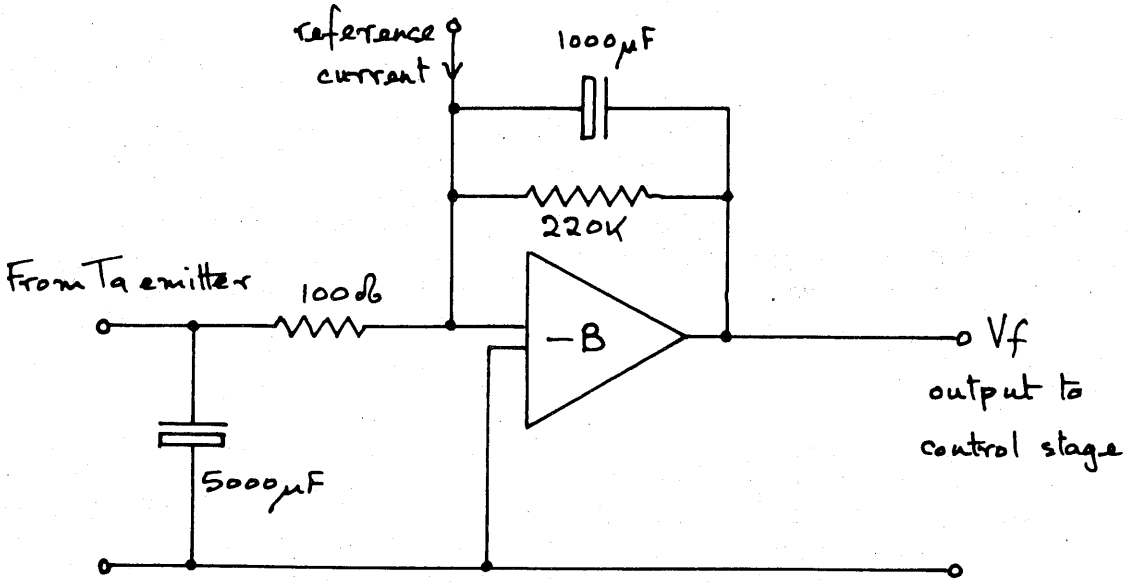

Fig 5.16 Stage 1 — Development of feedback filter.

(ii) low output impedance which allows low values for the trans-impedance to be obtained.

In the circuit of 5.16 the large values of capacity were required to provide the necessary reduction of the a.c. ripple and even with these values reductions of only 126 dB at 1800 cps and 92 dB at 30 cps were obtained due to the limiting effect of the d.c. amplifier open loop output resistance.

(c) Response time and stability

The stability of the control loop using the filter described above was poor and oscillation at about $\frac{1}{3}$ cps was liable to occur. The response time at a typical signal level was measured by applying a step decrease in signal level and observing the output waveform on a cathode ray oscilloscope. The oscillatory decay of the output waveform is shown in Fig. 5.18a. The final value is reached after about 5 seconds and the oscillation is at a frequency of $\frac{1}{3}$ cps.

5.12.3 Stage 2

The long response time was a result of the magnitude of the time constants in the filter circuit described in the preceding section. To reduce these and yet maintain sufficient attenuation at 30 cps required a special filter to reject 30 cps only. The parallel T circuit (14,15) shown in Fig. 5.17a was used for this purpose. Although the attenuation of this network is theoretically infinite at the selected frequency, in practice this condition cannot be realised due to variation of resistor and condenser values within the normal tolerance ranges. Furthermore the need for large values of capacity inevitably led to the use of electrolytic types with their attendant disadvantages. Nevertheless the performance of the circuit using 20% tolerance components gave adequate attenuation at 30 cps.

The rejection frequency and ideal impedance requirements of the parallel T circuit are given by:-

(i) $$2 Z_s Z_L = R^2$$

(ii) $$f_o = \frac{1}{2\pi R C}$$

where Z_s = source impedance
Z_L = load impedance
f_o = rejection frequency
R = resistance in arms
C = capacitance in arms

The values of the preceding capacitor C_{23} and the following resistor R_{41} were chosen to satisfy this relation approximately.

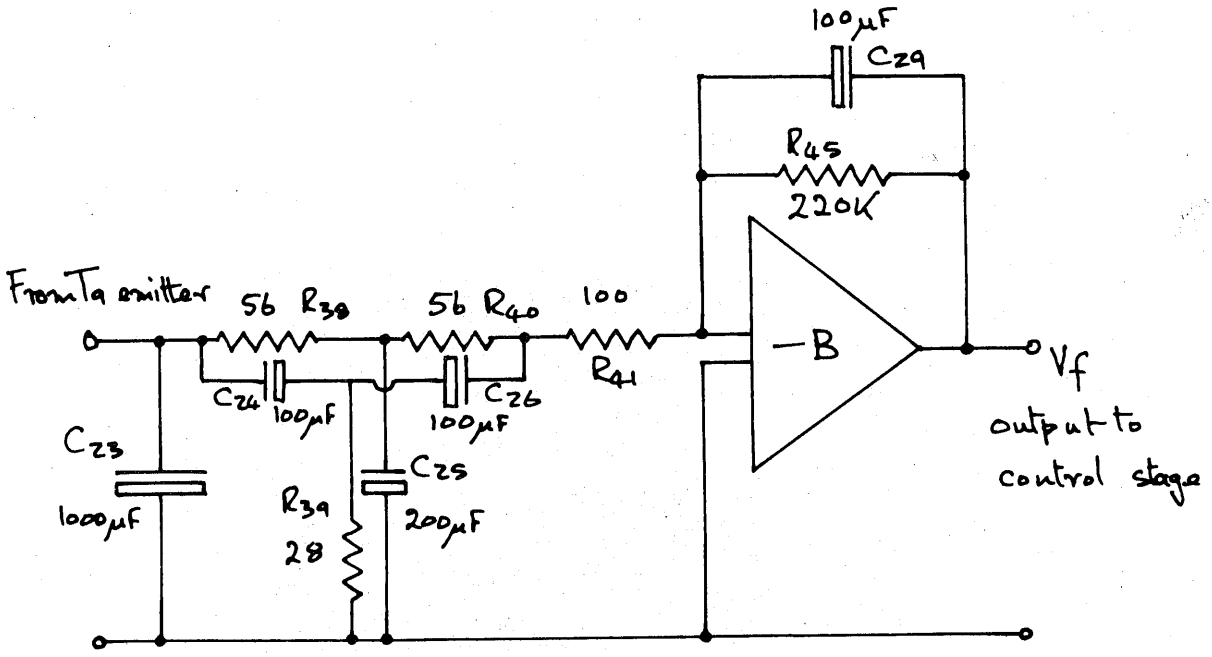

(a) Stage 2 – Development of feedback filter.

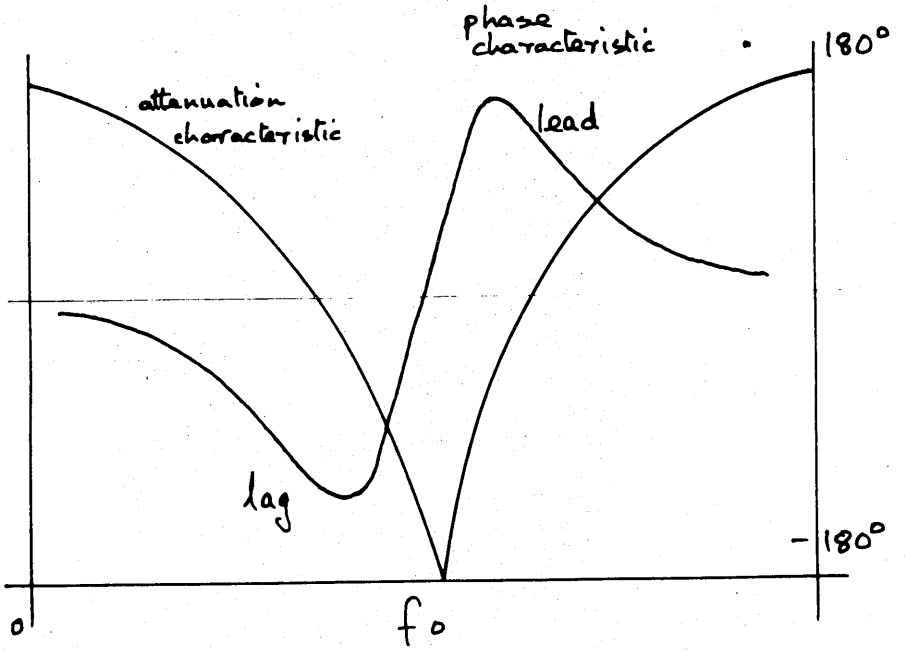

(b) Phase attenuation characteristic of Parallel T filter.

Fig 5.17 Stage 2 - Development of feedback filter.

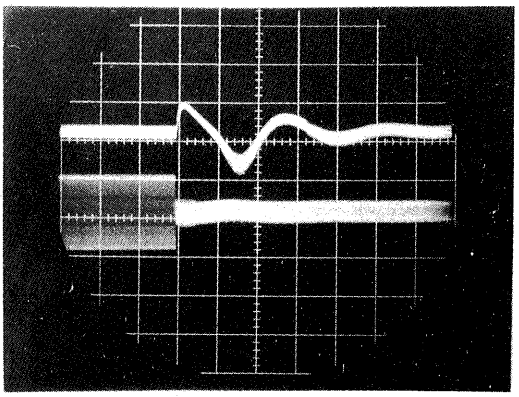

Output meter terminals

Amplifier input

Time base 1sec/division

Fig.5.18a

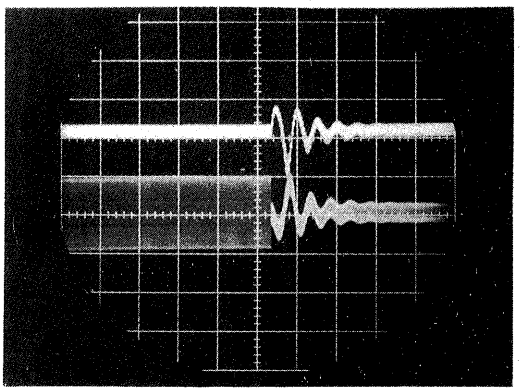

Output meter terminals

Amplifier input

Time base 1sec/division

Fig.5.18b

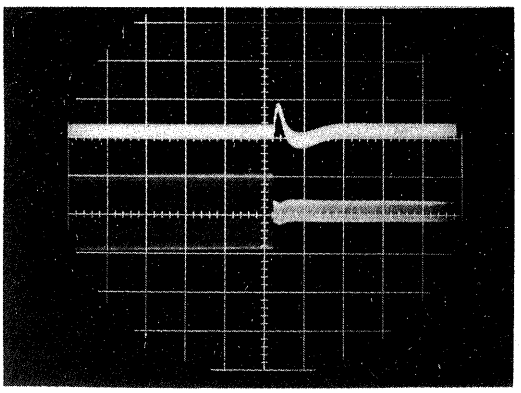

Output meter terminals

Amplifier input

Time base 1sec/division

Fig.5.18c

Response time to a step change at input.

Fig. 5.18. Response time to a step change

The stability of the system was not much improved over that described previously due to the additional phase lag introduced by the parallel T circuit at low frequencies (Fig. 5.17b). Spontaneous oscillation occurred at an input signal level of 20 m V, although the frequency of the oscillation was now much higher (2 cps) due to the reduction in the other time constants. The response time of the system, was now improved to about 2 seconds (see Fig. 5.18b).

5.12.4 Stage 3

In order to improve stability it was decided to introduce a series compensation network designed to advance the phase at the oscillation frequency. This consisted of V_{R_2} and C_{27} in parallel. The value of V_{R_2} was chosen to provide adequate transmission to d.c. and then C_{27} was added so that a phase advance occured at the oscillation frequency. The phase advance is due to the combination of C_{27} with R_{41} and we have:-

$$\text{phase advance} = \tan^{-1} \frac{1}{\omega R_{41} C_{27}}$$

$$= 18^\circ \quad \text{for an oscillation frequency of 2 cps}$$

With this network, stability for the entire input signal range was achieved and there was a corresponding improvement in response time to a step input, to 1 second (see Fig. 5.18c).

5.13 Conclusion

The transistor has been chosen as the active device in the system on account of its small size, low power consumption and optimistic reliability characteristics. It has been shown that the use of negative feedback is highly desirable in order to overcome the spread in transistor characteristics. The reliability thus obtained is further improved by the use of a ratio circuit in which the performance is dependent largely on a simple reference level. The ratio circuit has been analysed and the design of the signal circuit has been described stage by stage. To obtain the required sensitivity it has been necessary to adopt a phase sensitive rectification system operating at the signal carrier frequency of 900 cps. Finally the handling capacity of the ratio circuit has been examined and measurements illustrating a handling range of 1000:1 are discussed. Such a handling range is equivalent to a temperature range far in excess of that required for the application to magnox can temperature measurement. It has proved necessary however in the further application of the pyrometer system discussed in Chapter 8.

5.14 References

1. R.E. Fischbacher. A Guide to Instrument Design. Chapter 5. S.I.M.A. and S.I.R.A., London,Taylor and Francis,1963,p.235

2. A.J. Dekker. Solid State Physics. London,MacMillan,1958,p.213

3. M. Born. Atomic Physics,6th Edition. London,Blackie,1957,p.15

4. J.H. Simpson and R.S. Richards. Physical Principles and Applications of Junction Transistors. Oxford,Clarendon Press,1962,p.57

5. E.M. Cherry. J.Brit.Inst.Radio Eng.,1963,25,(2),p.127

6. J.H. Simpson and R.S. Richards. Physical Principles and Applications of Junction Transistors. Oxford,Clarendon Press,1962,p.295

7. D.G. Avery and R.C. Bowes. J.Sci.Instruments,1958,35,p.212

8. S. Guennou and H. Kenhadjian. Mullard Tech.Communications, 1960,5,(43),p.97

9. G.K. Korn and T.M. Korn. Electronic Analog Computers,2nd Edition. New York,McGraw-Hill,1956,p.215

10. M.V. Joyce and K.K. Clarke. Transistor Circuit Analysis. Reading,U.S.A.,Addison-Wesley,1961,p.98

11. J.H. Simpson and R.S. Richards. Physical Principles and Applications of Junction Transistors. Oxford,Clarendon Press,1962,p.222

12. Ibid.,p.297

13. R.C. Foss. Lecture notes. Brunel College,1963

14. Reference Data for Radio Engineers,5th Edition. New York, Federal Telephone and Radio Corp.,1959,p.270

15. H.C. Bertoya. A Twin-T Selective Amplifier with Stable Gain. BSIRA Report R266

CHAPTER 6 - THE AUXILIARY CIRCUIT

Introduction

A specification for the auxiliary circuit, which provides the galvanometer drive, stable line supplies and reference signals for the ratio circuit, is discussed. The master oscillator which provides the 900 cps carrier frequency and reference pulses is designed and the 30 cps channel selection pulses are obtained from this by direct division. Two forms of galvanometer drive circuit are developed and the individual merits of each examined. The distribution of supply voltage from a conventional stabilised supply is described and the importance of removing earth loops emphasised. The completed circuit including the ratio section is tested, using for convenience, a unit which simulates the optical system. Results of this test are presented together with a measurement of the temperature coefficient.

6.1. Specification for the auxiliary circuit

In order to function the signal processing system must be supplied with 900 cps and 30 cps reference pulses. The 900 cps pulses should be synchronised with the waveband selection frequency. Since the signal carrier and waveband selection frequencies are both determined by the oscillation of the galvanometer optical modulator, the drive waveforms to this component should be derived from the same sources as the signal system reference signals. Provision of these two frequencies in suitable forms is the function of the auxiliary circuit. Also discussed under this section is the $\pm$ 9v supply line which is used for the signal and auxiliary systems and the testing of the complete system.

The ideal motion of the galvanometer mirror is such that the incident energy is switched instaneously on and off, in which case the optimum signal to noise ratio is obtained from the detector (see 3.10). In practice however, the response of the galvanometer to a step input of current is limited by inertia and a significant phase lag occurs. Thus apart from requiring a 900 cps square wave drive to provide the signal carrier frequency and a 30 cps square wave drive to provide the alternate channel selection, a 900 cps phase adjusting circuit is required. The phase adjustment will ensure correct synchronisation of the signal with the phase sensitive rectifier reference pulses. Measurements on the galvanometer discussed under Appendix F show that a minimum of 1.6 volts peak to peak square wave at 900 cps and a 3.2 volt peak to peak square wave at 30cps are required.

The amplitude of the reference pulse must be larger than any signal or noise waveform in the signal channels, if the switches are to operate satisfactorily (see 5.10.1). It is advisable, therefore, that the reference pulses should be larger than the signal handling capacity of the phase sensitive rectifier, which is 7.5 volts peak to peak.

The channel selection switch also requires 7.5 volts peak to peak pulses at 30 cps for satisfactory operation for the reasons outlined in 5.10.2.

The specification may be summarised as follows:

(i) provision of 900 cps square wave at 1.6 volts peak to peak amplitude to drive galvanometer load of 70 Ω, with suitable phase adjustment.

(ii) provision of 900 cps square wave at 7.5 volts peak to peak amplitude to drive phase sensitive rectifier switch.

(iii) provision of 30 cps square wave at 3.2 volts peak to peak to be superimposed upon 900 cps square wave of (i) above.

(iv) provision of 30 cps square wave at 7.5 volts peak to peak amplitude to drive waveband selection switch.

(v) provision of ± 9 volt stabilised supply for signal and auxiliary circuits with mains or battery operation.

6.2. The oscillator

The output of the oscillator cannot be used to drive the galvanometer directly since a square wave with adjustable phase shift is required. It is nevertheless convenient to use an oscillator which will provide a square wave as well as a sine wave output, so that the phase sensitive rectifier reference pulse may be obtained directly. This is achieved in a circuit discussed by Foss[1,2] where the transistor is treated as a switch. The state of the switch is determined mainly by passive components and not by transistor parameters.

The equivalent circuit Fig. 6.1 shows that a current from a constant source is switched alternately by the switch S into either of two paths. In one path the load R_{55} will produce a square wave of voltage and in the other, if the switching frequency coincides with the resonant frequency of the parallel tuned circuit, a sine wave of voltage. This is because the tuned circuit rejects all components of the square wave other than the fundamental, which it passes with a peak amplitude determined by Fourier analysis and given by:

$$i_{peak} = \frac{4}{\pi} . i_t$$

The peak to peak voltage across the tuned circuit is given by:

$$V = \frac{4}{\pi} . i_t R_D \qquad \text{where } R_D = \text{dynamic resistance of the tuned circuit.} \qquad (6\text{-}1)$$

The dynamic resistance R_D is a function of the tuned circuit components L_2 and C_{32}. If a damping resistor R_{53} is added then although the rejection of harmonics of the fundamental deteriorates the voltage swing is determined mainly by R_{53} and is predictable. In the practical circuit we have:

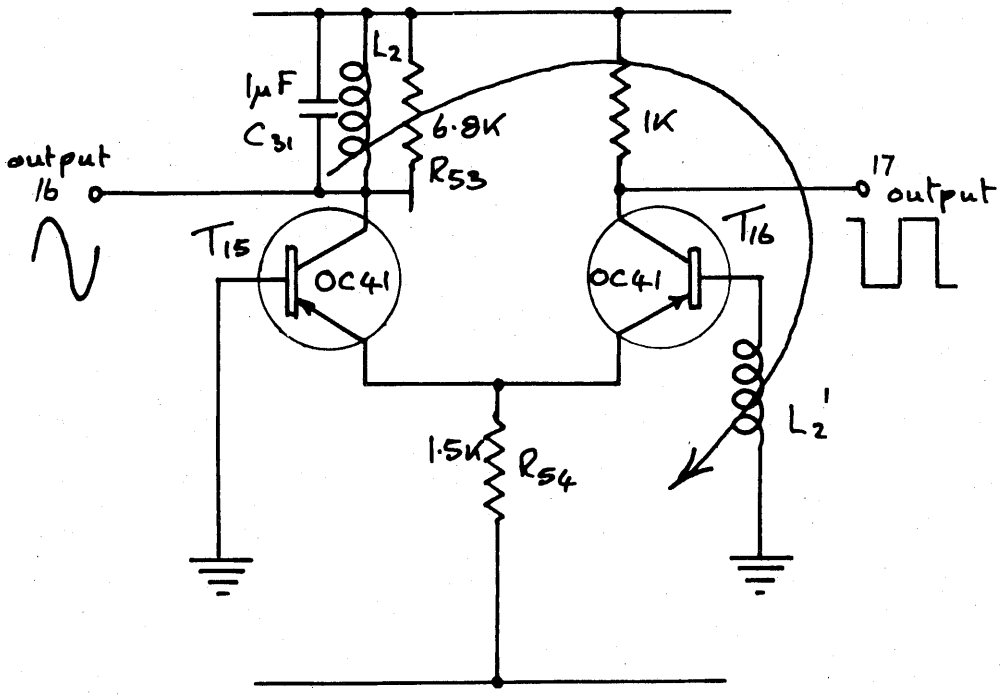

Fig 6.2 Oscillator circuit

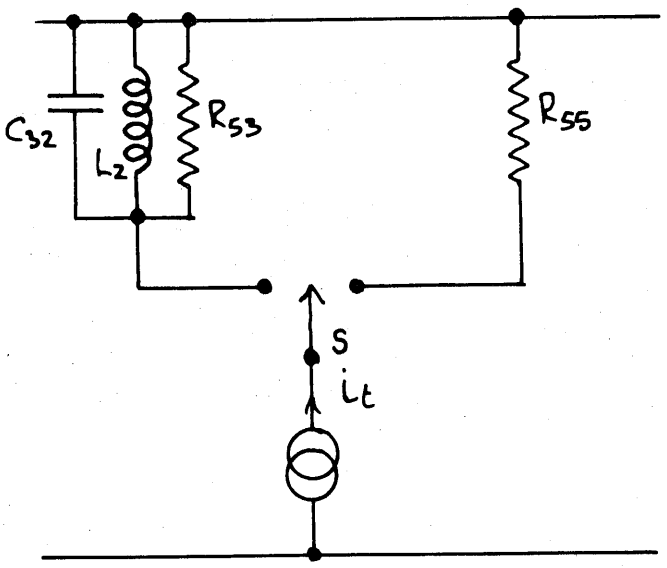

Fig 6.1 Equivalent circuit of oscillator

resonant frequency (f_o) = $\dfrac{1}{2\pi\sqrt{L_2 C_{31}}}$ (6-2)

$$L_2 C_{31} = \frac{1}{4\pi^2 \times 900^2} = 3.09.10^{-8}$$

The actual values of C_{32} and L_2 are governed by the Q value of the tuned circuit.

This is defined as $\dfrac{\omega_o L_2}{r_s}$ (6-3) where r_s = inductor effective series resistance.

For an inductance of reasonable dimensions at the frequency involved a Q of 15 is attainable.

The rejection of harmonics is given by (2)

$$V_n = V_1 \frac{1}{(n^2-1)Q}$$ where V_n is the peak to peak voltage of the n^{th} harmonic

Thus if 5% 3rd harmonic content is tolerated we have:

$$Q = \frac{20}{n^2-1} = 2.5$$

Thus for a working Q of 2.5 and an unloaded Q of 15 a damping resistor R_{53}, considerably smaller than R_D, may be used if necessary to reduce the effect of variations in R_D due to temperature and drift and to provide a usefully low output impedance. From (6-2) we have in the presence of the damping resistor R_{53}:-

$$\frac{R_D.R_{53}}{R_D+R_{53}} \cdot \frac{4}{\pi} i_t = V \qquad (6\text{-}4)$$

$$\therefore \frac{R_D.R_{53}}{R_D+R_{53}} = \frac{\pi V}{4 i_t} \qquad \text{but} \quad \frac{\frac{R_D.R_{53}}{R_D+R_{53}}}{R_D} = \frac{2.5}{15}$$

$$\therefore \quad R_D = 5 R_{53}$$

substitution in (6-4) gives

$$\therefore \quad R_D = 1.5 \frac{\pi V}{i_t} \qquad (6\text{-}5)$$

The dynamic resistance of the tuned circuit is given by:

$$R_D = \frac{L_2}{r_s . C_{32}} \qquad (6\text{-}6)$$

thus combining (6-2), (6-3), (6-5) and (6-6) and substituting $R_D = 2.7\ K\Omega$.

we obtain: $C_{32} = 1\mu F$; $L_2 = 30mH$; $R_D = 2.7K\Omega$; $R_{53} = 540\Omega$
$V_{pp} = 3.5v$; $i_t = 6.3mA$.

The practical circuit is shown in Fig. 6.2. The current source is provided by two transistors alternately, working in the common base configuration. Each transistor is switched on and off alternately by the other by means of the feedback from the collector of T_{15} to the base of T_{16} provided by the tightly coupled coil and the common emitter resistor R_{54}. The turns ratio is not critical since all that is required is a pulse of about 1v at the base of T_{16} to turn it off or on as the case may be. The square nature of the switch is achieved because the voltage required to render T_{16} conducting is a small fraction of the 1v pulse. When T_{16} is off the current in the emitter resistor is directed into T_{15} and vice versa. The output at the collector of T_{16} is a fair approximation to a square wave with amplitude 6v peak to peak.

It was not necessary in this application to take advantage of the increase in stability by making R_{53} smaller than R_D. Instead R_{53} was increased to 68KΩ which, when considered in parallel with R_D, produced a 12.2v peak to peak sine wave for a switch current of 6.3mA. This sine wave provided a useful dummy signal source which was used during the assessment of the electronic system (see 6.11).

6.3. 900 cps reference for phase sensitive rectifier

The phase sensitive rectifier is operated by a 900 cps square wave of suitable phase (see 5.10.1). This was conveniently obtained from the collector of T_{16} in the oscillator circuit using transformer coupling. The load is effectively 2.2 KΩ alternately on each half of the phase sensitive rectifier which reflects as 1.4 KΩ in the primary of TT_2. If the collector load of T_{16} is the transformer primary therefore, the square wave output is stepped up to about 7.5v at the secondary when the turns ratio is 1:1.25 + 1.25. This amplitude is adequate to operate the phase sensitive transistor switches. The introduction of R_{55} in series with the transformer primary would cause an even larger voltage swing but for the clipping action which occurs when T_{16} bottoms. This has the effect of improving the shape of the reference square wave pulses.

6.4. Dividing circuit for 30 cps pulses.

The 30 cps square wave is derived from the oscillator through a dividing circuit. There is no justification for synchronous division, providing the 30 cps pulses to the galvanometer and the wavelength selection switch are themselves synchronised. This means a simple circuit may be used which depends for its operation upon a single time constant. The stability of the frequency must be sufficient to allow the parallel T filter in the feedback loop of the control system to attenuate satisfactorily, and measurements have shown that ± 5% is adequate since the parallel T does not contain specially selected components. The circuit is shown in Fig. 6.3. It is based on a circuit

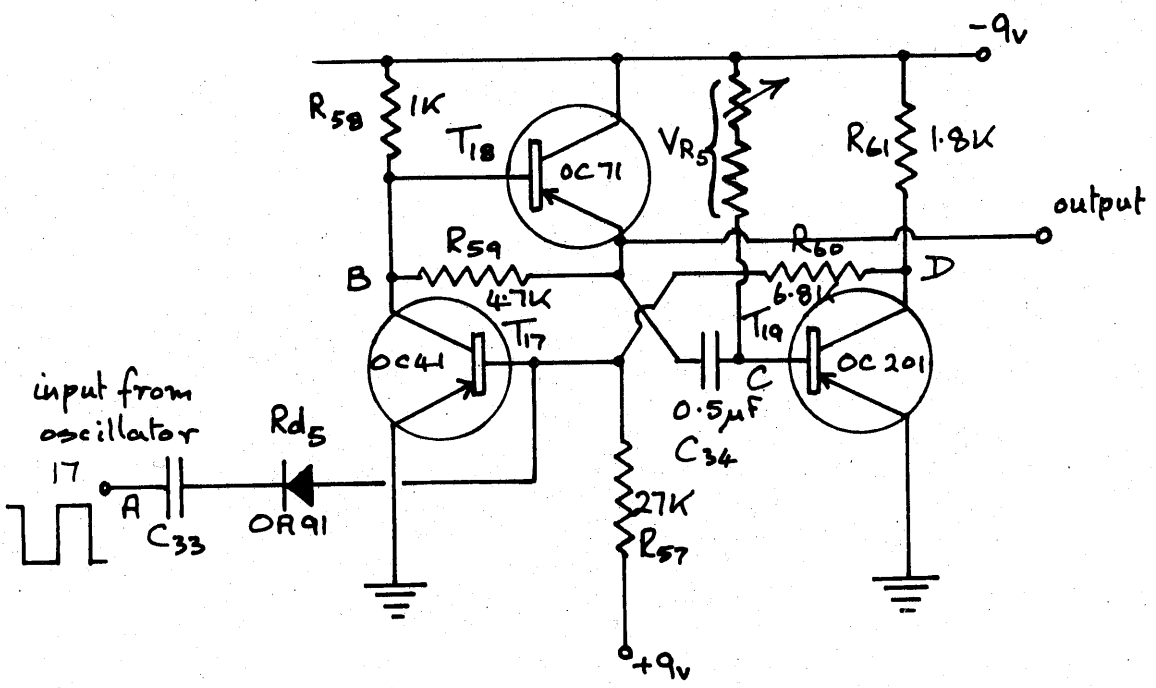

Fig 6.3 Divide by fifteen circuit.

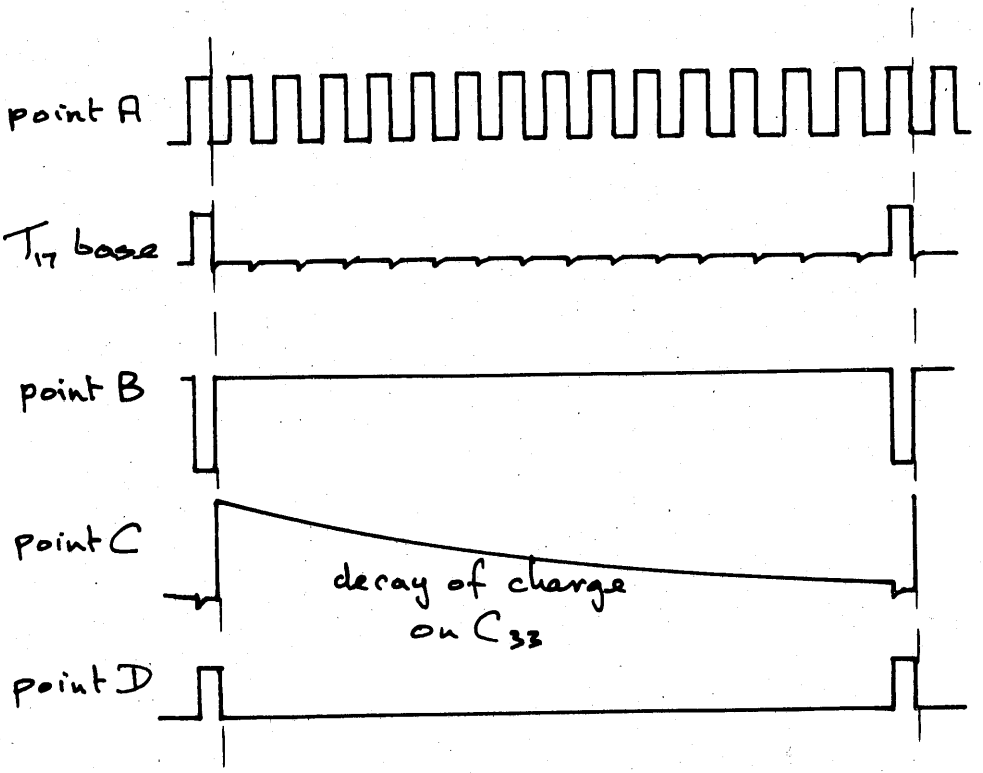

described by RACAL (3) Consider an initial condition when T_{17} is off and T_{19} is on. A negative pulse provided by a differentiating circuit appearing at the input, will cause the diode R_{d_5} to conduct allowing the negative pulse to turn on T_{17}. The resulting positive swing at B will drive C positive, turning T_{19} off and causing a negative swing to appear at D which turns T_{17} further on. The circuit will remain in this state while the capacitor C_{34} discharges through V_{R_5}.
When this process nears completion C will pass the turning on point of T_{19} and the resulting positive swing at D will turn off T_{17} until the next negative pulse appears. At the same time T_{18} is rendered conducting by the negative swing at B and since it is connected in the common collector configuration, it will deliver a negative pulse at the output from its low impedance source. The next negative pulse at the input commences the cycle again and causes T_{18} to turn off, leaving a short duration pulse at the output. The time interval between the output pulses is determined by the time constant $V_{R_5}C_{34}$. Although this could be designed to give a pulse repetition frequency of 30 cps there is no point since the circuit cannot provide the required 30 cps square wave. Thus division by 15 is sufficient and the further factor of 2 is obtained in the following bistable unit. The exact value of the time constant cannot be predicted any more accurately than the turning on point of T_{19} can be defined. This will occur when $V_{be} \sim 600mV$. Thus if we assume a 6 volt swing at B then C will have to change by 6.6 volts before T_{19} turns on. Using the exponential decay of the voltage at C and the 15 volt difference across V_{R_5} we have

$$\text{Voltage across } V_{R_5} = 15\, e^{\frac{-t}{V_{R_5}C_{34}}}$$

$$= 8.4 \text{ volts}$$

$$\therefore V_{R_5}C_{34} = \frac{t}{0.57} \qquad t = 0.0165 \text{ secs for } \div 15$$

$$\therefore V_{R_5}C_{34} = 0.029$$

The value of V_{R_5} is such that sufficient base current may be drawn by T_{19} to keep it fully on when required. The current will be about $200\mu A$ leading to a value for V_{R_5} of $58K\Omega$ for a condensor of reasonable size, $0.5\mu F$.

A small pre-set potentiometer is provided in series with a 56 KΩ resistor to provide means for adjusting the pulse repetition frequency to suit the parallel T filter in the control loop. Use is made of the positive supply for the bias chain for T_{17}. The transistor is held off more readily in this manner and the large resistor does not draw current from the input pulse.

The second half of the dividing circuit, Fig. 6.4, consists of a conventional bistable unit each half of which drives half of the primary of TT_3.

If T_{21} is on and T_{22} is off initially then A will be at the same potential as B, there being no voltage drop over T_{21}. This means that Rd_6 will be nearly conducting and it presents a low resistance to an input pulse. On the other hand C is at a positive voltage T_{22} being off, rendering Rd_7 non-conducting. Thus a negative pulse at the input will turn T_{21} off and feedback from A to D will turn T_{22} on. The circuit will remain in this state until another negative pulse turns T_{22} off via Rd_7 which is now nearly conducting. Thus for every two input pulses a single operating cycle is performed. The collector waveforms will be square pulses at a frequency of 30 cps and almost 9v peak to peak.

The pulses are fed to the two halves of the primary of TT_3 via emitter followers T_{20} & T_{23} and a large voltage swing is obtained at the secondaries from the reflected low impedance source. Furthermore since the primaries are fed in opposite phase the resultant dc component is zero, which means that saturation of the transformer core by a large standing current is avoided.

6.5. The galvanometer drive circuit

The measurement of the current drawn by the galvanometer for typical amplitude of vibration is discussed in Appendix F.

From these measurements a carrier drive waveform of 1.6 volts was predicted for the galvanometer magnet combination employed in the optical system. This figure was used as a basis for the design of the galvanometer drive circuit. Two forms of drive have been considered and assessed (see 7.6.5) and the equivalent circuits of these and the galvanometer drive waveform they produce are shown in Fig. 6.5. In (a) the 900 cps waveform is restored by C and D above the earth line and fed to the galvanometer coil in either direction, determined by the alternate switching of one end of the galvanometer coil to earth at 30cps. It is called the symmetrical drive because the mechanical zero position of the galvanometer mirror M_3 corresponds to zero signal at the detector. This mode of operation is simple and although it gave adequate performance when the pyrometer was measuring the temperature of a flat surface, errors were introduced on the reentrant surface encountered on a fuel element.

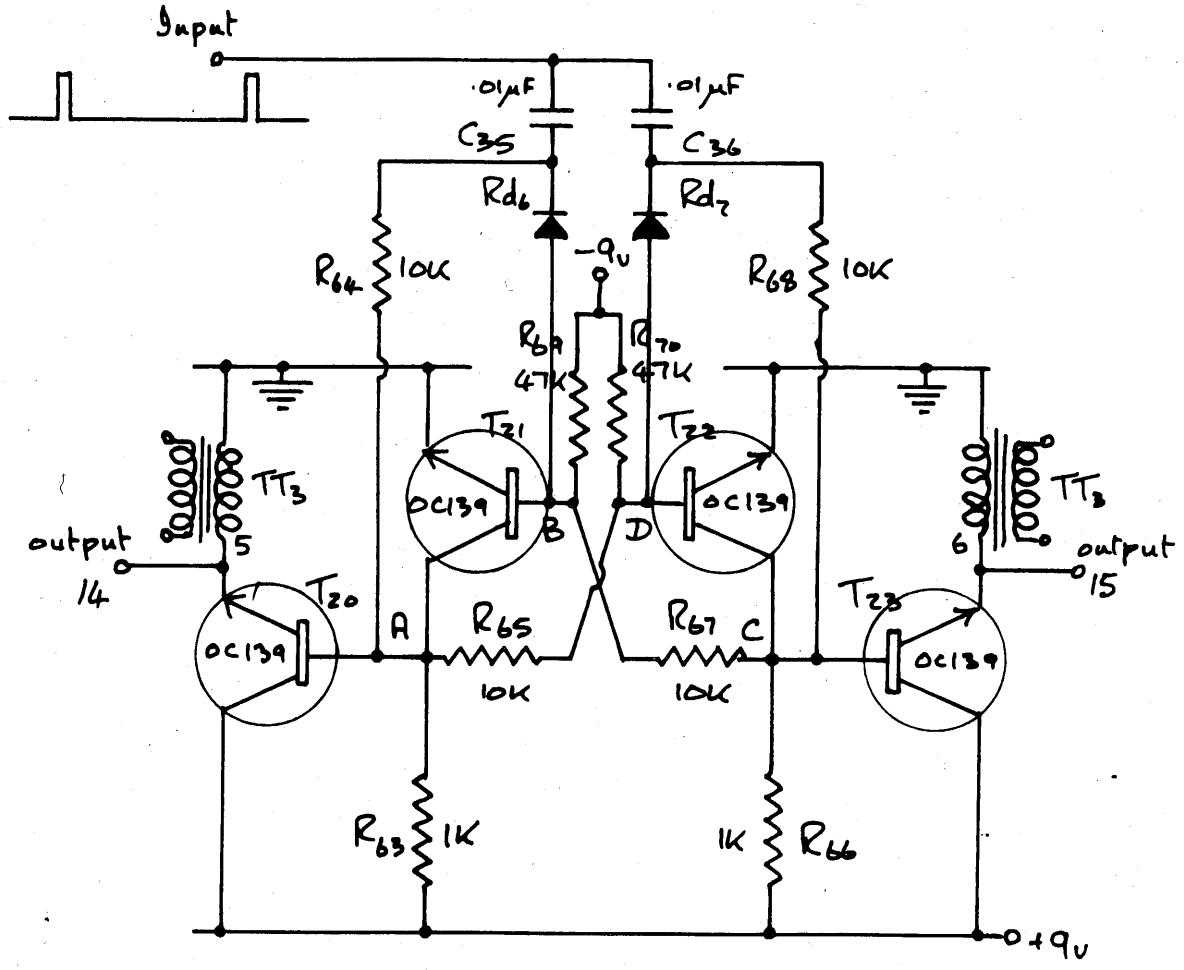

Fig 6.4 Conventional bistable circuit.

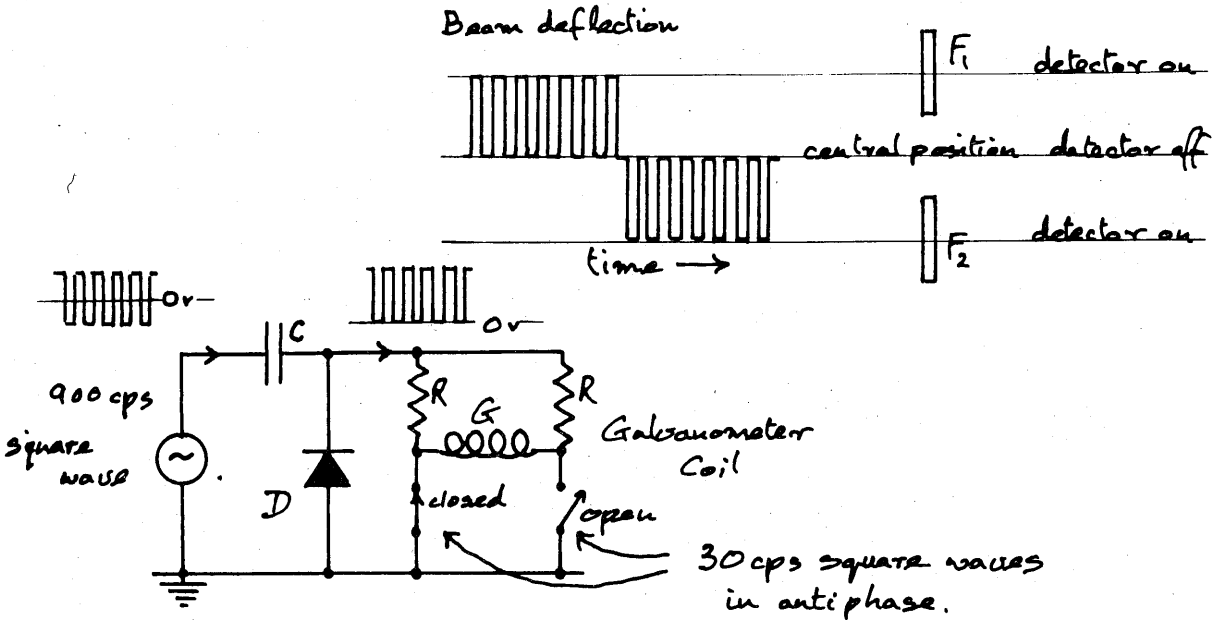

(a) Symmetrical drive circuit.

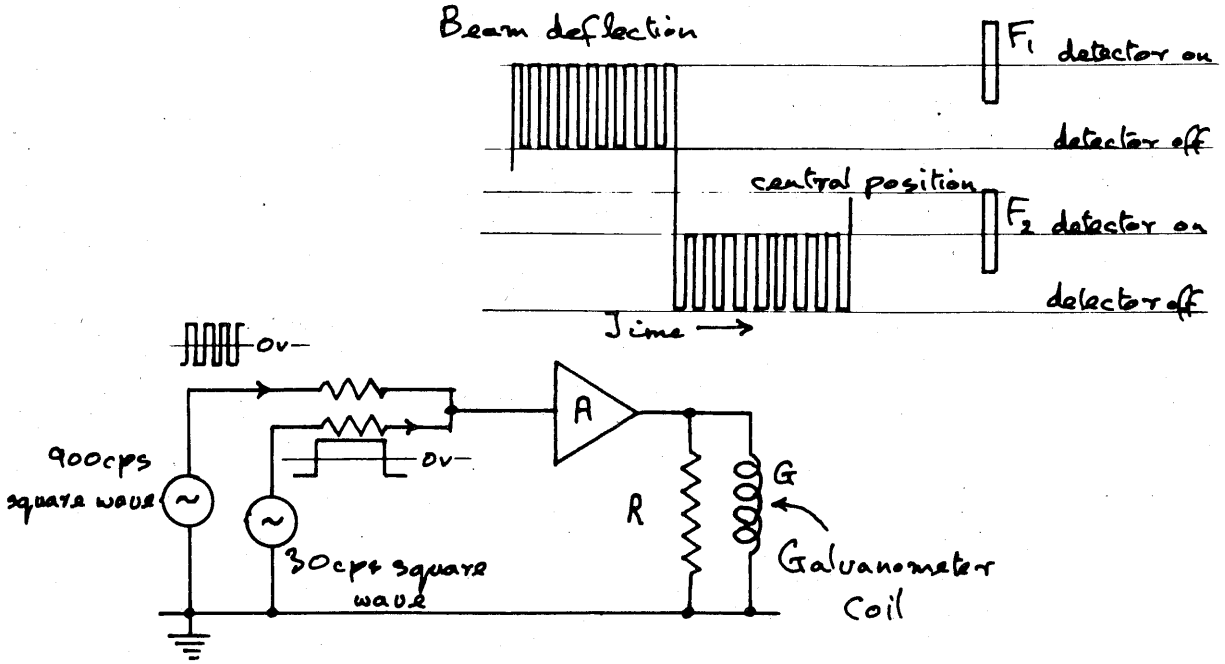

(b) Asymmetrical galvanometer drive circuit.

Fig 6.5 Galvanometer drive circuits.

An alternate form of drive is shown in (b). It will be noted that the mechanical zero of the galvanometer no longer corresponds to the position for zero signal at the detector (asymmetrical drive). Furthermore the detector zero occurs for a different position of the galvanometer in each channel. Although this mode of operation is more complex than that described above it gave better performance on both flat and reentrant surfaces for reasons which are dealt with more fully later (7.6.5). The complete circuits Fig. 6.6 and 6.7 each consists of a phase adjuster T_{24} which derives a 900 cps sine wave from the master oscillator. This allows synchronisation of the signal from the detector, whose phase is determined by the motion of the galvanometer mirror M_3, with the phase sensitive rectifier reference pulses (5.10.1). The sine wave is then amplified in a circuit which employs shunt voltage feedback (Fig. 5.6 b) and converted to a square waveform by the clipping action of Rd_8 and Rd_9. The amplitude of the square wave is thus determined by the quiescent current in R_{82} and R_{83} which have high stability. The 900cps square wave is now available from a low impedance source.

In the case of Fig. 6.5a the alternate switching of each end of the galvanometer coil is achieved by switching T_{29} amd T_{30} on and off with 30cps square waves derived from the emitters of T_{20} and T_{23}. In order to accomplish this the two resistors R_{85} and R_{86} are required which unfortunately increases the power consumption. The circuit draws a quiescent current of about 120 mA which represents more than half of the consumption of the entire pyrometer system.

In the circuit of Fig. 6.5b a 30cps square wave from T_{20} is added to the 900 cps square wave and amplified by an OC22. The function of the other OC22 is to predict the dc level at the output and yet enable current drive of the galvanometer if required because of the feedback action of the 5000 μF condenser.

In this form of drive there is only dissipation of power in the galvanometer coil itself. The circuit still runs at a high quiescent level of 100 mA however, because the galvanometer mirror undergoes a larger 30cps swing than previously.

6.6. Development of the circuit

The development programme for the electronic system is shown in Fig. 6.8. The circuit was assembled on the traditional breadboard at the outset and this was used for many of the measurements described. During the development, individual battery supplies were used for the various circuit blocks and as each section of the circuit was completed it was added with suitable decoupling networks to the breadboard which was driven from a transistorised power supply unit. When the circuit was completed the power pack was replaced by a unit suitable for ac mains and/or battery operation.

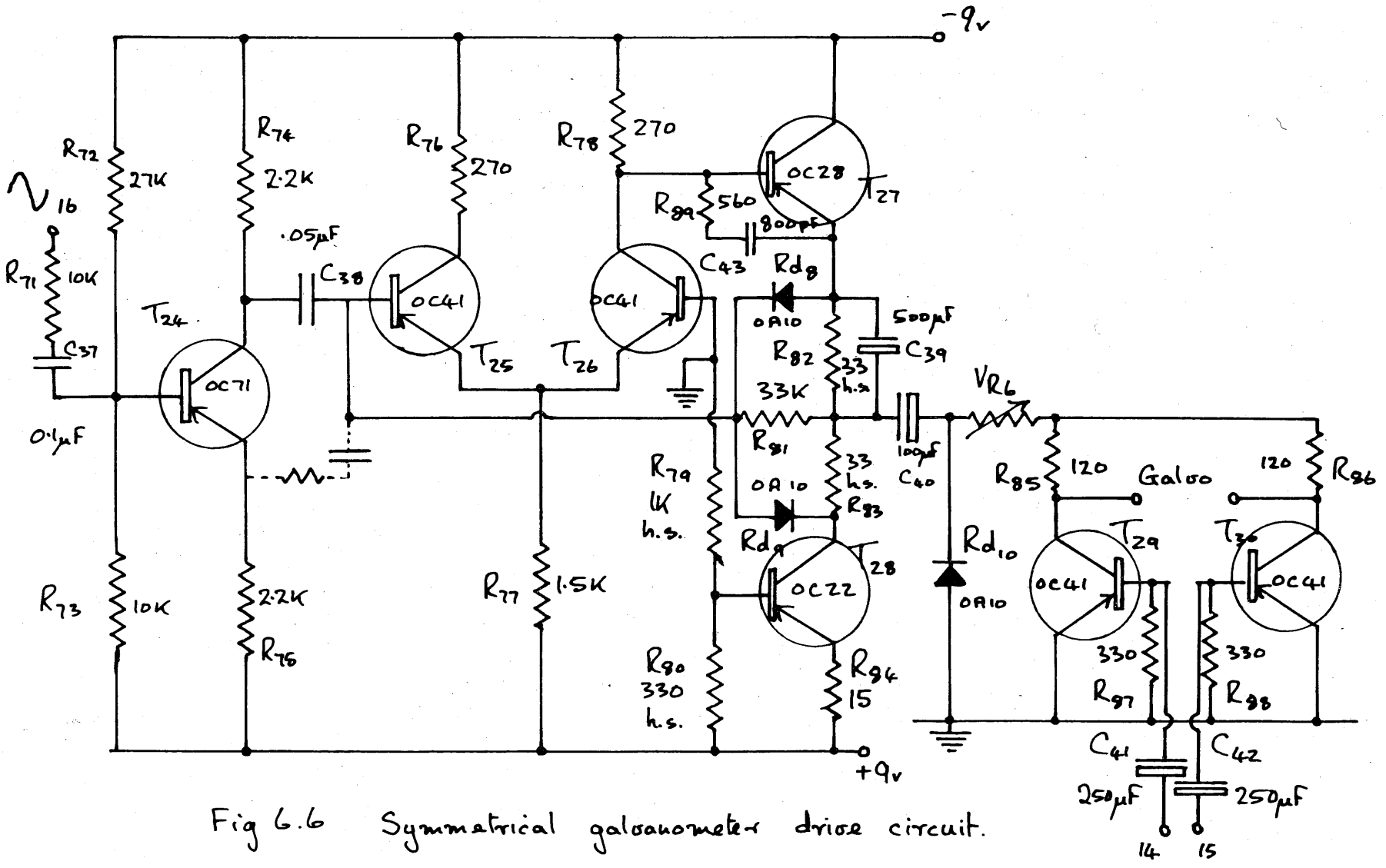

Fig 6.6 Symmatrical galvanometer drive circuit.

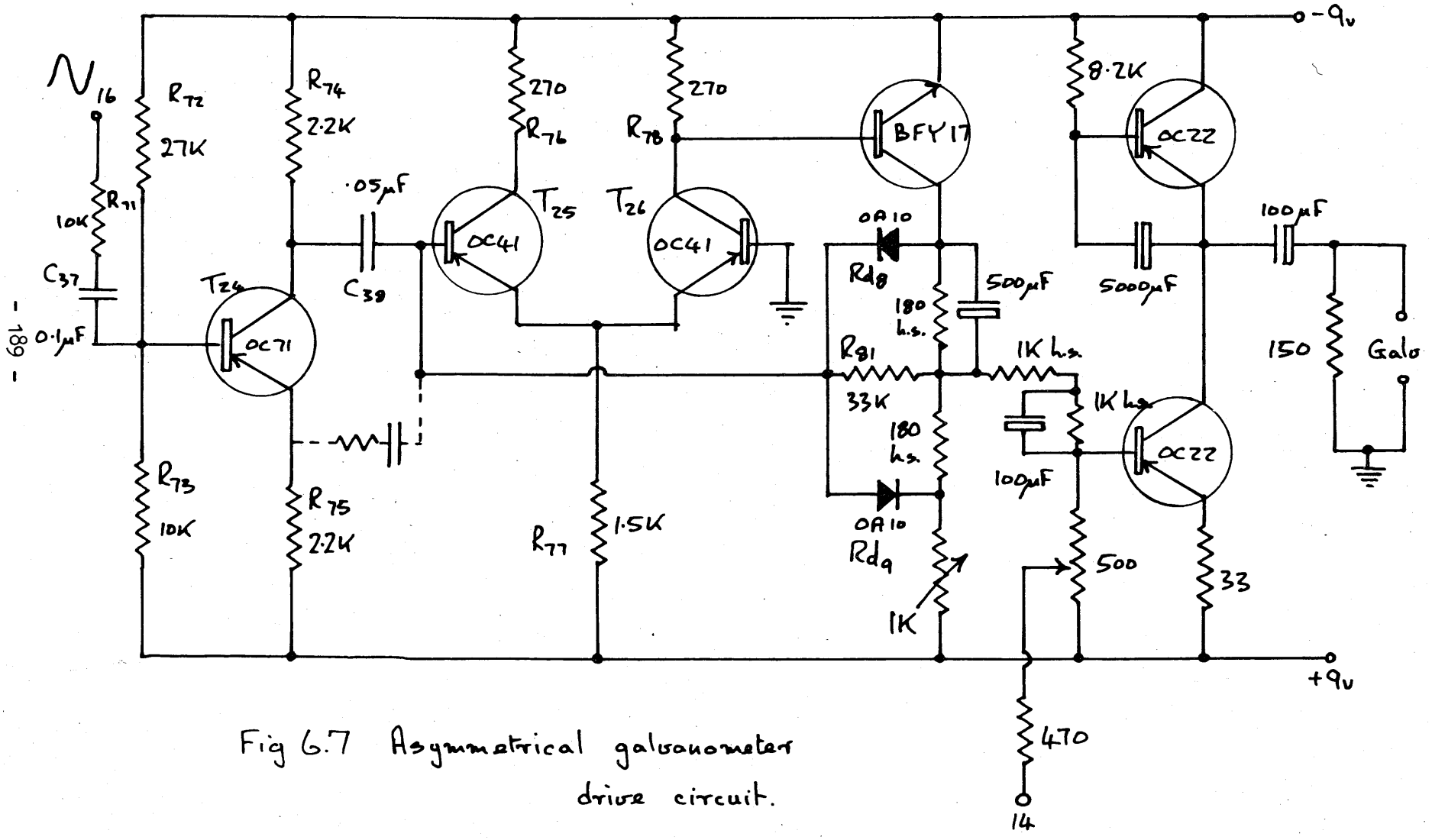

Fig 6.7 Asymmetrical galvanometer drive circuit.

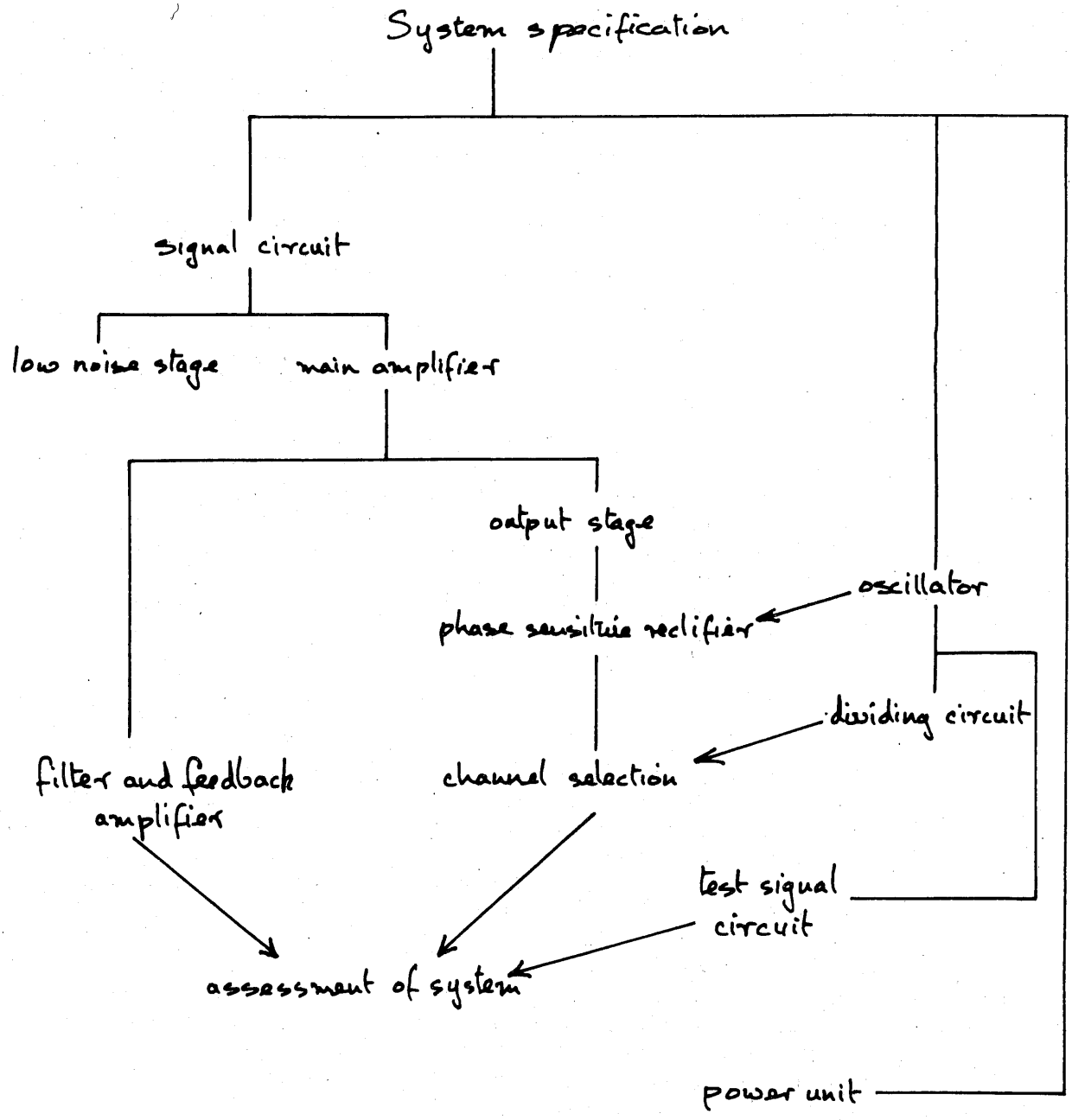

Fig 6.8 Development programme for electronic system

The entire circuit wiring was now reproduced in a suitable case. For this purpose the circuit was divided into seven blocks as follows.

(i) signal amplifier

(ii) feedback amplifier

(iii) phase sensitive rectifier and channel selection

(iv) oscillator and dividing circuit

(v) supply distribution

(vi) galvanometer drive

(vii) stabilised supply.

Each block was assembled on a Lektrokit plug in board fitted with high quality connectors. The mating sockets were supported in such a way that routine servicing of the unit was straightforward. The additional facility of range change and zero suppression was included in the new system providing four expanded ranges of 200-400μA, 400-600μA, 600-800μA, 800-1000μA. This enabled accurate measurements of small temperature differences to be carried out.

6.7. Supply line circuit

The distribution of the supply voltages is shown in Fig. 6.9. The auxiliary circuit draws a quiescent current of about 200 mA at + 9v and 150mA at -9v and the signal circuit draws about 15mA at -9v, giving a total consumption of 3.3 watts . Most of the auxiliary circuit current is drawn by the galvanometer drive unit and there is a large ac component of 70 mA peak to peak at 900cps and 120 mA peak to peak at 30cps. For this reason the auxiliary circuit is supplied directly from the power unit and reduction of the ac ripple is provided by the decoupling chains shown, which supply the various sections of the circuit from the numbered junctions. In this way the low noise input stage and the early stages of the amplifier are provided with maximum decoupling to supply line ripple. The sizes of the decoupling condensors were chosen to reduce the 900 cps ripple until it contributed a negligible amount to the signal at the bases of the transistors in the early stages of the signal circuit.

The performance of the decoupling network was satisfactory when the power pack was used because of its low output impedance (0.25Ω). In the other extreme, operation from dry batteries (4x4.5v) gave greater than 1% inaccuracy at signal levels near the minimum handling level.

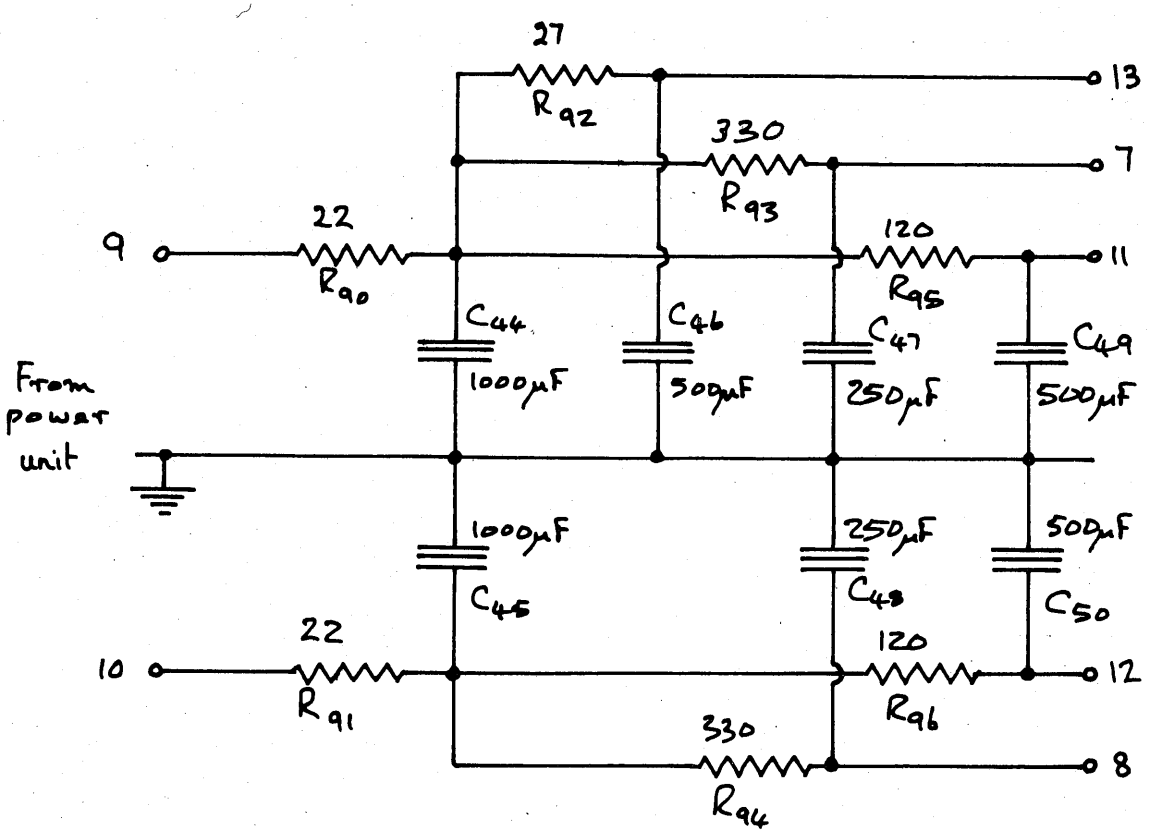

Fig 6.9 Supply distribution circuit

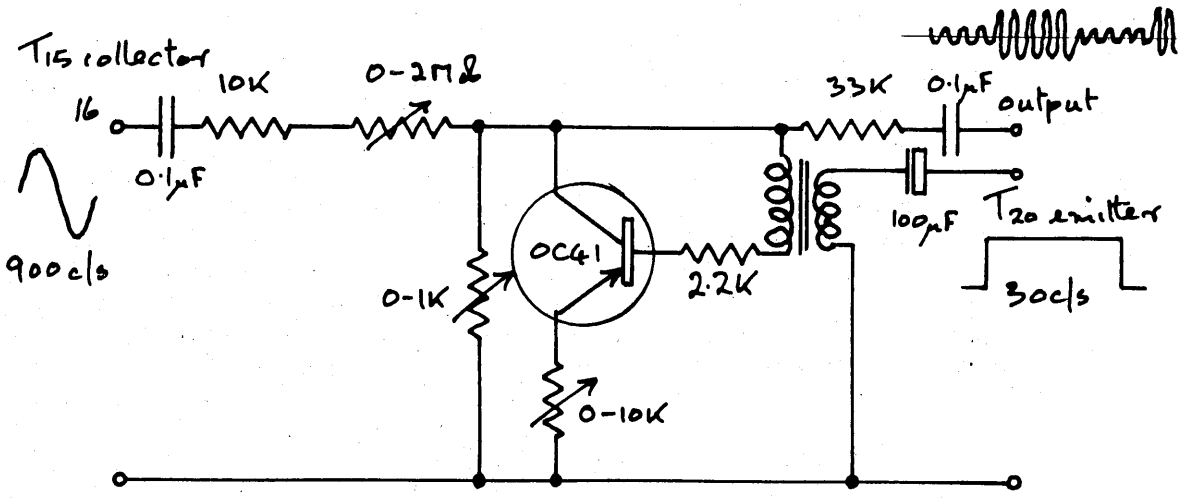

Fig 6.11 Signal simulation circuit.

It was decided to combine the required ac mains and/or battery operation by using rechargeable cells for the power supply unit. The cells used were nickel/cadmium with a source voltage of 1.4 volts/cell in the charged state. The charging circuit, Fig. 6.10, is so arranged that when the system is run from the ac mains, the cells are charged up to a trickle charge level. Provision is also made for charging of the cells when the system is not in use and not providing any current. In this case the zenor diodes Zd_1 and Zd_2 are used to prevent overcharging of the cells. The mains and battery supplies were both stabilised by a conventional circuit(4). This circuit has a measured output impedance of ¼ ohm.

6.8. Earth Connections

Considerable attention was paid to the connections of the common line throughout the system. Any 900cps ripple occuring on the common line adds to the signal in the same way as ripple on the supply line. Thus it would be inadvisable to return a common line from a circuit block in the auxiliary system to earth via the main amplifier common line because of the large ac current carried by the former. The recommended practice of connecting the common lines of each circuit to a single point was adopted. This point was then attached to the centre tap on the battery and connected to real earth. In this way circuit blocks drawing a large current did not interfere with the low signal sections of the circuit.

The phenomenon of earth loop induced signals in which a dc or ac loop in the system acts as an aerial to electromagnetic radiation was also carefully avoided were possible. Such a loop would introduce unwanted 900 cps from the oscillator and 50 cps from the ac mains.

6.9 Testing the complete electronic system

6.9.1 The completed circuit was tested for accuracy of control over the specified control range with the aid of a circuit which could be made to simulate any ratio in the range 0 to 1 at any level from 0 to 500 mV. Simulation of typical signals was used so that the electronic system could be developed while the optical system was undergoing construction. The circuit shown in Fig. 6.11 produces a signal level determined by VR_{11} and a signal ratio determined by VR_{13}. It was driven from the oscillator in the system to provide synchronisation with the phase sensitive rectifier reference pulses and the resistor VR_{13} was switched in and out by the transistor T_{37}, which was synchronised to the channel selection switch, to provide the second channel level.

The following Table X and Fig. 6.12 show the small variations, which occur in practice for a signal ratio of unity, as the signal input level is varied over the entire control range for various values of the gain of the feedback amplifier determined by R_{45}. The output current was measured on a precision moving coil ammeter.

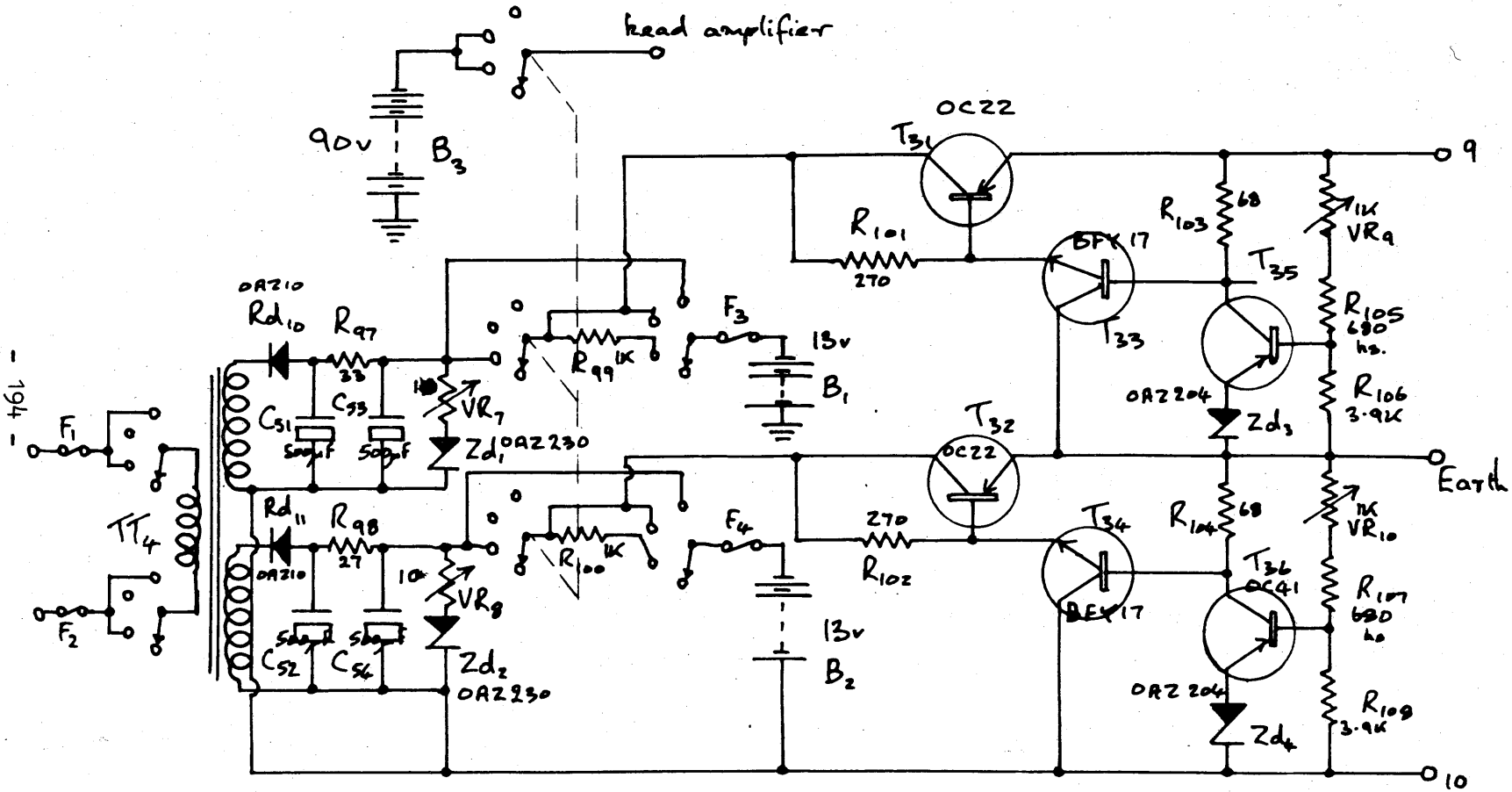

Fig 6.10 Charging circuit and stabilised supply

TABLE X

Electronic system control range

Input T_2 base	Output current R_{45} = 10KΩ	Output current R_{45} = 100KΩ	Output current R_{45} = 2.1 MΩ
0.1 mV	816 μA	972 μA	990 μA
0.2	902	984	993
0.5	934	989	990
0.7	943	989	994
1	950	993	991
2	958	991	991
5	967	992	993
7	973	993	993
10	973	992	993
20	982	998	994
50	992	997	996
70	996	998	994
100	998	998	994
140	999	997	996
200	1001	998	996
oscillation and overload			

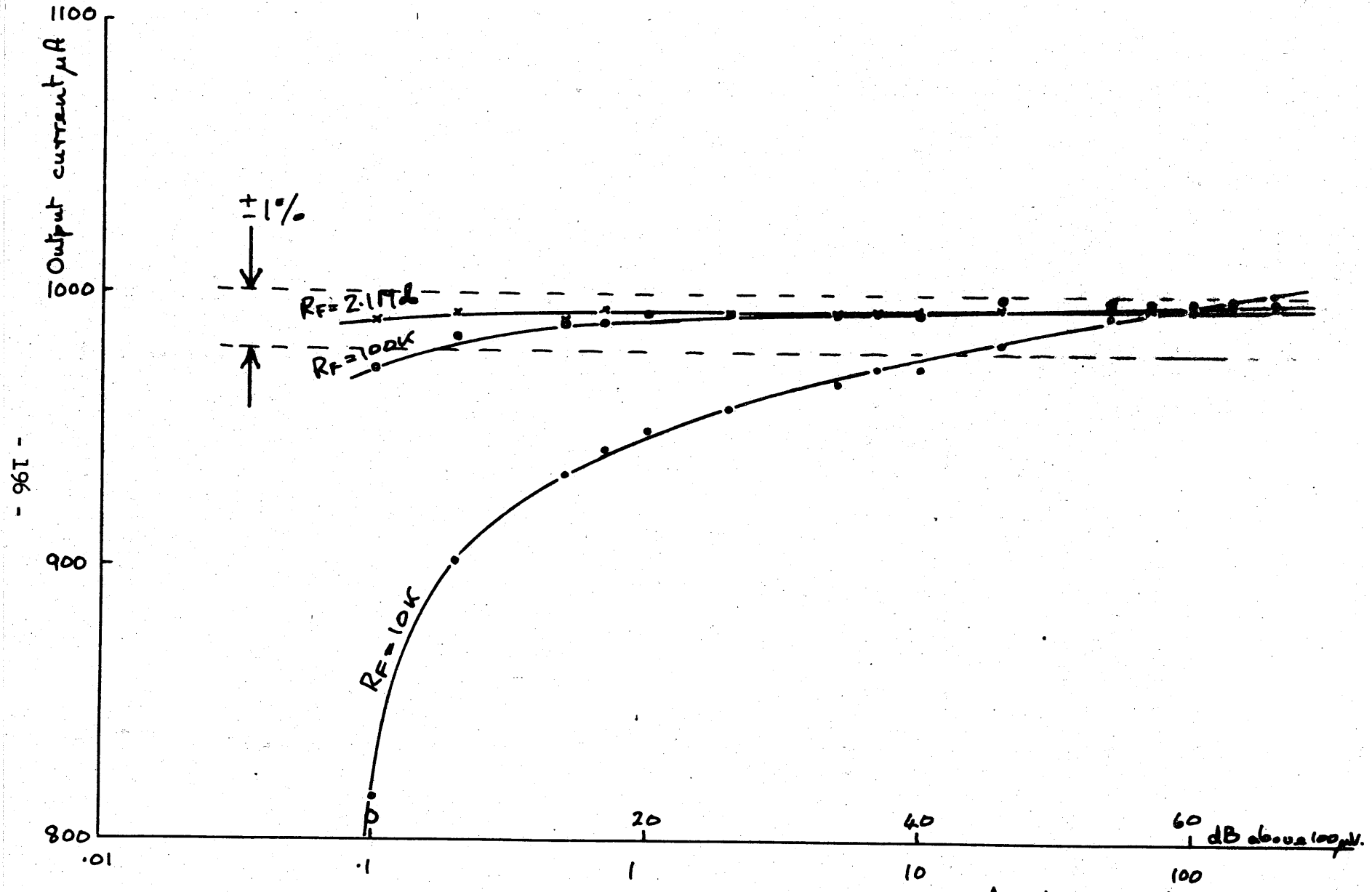

Fig 6.12 Electronic system control range.

6.9.2 Temperature coefficient

The susceptibility of the circuit to ambient temperature changes was measured in the range 5° to 50°C using a temperature controlled cabinet. The measurement was carried out at a signal ratio of unity to remove any errors introduced by the signal simulation circuit which was not designed to be temperature independent. Table XI shows that a change in ratio of about 1.2% occured over the entire temperature range.

Table XI

Temp °C	Ratio
5	912
10	910.5
15	908
20	907
25	905
30	906
35	904
40	901
45	896
50	894

It will be seen that the temperature coefficient of the control loop is .035% per °C at 20°C

The coefficient is attributed to the drift at the input of the feedback amplifier due to the differential temperature coefficients of the longtail pair T_{11} and T_{12}. An improvement by a factor of 2 was later obtained when two silicon transistors were inserted at this point. The coefficient corresponds to a change in reading of 1°C at 300°C for an ambient change of 10°C which is quite acceptable.

6.10 Conclusion

The source of the 900 cps carrier frequency has been designed so that it is largely dependent on the characteristics of a single L/C circuit. Thus, the carrier frequency is stable and should vary only slowly with temperature. The stability becomes important both when the

dividing mechanism and the galvanometer drive waveform are considered. In the first case, an unstable carrier frequency would cause the dividing circuit to be unstable and in the second case the amplitude of the galvanometer would be unstable due to its variation in sensitivity with frequency. Considerable attention has also been devoted to the stability of the galvanometer drive circuit, again to avoid fluctuations in galvanometer amplitude for the reasons discussed in Chapter 7.

The provision of stable supply lines has been emphasised. Apart from aiding the stability in the above circuits, this also provides the reference level for the ratio circuit. In this connection the stabilised supply represents the added complication which must be introduced as a result of the departure from the ideal null system described in Chapter 5.

Finally, the completed circuit was tested and shown to be capable of handling an input signal range of 1000:1. In addition a temperature coefficient of -.035% per ^{o}C at 20^{o}C has been measured.

6.11. References

1. R.C. Foss and M.F. Sizmuir. Wireless World, 1962, 68, (11), p.535, p.595

2. P.J. Baxandall. Proc.IEE., 1959, 106, Pt.B, Suppl.No.16, p.748

3. RACAL - Digital frequency meter. (type SA520), 1963

4. D.J. Collins. Electronic Eng., 1964, 36, p.435

CHAPTER 7 - CONSTRUCTION, ASSEMBLY AND ASSESSMENT OF THE INSTRUMENT ON MAGNOX CANS

Introduction

The general construction, component mountings and optical alignment are described. After combining the optical and electronic systems, an assessment of the instrument is carried out along the lines of the specification of Chapter 1. A calibration on a black body and magnox is performed, the ultimate sensitivity is measured and the performance examined on a magnox can. It is shown that although the instrument is sensitive to the surface geometry of the can, measurement of fin root temperature is possible if the operational wavebands are carefully chosen.

7.1 The optical system

7.1.1 General construction

The principles of the optical system and the relative positions of the optical elements have been considered in Chapter 4. The detailed mechanical design is now discussed with particular attention being paid to the mounting and fine adjustment of the components. A schematic of the complete system is shown in Fig. 7.1.

It was decided for the prototype instrument to use a box construction for the optical modulator. The large spherical mirror is attached to the front of this box and the whole assembly is rigidly bolted to a base plate to which is also attached the small convex mirror mounting. The material used for the chassis was duralumin on account of its strength, lightness and machining qualities.

The box is drilled and screwed together and all the optical element support members are attached with countersunk allen screws. The inside of the box is painted with a high absorbtivity paint to prevent multiple reflections internally of stray energy entering the system through the central holes in M_1 and M_4. Apart from this hole the box is light tight to prevent excessive background illumination of the lead sulphide cell. The optical axis was used as a reference in both the side and plan elevations.

7.1.2 Accuracy of mirror figures

The aberrations introduced by the optical system have been discussed in detail in Chapter 4. The aberrations are introduced because spheroidal surfaces have been used throughout for economic reasons, where ideally parabolic and hyperbolic surfaces were required. Superimposed upon the aberrations already discussed will be aberrations due to local departures

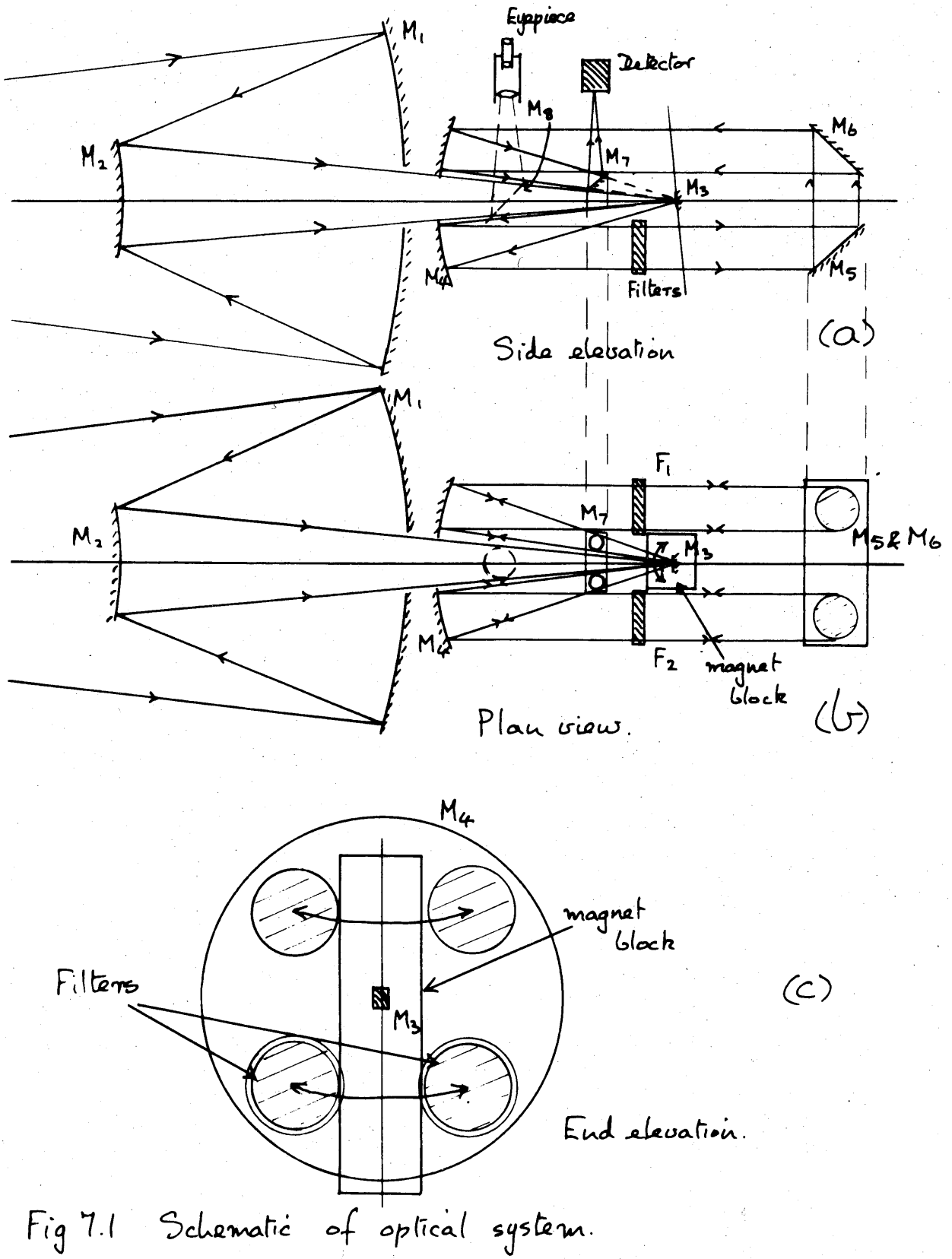

Fig 7.1 Schematic of optical system.

of the mirror surfaces from their expected shapes. These departures are measured in fringes, where a fringe refers to half the wavelength of green light. It is shown in Appendix G that if the maximum error in the figures of each mirror is 4 fringes per cm then the resultant aberrations introduced will be less than the spherical aberration in the system. A mirror figured to 4 fringes per cm can be quite thin by optical standards since a comparatively large degree of distortion can be tolerated. The thickness of the mirrors used is 4.8 mm for M_1 and M_4 and 3.2 mm for the rest apart from M_3 on the galvanometer which is only a few thousands of a cm thick. According to the manufacturers this mirror is figured to 2 fringes per cm in spite of its small thickness. All mirrors are surface aluminised glass, again apart from M_3, which is made from a special alloy.

7.1.3 Optical adjustments

An important feature of the ratio pyrometer is its ability to reduce considerably the effects caused by the variable parameters of the detector which prove troublesome in a single channel system (see Chapter 3). These are, briefly

(i) variation of sensitivity with temperature

(ii) variation of sensitivity over the sensitive area

To achieve indpendence of these parameters in practice means that the energy in both channels must fall on the same region of the sensitive area. Furthermore, the maximum sensitivity is achieved if the most sensitive region of the detecting element is used. This introduces the need for adjustment of the detector effectively in three perpendicular directions. It is inconvenient to combine these adjustments at the detector itself and only a simple vertical focusing adjustment is used to render the images in the two channels coincident. Longitudinal and axial adjustment is most readily incorporated into the back mirror system M_5 and M_6. This gives the additional advantage of being able to correct for any small errors in the assembly of the mirror M_3 to the galvanometer during manufacture and also a larger range of adjustment is more readily obtainable. Longitudinal adjustment of the galvanometer mounting is included to provide means for obtaining parallel beams between mirrors M_4, M_5 and M_6.

The vertical adjustment of the detector consists of a paxolin sleeve for electrical insulation purposes mounted inside a split ring assembly. The detector is held firmly in the desired position by this means. Three point kinematic supports based upon the cone, vee and flat principle (1) are used for the back mirror adjustment. The cone locates the mirror in the plane of its surface (two degrees of freedom); the vee prevents rotation about a perpendicular axis (one degree of freedom); and the flat combined with the other two prevents rotation around the remaining perpendicular axis (two degrees of freedom). To remove the final degree of freedom a

spring mounting is used at the centroid of the triangle joining the three supports. The mirror can thus be adjusted independently in both vertical and horizontal planes to provide axial and longitudinal adjustment of the image at the detector.

The presence of these adjustments reduces the need for close tolerances on the angles of inclination of the remaining fixed components thus simplifying the assembly and alignment of the system.

The optical sighting means requires a mirror which can be inserted into the path of the radiation. This mirror is carried on a hinged optical arm which can be withdrawn when not in use. A locating stop is provided for the mirror in the viewing position and when not in use the mirror is located at the side of the instrument so as not to interrupt any of the beams.

7.2 Mounting of components

7.2.1 (i) The spherical mirrors

These mirrors are all mounted in a similar manner. The method consists of a short cylinder of suitable diameter with a flanged end against which the mirror may rest. The clearance is made small, there being no danger of damage if the ambient temperature increases, because of the differential expansion of glass and duralamin. The cylinder is bolted to a back plate which carries sponge rubber discs, which locate the mirror against the flanged end of the cylinder. Three point fixing of the back plate to the pyrometer chassis is used.

(ii) The flat mirrors

These are attached with araldite adhesive to backing plates, which are themselves bolted to the chassis. This enables them to be replaced easily and efficiently without damaging the supporting member.

7.2.2 The galvanometer mounting block

The galvanometer is mounted vertically through the hole in the back of the horseshoe magnet used for the measurements described in Appendix F. The magnet has the soft iron pole pieces attached to its faces with Araldite adhesive, Fig. 7.2, and it is itself glued to the mounting block. To isolate the galvanometer from the chassis a small air gap exists at the pole piece and the top and bottom are supported with a nylon plate and bush respectively. The galvanometer is a push fit into these supports which has proved satisfactory. Electrical connections are made via two spring loaded pins which slide inside tufnol inserts mounted in the block. The angle of inclination is arranged to provide adequate deflection of the beams in the beam modulating system out of the way of the incoming energy. The fixing holes at the base are slotted to enable longitudinal adjustment so that the galvanometer mirror may be located at the optimum position with respect to M_4.

7.2.3 The detector housing and M7 mounting

The infra red detector inside its paxolin sleeve is supported on a rigid cross member which is attached to the side walls of the box.

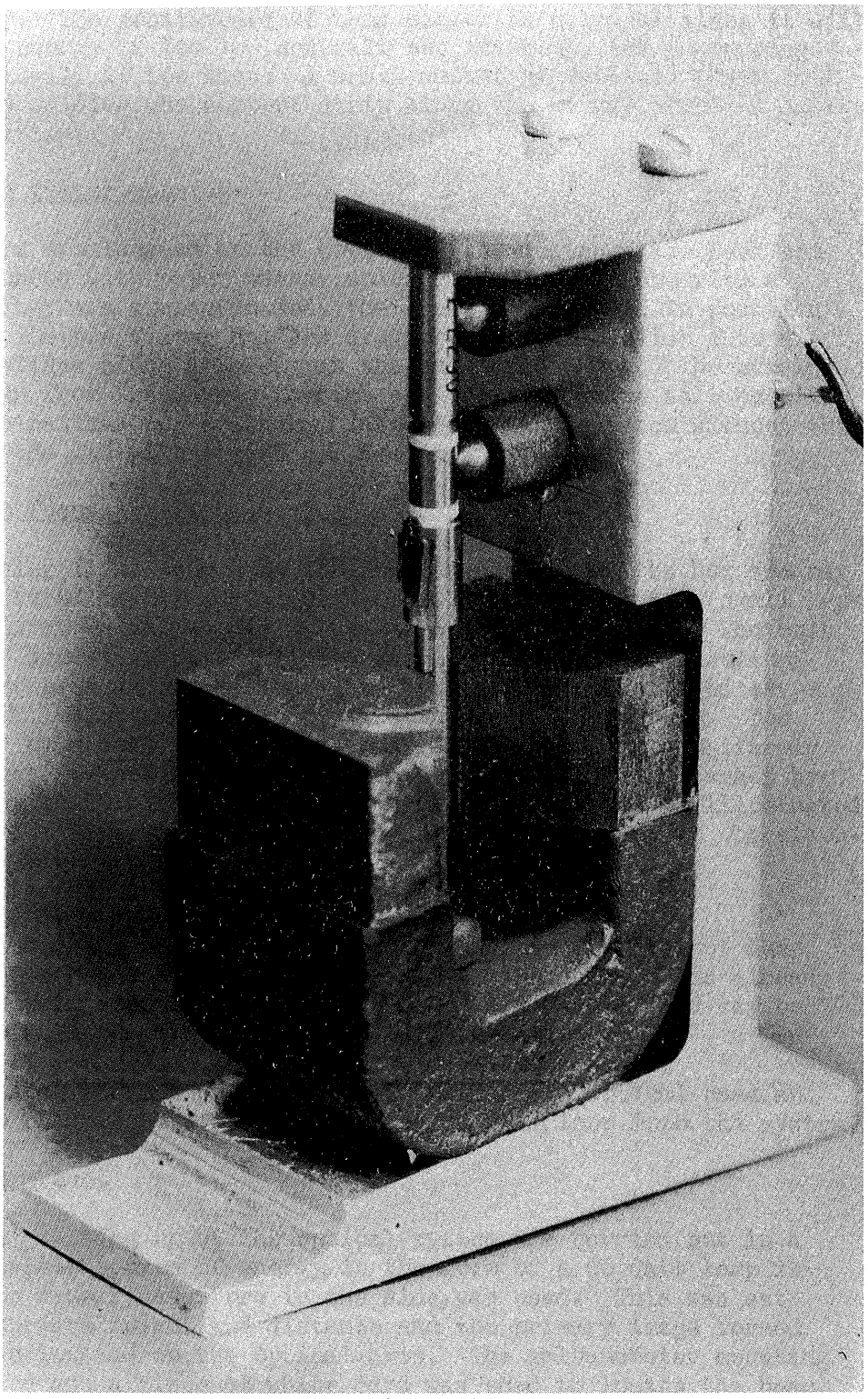

Fig. 7.2. Optical modulator and mounting block

The mounting of M_7 is suspended from the detector using a 3 mm thick duralamin strip. The positioning of this mirror is critical since it will block incoming energy if too low and will not intercept the converging beams satisfactorily if too high. A small amount of vertical adjustment is available by sliding the support strip along the keyway provided before locking in position.

7.2.4 The filter housing

The filters are located at the bottom of the instrument. Each combination is mounted with paper washer spacers in a small tube with a flanged end. They are spring loaded, the spring being held in position by a circlip. The two filter holders are screwed side by side into a housing which slides along a keyway at the base of the box. The housing can be withdrawn from the keyway through a slot in the side wall enabling the filter combinations to be inserted into the optical system without the need to remove the lid of the system. See Fig. 7.3.

7.2.5 The focussing light source

The focussing light source is attached to the lid of the box and may be raised or lowered inside its support bush. It consists of a small lens capped bulb against which two dry batteries are spring loaded. The bulb is turned on by screwing the end button which completes the circuit to the bulb via the case of the device. The size of the target area is defined by a small slot machinedin a plate in front of the bulb. The slot is covered by a small disc of frosted glass to provide a uniformly illuminated light source. When the light is projected to the target by means of the auxiliary mirror M_8 a small area of the target is illuminated, which is the small area viewed by the instrument itself when in operation.

7.3 Electrical connections

The leads from the galvanometer are routed along the base of the box to a twin screened socket on the back wall. The detector is already provided with a twin screened outlet socket and a screened lead may be plugged to this when the lid of the case is in position.

A single earth connection only exists between the optical case and the electronics chassis to avoid introducing an earth loop into the system.

7.4 Optical alignment

The initial setting up of the optical system was carried out in a darkroom. A visible source of energy, in the form of a 60 watt lamp in a metal box with a small aperture in the side, was used. This was set up at the appropriate height and distance and the primary image formed by M_1 and M_2 was located on the optical axis. The galvanometer mounting was then inserted and a piece of white card was used to locate the beam of light reflected from the galvanometer mirror M_3 onto the concave mirror M_4. The galvanometer was rotated by hand to project the beam from side to side into each channel. The dimensions of the beam striking M_4 corresponded to the diameter of the central hole through which the beam entered before striking the galvanometer and an image of the objective mirror M_1, with the shadow cast by M_2, was obtained. The position of the galvanometer

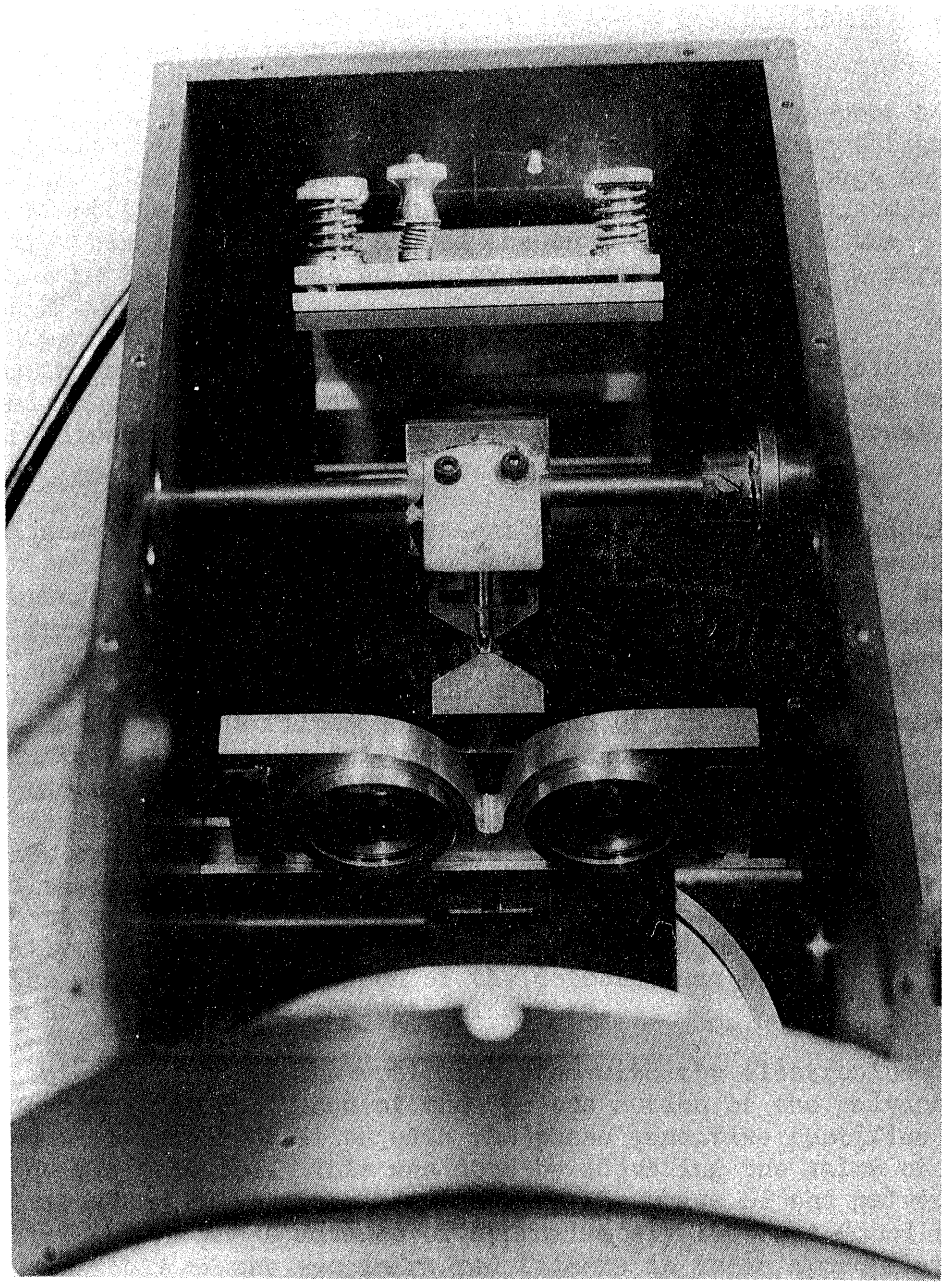

Fig. 7.3. View towards rear of instrument with M_7 and detector removed

mounting and M_5 were now adjusted until the beam of light leaving M_4 arrived back after reflection from M_5 and M_6 at the appropriate position which was the same distance from the optical axis and vertically above its point of departure. (See end elevation Fig. 7.1c). Adjustment was continued until this applied to the beam for each channel.

The angled mirror M_7 was now inserted and lowered in its support as far as possible, without intercepting the incoming energy striking the galvanometer mirror M_3. Fine adjustment of M_6 enabled the secondary image to be suitably located at the detector housing. With these adjustments completed the beam of light was then followed around the entire system with the piece of white card to ensure that no energy was lost anywhere at a mirror's edge.

The focussing mirror M_8 was assembled on its slide and the position of the internal lamp housing adjusted, until a light spot was obtained on a piece of card directly in front of the aperture forming the external light source.

The final stage of the optical alignment consists of the fine adjustment of the image on the sensitive area of the detector. It is necessary initially, to ensure that the images from each channel are coincident so that the same portion of the sensitive area is being used by each waveband and secondly, that the most sensitive region of the detector is being used. This adjustment is best carried out in conjunction with the electronic system. After inserting the filter housing devoid of filters, the preset resistor V_{R6} in the galvanometer drive unit was adjusted to give the correct amplitude of vibration, which was judged visually from the position of the light beam passing through the filter housing. The detector output waveform was now examined at T_2 base and the height of the detector was adjusted until the ratio of the signals for each channel was independent of the adjustment of M_6. This ensured coincidence of the image for each channel. Finally, the maximum signal was obtained by adjusting M_6 which ensured that the most sensitive region of the detector was being used. This completes the alignment of the optical system.

Complete intermarriage of the optical system with the electronics was achieved by adjusting the phase of the 900 cps motion of the galvanometer mirror so that synchronisation with the phase sensitive rectifier reference pulses was obtained. This was done by adjusting the value of C_{38} in the galvanometer drive circuit to advance the phase of the galvanometer drive waveform. A phase advance of approximately 180° was found to be necessary. Assembly of the two infra red filters in their appropriate housings completed the alignment and adjustment of the pyrometer.

7.5 Temperature coefficient of head unit

The temperature coefficient of the head unit was measured with no filters in the pyrometer. This gave equal signals in each channel and

the ratio was thus independent of the target material removing the need for fine temperature control. Initially a large temperature coefficient of + 0.25%/°C was measured. Examination of the signal waveform showed that this was due to a large increase in the amplitude of the galvanometer at 900 cps. This was found to be due to a reduction in the viscosity of the damping fluid causing a marked decrease in damping with temperature. The performance of the instrument was affected because overshoot occurred between channels, which was a function of temperature. The effect was reduced by careful adjustment of the galvanometer zero but a significant reduction was only possible when a thermistor correction was applied across the galvanometer coil. In this case the temperature coefficient was reduced to .02%/°C at 20°C although the value was still sensitive to the zero position of the galvanometer.

The temperature coefficients of the head unit and electronic system combine to give -.01%/°C at best and + .05%/°C at worst depending on the initial setting of the galvanometer zero position. The worst value obtained corresponds to a 1.5°C change in reading at 300°C for an ambient change of 10°C which is quite acceptable.

7.6 Assessment of instrumental accuracy and performance

7.6.1 Once the completed optical and electronics systems were operational a logical sequence of tests was carried out. The object of these tests was to verify the design of the instrument and to make suitable modifications were necessary to improve the performance to an acceptable level. The items of performance presented below were examined and when modifications were necessary these were incorporated before proceeding to the next stage.

(i) calibration on a black body
(ii) calibration on magnox
(iii) ultimate detectivity
(iv) performance on re-entrant surfaces of fuel can

7.6.2 Calibration on a black body

The pyrometer system was calibrated using the black body cavity of the spectral emissivity apparatus described in Appendix A. The calibration was carried out over the temperature range 200° to 600°C. The temperature of the cavity was measured to within 1° centigrade but allowing for the deterioration in calibration of the monitoring thermocouples and non uniform temperature distribution an accuracy of ± 1% is placed on the measured black body temperature. The pyrometer was used on the expanded scale ranges (see 6.6) which enabled the output to be read to the nearest microamp.

The pyrometer was calibrated near the centre of its range by adjustment of R_{V_3} so that at a black body temperature of 327°C a reading of

327 μA was obtained. The temperature of the black body was then decreased by approximately 50°C steps from 550°C, until a temperature where insufficient signal was available to provide a readable output was reached. The first calibration curve which was obtained is shown by the broken line in Fig. 7.4. The decrease in slope at the lower end is explained by the presence of a small ripple on the earth and supply lines of the electronic system. The ripple which possessed a fundamental frequency equal to the oscillator frequency added a constant level to each channel. Thus as the target temperature decreased, causing a decrease in the ratio of signals in each channel a positive error in the displayed ratio occurred. The effect was reduced by careful reconnection of the earth points of each circuit block as discussed in 6.8. A repeat calibration curve with the above fault removed is also shown in Fig. 7.4.

It can be seen that the calibration is very nearly linear over the range 200° to 600°C. This was predicted by equation 2-10 over the central portion of the curve of Fig. 2.6 where it was assumed that the operating wavebands were of negligible width. The theoretical calibration curve, which is obtained using the detector response curve of Fig. 3.1, the transmission curves for the filter batch of Fig. 4.4 and black body tables (2) is also shown in Fig. 7.4. The discrepancy between this curve and the experimental values may be due to a departure of the detector or the filters from the manufacturers characteristics or a small difference in reflectivity of the mirrors in the optical system at the operating wavebands. However, no attempt was made to discover the cause of the discrepancy at this stage since by adjustment of the calibration poteniometer (Rv_3), coincidence of the two curves to within a few degrees above 300°C was obtained. It can be seen that agreement between pyrometer indication in μA and black body temperature in °C to within $\pm$ 5°C is obtained for a pyrometer sensitivity of 1 μA per °C.

7.6.3 Calibration on magnox

The calibration setting of the pyrometer was left at the above setting for a black body target and a magnox specimen was mounted in the spectral emissivity measuring apparatus, which was modified to take a suitably shaped specimen of any metal. The magnox specimen used was cut from a piece of fuel can splitter material (type AL80) and cleaned with citric acid and warm water as recommended during fuel element preparation(3).

The calibration was carried out over a period of 5 hours and consisted of a single temperature cycle from 250°C to 550°C and back to 250°C. In this calibration the specimen temperature was measured by a thermocouple inserted below the surface of the magnox. From the temperature gradient existing across the magnox holder, between the black body enclosure and the specimen thermocouple, (see Appendix A) it was deduced that the surface temperature was between 1° and 2°C lower than that indicated by the specimen thermocouple. Thus the absolute accuracy of the calibration has the additional 1 to 2°C uncertainty imposed upon it as well as the 1% error due to the thermocouple calibration and non uniform temperature distribution in the black body.

TABLE XII

Comparison of Theoretical and Experimental Black Body Calibration Curves.

Temperature °C	Pyrometer output μA	Theoretical Ratio*
200	200±5	
227		0.465
235	238±2	
260	262±2	
272	276	
277		0.561
313	313	
327	326	
368	365	
377	373	
419	415	
427		0.823
439	436	
477		0.920
486	482	
517	513	
527		1.001
540	538	
577		1.090
591	600	
627		1.185

*These values have been normalised for plotting in Fig.7.4 such that a ratio of unity occurs at 653μA which is the output obtained from the pyrometer for a signal ratio of unity supplied by the test board.

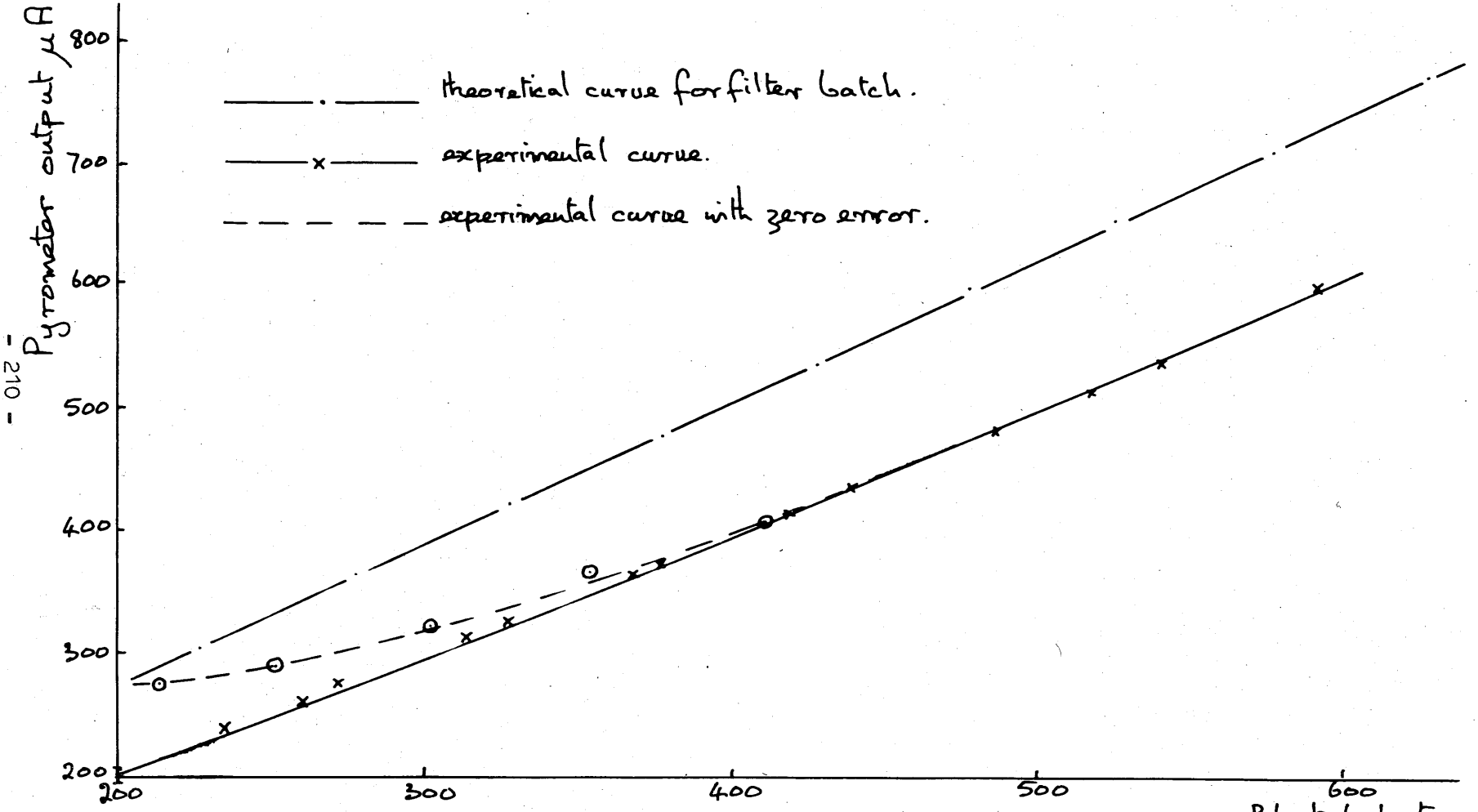

Fig 7.4 A comparison of theoretical and experimental black body calibration curves.

The results obtained are illustrated in Fig. 7.5. Since the running time of the experiment was about 5 hours, an indication of the drift of calibration with oxidation in air is obtained (10°C). It is known from other work that an increase in total emissivity of magnox due to surface oxidation by a factor of up to 1.5 is to be expected under the above conditions (4).

A close comparison of the calibration curves on a black body and magnox shows an increase in slope of approximately 6%. This is disturbing since it implies an emissivity ratio at the operating wavebands of 1.06 which will introduce errors on the re-entrant surface of a fuel can as discussed earlier 2.6. This phenomenon is dealt with later in more detail when the performance of the pyrometer on the re-entrant surface of a fuel can is discussed.

7.6.4 Ultimate sensitivity of the pyrometer

The ultimate sensitivity of the pyrometer system is the result of a compromise in the choice of various parameters. These were discussed in detail when the choice of the detector was considered in Chapter 3. The more important contributing factors are:-

(i) the small target size required

(ii) the width of the operational wavebands

(iii) the sensitivity of the detector

(iv) the emissivity of the target material at the lower waveband.

The first two parameters are fixed in the instrument. The third is fixed if an ambient temperature is specified and the fourth is fixed if a target material of known emissivity is used. For these reasons therefore, the sensitivity of the pyrometer was measured at an ambient temperature of 20°C with the black body as target.

For this purpose a recording of the pyrometer output was obtained using a potentiometric chart recorder with a nominal response time of 1 second. Recordings were obtained at black body temperatures of 195°C, 240°C, 292°C, 345°C and 416°C. The recordings are illustrated in Fig. 7.6 a to e. The scale is 2°C per division for all traces except 7.6a which is 10°C per division. The sinusoidal oscillation of the record, which was made at a speed of 2.5 cm per 1 minute, is due to the temperature cycling of the black body which was controlled with an on/off temperature controller. The oscillation has a peak-to-peak value of approximately 5°C at all the above temperatures. It can be seen that the sensitivity of the pyrometer is about 2°C at 240°C deteriorating to about 10°C at 195°C. Above 240°C the sensitivity improves until at 416°C it is limited not by the pyrometer at all but by the noise level of the chart recorder.

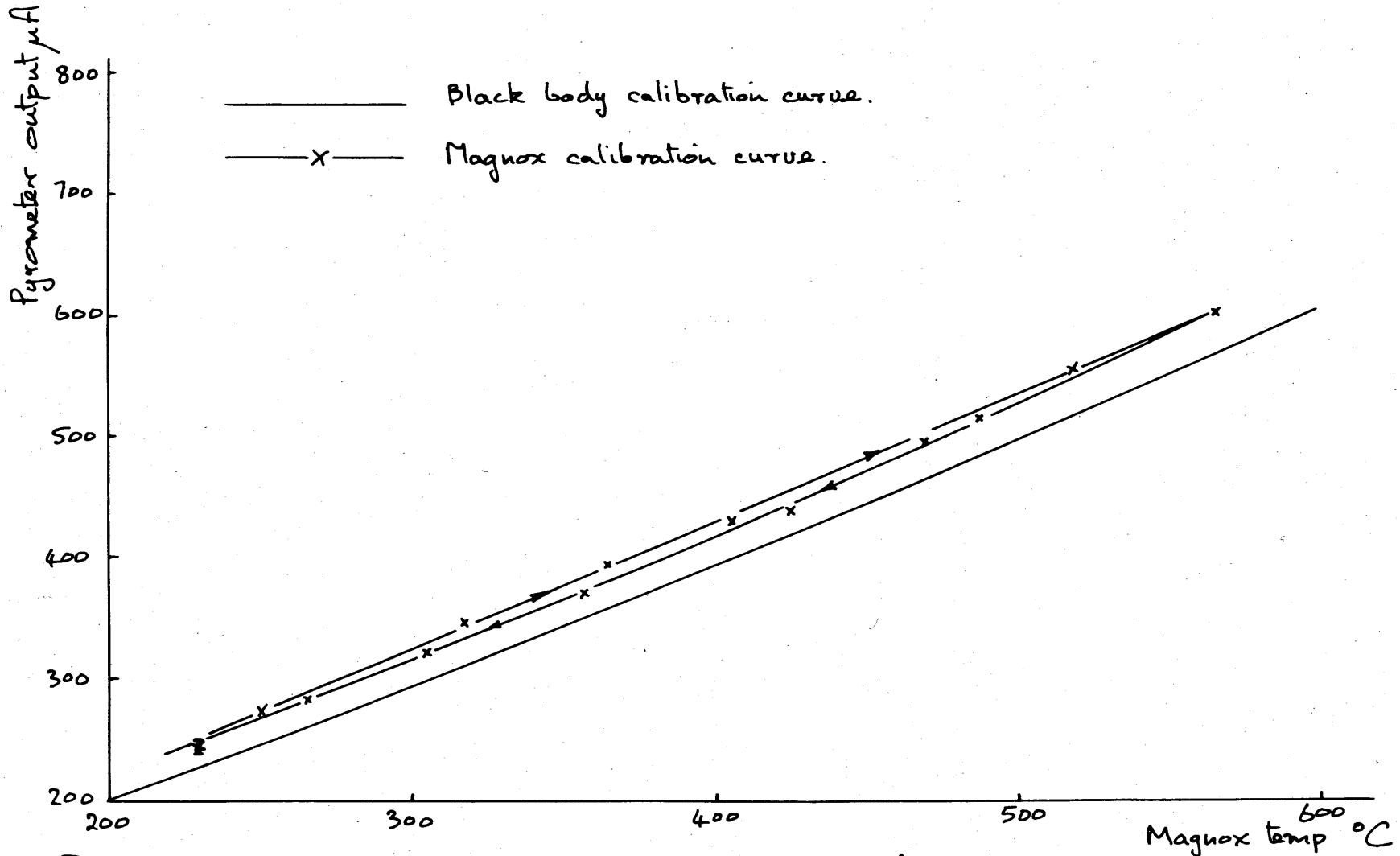

Fig 7.5 Calibration curve for magnox, type A180.

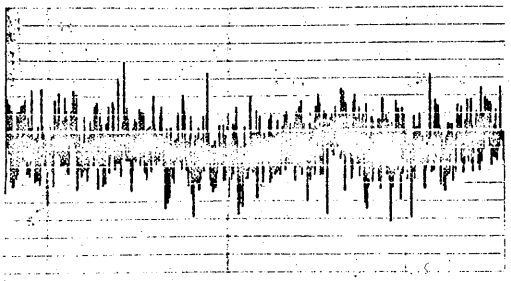

Black body at 195°C
Scale – 10°C per division
(a)

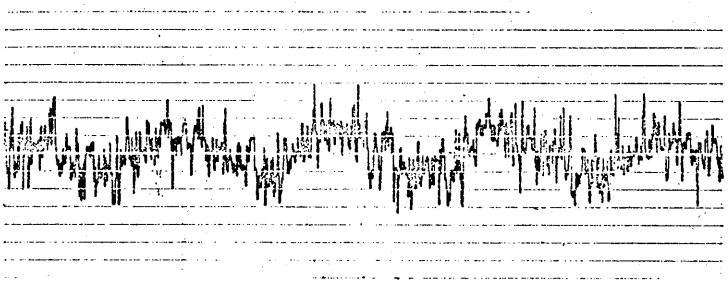

Black body at 240°C
Scale - 2°C/division
(b)

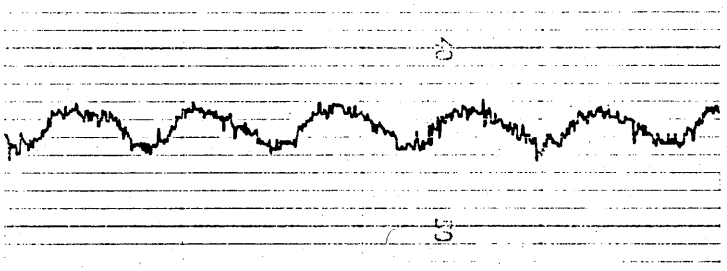

Black body at 292°C
Scale - 2°C/division
(c)

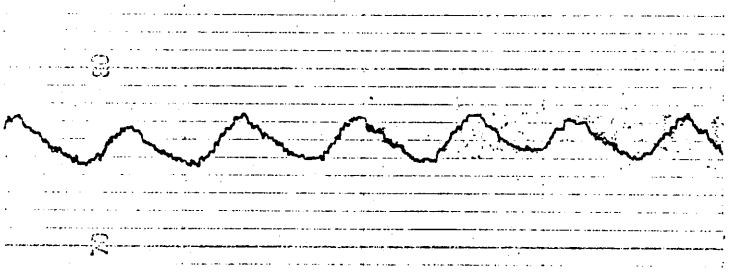

Black body at 345°C
Scale - 2°C/division
(d)

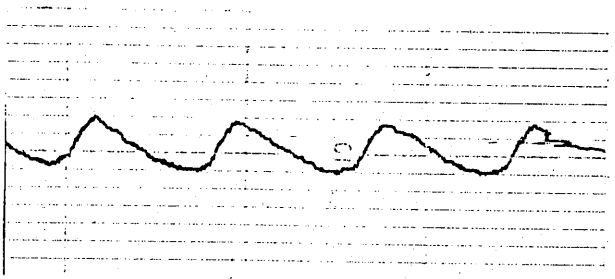

Black body at 416°C
Scale - 2°C/division.
(e)

Fig 7.6 Ultimate sensitivity of pyrometer.

Since magnox has a lower emissivity than a black body it is deduced that the performance on magnox will deteriorate by a factor of about 5 for an assumed emissivity of 0.2 (Appendix A). Thus a sensitivity of about 10°C is to be expected on magnox at 240°C improving to about 3°C at 292°C.

7.6.5 Performance on re-entrant surfaces without filters

The re-entrant surface used in this investigation was a portion of magnox fuel can. This was resistance heated with an internal heater bar to a temperature of about 300°C and the pyrometer was focussed so that it received energy either from a cavity between fins or from a fin tip itself. The filters were removed so that an equal signal was obtained in each channel corresponding to energy in a waveband determined by the detector response characteristic.

It was found that if the galvanometer was driven in the manner shown in Fig. 6.5a, where the signal zero position for both channels occurred for M_3 in the central position, the ratio of energy in the two channels changed as the pyrometer was scanned over the fins and troughs of the fuel can surface. The change in ratio obtained amounted to about 2% of the reading indicated on the output meter. This performance was clearly unacceptable and the mechanism responsible for the variation was sought.

A tungsten lamp source was mounted at the focus of the pyrometer in a dark-room and the optical image produced was intercepted at various positions throughout the system with the aid of a piece of white card. The image was the same in each channel and its shape at the filter positions is shown in Fig. 7.7a which represents a cross sectional view of the optical system. It will be noted that since the light forms a parallel beam at this stage in the system, it forms effectively an image of the object mirror M_1 with the central shadow of M_2 and its support. The observations were made with the galvanometer mirror M_3 stationary. Its angle of deflection was adjusted by rotating the galvanometer assembly in its mounting block.

If a screen was now introduced from the right hand side of the instrument at the position shown in Fig. 7.7a then the left hand side of the image in each channel became dark. During normal operation the energy waveform seen by the detector is decided by the time integral of the beam as it passes from the full on position at the filter to the off position behind the galvanometer mounting. Thus the energy forming the image on the left hand side goes into shadow relatively sooner than the energy forming the image on the right hand side while the shadow is present. The resulting waveform at the detector is shown in Fig. 7.7b. The waveform has a square shape in the off position for channel 1 and a rounded shape in the on position. Conversely it is rounded in the off position and square in the on position in channel 2. The result is a phase shift

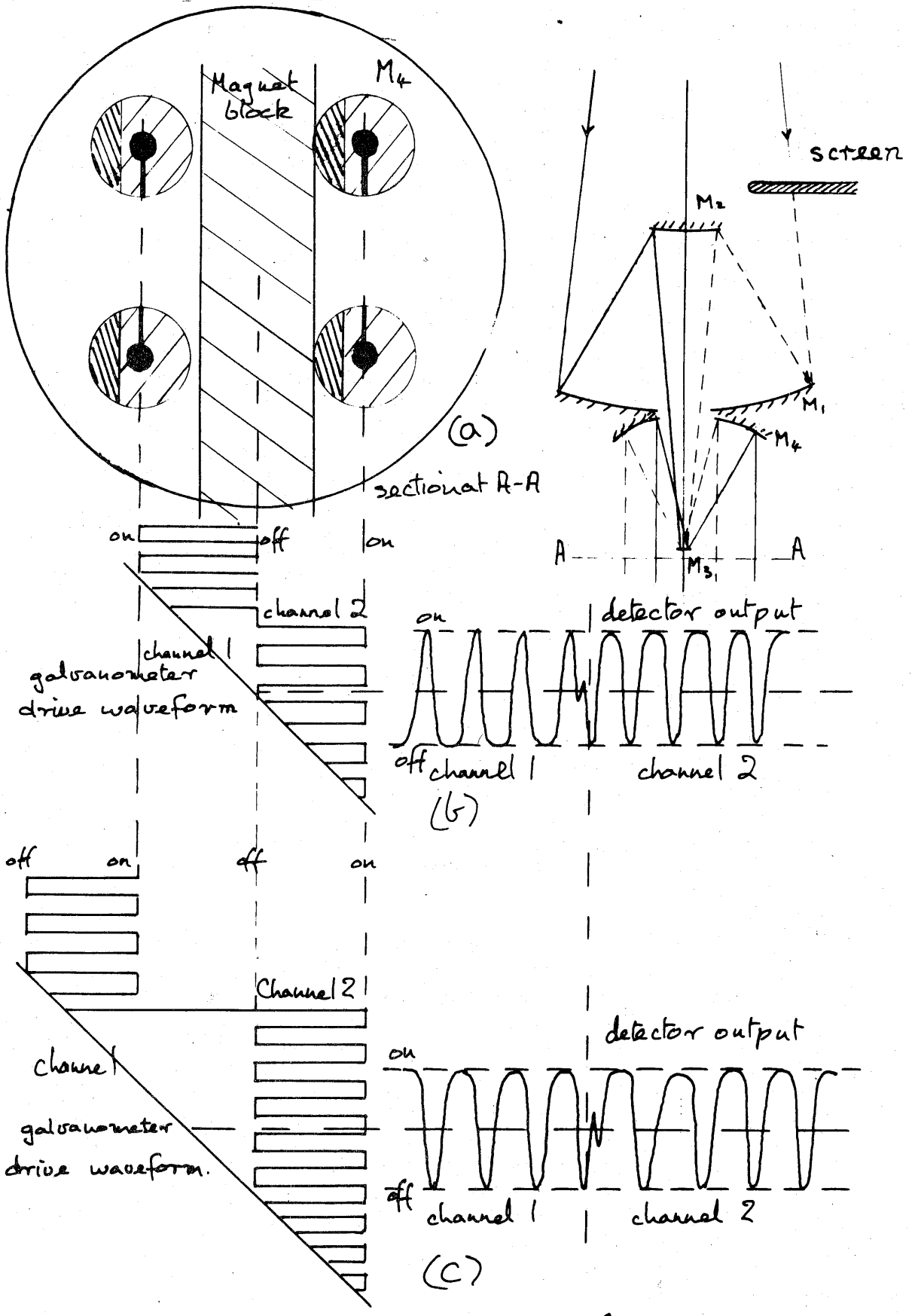

Fig 7.7 Effect of partial blockage of entrance aperture.

of 180° between channels in the rectified waveform. Since full wave rectification is used, however, this should not matter and no change in ratio should be apparent when a screen is introduced.

In practice it was found that if the amplitude of swing of M_3 was carefully adjusted errors of about 1% occurred in normal operation when the screen was introduced providing the latter did not obscure more than 80% of the aperture.

It was thought that fluctuations obtained when scanning a fuel can may be related to the effect produced by a screen in that the fin tips were themselves producing a shadow effect. With this in mind the arrangement of Fig. 7.7c was explored using the circuit of Fig. 6.5b. Here the identical nature of the chopping in each channel (i.e. the beam moves in the same direction into the on and off position for each channel respectively), causes the waveform shape to be affected in a similar manner in each channel but with no phase shift between channels. Careful adjustment of the amplitude of the 900 cps and 30 cps galvanometer drive waveforms led to a minimum error of about 0.5% for 80% blockage of the entrance aperture when the screen was introduced.

Since the performance of the second type of drive was marginally better when a screen was introduced the performance of the pyrometer on the re-entrant surface of the fuel can with this alternative form of drive was examined. There was no significant improvement however over the former galvanometer drive arrangement.

It appeared therefore that the fluctuations obtained when scanning a fuel can were not connected with the effect obtained by introducing a screen. To test this the performance on a fuel can surface, with three different settings, namely 105%, 100%, and 95% of the galvanometer amplitude, was examined. The three settings gave errors of $\pm$ 2% in each case when scanning the fuel can and $\pm$ 10%, $\pm$ 1% and $\pm$ 10% respectively when the screen was introduced. This comparison shows that there is no significant connection between the screen effect and the performance on a re-entrant surface.

A possible explanation of the fluctuations obtained on a re-entrant surface was eventually discovered. Consider the energy deflected by the galvanometer mirror M_3 into each channel. As the mirror oscillates it will select a different portion of the energy in the entrance cone as shown in Fig. 7.8. As far as the pyrometer is concerned a minute shift in the target area will occur so that each channel sees effectively a different part of the target. The result will become apparent when abrupt changes in emission occur over a small region of the target because one channel will receive slightly more energy than the other. This is precisely the case during scanning along the re-entrant surface of a fuel can. The effect was further tested by painting the flat surface of a magnox specimen with a black paint of high emissivity. When the specimen was heated and scanned with the pyrometer, the characteristic disturbance in the recording was obtained as the edge of the painted region passed across the field of view of the pyrometer.

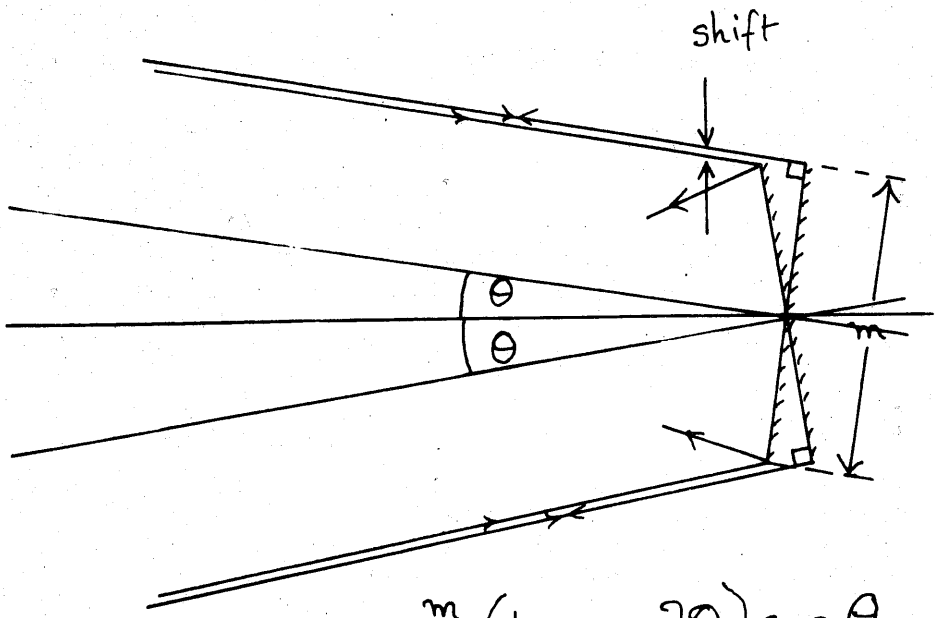

Apparent shift is $\frac{m}{2}(1-\cos 2\theta)\sec\theta$

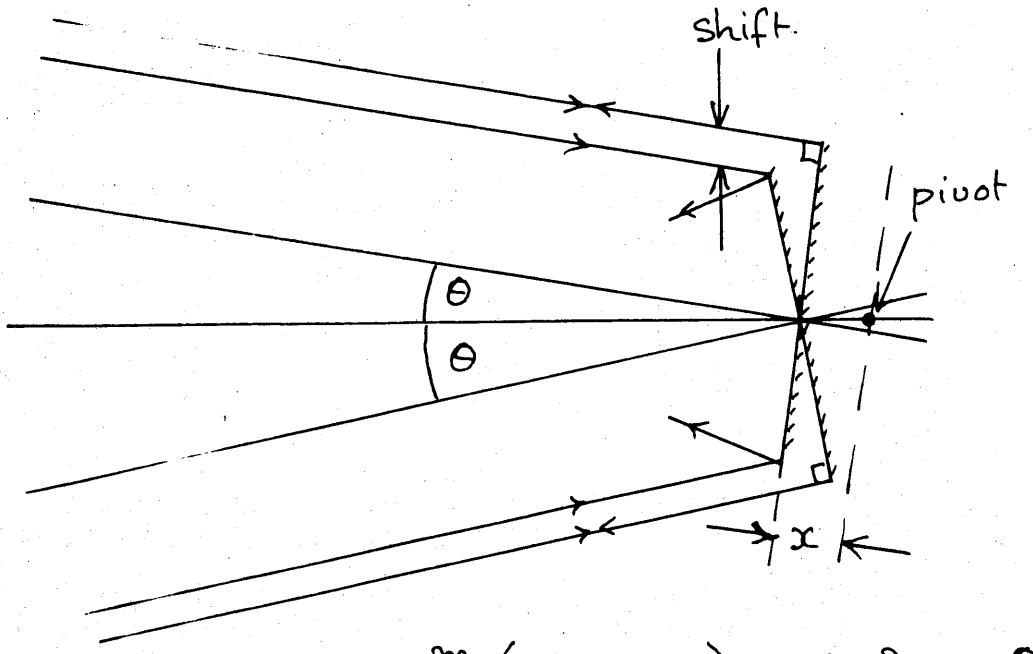

Apparent shift is $\frac{m}{2}(1-\cos 2\theta)\sec\theta + 2x\sin\theta$

Fig 7.8 Effect of transverse shift of mirror M_3.

The expected magnitude of the effect may be estimated as follows:-

If the deflection of the galvanometer mirror M_3 is θ and its width is m then it can be seen from Fig. 7.8 that the apparent shift is given by:-

$$\text{Shift} = \frac{m}{2}(1 - \cos 2\theta) \sec\theta$$
$$= 0.009m.$$

or just less than 1% of the mirror width.

In practice however the mirror is pivoted about a point behind the reflecting surface and the effective shift is magnified to

$$\text{Shift} = \frac{m}{2}(1 - \cos 2\theta) \sec\theta + 2x \sin\theta$$
$$= 0.028m.$$

In an extreme case when the overlapping region of the two target areas has an effective emissivity of zero, an error in the ratio of the energy in each channel of 2.8% will occur. This error will halve when the effective emissivity of the two regions is different by a factor of 2 and will reduce to zero when the effective emissivity of the two regions is the same.

During scanning along a fuel can the effective emissivity is different by a factor of 2 or 3 from fin tip to the cavity between fins and an error of a few percent in the ratio is to be expected. Furthermore the error will take the form of an initial increase or decrease, depending on the direction of scan, as the step change in emission caused by the fin appears in the field of view. This will then reverse as the fin leaves the field of view.

If the mechanism outlined above is responsible for the performance on a re-entrant surface, it seems likely that it should be possible to eliminate the errors if the fuel can is transversed with the pyrometer in such a position that the effective shift of the mirror M_3 takes place parallel to a fin rather than at right angles to it. The error under these conditions was reduced to about $\pm$ 0.7%. A further improvement is obtained if the pyrometer is focussed on the fin roots. In this case the change in emission as the fin enters the field of view is not so sudden since the fin tip is now out of focus.

7.6.6 Performance on re-entrant surfaces with filters and the measurement of fin root temperature

During the calibration of the pyrometer on a black body and on magnox described earlier (7.5) it was discovered that a difference in slope of approximately 6% occurred between the two calibration curves. The implied ratio of $\varepsilon_1/\varepsilon_2 = 1.06$ is in contradiction with that of unity predicted by the measurements described in Appendix A, the accuracy of these being quoted as $\pm$ 2.5% at the relevant region of the spectrum. Incorrect spectral transmission of the filters was suspected as a cause for this discrepancy and

transmission curves were obtained from the manufacturer , together with further filters having passbands on the left of the peak in the spectral emissivity curve.

The pyrometer was now used to check the shape of the spectral emissivity curve obtained in Appendix A by comparing the readings obtained with pairs of filters on both the black body and a magnox specimen. It was assumed in each case that the emissivity at each wavelength was unity for the black body and therefore, the ratio of the readings obtained on the magnox to the readings obtained on a black body was equal to the ratio of the emissivities at the two wavelengths used. The results obtained are listed in Table XIII. The emissivity at each wavelength has been referred to the emissivity at 2.3 microns and the values obtained have been plotted on the spectral emissivity curve of Fig. A.3. Each point represents an average emissivity over the transmission band of the filter and thus some uncertainty exists in their positions on the wavelength scale. Nevertheless a verification of the peak in the spectral emissivity curve was established and the reason for the 6% change in calibration from nagnox to the black body in the case of the original pair of filters was discovered.

It was decided to proceed with the assessment of the pyrometer on a fuel can surface with two pairs of filters namely 2.3 and 2.0 microns and 2.0 and 1.8 microns.

A 30 cm length of fuel can was mounted on a graded heater bar in still air such that a large temperature distribution could be obtained along its length. Fine wire chromel - alumel thermocouples were welded at the fin roots at equal intervals along the can length, five fins apart. A calibration curve for the pair of filters used in the pyrometer was obtained at the central thermocouple and the pyrometer was then used to scan along the can to investigate the agreement obtained between pyrometer and thermocouples. In each case a chart recording was obtained with no filters in the pyrometer to show the magnitude of the error due to the can geometry.

With the can at uniform temperature traces were obtained using each pair of filters. In each case the pyrometer was focussed both on the fin tips and on the fin roots. (See Fig. 7.9 and 7.10). It can be seen that it is difficult to isolate the temperature distribution from the geometry effect when the pyrometer was focussed on the fin tips and it was decided that focussing on the fin roots gave the most reliable performance. The heater bar was now adjusted so that a large temperature variation occurred along the can. Four traces were obtained (Fig. 7.11-14) two for each set of filters focussed on the fin roots, for different can gradients. The temperature indicated by the thermocouples has been plotted on the recordings in each case, the calibration being carried out at thermocouple No.6. A calibration run for Fig. 7.13 is shown in Fig. 7.15. The pyrometer agrees with the thermocouples within about two degrees in most cases except for thermocouple No.10 which became suspect during the

TABLE XIII

Relative emissivity of magnox at various wavebands

Control channel (microns)	Measure channel (microns)	Black body temp. °C	Pyrometer output black body	Magnox temp. °C	Pyrometer output magnox	B. B. output corrected to magnox temp.	Output Mx / Output B. B.	Cross checks
2.4x	3.3*	394	57.6	390.5	37.5	58.1	0.65≠ A	DH =.63 CE =.64
2.4x	2.1*	396	156	394.5	169	155.6	1.09 B	CF =1.08
2.4x	2.0x	394	143.7	390	151.5	142.2	1.07 C	$\frac{D}{G}$ =1.03 $\frac{B}{F}$ =1.07
2.4x	1.8*	394	54.5	390.5	52	54	.96 D	$\frac{A}{H}$ =.99 CG =1.00
2.0x	3.3*	394	70	396.5	41.5	69.6	.60≠ E	GH =.61 $\frac{A}{C}$ =.61
2.0x	2.1*	396	300.5	395.5	304	300.5	1.01≠ F	$\frac{B}{C}$ =1.02
2.0x	1.8*	396	68	391.5	63	57.3	.94 G	$\frac{E}{H}$ =.92 $\frac{D}{C}$ =.90
1.8*	3.3*	396	299	390	197	303	.65≠ H	$\frac{A}{D}$ =.67 $\frac{E}{G}$ =.64

≠ Inverted calibration because $\lambda_{control} < \lambda_{measure}$
* Transmission curves available for actual filter used
x Transmission curves available for filter batch

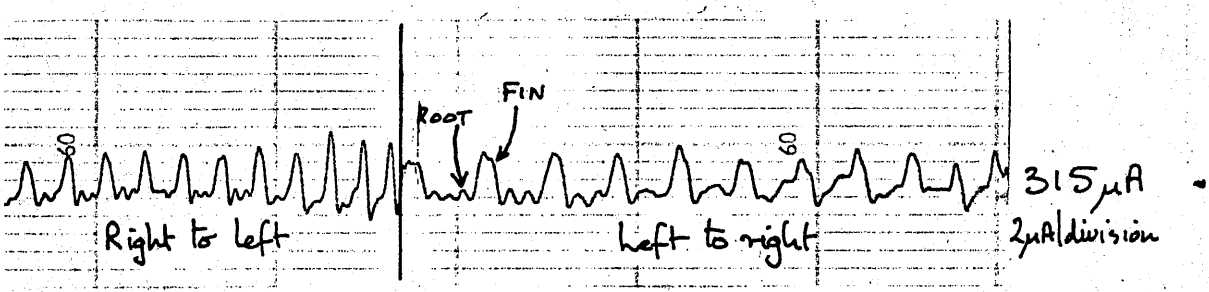

(a) No filters
Focussed on fin tips

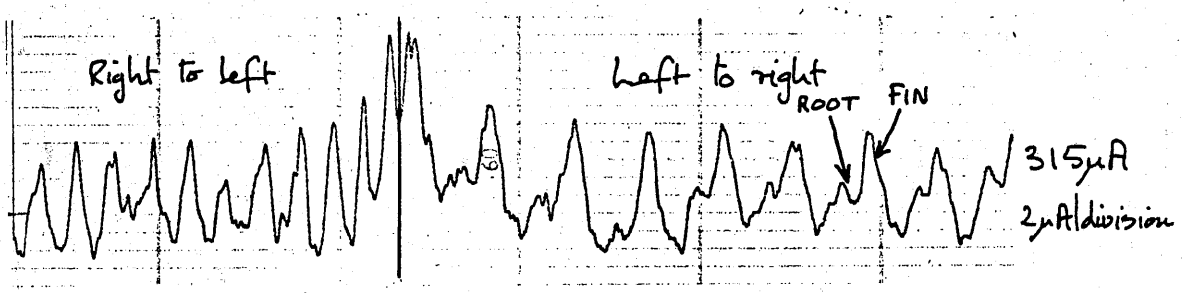

(b) 2·0 and 1·8 microns
Focussed on fin tips

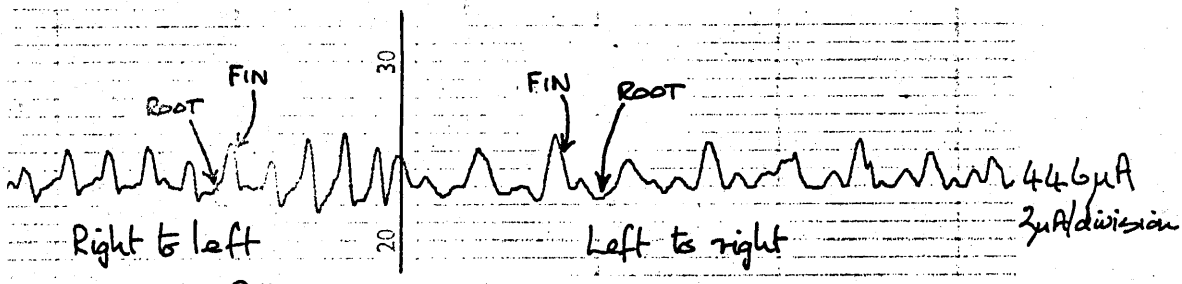

(c) No filters
Focussed on fin tips

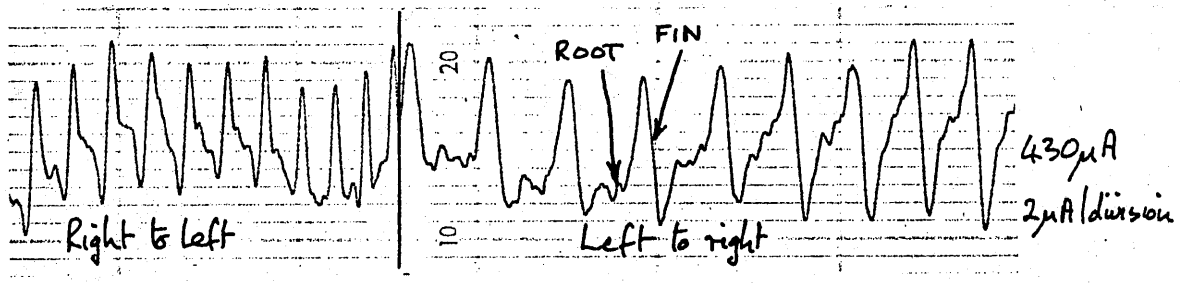

(d) 2·3 and 2·0 microns
Focussed on fin tips.

Fig 7.9 Chart recording of pyrometer scanning a fuel can.

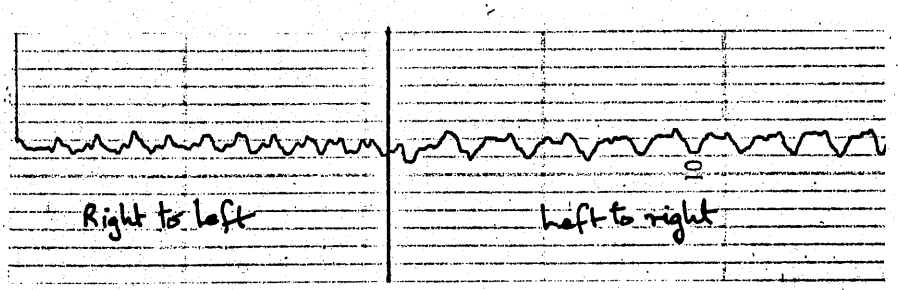

223μA
2μA/division

(a) No filters Focussed on roots.

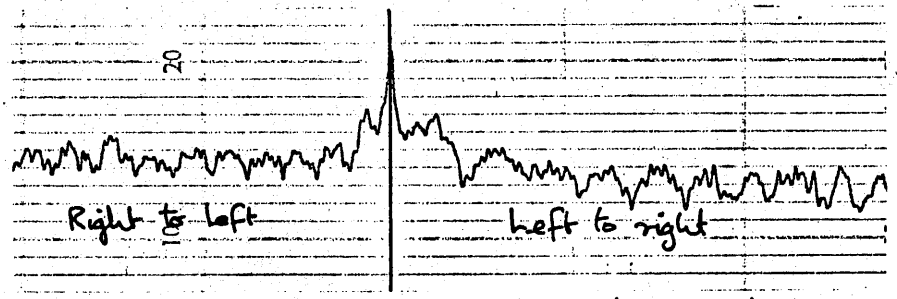

226μA
2μA/division

(b) 2.0 and 1.8 microns Focussed on roots.

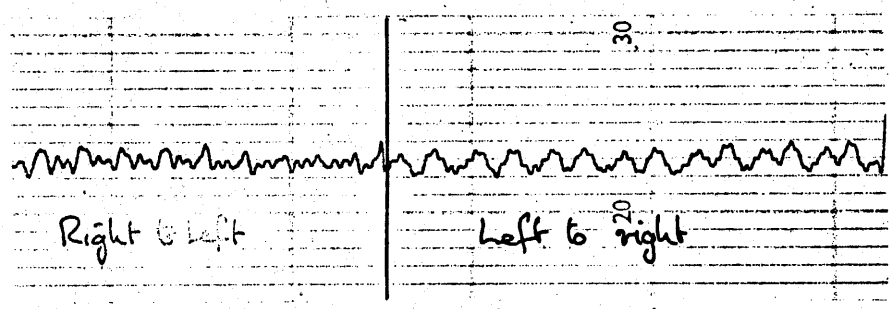

446μA
2μA/division

(c) No filters Focussed on roots

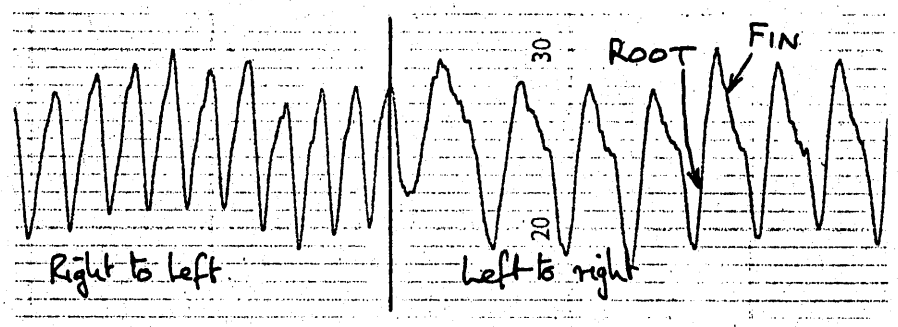

448μA
2μA/division

(d) 2.3 and 2.0 microns Focussed on roots.

Fig 7.10 Chart recordings of pyrometer scanning a fuel can.

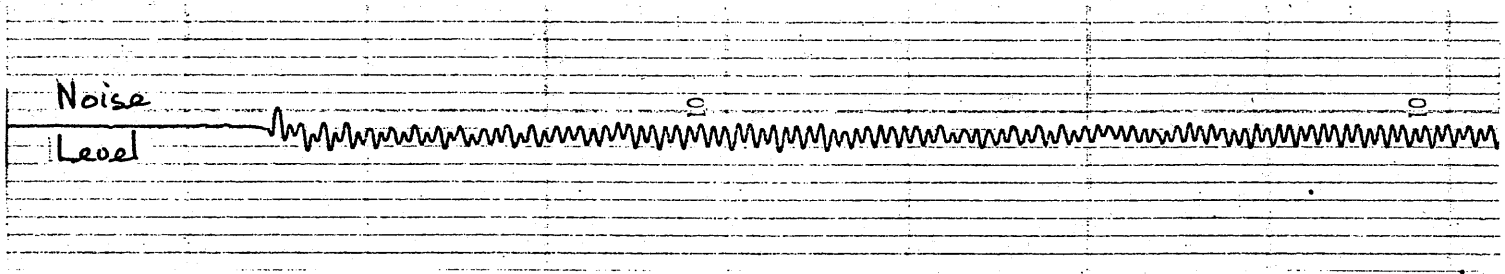

Fig 11(a) Traverse along can focussed on fin roots 2μA/division
No filters

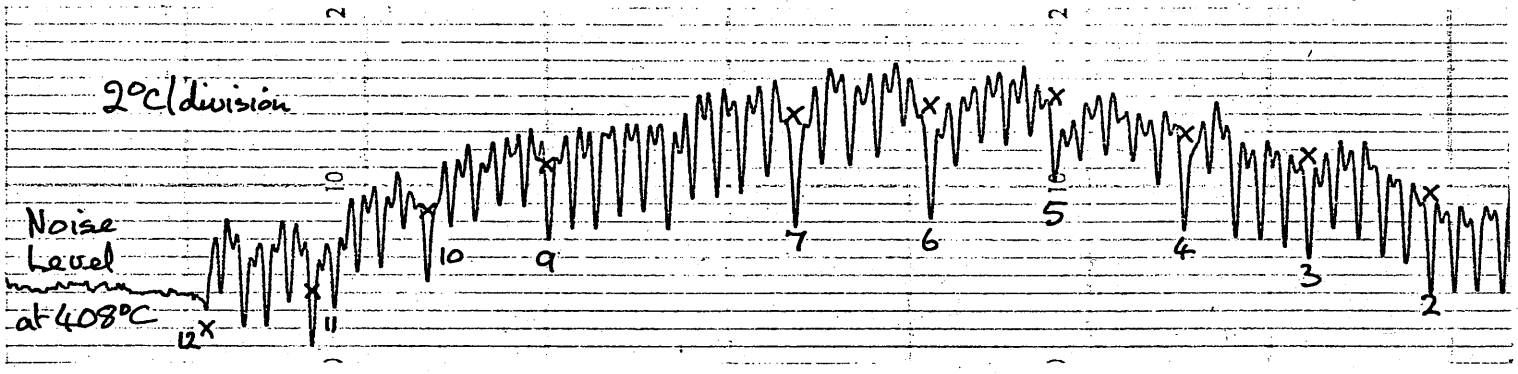

Fig 11(b) Traverse along can focussed on fin roots
2.3 and 2.0 microns
x Thermocouple readings.

Fig 7.11

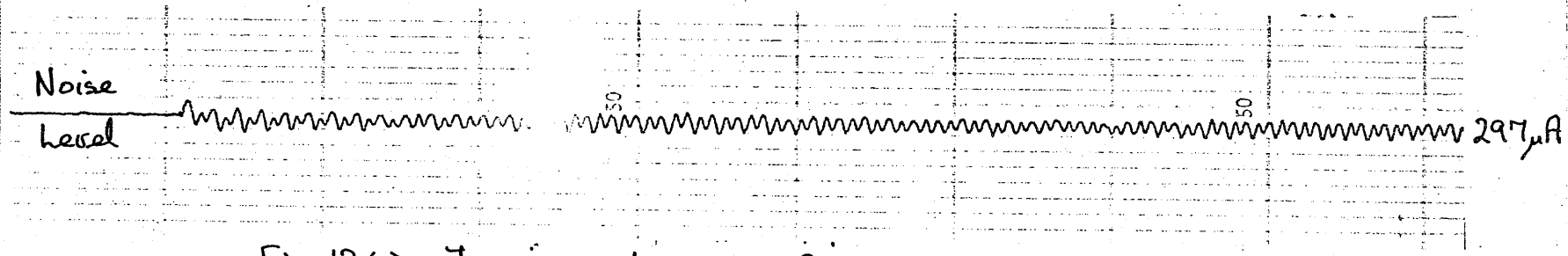

Fig 12(a) Traverse along can focussed on fin roots
No filters

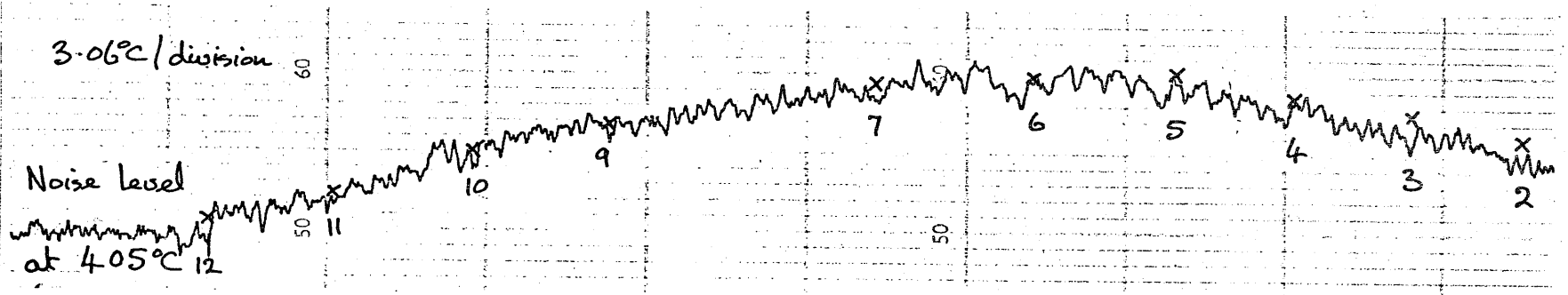

Fig 12(b) Traverse along can focussed on fin roots
2·0 and 1·8 micron filters.
× Thermocouple readings.

Fig 7.12

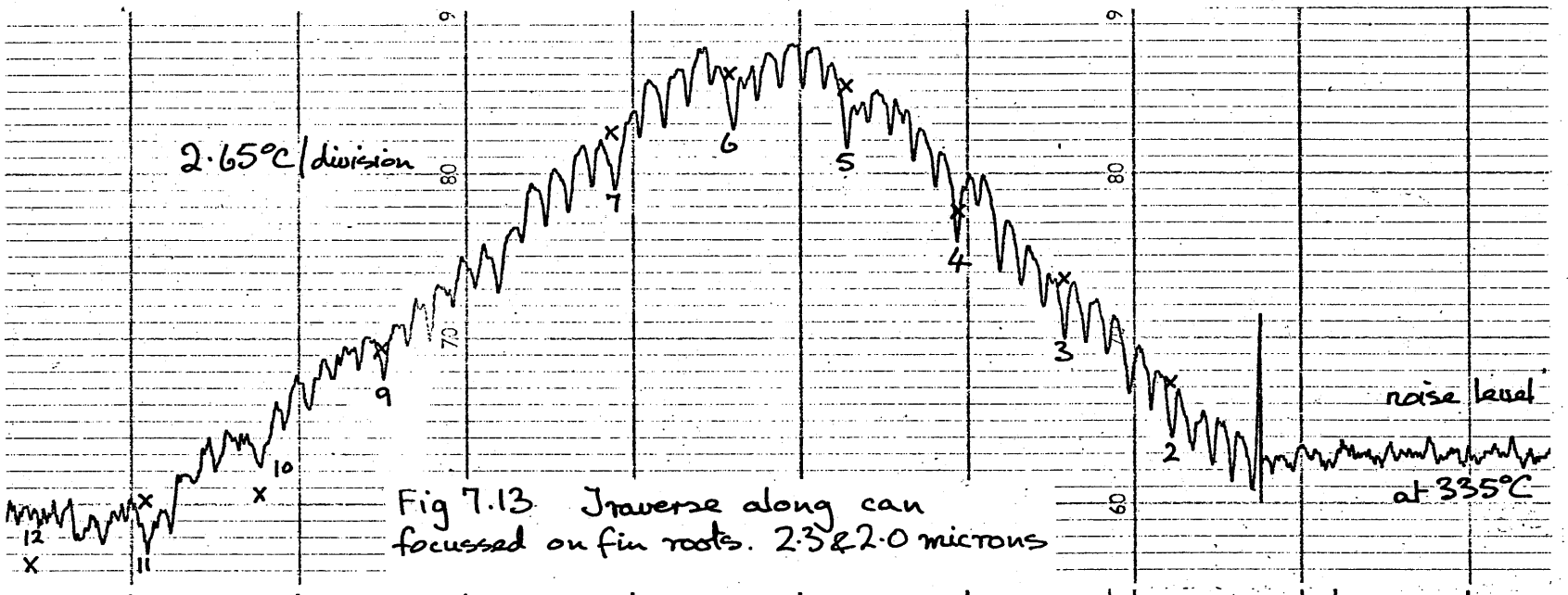

Fig 7.13 Traverse along can focussed on fin roots. 2.3 & 2.0 microns

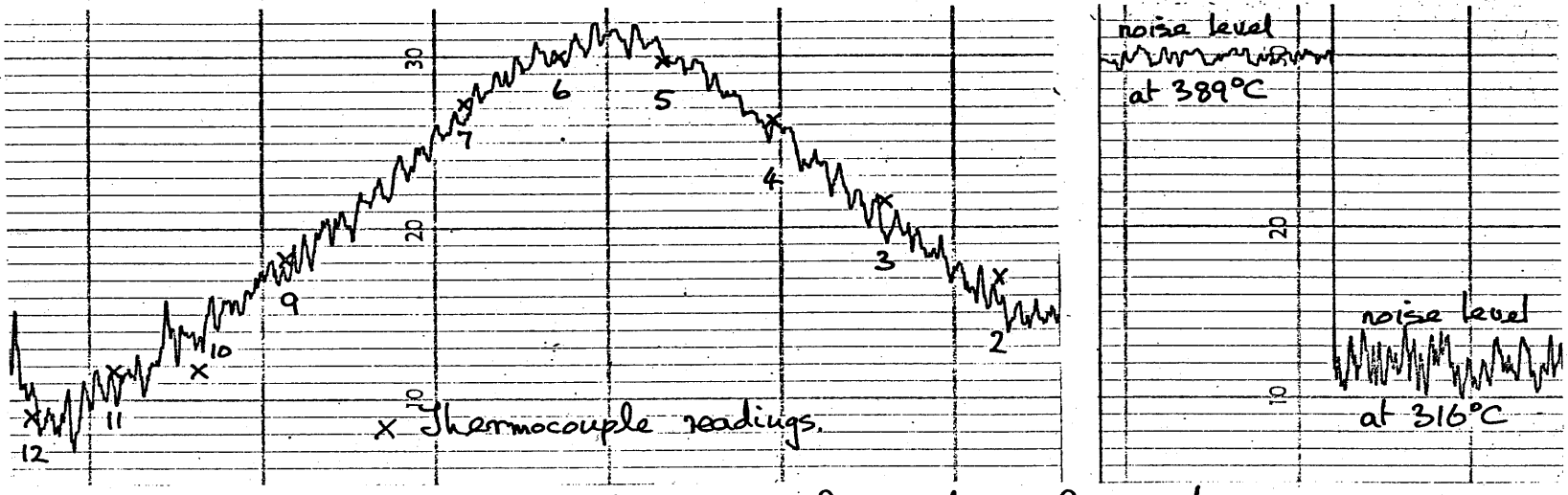

Fig 7.14 Traverse along can focussed on fin roots. 2.0 & 1.8 microns

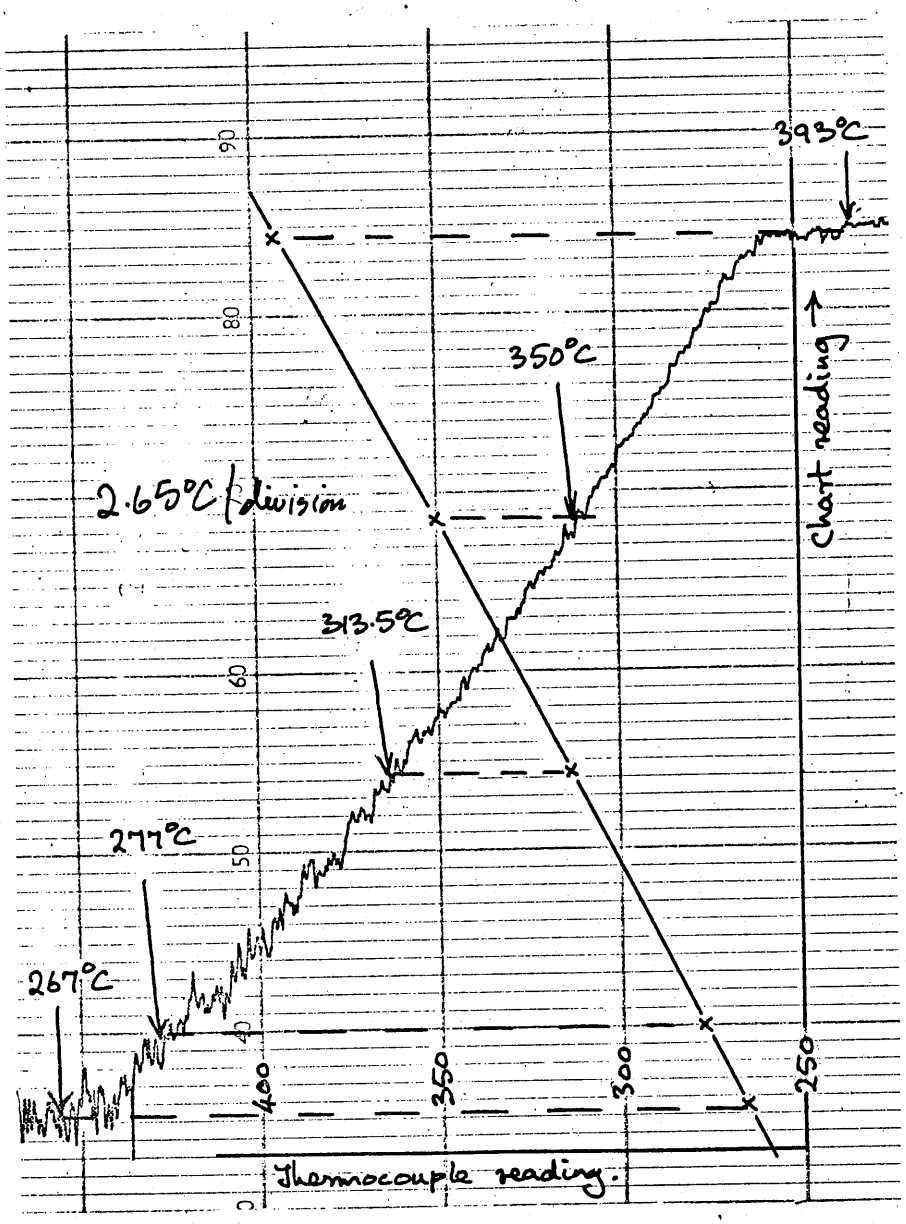

Fig 7.15 Method of calibration of chart.
(Calibration against T/c no 6. of fig 13).

period of the tests. The better performance is obtained with filters at 2.0 and 1.8 microns where little temperature difference is indicated between fins and roots. The two filters 2.3 and 2.0 microns indicated a higher temperature for the fins than the roots which is obviously incorrect and is thought to be due to the emissivity ratio of 1.06 for these two wavelengths on a magnox target.

The performance of the pyrometer described above represents the present stage of its development for temperature measurement of a magnox can. The implication is that the pyrometer is able to measure fin root temperatures to the required sensitivity but it cannot be relied upon for accurate temperature difference measurements between fin roots and fin tips.

7.7 Conclusion

It has been shown that the pyrometer system meets the specification of Chapter 1 in the following respects:-

Temperature discrimination: better than 3°C at 300°C on magnox.

Absolute accuracy: $\pm$ 5°C on a black body; within 10°C when calibrated on magnox

Response time: 1 second approx. (see Chapter 5)

Target area: size of galvanometer mirror - 0.125 x 0.050 cm^2 $\simeq$ 1 mm^2

Temperature range: 250°C-600°C on magnox

Surface geometry: fluctuations of 1% of indication occur when scanning along magnox can.

Measurements in the environment of a heat transfer rig have not been carried out due to the increased importance of other applications (see Chapter 8). Thus, the effect of the hot quartz window cannot be specified. Apart from this, however, the pyrometer does not fall far short of the original specification. It is unfortunate, however, that the geometry effect has not been eliminated since this prevents the measurement of temperature differences between fin tips and fin roots.

7.8 References

1. H.J.J. Braddick. Physics of Experimental Method,2nd Edition. London,Chapman and Hall,1963,p.162

2. American Inst. of Physics Handbook,2nd Edition. New York, McGraw-Hill,1957,p.6-65

3. R. Berenbaum and J.W. Northey. APC Internal document

4. G.K. Caulton. UPC Internal document

CHAPTER 8 - THE GENERAL APPLICATION OF THE RATIO PYROMETER

Introduction

A change in emphasis in the application of the pyrometer has occurred during the period in which it was developed. The reasons for the change in emphasis are given and the wider application of the pyrometer which resulted is described. The most important of the new applications is the measurement of AGR can temperatures during experimental work. A second line of investigation which is being carried out is that of temperature measurement of extruded aluminium where an improvement in present techniques is being sought. Two further applications, the temperature measurement of steel ropes and the temperature measurement of fine wires during annealing are also discussed.

Finally, the Mark II pyrometer system, which has been developed for the commercial market, is described briefly.

8.1. Applications arising since the conception of the pyrometer

During the development and manufacture of the pyrometer system described, the design of nuclear power reactors has entered a new stage of development, resulting in the Advanced Gas Reactor (AGR). The design of fuel elements has changed from the helically finned magnox can, to a cluster of fuel pins using stainless steel as the canning material. Heat transfer work is now being carried out on the AGR pins and the work on magnox has diminished.

In addition the company has expanded its interests to include sponsored research at the Heston Laboratories. The pyrometer has attracted a variety of interest in this respect from various branches of industry and many possible applications have arisen outside the nuclear field.

The above factors have influenced the development of the pyrometer and the emphasis has changed to providing an instrument for the surface temperature measurement of stainless steel fuel pins during heat transfer measurements and for general use in industry in the moderate temperature range of 250°C to 1000°C.

The change in emphasis occured when about 60% of the work described was completed. Thus in the assessment of the pyrometer described in Chapter 7 the small departures in performance from the specification set out in Chapter 1 have not greatly affected the development. Indeed rather than devote further effort to the measurement of magnox can temperatures it has been necessary to proceed to the measurement of stainless steel and the commercialisation and wider application of the instrument described in this chapter.

Nevertheless the specification for the surface temperature measurement of magnox cans has been adhered to as far as possible and has provided a basis for the development of the instrument.

8.2. Application in the development of Advanced Gas Reactor fuel pins

The fuel element canning material in the Advanced Gas Reactor (1) is stainless steel and each can consists of a thin walled tube approximately 120cm long and 9.5mm diameter with a single helical ridge 0.38mm high on the surface performing 4.3 turns per cm. The elements are rated to run at about 650°C as opposed to 475°C in the case of magnox. Although the running temperature of an AGR can is less critical as far as the stainless steel is concerned it is still necessary to measure and control it. The reactor thermocouples used, however, are sufficiently bulky to cause conduction of heat away from their attachment points on the can wall, which is very thin. It is necessary to take the error so produced into account when calibrating the reactor thermocouples and the pyrometer provides a suitable means.

The reactor thermocouple produces a depression in the surface temperature of the fuel can during forced convective cooling and the purpose of the pyrometer is to monitor the shape of the depression and provide a figure for the undisturbed temperature. The measurement is to be carried out in an experimental heat transfer rig which is similar in many respects to those used to develop the magnox can. It is proposed that the test be carried out initially in air and then in carbon dioxide atmosphere which is the reactor gas.

As a preliminary investigation to the work on the AGR can the calibration of the pyrometer on the stainless steel canning material has been carried out. Can specimens were heated in still air for this purpose and calibration curves were obtained in the range 250° to 600°C using a fine Pt/Pt 13% rhodium thermocouple as a standard. The results obtained show that the calibration can be relied upon to remain unchanged for a period of a few hours providing the cans are pre-heated at temperatures above the temperature at which measurements are to be made. Thus the changing effect of oxidation on the calibration may be halted at any stage during the oxidation by this means. A typical calibration curve, using a Mark II pyrometer (see section 8.5), is shown in Fig. 8.1. A preheating treatment was carried out at 600°C for a period of 25 minutes followed by heating at 565°C for a period of 2½ hours during which the drift did not exceed 5°C. The specimen was then cycled repeatedly in the range 250°C to 580°C over a period of 3 days. A repeatability of ± 5°C at each end of the range was maintained improving to ± 3°C at the centre of the range. The effect of heating in carbon dioxide has not yet been examined but it is expected that smaller changes will occur due to less severe oxidation.

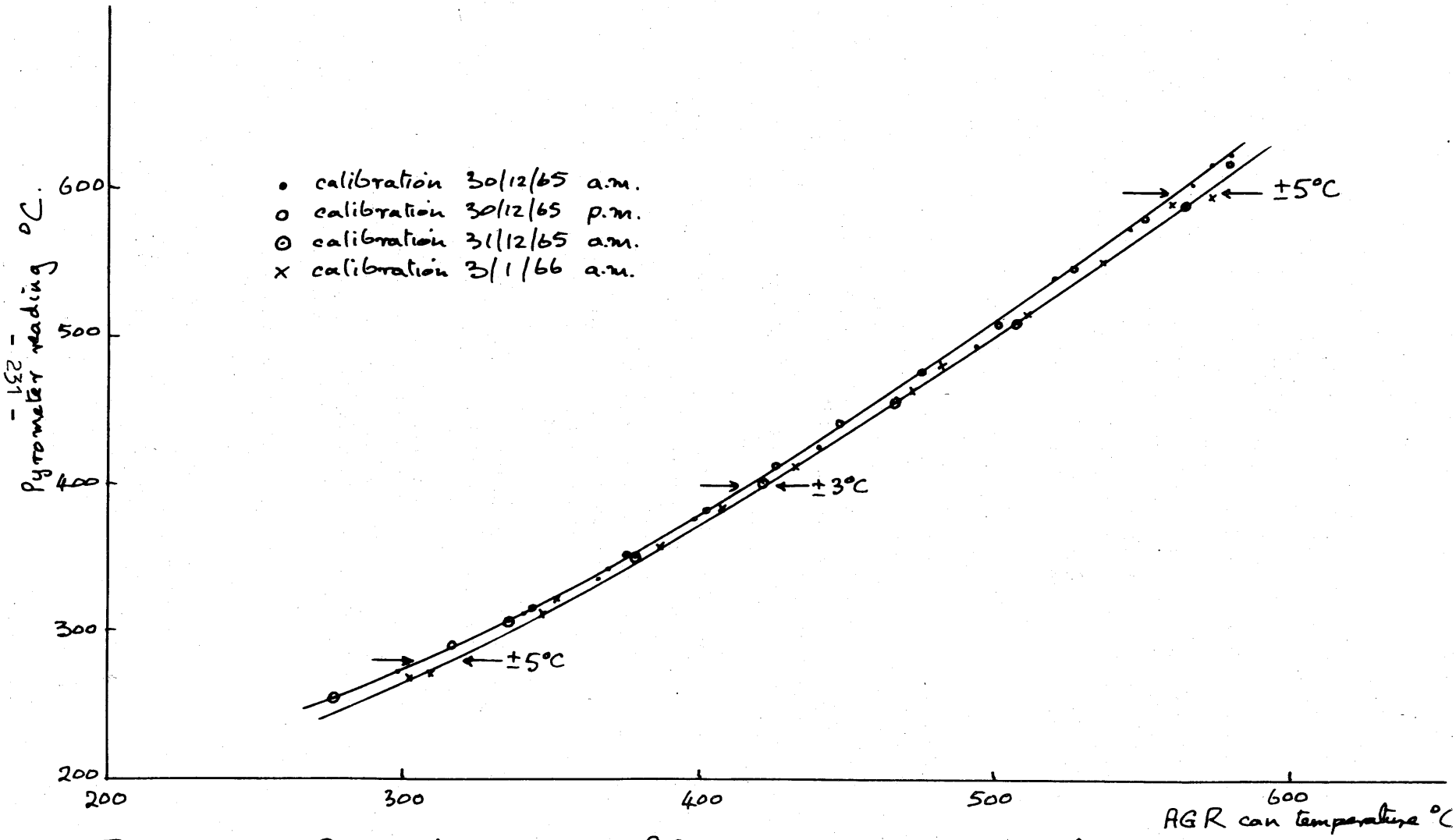

Fig 8.1 Repeated cycling of AGR can specimen – typical calibration curves.

There is also a surface geometry problem associated with the AGR can but this is far less prominent than that on the surface of a magnox can. It was found that the helical ridge on the AGR can produced a small oscillation during scanning which was reduced when the pyrometer was operated in the preferred orientation (see section 7.6.6). As with the magnox can the oscillation was a function of emission since it persisted when the filters were removed, and it is again thought to be connected with the galvanometer mirror. A chart recording of a typical scan along a heated AGR can specimen heated in still air is shown in Fig. 8.2. The arrows indicate the temperature as recorded by fine wire thermocouples welded to the can surface near to the line of scan. It can be seen that agreement to within two degrees is obtained between the thermocouple and the pyrometer in spite of the surface variation caused by oxidation.

8.3. Application of the pyrometer in aluminium alloy extrusion

When aluminium and its alloys are extruded the temperature of the metal as it leaves the die plays an important part in determining the physical properties of the finished product. Since the extrusion is moving a non-contact temperature measurement method is desirable, and to be of value the performance of the instrument should be unaffected by the composition of the extruded material and its surface geometry. Furthermore, a quick response measurement is required in order that temperature should be measured as close to the die as possible.

The application of single channel pyrometers to temperature measurement of aluminium alloys during extrusion has been examined previously (2). It was found during this investigation that the calibration of a single channel pyrometer was affected not only by the variation in emissivity caused by oxidation but also by the composition of the extruded alloy. In particular the alloys with a large magnesium content produce unacceptable changes in calibration.

It was decided to compare the performance of the ratio pyrometer with that of a single channel lead sulphide cell instrument to determine whether the ratio method could produce smaller calibration variation between specimens of various alloys. For the purpose of the comparison the two pyrometers were set up to measure simultaneously the temperature of specimens mounted in the spectral emissivity apparatus described in Appendix A. At the start of the investigation the calibration of each pyrometer was adjusted as follows

(i) the ratio pyrometer was adjusted to read correctly on the black body cavity at 312°C

(ii) the single channel pyrometer was adjusted for the lowest emissivity on its scale ($\varepsilon = 0.2$) since it was thought that no specimen would exceed this figure.

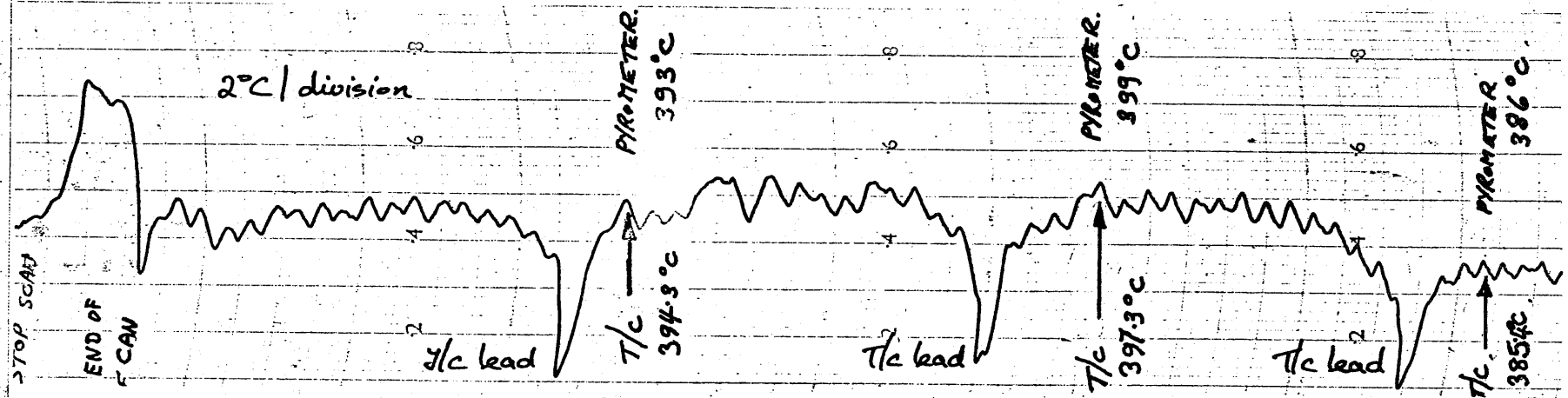

(a) 2·3 and 2·0 micron filters. Time constant 1·4 seconds.

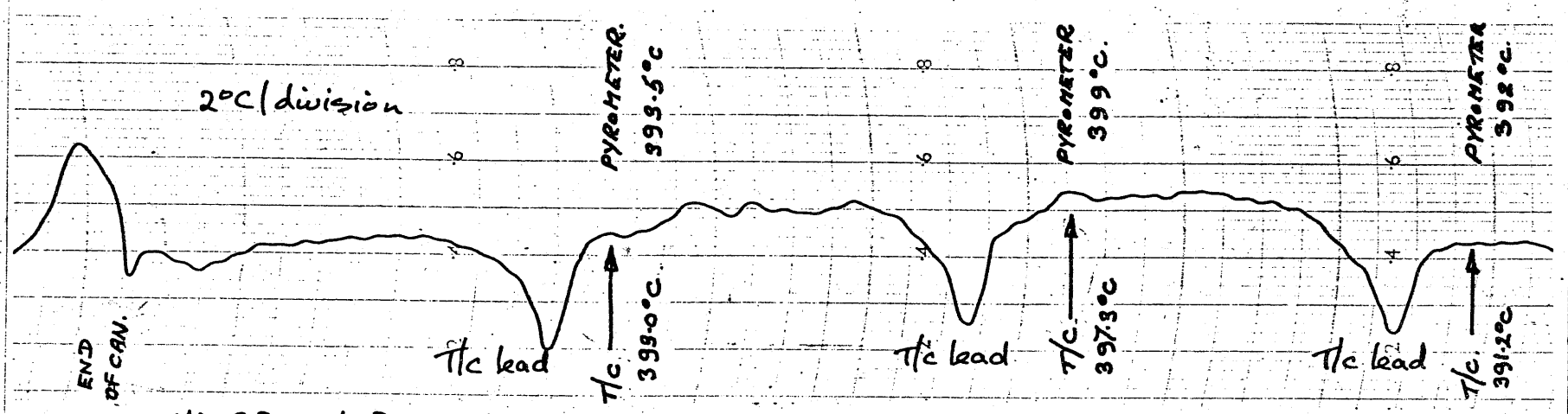

(b) 2·3 and 2·0 micron filters Time constant 6 seconds

Fig 8.2 Pyrometer scan along AGR can heated in still air.

The calibration adjustment of each instrument was left at the above settings for the duration of the investigation.

Specimens of five alloys, whose type numbers and composition details are shown in Table XIV, were examined. Measurements on each lasted for about six hours, during which time a calibration curve over the range 250° to 550° to 250°C was obtained. In addition as a check on the stability of the pyrometers the reading of each on the black body cavity over the same temperature range was obtained. The results of the comparison (3) and the stability for the period of the investigation (5 days) may be judged from Fig. 8.3. It can be seen that for a reading of 400°C on the single channel instrument the specimen temperatures occupied a band from 320° to 425°C which is approximately 100°C wide. In the case of the ratio pyrometer for a reading of 400°C on the pyrometer the specimen temperatures occupied a band from 355° to 388°C which is approximately 30°C wide.

The improvement in performance by a factor of three obtained with the two colour pyrometer as compared with the single channel pyrometer is encouraging, even though the variation is wider than the industry would like. It is realised, however, that the above laboratory investigation is not truly representative of conditions existing during extrusion. It is hoped, therefore, that a test on an extrusion press will be mounted in the near future when the performance of the ratio pyrometer under more realistic conditions will be examined.

8.4. Temperature measurement of steel ropes

During the preparation of steel rope an annealing process in which the rope is passed continuously through a furnace at about 330°C is carried out. The rope enters the furnace in a condition which is nominally clean but there may be traces of oil present. It has been found that during the short period which the rope spends inside the furnace a light oxidation film forms and various deposits are left on the surface due to the initial surface contamination. At the exit of the furnace it is desirable to monitor the rope temperature and adjust the furnace temperature as necessary to maintain the most suitable conditions.

It is desirable in this application of the pyrometer that the variation in calibration for all surface conditions of rope at about 350°C should not be greater than ±5°C. The performance of the Mark II pyrometer (see section 8.5) has been investigated on a number of samples which fall into two categories

(i) variation in calibration over three thermocoupled samples which were cleaned and then oxidised by thermal cycling for a period of a few minutes.

(ii) drift in calibration on a number of thermocoupled samples maintained at constant temperature for a longer period of time up to 15 minutes.

TABLE XIV

Composition of aluminium alloys.

		B.S. Specified composition (%)								
BS 1476	Alcan	Al	Cu	Mg	Si	Fe	Mn	Ni	Zn	Cr
E1C	GB2S	99.0	0.1	-	0.5	0.7	0.1	-	0.1	-
NE6	GB B56S	Rem	0.1	4.5-5.5	0.6	0.5	1.0	-	0.2	0.25
HE15 (2L64)	GB 26S	Rem	3.6-4.8	0.2-0.8	0.5-0.9	0.7	0.3-1.2	0.2	0.2	-
HE30	GB B51S	Rem	0.1	0.4-1.4	0.6-1.3	0.5	0.4-1.0	-	0.1	0.3
HE9	GB 50S	Rem	0.1	0.4-0.9	0.3-0.7	0.5	0.3	-	0.1	0.1

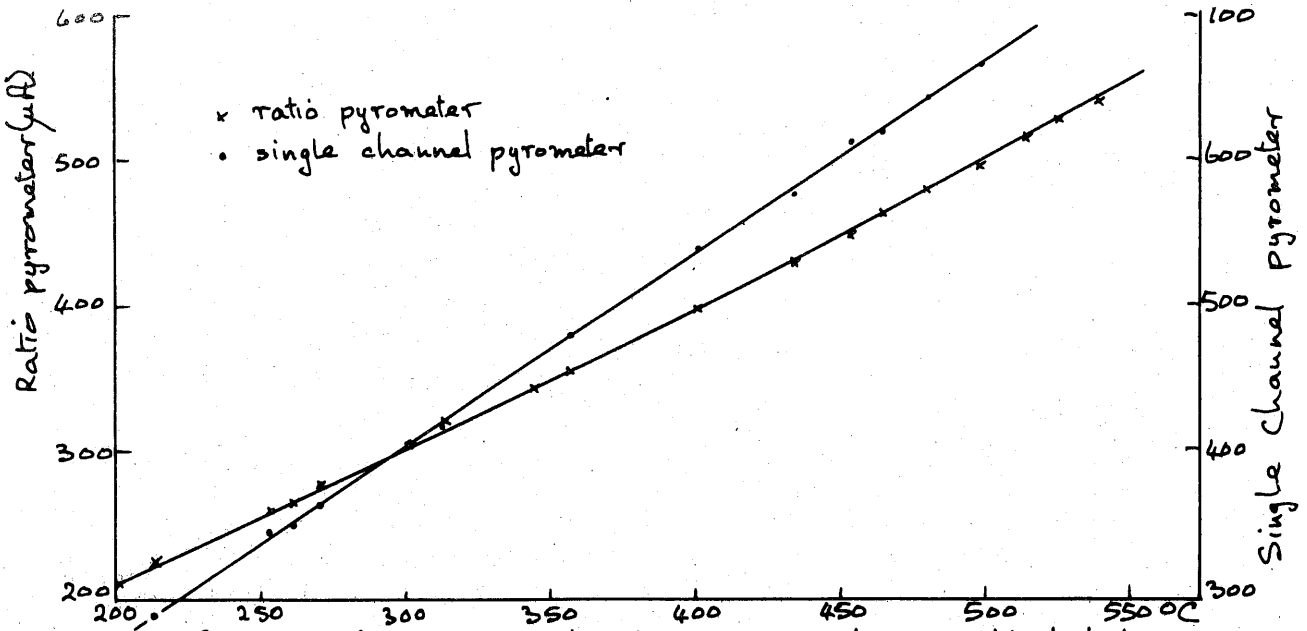

(a) Stability of single channel and ratio pyrometers on black body.

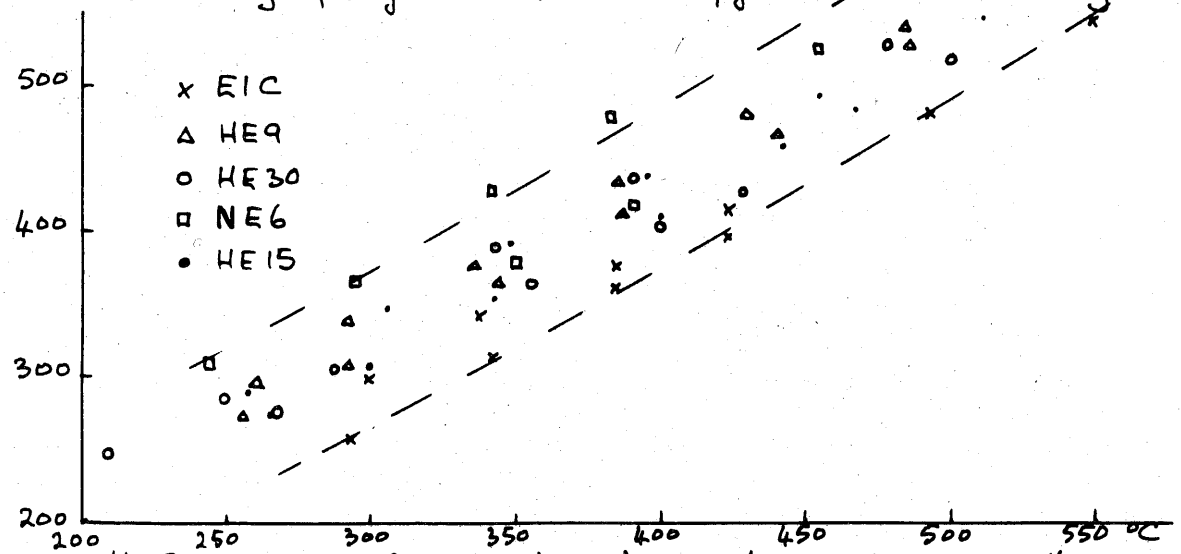

(b) Performance of single channel pyrometer on aluminium alloys.

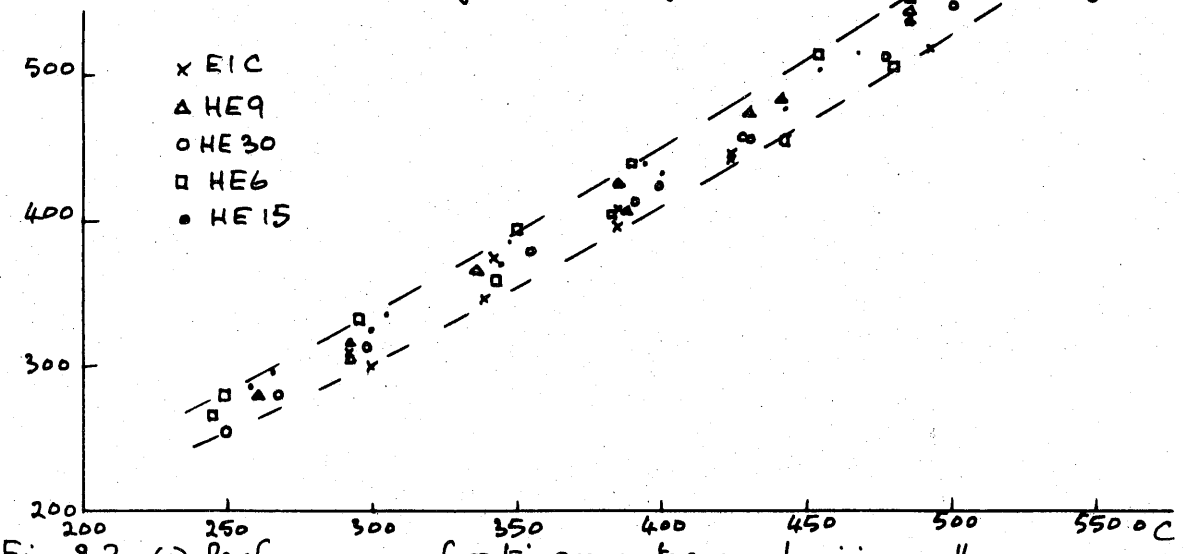

Fig 8.3 (c) Performance of ratio pyrometer on aluminium alloys.

The results of (i) are given in Fig. 8.4. It can be seen that the repeatability from one specimen to the next is within 16°C at 320°C and that the change in calibration after cleaning is about +15°C. The total calibration variation obtained covers a band of about ± 14°C and although this is outside the initial requirement the manufacturer considers that the performance justifies further tests on the production line.

8.5. Temperature measurement of fine wires

It has been found that the pyrometer will produce a sensible temperature measurement on fine wires providing that the wire is viewed so that it lies perpendicular to the scanning direction of the galvanometer for the reasons outlined in 7.5.6. The problem in this application is that of calibration because the specimen is too small to attach a fine wire thermocouple. Thus calibration on a larger specimen of the same material may be necessary. There is an application for this type of measurement during extrusion of copper wire where wire diameter down to 0.006" and drawing speeds measured in thousands of feet per minute are being considered.

8.6. The Mark II Instrument

Sufficient interest has been aroused in industry by the ratio pyrometer to justify further development to produce an instrument capable of manufacture in production quantities with a more general specification. The Mark II instrument which will shortly be available commercially, covers the temperature range 250° to 1000°C and is equipped with zero suppression and range change facilities to provide four scale spans of 200° in the above range. It is provided with battery as well as mains operation and the cells used are rechargeable in-situ. Apart from the increased temperature range, which has been made possible with an optical attenuator, the performance is similar to the pyrometer described in the preceding chapters. It is, however, constructed in a more robust manner to suit industrial application. The head unit is cylindrical in construction and houses in addition to the optics, the field effect transistor preamplifier. It is also provided with variable focussing. The electronics unit is made up of printed circuit plug in board units for increased reliability and has been tailored to suit the commercial market. The Mark II pyrometer system is shown in Fig. 8.5. This photograph was obtained in April 1965 when the pyrometer was exhibited on the Company stand at the Physical Society Exhibition.

8.7. Conclusion

The more general application of the ratio pyrometer has been described. It has been shown that the pyrometer can measure the surface temperature of stainless steel AGR fuel elements with a repeatability of 10°C in the range 250° to 650°C providing the calibration is performed after heat treating the fuel element. Furthermore, the pyrometer is capable of detecting temperature differences of about 2°C under the same conditions.

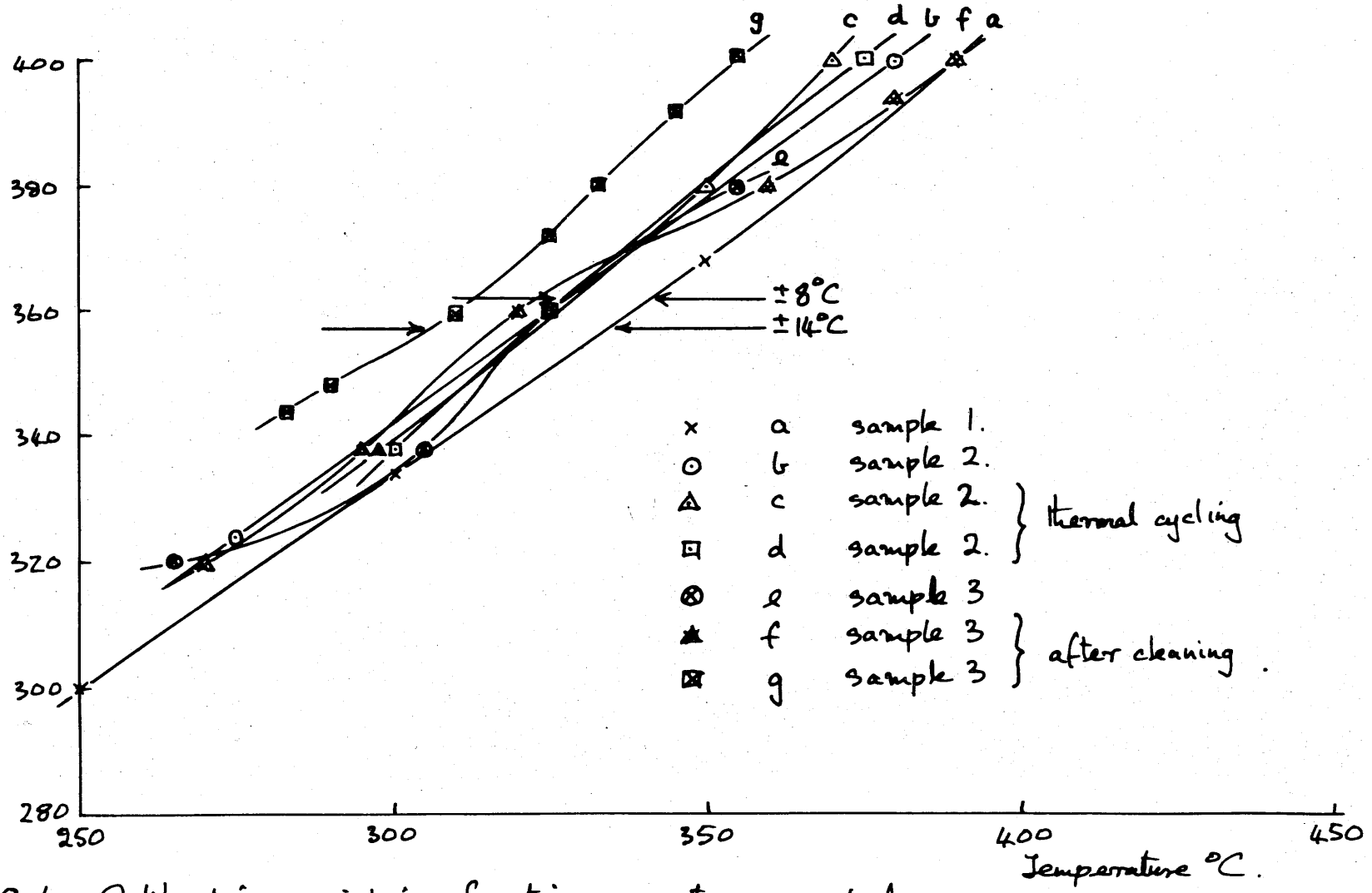

Fig 8.4 Calibration variation of ratio pyrometer on steel rope specimens.

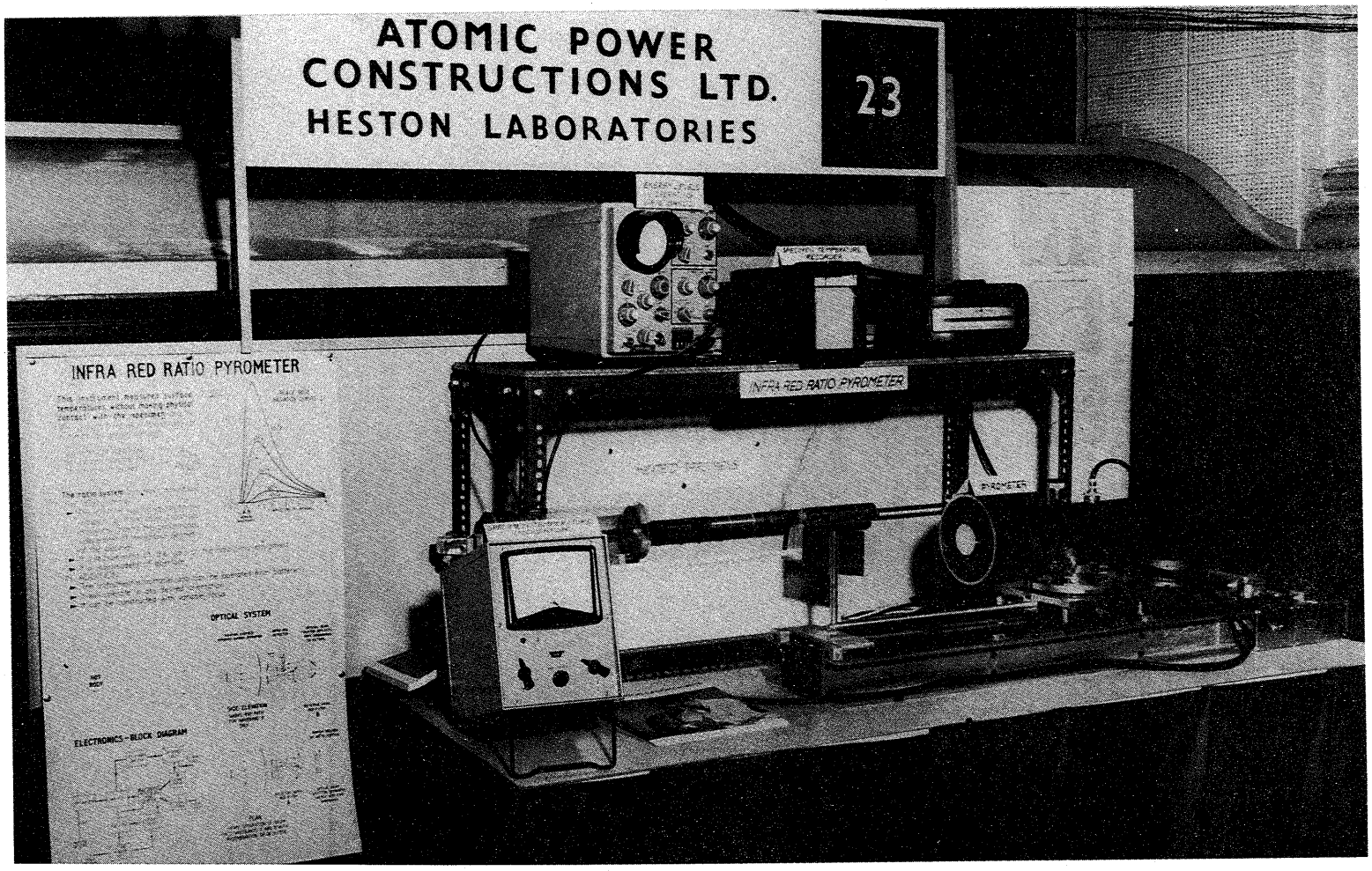

Fig. 8.5 Demonstration of Mark II pyrometer at the Physical Society Exhibition

A calibration variation of 30°C in the range 300° to 500°C on various aluminium alloy samples has been measured. Although this is not as accurate as the industry requires, the improvement over present single channel techniques is encouraging.

A calibration variation of 16°C has been recorded on typical steel rope specimens as received from the manufacturer. This is a similar application to that of aluminium where the pyrometer is required to detect departures from the ideal temperature in an industrial process where a non-contact method of temperature measurement is highly desirable.

8.8. References

1. The Advanced Gas Reactor Symposium. U.K.A.E.A., Risley, July 1959

2. Measurement of Aluminium extrusion temperature. B.N.F.M.R.A. Report No.A 1534, April 1965

3. G.K. Caulton Improved Temperature Measurement of Extruded Aluminium Alloys. B.N.F.M.R.A. Report No.A 1545, July 1965

CONCLUSION AND RECOMMENDATIONS

An infra red temperature measuring instrument has been conceived, designed and developed to the production stage. The original application for which the instrument was intended has been adhered to as far as possible and has provided a basic design specification. The instrument has been assessed and it has been shown that it conforms in general with the design specification. Due to the decreasing importance of the magnox work it has been necessary to develop the instrument for a wider application and a few examples have been given.

The instrument falls short of the design specification in one respect in that even when the filters are removed there is a small dependence on the surface geometry of the target amounting to about 1%. This must mean that each channel of the pyrometer is not "seeing" an identical portion of the target in an identical manner during successive similar time intervals. One possible explanation, namely the transverse shift of the galvanometer mirror has been offered but, as yet, has not been demonstrated to be the cause. However, it has been found during development that about 1% of the incoming energy is diverted into the wrong channel due to diffuse reflection by the galvanometer mirror. There are also some diffuse reflections from the edges of this mirror, which can be seen by an observer if the detector is removed and a tungsten lamp is viewed through the optical system while it is operational with the filters removed. This effect will also contribute to the geometry effect if it is not exactly the same for each channel.

The foregoing arguments serve to illustrate two of the disadvantages of a reflecting galvanometer modulator. A third disadvantage is that of galvanometer amplitude variation with temperature which causes a deterioration in accuracy when the aperture is partially obscured. It might be possible to cure the first effect by introducing suitable aperture stops into the system. It should also be possible to cure the third effect if the system was designed around a resistance damped galvanometer rather than the oil damped type. It would be optimistic to suggest, however, that there exists a complete solution for the second effect since no surface is capable of perfect specular reflection.

The disadvantages of the reflecting galvanometer chopper discussed above limit the accuracy of the instrument to 1 or 2% when it is considered as an energy ratioing device. Fortunately such an accuracy is acceptable in most applications so far encountered, where variations in the spectral emissivity of the target material are usually the limiting factor.

Appendix A - The Spectral Emissivity of Magnox and the Effect of Oxidation

A1 Theoretical approximation

Maxwell's equations may be solved under suitable boundary conditions to predict the behaviour of electromagnetic waves when they interact with matter. The assumption is made however that the matter is continuous with no atomistic structure and the solution is therefore only approximate.

It may be shown(1) that when a plain polarised electromagnetic wave strikes a metallic surface the wave propagated in the x direction is

$$E_x = A\, e^{j\omega\left(t - \frac{Ux}{c}\right)} \qquad (A-1)$$

where $$U^2 = \varepsilon_0\left(1 - j\frac{4\pi\sigma}{\varepsilon_0\omega}\right) \qquad (A-2)$$

σ = conductivity of metal
$j = \sqrt{-1}$
c = velocity of light
A = amplitude coefficient
ω = angular frequency
ε_0 = dielectric constant

The significance of the complex index is that the wave is absorbed as it enters the metal. This is due to the high conductivity which exists, giving rise to power loss due to Joule heating. If we write

$$U = \mu - jK \qquad (A-3)$$

then equating the real and imaginary parts of (A-2) and (A-3), we obtain

$$U^2 = \mu^2 - 2j\mu K - K^2 = \varepsilon_0 - j\frac{4\pi\sigma}{\omega}$$

$$\therefore \mu^2 - K^2 = \varepsilon_0 \qquad (A-4)$$

$$\text{and} \quad \mu K = \frac{2\pi\sigma}{\omega} = \sigma\tau \qquad (A-5)$$

where τ = periodic time of wave.

In the case of a metal, beeause of the free electrons, the conduction current is considerably larger than the displacement current Thus equation (A-4) becomes

$$\mu^2 \triangleq K^2$$

and equation (A-5) reduces to

$$\mu \triangleq K \triangleq (\sigma\tau)^{\frac{1}{2}} \qquad (A-6)$$

The reflection coefficient may be obtained by solving the equations describing the incident, the transmitted and the reflected waves at the boundary (1). The result is:-

$$r_\lambda = \frac{(\mu-1)^2 + K^2}{(\mu+1)^2 + K^2} \qquad \text{(A-7)}$$

combining (A-6) and (A-7) we have

$$r_\lambda = 1 - \frac{2}{\sqrt{\sigma\tau}} \quad \text{providing} \quad \sigma\tau \gg 1$$

and since there is no transmission

$$\varepsilon_\lambda = 1 - r_\lambda = \frac{2}{\sqrt{\sigma\tau}} \qquad \text{(A-8)}$$

Measurements of the electrical conductivity of magnox wire have been carried out at a nominal temperature of 400°C. The value obtained in m.k.s. units was 1.133×10^7 ohms^{-1} metres^{-1}. Converting this value to electrostatic units we have

$$\sigma = 1.133 \cdot 10^7 \times \frac{c^2}{10^9} \times 10^{-2} = 1.02 \cdot 10^{17}$$

Thus the emissivity in the range 1 to 4 microns is

λ microns	$\sqrt{\sigma\tau}$	$\frac{2}{\sqrt{\sigma\tau}}$
1	18.3	.109
2	27.1	.063
3	33.1	.054
4	42.8	.048

The spectral emissivity curve predicted by these values is given in Fig. A.3a

The assumption that a metal is a continuous medium is valid only at long wavelengths, where there is no effect due to bound electrons. In practice the approximation breaks down as the ultra violet region is approached. It was thought desirable therefore to measure the spectral emissivity in the region 1 to 4 microns. These measurements are now described.

A2 The measurement of the spectral emissivity of Magnox AL80 and the effect of oxidation

A.2.1 Apparatus and method

The spectral emissivity of a material has already been defined, section 2.1. The method adopted for its determination follows from the definition. A specimen of magnox was constructed in such a way that one part formed the surface of interest while another part was a close approximation to a black body radiator. The entire specimen was

maintained at a uniform temperature ($\pm 5^{\circ}C$) and could be displaced relative to a radiation measuring system so that the energy emitted by the specimen surface or the black body radiator could be examined. The ratio of the two measured values of radiation emitted for any specified sample temperature and selected wavelength gave the spectral emissivity of the specimen.

The magnox specimen (Fig. A.1.) consisted of a hollow cylindrical chamber approximately 2.5cm in diameter and 6cm long. The outer surface of the closed end of the chamber formed the specimen surface and the opposite end which was closed save for a slit, (1cm x .375cm) when viewed through the slit, formed the black body radiator. The inside of the chamber was grooved and painted with a heat resistant black paint (2). The emissivity of the black body cavity was calculated using the method of de Vos (3) and assuming an emissivity for the walls of 0.1. A figure of 0.992 was obtained which represents the most pessimistic value since it neglects the higher emissivity of the walls brought about by painting and grooving.

The magnox specimen and black body cavity combined was surrounded by four soldering iron elements for heating purposes and assembled horizontally between Sindanyo insulating slabs inside an enclosure. The mounting incorporated precision bearings with locating stops so that the specimen could be turned through 180° about a vertical axis. In this way either the magnox surface or the black body radiator could be brought precisely into the required position for measurement. The temperature of the device was monitored with twelve chromel alumel thermocouples attached to the specimen at various points and the enclosure was blackened, to avoid internal reflections and water cooled, to prevent it radiating significantly.

Radiation from the exit slit of the black body radiator (See Fig. A.2) was collected by a surface aluminised mirror system and focussed onto the entrance slit of a fluorite prism monochromator. The system was so arranged that the image of the black body radiator completely filled the entrance slit of the monochromator. The detector used was a thermopile connected to a sensitive galvanometer amplifier.

A.2.2 Results

Readings were taken at 0.1 micron intervals throughout the spectral range 1.8 to 4 microns at specimen temperatures of 350°, 400° and $450^{\circ}C$. The measurements were made initially in an air atmosphere and then carbon dioxide was introduced and the measurements were repeated after 40 hours and 70 hours oxidation at 350° to $450^{\circ}C$ had occurred.

The results are presented graphically in Fig. A.3. Fig. A.3a shows some individual determinations followed by an average of six experiments in Fig. A.3b . Also included are curves for various degrees of oxidation in the presence of CO_2 at atmospheric pressure.

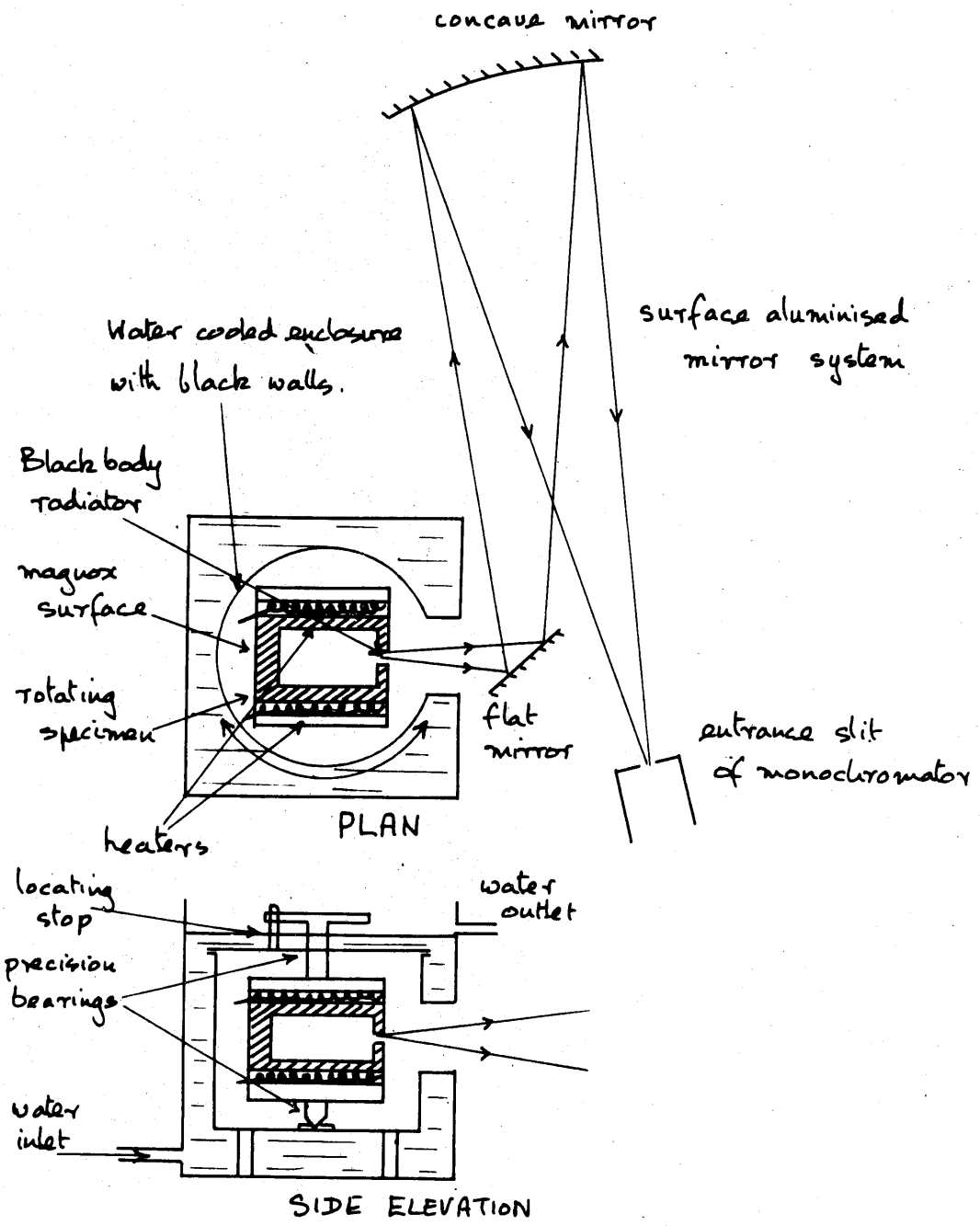

FIG A.1 Spectral emissivity apparatus.

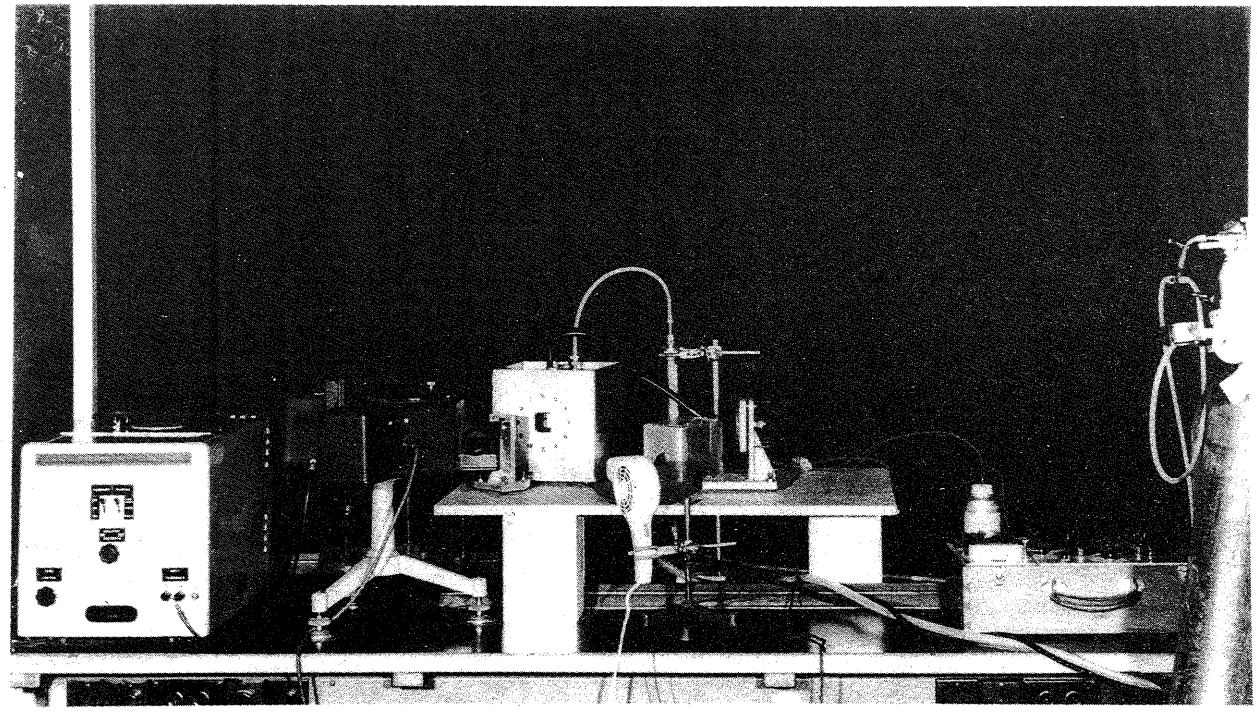

Fig. A.2 Apparatus used for measurement of the spectral emissivity of magnox

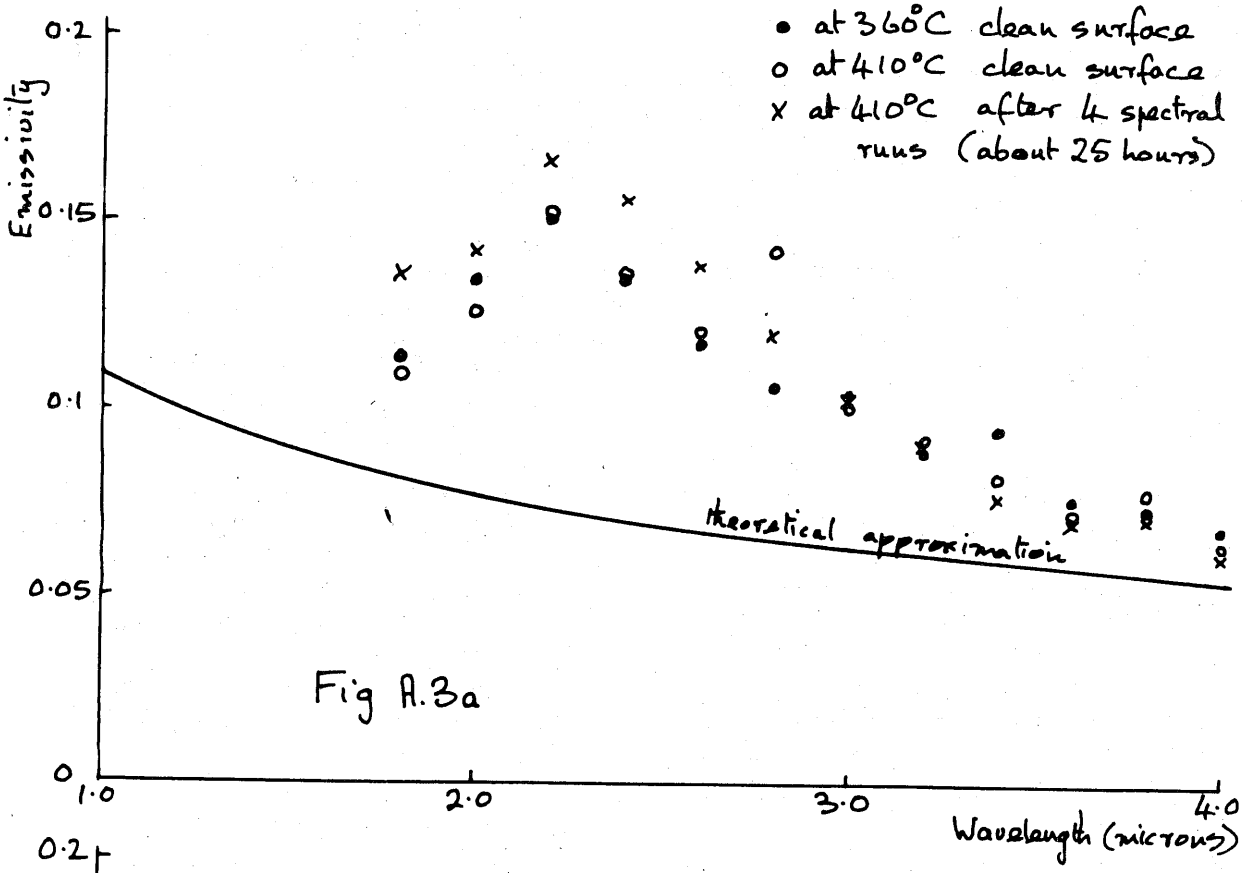

Fig A.3a

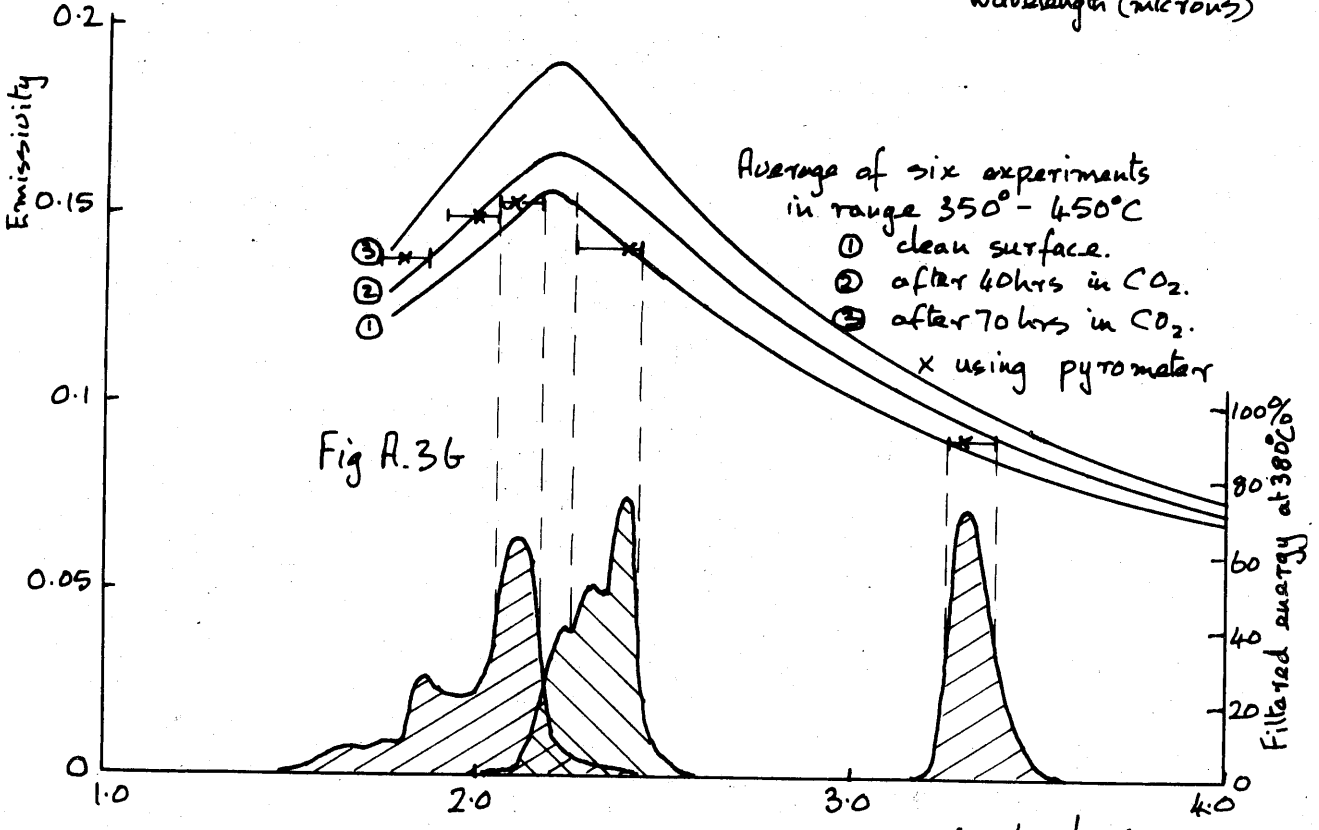

Fig A.3b

Fig A.3 The spectral emissivity of magnox.

It can be seen that the spectral emissivity for clean magnox does not follow as flat a curve as theoretical considerations (see A.1) suggest due to the presence of a peak at 2.2 microns.

Nevertheless it is possible to select two wavebands on either side of the peak where the emissivity is the same, providing the ideal situation for the ratio pyrometer. Furthermore the change in the shape of the emissivity curve as oxidation proceeds is small and it seems likely that a calibration of a ratio pyrometer on a freshly prepared surface would be maintained within a few percent, for an operational period of a few days.

A.2.3 Accuracy

The experimental error inherent in these measurements is claimed to be $\pm$2.5% for values at 2.2 microns and $\pm$5.5% for values at 4 microns.

The work described in this appendix was carried out both at A.P.C., Heston and G.E.C., Hirst Research Centre, Wembley. The experiment was conceived and the specimen heating apparatus designed at Heston, but the measurements were carried out at Wembley by the Physical Optics Group, where a Hilger and Watts fluorite prism monochromator was available. The results described above were presented by G.E.C. in report form (4).

A.3. References

1. R.W. Ditchburn. Light. London, Blackie, 1958, p.449

2. Ripolin type D.

3. J.C. de Vos. Physica. 1954, 20, p.669

4. S.E.F. Smallwood and B.J. Isherwood: G.E.C. Report number 14365 W. (Limited circulation)

Appendix B - The relation between the normal radiant intensity and the hemispherical radiant intensity from a finite surface

Consider a finite surface δs which radiates isotropically into a hemisphere. Let the radiant intensity normal to the surface be I_n watts cm^{-2} per unit solid angle. Thus the energy radiated into a hemisphere is given by

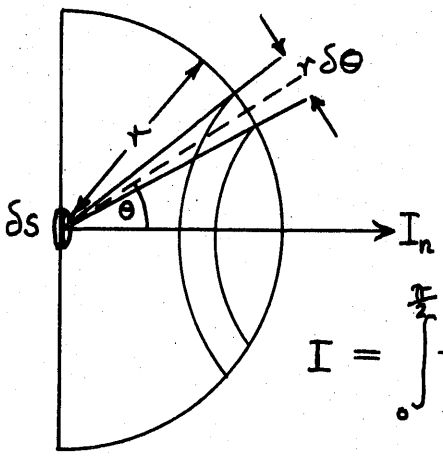

$$I = \int_0^{\frac{\pi}{2}} \frac{I_n \cos\theta \, \delta s \cdot 2\pi r \sin\theta \, d\theta}{r^2}$$

$$= 2\pi \, \delta s \int_0^{\frac{\pi}{2}} I_n \sin\theta \cos\theta \, d\theta$$

$$= 2\pi \, I_n \, \delta s \left[\frac{\sin^2\theta}{2} \right]_0^{\frac{\pi}{2}}$$

$$\therefore I = \pi \, I_n \, \delta s$$

Thus the normal radiant intensity is less than the hemispherical radiant intensity by a factor of π.

Appendix C - The design and performance of the input stage

It has been shown in 3.9 that the best signal to noise ratio from the detector is maintained if suitable impedance matching between the detector and the input stage is undertaken. The ideal source impedance for the transistor amplifier is between 1KΩ and 10KΩ and the impedance of the detector (1) is between 1MΩ and 4MΩ. An alternative impedance matching device to the transformer in this instance is a field effect transistor. This has a typical input resistance of 5MΩ and an output resistance of a few thousand ohms. Furthermore, recent manufacturing techniques have led to low noise figures in the range 1-5 dB, enabling the performance of the system to be limited by detector noise only.

The circuit, Fig. C.1, uses a silicon field effect transistor operating at a quiescent current of 1 mA. The transistor is biased by the large resistor R_4 which appears in parallel with the transistor as far as the load on the detector is concerned. The signal is obtained from the detector by connecting it in a bridge circuit with as large a series resistor as possible (R_1) to give maximum detector voltage for a given current. The detector bias current is derived from a 90v battery and for this reason the decoupling circuits R_2C_2 and R_3C_3 are incorporated to remove noise originating in the battery. The circuit uses paper condensers and low noise or good quality carbon resistors at critical positions.

The noise performance of the circuit was measured using a low noise amplifier (Solartron AA 900 and a Muirhead Wave Analyser Model No. D.489). This enabled the mean noise level to be measured in narrow well defined frequency bands and thus a complete noise spectrum for the circuit was obtained. The performance of the circuit was measured with a low noise metal oxide resistor in place of the lead sulphide detector. The noise generated in the circuit is compared with that due to the theoretical thermal noise alone and the results are plotted in Fig. C.2. It should be realised that the level meter in the wave analyser was measuring the average level of the ac waveform and was calibrated in rms for a sine wave only. Since the noise waveform of a given rms value contains relatively sharper and higher peaks than the corresponding sine wave with the same rms value (2), the noise figures obtained will be less than the true rms noise level. This may account for the error above 1000cps where a negative noise figure was obtained. Since comparison measurements were being made however the error was not important. It can be seen that the performance of the circuit at frequencies above 1000cps approaches the ideal, but at lower frequencies the performance deteriorates according to the $\frac{1}{f}$ law which is probably due to noise generated in the circuit resistors.

The above measurements were repeated with a typical cell as a source resistance with its bias current applied. It can be seen that the noise level increases now to about 10dB above thermal at 1000cps which agrees well with the typical curve (3) of Fig. 3.3 which considors thermal, generation recombination and current noise.

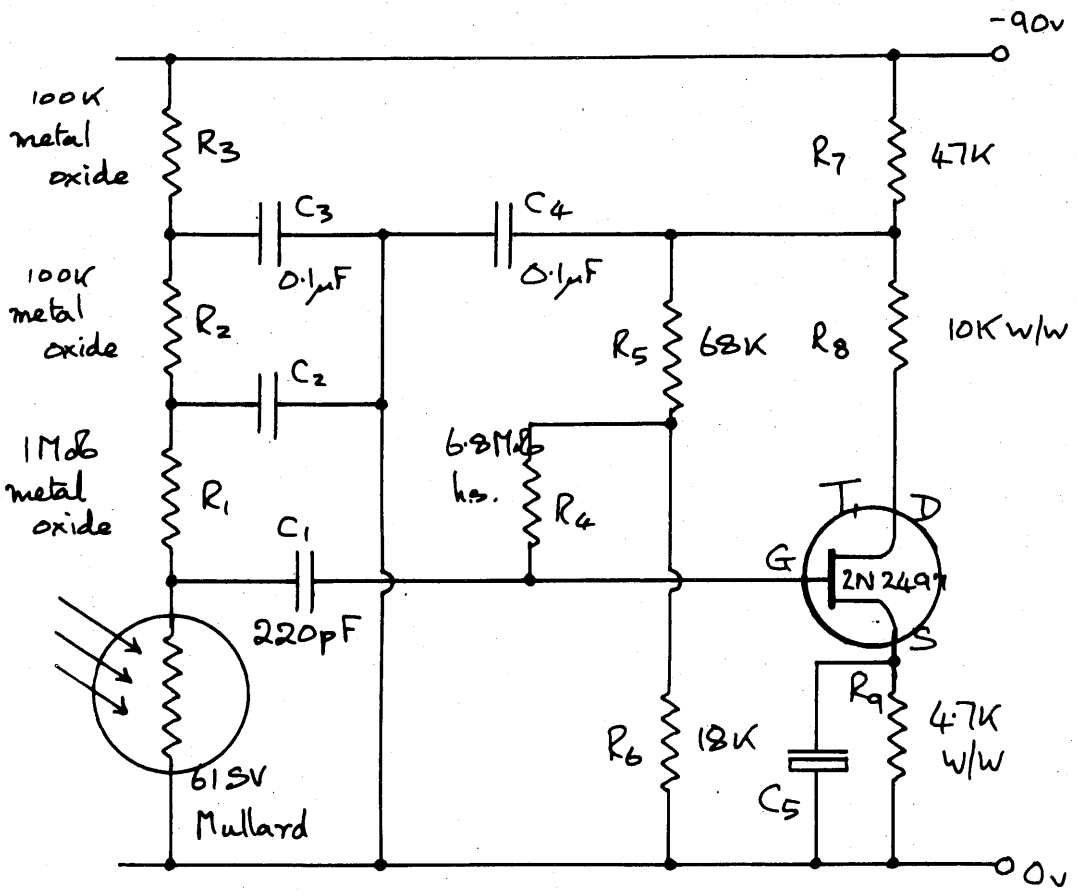

Fig C.1 Low noise preamplifier circuit.

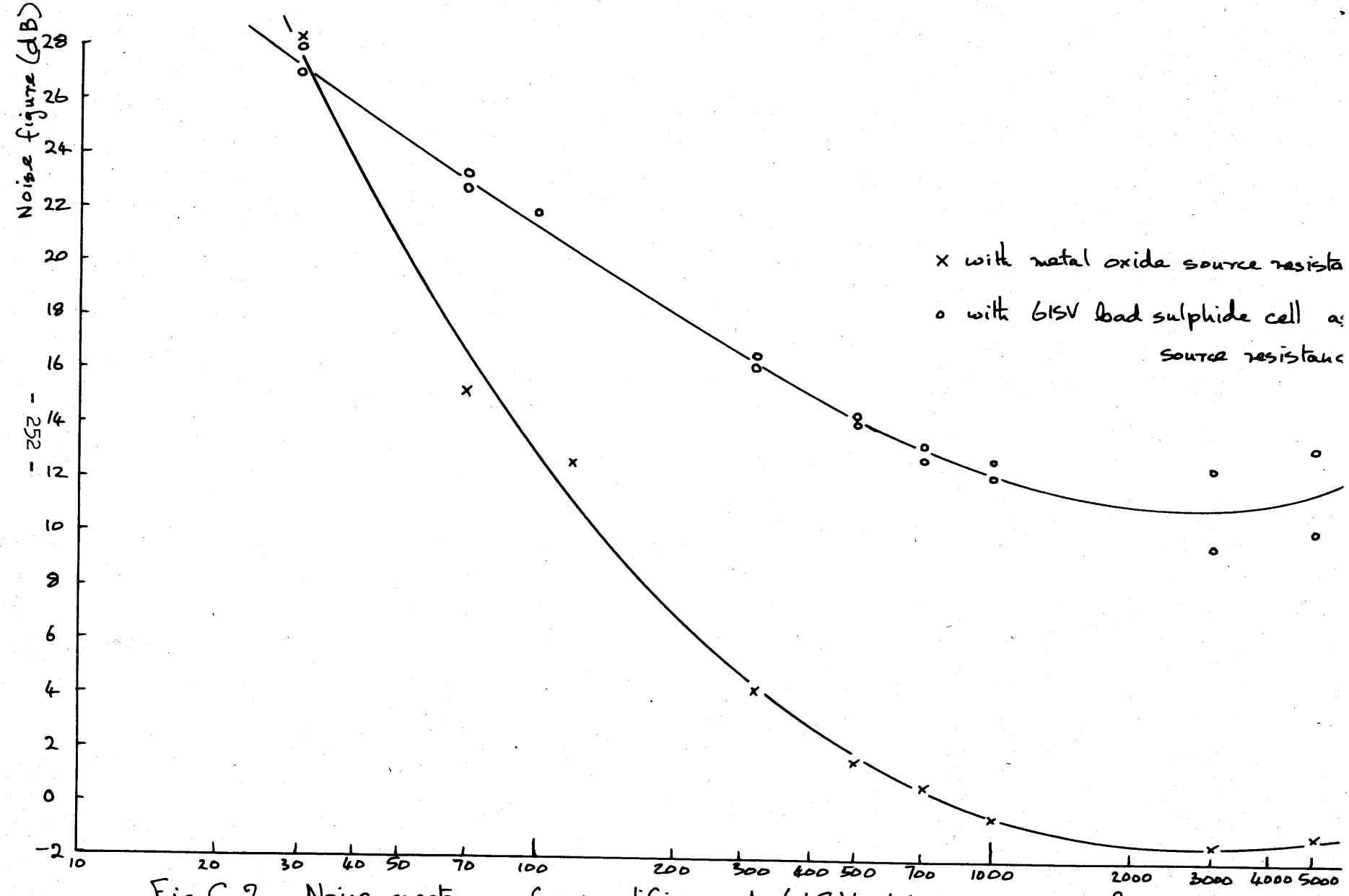

- 252 -

Fig C.2 Noise spectrum of preamplifier and 615V detector

Since the noise level in the circuit increased when the detector was added in place of its equivalent resistor, the circuit itself was acceptable. The power gain of the circuit at 1000 cps is about 250 and as a result the noise performance of the following stage is not critical according to equation (3 - 4.)

References

1. Mullard Technical Data Sheets, Photoelectric Devices 1963/4

2. A. van der Ziel. Noise. London,Chapman and Hall,1964

3. J.A. Jamieson et al. Infrared Physics and Engineering. New York,McGraw-Hill,1963,p.162

Appendix D - Fourier analysis of the signal waveform

During normal operation of the ratio pyrometer the detector is illuminated alternately by a different energy level in each channel, each level being chopped at 900cps to give the carrier frequency. This means that the detector output waveform is not symmetrical but consists of a sine wave of alternating amplitude raised above a common level which represents the non-illuminated condition of the detector, see Fig. D.1.

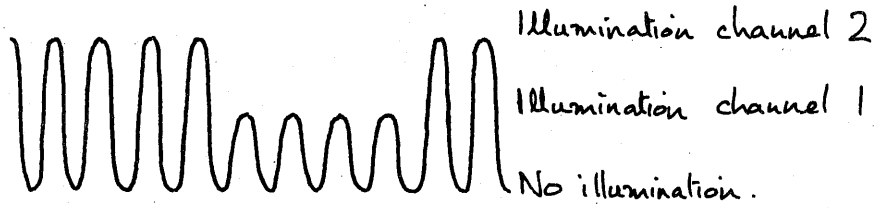

Fig D.1 Detector output waveform.

The waveform shape is inconvenient to process due to the non-linear characteristic of the control stages, where a symmetrical waveform is needed (Appendix H) and also it is difficult to preserve since a frequency response extending down to 30cps is required. The ideal waveform can be obtained from that of Fig. D.1 during the early stages of amplification by removing some of the component frequencies.

The Fourier analysis of the incoming waveform of Fig. D.1 was carried out as follows over a period corresponding to a single modulation cycle for the extreme case of zero signal in channel 1.

In this case we have

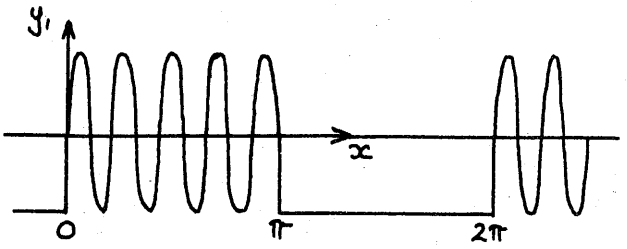

$$y_1 = a \sin 30x \qquad \text{from } x = 0 \text{ to } \pi$$

$$y_1 = -a \qquad \text{from } x = \pi \text{ to } 2\pi$$

$$y_1 = a_0 + a_1 \cos x + a_2 \cos 2x + \cdots + a_n \cos nx + b_1 \sin x + b_2 \sin 2x + \cdots + b_n \sin nx$$

where:-

$$a_0 = \frac{1}{2\pi} \int_0^{2\pi} y \, dx$$

$$a_n = \frac{1}{\pi} \int_0^{2\pi} y \cos nx \, dx$$

$$b_n = \frac{1}{\pi} \int_0^{2\pi} y \sin nx \, dx$$

These coefficients were evaluated using the boundary conditions above and the sum of the individual components was obtained.

$$y_1 = -\frac{a}{2} + \underset{(900\text{cps})}{\frac{a}{2} \sin 30x}$$

$$= \underset{(30\text{cps})}{+\frac{a}{\pi}\left(\frac{1}{29} + \frac{1}{31}\right) \cos x} + \cdots \underset{(30(2n-1)\text{ cps})}{\frac{a}{\pi}\left(\frac{1}{30-(2n+1)} + \frac{1}{30+(2n-1)}\right) \cos(2n-1)x}$$

$$= \underset{(30\text{cps})}{+\frac{2a}{\pi} \sin x} + \underset{(90\text{cps})}{\frac{2a}{3\pi} \sin 3x} + \cdots \underset{(30(2n-1)\text{cps})}{\frac{2a}{(2n-1)\pi} \sin(2n-1)x}$$

The amplitude of each component was calculated and plotted in the histogram of Fig. D.3a relating amplitude to frequency.

The process was now repeated for the required wavefrom of Fig. D.2.

In this case

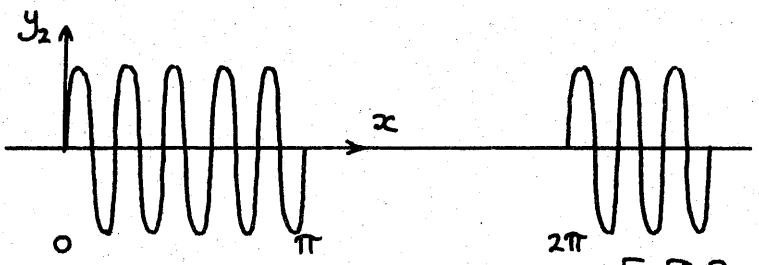

Fig D.2 Ideal waveform

$y_2 = a \sin 30x$ from $x=0$ to π

$y_2 = 0$ from $x=\pi$ to 2π

Again the Fourier coefficients were evaluated using these boundary conditions and the following sum was obtained, see Fig. D.3b .

$$y_2 = \underset{(900\,cps)}{\frac{a}{2}\sin 30x} + \frac{a}{\pi}\left(\frac{1}{29}+\frac{1}{31}\right)\underset{(30\,cps)}{\cos x} + \frac{a}{\pi}\left(\frac{1}{27}+\frac{1}{33}\right)\underset{(90\,cps)}{\cos 3x} + \cdots\cdots \frac{a}{\pi}\left(\frac{1}{30-(2n-1)}+\frac{1}{30+(2n-1)}\right)\underset{(30(2n-1)\,cps)}{\cos(2n-1)x}$$

If the subtraction $y_2 - y_1$ is performed then we obtain a 30cps square wave

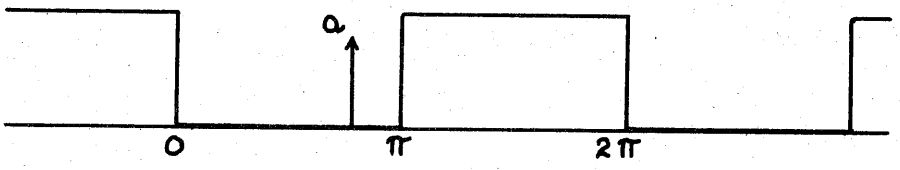

with components.

$$y_2 - y_1 = \frac{a}{2} - \underset{(30\,cps)}{\frac{2a}{\pi}\left(\frac{1}{29}+\frac{1}{31}\right)\cos x} - \underset{-256-}{\frac{2a}{3\pi}\sin 3x} \cdots\cdots - \underset{(90\,cps)}{\frac{2a}{(2n-1)\pi}\sin(2n-1)x}$$

$(30(2n-1)\,cps)$

It can be seen that the amplitude of the n^{th} component in the signal waveform y_1 is the sum of a sine and cosine term of the form

$$\frac{2a}{(2n-1)\pi}\sin(2n-1)x + \frac{a}{\pi}\left(\frac{1}{30-(2n+1)} + \frac{1}{30+(2n-1)}\right)\cos(2n-1)x$$

and performing the subtraction reduces the amplitude of the n^{th} component to

$$\frac{2a}{(2n-1)\pi}\sin(2n-1)x$$

Consider now the 30cps component

let us define an angle θ by:

$$\cos\theta = \frac{A}{\sqrt{A^2+B^2}} \; ; \; \sin\theta = \frac{B}{\sqrt{A^2+B^2}}$$

which is permissible since

$$\sin^2\theta + \cos^2\theta = 1$$

where $A = \frac{1}{30-(2n-1)} + \frac{1}{30+(2n-1)}$

$$B = \frac{2}{2n-1}$$

$$\therefore A\cos x + B\sin x = \sqrt{A^2+B^2}(\cos x\cos\theta + \sin x\sin\theta)$$

$$= \sqrt{A^2+B^2}.\cos(x-\theta)$$

Thus if the instantaneous amplitude of each component in y_1 of the form A cos x + B sin x is multiplied by $\frac{A}{\sqrt{A^2+B^2}}$ and the phase is advanced by θ then terms of the form A cos x in y_2 are obtained. This transformation may be achieved to a close approximation by the following circuit.

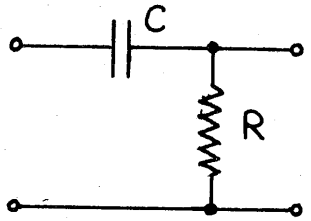

$$\text{attenuation} = \frac{R}{\sqrt{R^2 + \frac{1}{\omega^2C^2}}}$$

$$\text{phase change} = \theta$$

$$\text{where } \tan\theta = \frac{B}{A} = \frac{1}{\omega CR}$$

The time constant required to transform each term the correct amount is given in Table XV and the reduction in amplitude is compared with that given by a time constant chosen near the centre of the range.

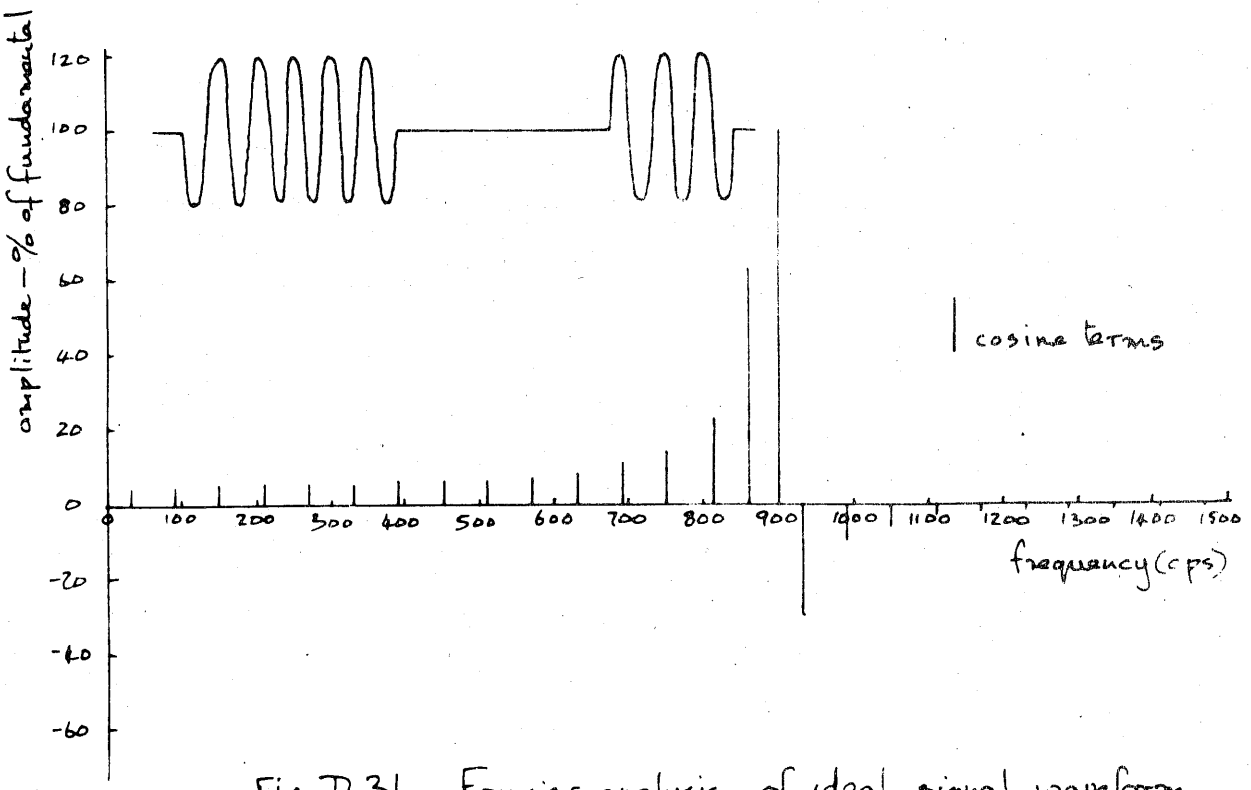

Fig D.3b Fourier analysis of ideal signal waveform

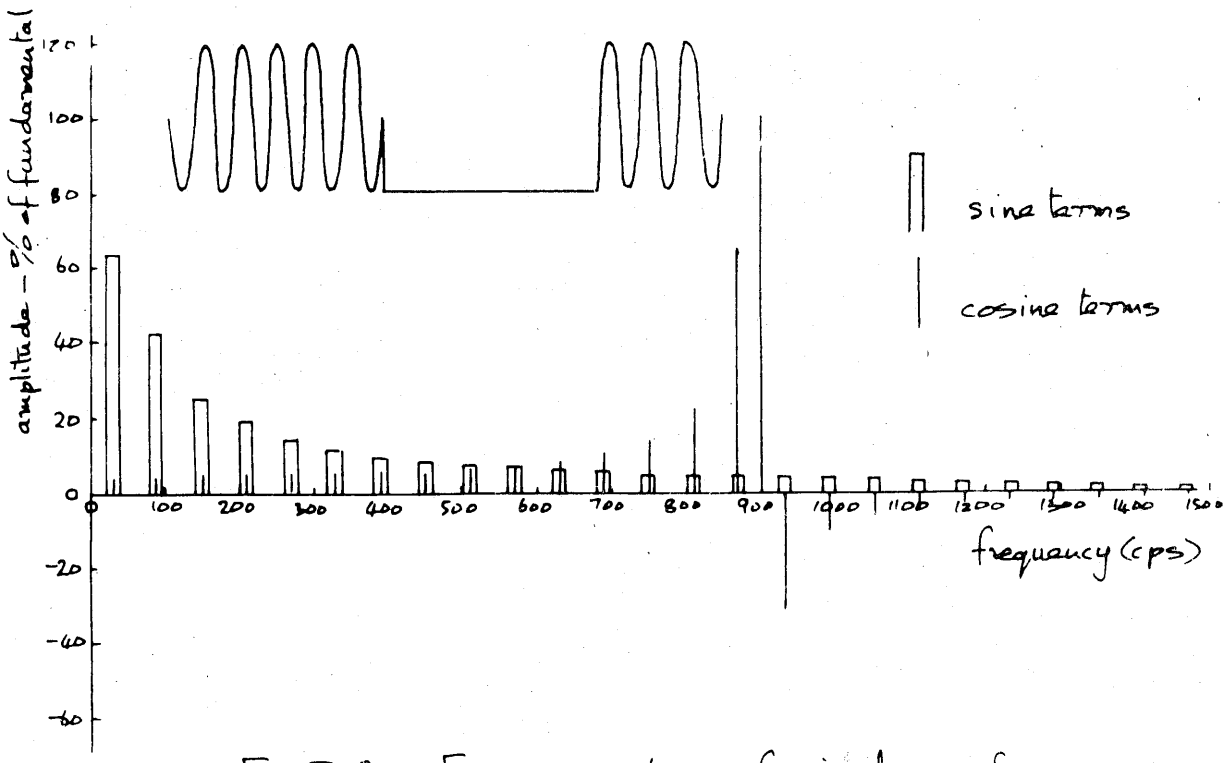

Fig D.3a Fourier analysis of signal waveform

TABLE XV

n	RCx 10^{-4}	Reduction in amplitude dB	Reduction in amplitude by RC = 2.6 x 10^{-4}
1	1.776	29.6	26.2
2	1.783	20	16.7
3	1.818	18.4	12.5
4	1.866	12.4	9.8
5	1.942	10.8	7.9
6	2.041	8.2	6.4
7	2.179	6.6	5.4
8	2.353	5.1	4.5
9	2.611	3.9	3.9
10	2.959	2.8	3.3
11	3.48	1.4	2.9
12	4.27	1.1	2.5
13	5.81	0.58	2.2
14	9.26	0.26	2.0
15	20.68	0.08	1.7

The circuit with time constant 2.6×10^{-4} produces more phase change and attenuation at 900cps than the ideal but this is nevertheless quite small amounting to an attenuation of 1dB and a phase advance of approximately 30°.

Thus when the signal waveform is passed through the above circuit a good approximation to the required waveform is to be expected. In practice a small amount of overshoot occurs between channels. This is due to the inability of the circuit to operate satisfactorily on the high frequency components of the 30cps square wave, which is removed in the transformation.

The operation on the signal waveform described above is performed with C_1 and the parallel combination of R_4 and the input resistance of T_1, at the input to the head amplifier. The time constant of this circuit is approximately 6×10^{-4}.

Appendix E - A System employing Focal Isolation (1)

E.1. Dispersion in a lens

Consider a thin lens in air with focal length f having surfaces with radii r_1 and r_2 and made from a material of refractive index μ. The simple thin lens formula (2) states that

$$\frac{1}{f} = (\mu - \mu')\left(\frac{\mu'}{r_1} - \frac{\mu'}{r_2}\right) \qquad \text{(E-1)}$$

$$\therefore \frac{1}{f} = (\mu - 1)\left(\frac{1}{r_1} - \frac{1}{r_2}\right) \qquad \text{(E-2)}$$

since $\mu' = 1$ for air

differentiating

$$-\frac{1}{f^2}\cdot\frac{df}{d\mu} = \frac{1}{r_1} - \frac{1}{r_2}$$

$$\therefore \frac{df}{f} = \left(\frac{1}{r_1} - \frac{1}{r_2}\right) d\mu\,(-f)$$

substitution of f from equation (E-2) and cancelling gives

$$\frac{df}{f} = -\frac{d\mu}{\mu - 1} \qquad \text{(E-3)}$$

Thus for the small wavelength range $\Delta\lambda$ the change of focus Δf occurs since the refractive index is a function of the wavelength. The variation of refractive index of a material with wavelength is known as the dispersion and data are available in the form: dispersion $= \frac{d\mu}{d\lambda}$
Over a small wavelength range $\Delta\lambda$ the change in refractive index associated with it is

$$\Delta\mu = \frac{\Delta\mu}{\Delta\lambda}\cdot\Delta\lambda$$

substitution in (E-3) gives

$$\Delta f = \frac{-f}{\mu - 1}\cdot\frac{\Delta\mu}{\Delta\lambda}\cdot\Delta\lambda \qquad \text{(E-4)}$$

The wavelength range of interest is either 1.75 to 2.3 microns or 2.3 to 3.5 microns. To obtain maximum change of focus the dispersion and refractive index should be as large as possible. The dispersion curves for various optical materials (3) are given in Fig. E.1 to 5. The slopes of these curves at the above wavelengths are given in Table XVI in microns^{-1}.

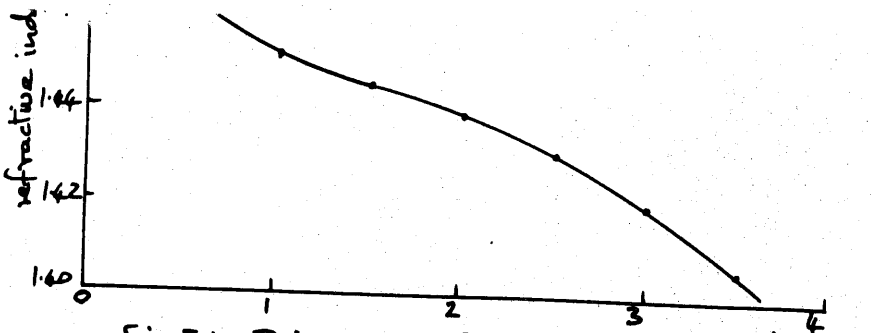

Fig E.1 Dispersion of fused silica

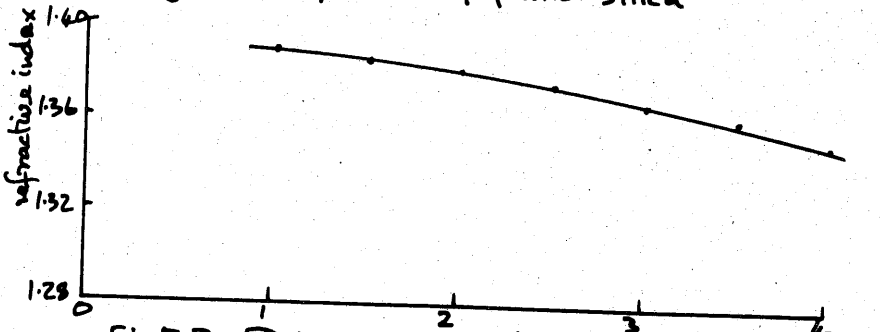

Fig E.2 Dispersion of lithium fluoride

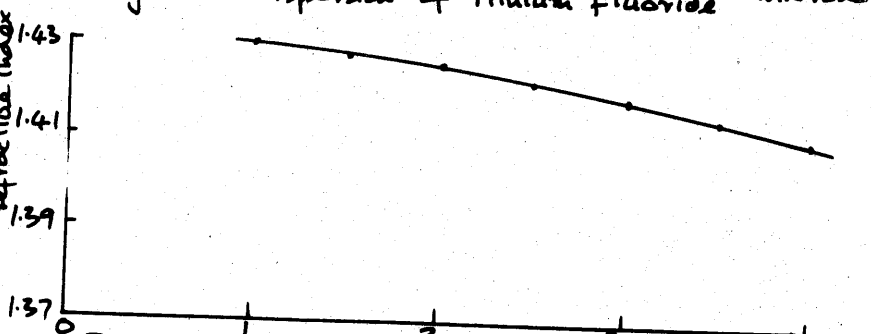

Fig E.3 Dispersion of calcium fluoride

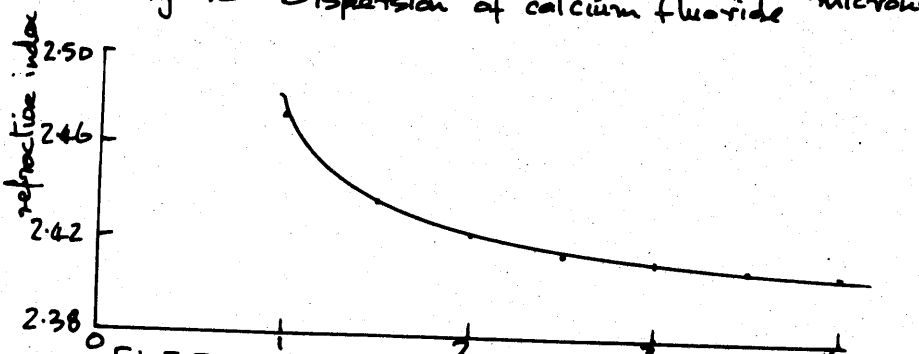

Fig E.5 Dispersion of arsenic trisulphide

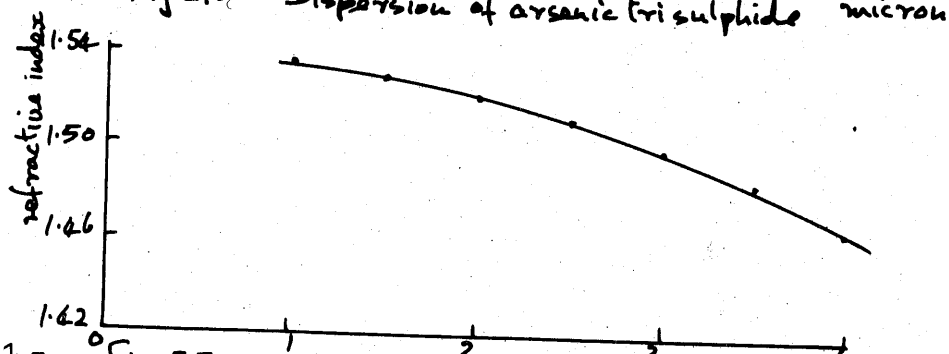

Fig E.5 Dispersion of crystalline quartz

TABLE XVI

Material	$\frac{d\mu}{d\lambda}$ at 1.75 microns	$\frac{d\mu}{d\lambda}$ at 2.3 microns	$\frac{d\mu}{d\lambda}$ at 3.5 microns
Fused silica	0.013	0.016	0.028
Lithium fluoride	0.0093	0.0113	0.017
Calcium fluoride	0.0048	0.0058	0.008
Arsenic trisulphide	0.0280	0.013	0.004
Crystalline quartz	0.0144	0.0184	0.034

And in the ranges 1.75 to 2.3 microns and 2.3 to 3.5 microns

	1.75 to 2.3 microns	2.3 to 3.5 microns
Fused silica	.0145	.022
Lithium fluoride	.0103	.0142
Calcium fluoride	.0053	.0069
Arsenic trisulphide	.0205	.008
Crystalline quartz	.0164	.0262

The largest dispersion occurs for arsenic trisulphide followed by crystalline and fused quartz in the range 1.75 to 2.3 microns and for crystalline and fused quartz in the range 2.3 to 3.5 microns. It would be convenient to use fused quartz because it permits operation at both sets of wavebands without component change, should an alternative detector to lead sulphide be used at any time, since it has a consistently high dispersion over the whole wavelength range of interest. Furthermore, it does not suffer birefringence which occurs in crystalline quartz.

The following calculations are based therefore, on the figures for fused quartz. They have been carried out for the wavebands 1.75 microns to 2.3 microns. Figures for 2.3 to 3.5 microns would be similar due to the similar dispersions in this range. The fractional change of focal length between the two wavebands will be.

$$\frac{\Delta f}{f} = -\frac{\Delta\mu}{\Delta\lambda}\cdot\frac{\Delta\lambda}{\mu-1} = \frac{-.0145 \times .55}{.451}$$

$$= 1.77.10^{-2}$$

and over the waveband at 1.75 microns

$$\frac{\Delta f}{f} = -\frac{.013 \times .3}{.455} = 8.57.10^{-3}$$

and at 2.3 microns

$$\frac{\Delta f}{f} = -\frac{.016 \times .4}{.447} = 1.43.10^{-2}$$

E.2. For a point object at infinity

If we assume for the moment that the object is a point source at infinity then we require the stop size necessary to pass a bandwidth $\Delta\lambda$ without interruption. Consider Fig. E.6

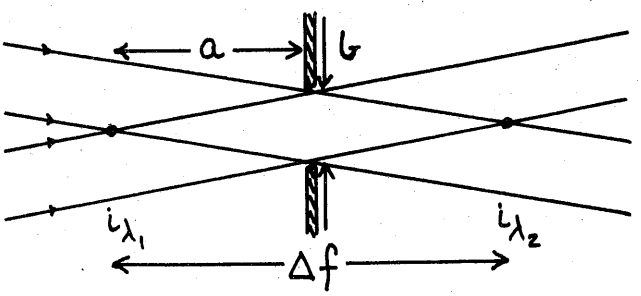

Fig E.6

i_{λ_1}, i_{λ_2} are the images due to wavelengths at the opposite extremities of each waveband.

The focal ratio is defined as $\frac{\text{diameter}}{\text{focal length of objective element}}$

i.e. $F = \frac{D}{f} = \frac{b}{a}$ where $a = \frac{\Delta f}{2}$

$$\therefore b = \frac{F.\Delta f}{2}$$

The illumination at a surface removed from the focus can be considered uniform to a first approximation to the extremity of the circular image for a point object Fig. E.7.

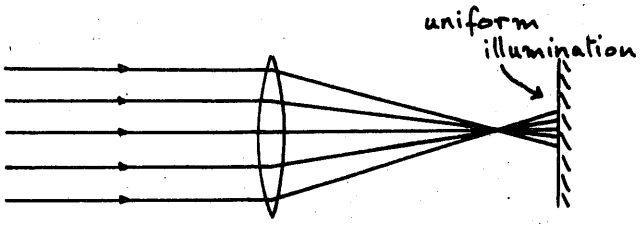

Fig E.7

thus to reduce the energy passed by the aperture stop to 50% at i_{λ_1} and i_{λ_2} a diameter of $\frac{F.\Delta f}{2\sqrt{2}}$ is required.

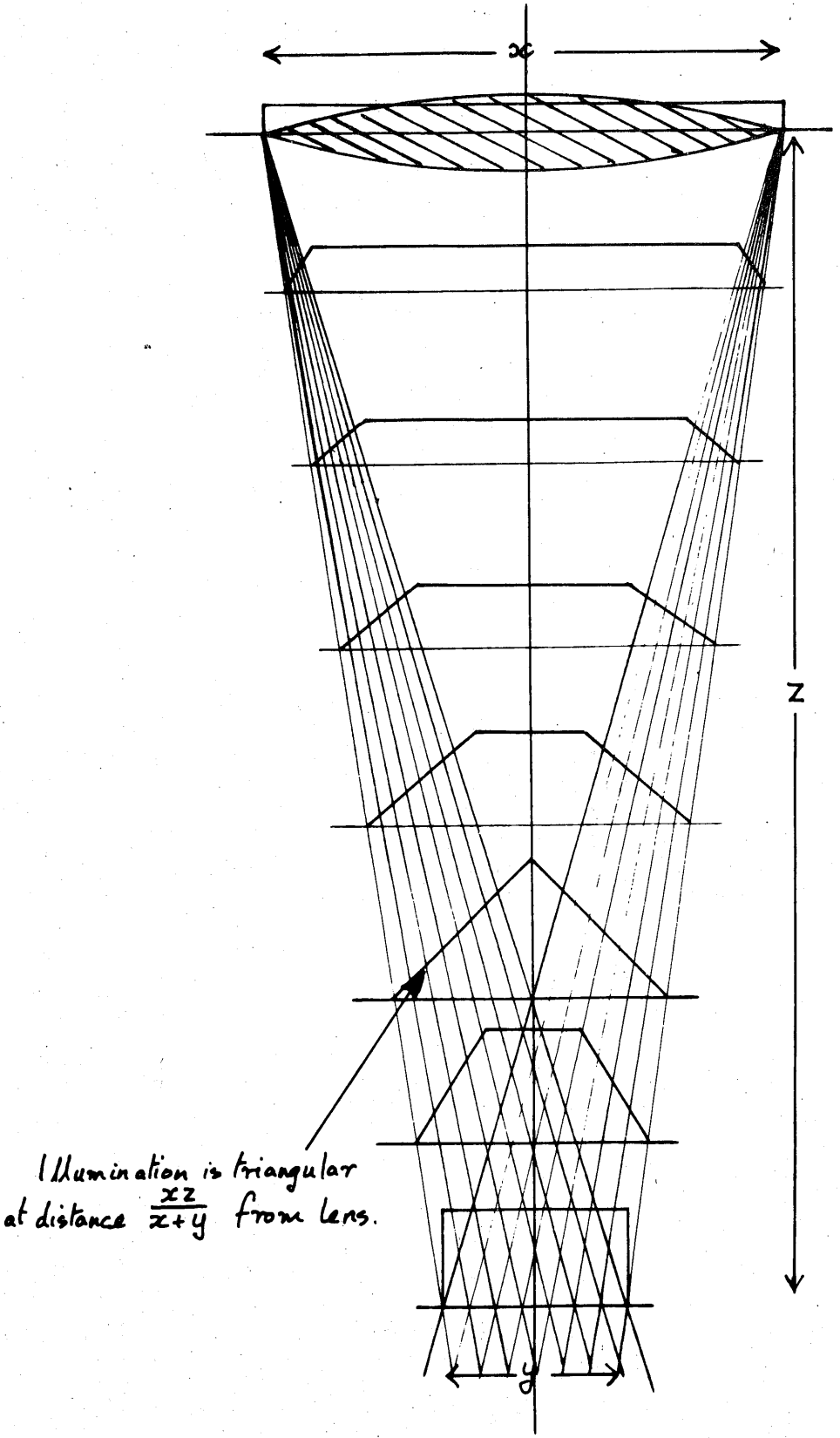

FIG. E.8 Illumination at points along lens axis due to uniformly illuminated object.

E.3 For an extended object at infinity

In the practical case an extended source must be considered. Figure E.8. shows graphically how the illumination will vary away from the focus for an extended source.

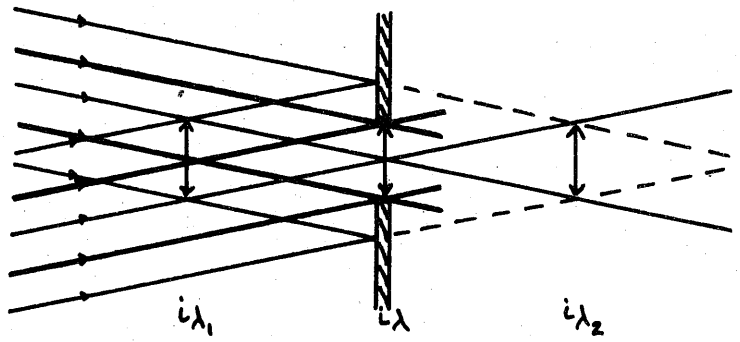

Fig E.9

Thus in Fig. E.9 energy forming images at points i_{λ_1} and i_{λ_2} will illuminate a surface coinciding with the aperture stop in the same way as energy forming an image at i_λ will illuminate a surface placed at i_{λ_1} or i_{λ_2} . The illumination now takes the form of the volume of a cone in intensity. The stop diameter which will reduce the energy forming images at i_{λ_1} and i_{λ_2} by 50% is S which may be calculated with the aid of Fig. E.10, the volume of revolution of the shaded area being half the volume of the cone. In this case:-

$$S = \frac{1}{2}r \qquad (E\text{-}5)$$

Fig E.10

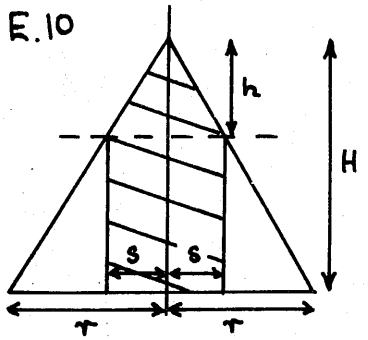

i.e. the stop diameter is $\frac{F.\Delta f}{2}$ for a reduction of 50% at i_{λ_1} and i_{λ_2} with no reduction at i_λ.

If the source is further extended then a point is soon reached where the energy due to both i_{λ_1}, i_{λ_2} and i_λ is the same Fig. E.11

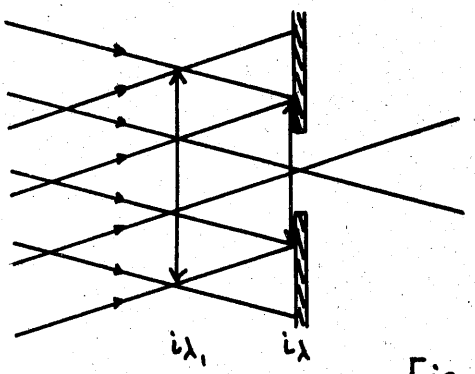

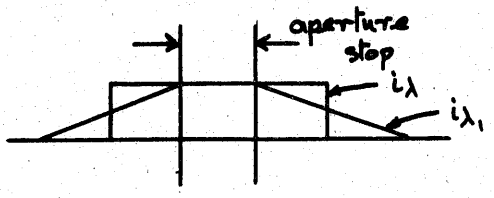

Fig E.11

This emphasises the need to provide a finite image at the aperture stop.

Thus we have:

(i) for a given stop size the size of image required for just 100% pass is the same as the stop.

(ii) for a point source the resolution approaches infinity theoretically as the stop size approaches zero.

(iii) if loss in energy can be tolerated a stop which is smaller than the image produces a more square bandpass than (i).

E.4. For an extended object at a finite distance

The argument of focal isolation is now extended to an object at a finite distance and the parameters are optimised. An estimation of the shape of the band pass for the optimum system is then made. If we consider the equation relating image and object distance for a thin lens in air.

$$\frac{1}{u} + \frac{1}{v} = \frac{1}{f} \qquad (E\text{-}6) \qquad \therefore -\frac{du}{u^2} - \frac{dv}{v^2} = 0 \qquad (E\text{-}7)$$

the system will have a minimum length when $u+v$ = minimum

$$\text{ie. } \frac{u+v}{uv} = \frac{1}{f} \qquad \therefore \frac{d(u+v)}{dv} = \frac{v}{f}\cdot\frac{du}{dv} + \frac{u}{f}$$

$$= \frac{u^2}{f.v} + \frac{u}{f} \quad \text{using (E-7)}$$

when $u+v$ is a minimum $\dfrac{d(u+v)}{dv} = 0$

$$\therefore u = v$$

substitution back in (E-6) leads to $u+v = 4f$

We now assume that a primary finite image of a portion of the extended source is available. If we have an object diameter a and the object lens focal length is adjusted to produce an image size a also, then $u = v$ since the magnification is unity. We require the variation of image distance v with focal length

$$\frac{1}{u} + \frac{1}{v} = \frac{1}{f}$$

for u = constant

$$-\frac{dv}{v^2} = -\frac{df}{f^2} \qquad \therefore \quad \frac{dv}{df} = \frac{v^2}{f^2}$$

or over a small range of focus Δf;

$$\Delta v = \frac{v^2}{f^2}\Delta f \qquad \text{(E-8)}$$

In order to pass 100% radiation at the centres of the wavebands and 50% at the edges we have by a similar argument as in the deduction of (4-5):-

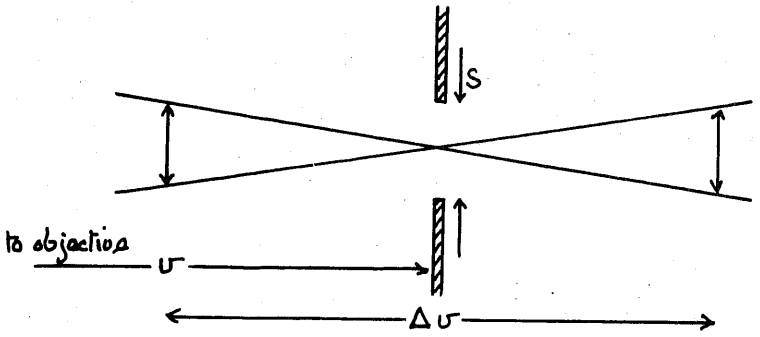

Fig E.12

$$\frac{\Delta v}{2s} = \frac{v}{D}$$

$$\therefore \quad s = \frac{D\Delta v}{2v} \qquad \text{(E-9)}$$

If we use an f/4 entrance aperture as in the feasibility study (section 2.7) we find that for equal object and image distances:-

$$f = 2D \qquad \text{(E-10)}$$

Combining equations (E-8) (E-9) and (E-10) we obtain $v = \frac{2f^2 s}{D\Delta f} = \frac{4fs}{\Delta f}$

If the system is to be as short as possible then v should be small. This leads to small values for s and f and a large value for Δf. Using the values of $\frac{\Delta f}{f}$ for fused quartz already given we have

$$v_{1.75} = \frac{4.10^3}{8.57} s_{1.75} = 467 s_{1.75}$$

$$v_{2.3} = \frac{4.10^2}{1.43} s_{2.3} = 280 s_{2.3}$$

$$\text{Since } v_{2.3} \simeq v_{1.75} = v$$

$$\therefore v = 280 s_{2.3} = 467 s_{1.75}$$

The stops are not the same diameter because of the different dispersion of quartz at the two wavebands. This will lead inevitably to different transmission curve shapes at each waveband if the same stop is used for each. For an object size of 0.1cm diameter and a stop diameter of 0.1cm also, to give the required attenuation at the edges of the waveband,

$$v = 467 \times 0.1 = 46.7\text{cm}$$

Thus the system would be 187cm long with a lens 12cm in diameter

E.5. Diffraction effects

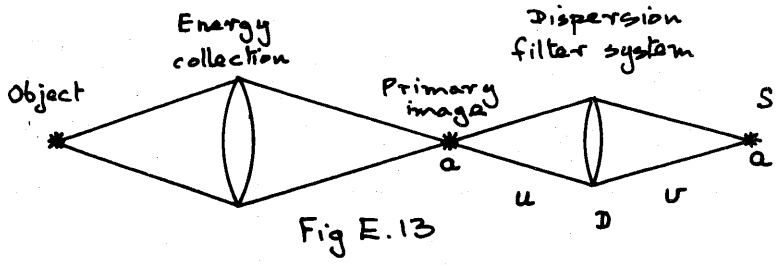

Fig E.13

for a circular aperture the limit of resolution of the lens occurs at the Rayleigh limit when

$$\theta = \frac{1.22\lambda}{D} = \frac{s}{v}$$

where θ is the angle subtended by the image from the lens.

$$\therefore \frac{s}{v} = \frac{1.22\lambda}{D}$$

$$\therefore D = \frac{1.22\lambda v}{s} = 0.114\text{cm}$$

In the above case D is 12cm which is 100x larger than the limit of resolution. A similar argument will apply to the primary imaging system.

E.6. Transmission curves for filters

If the illumination curves for the aperture stop at various positions on the axis are used, for wavelengths in the region around 1.75 microns and 2.3 microns then the spectral transmission characteristics of the aperture may be calculated

we have:- $\frac{1}{f}\left(\frac{\Delta f}{\Delta\lambda}\right)_{1.75} = 2.86.10^{-2}$ per micron

$\frac{1}{f}\left(\frac{\Delta f}{\Delta\lambda}\right)_{2.3} = 3.58.10^{-2}$ per micron

$\Delta v = \frac{v^2}{f} \cdot \frac{\Delta f}{f}$; $f = 24$cm ; $D = 12$cm.

1.75 micron waveband		2.3 micron waveband	
Wavelength	Δv (cm)	Wavelength	Δv (cm)
$1.75 \pm .2$	$\pm .52$	$2.3 \pm .2$	$\pm .65$
$1.75 \pm .15$	$\pm .39$	$2.3 \pm .15$	$\pm .49$
$1.75 \pm .1$	$\pm .26$	$2.3 \pm .1$	$\pm .33$
$1.75 \pm .05$	$\pm .13$	$2.3 \pm .05$	$\pm .16$
1.75	0	2.3	0

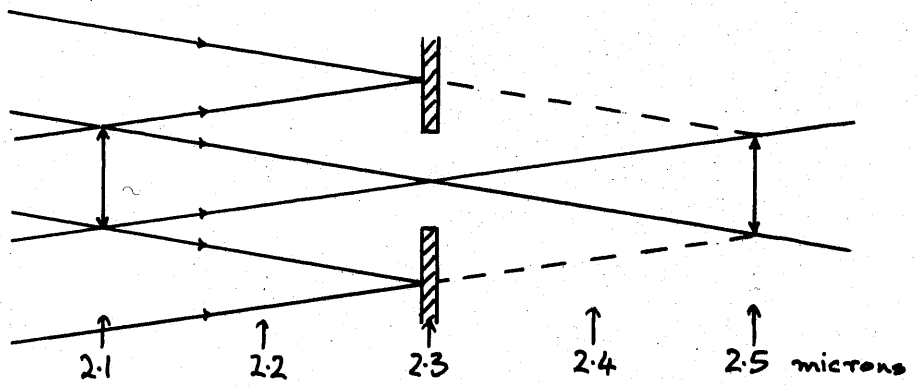

Fig E.14

The fraction of the energy at each wavelength which passes through a stop of diameter 0.1cm is required. The figures have been calculated by considering the fraction of the volume under revolutions of the illumination curves which lie directly over the aperture for the stop in each position. Fig. E.14 shows the situation for the 2.3 micron waveband and Fig. E.15 shows the resulting spectral transmission for both wavebands.

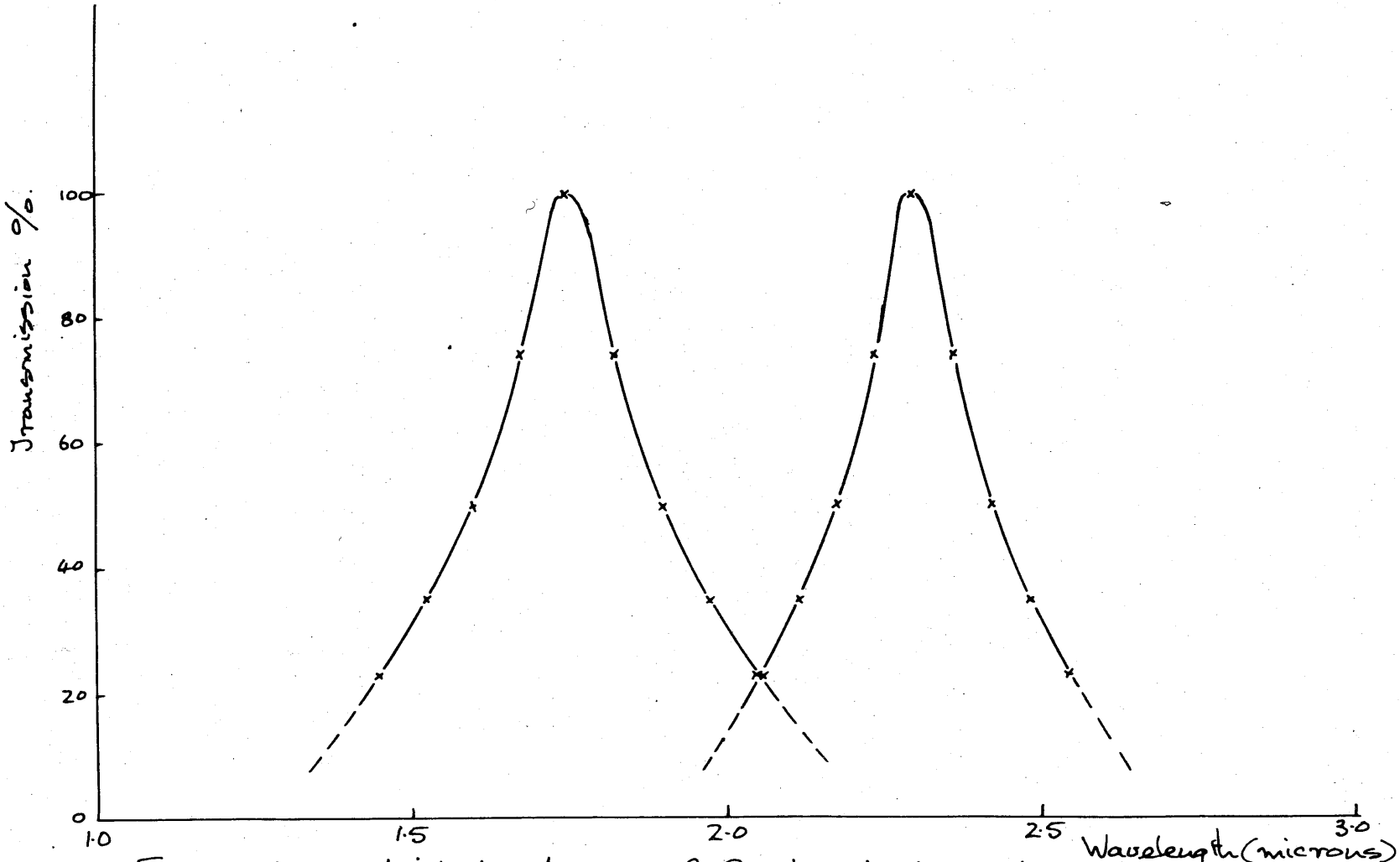

Fig. E.15 Optical band pass of focal isolation system.

Although in principle this system appears feasible the degree of filtering required leads inevitably to large diameter lens and large image distances. Various layouts were considered where the energy is collected via a Cassegrainian type mirror system to produce the primary image and the waveband selection is achieved by moving a plane mirror back and forth along the optical axis of the system, the motion being synchronised with a motor driving a 1000cps chopper wheel to provide the signal carrier frequency.

E.7. Effect of optical aberration

Apart from the size of such a system the need to reduce aberrations to a low level provided the main reason for rejecting the technique.

The five Seidel aberrations (3,4) were considered for the system using third order theory when the approximations $\sin\theta \to \theta$ for small angles is improved to $\sin\theta \to \theta - \theta^3/3!$. Since the system produces a small image on axis the effects of coma, astigmation, curvature of field and distortion were neglected. To reduce spherical aberration a lens where the refraction is shared equally at both surfaces is required. The results of calculations for two single lens are given; a double convex lens (f = 24cm) and two plano-convex lenses ($f_1 = f_2$ = 48cm) with the convex surfaces adjacent. The lateral spherical aberration is defined in terms of the difference in the reciprocals of the image distances for paraxial and marginal rays (3). This relationship applies toasingle lens and in the case of the doublet the spherical aberration due to each lens has been added.

$$\text{Lat S.A.} = \frac{1}{v_h} - \frac{1}{v_p}$$

$$= \frac{h^2}{8f^3} \cdot \frac{1}{\mu(\mu-1)} \left[\frac{\mu+2}{\mu-2} q^2 + 4(\mu+1)pq + (3\mu+2)(\mu-1)p^2 + \frac{\mu^3}{\mu-1} \right] \quad \text{(E-11)}$$

where $p = \dfrac{v-u}{v+u} = \dfrac{2f}{u} - 1$ known as position factor (E-12)

$q = \dfrac{r_2 + r_1}{r_2 - r_1}$ known as shape factor (E-13)

v_m = image distance for marginal ray

v_p = image distance for paraxial ray

The lateral spherical aberration is a minimum for a particular value of the shape factor q in equation (E-11). By differentiating and equating to zero we obtain:- $q = \dfrac{2(\mu^2-1)p}{\mu+2}$ (E-14)

E.8. Application to double convex lens

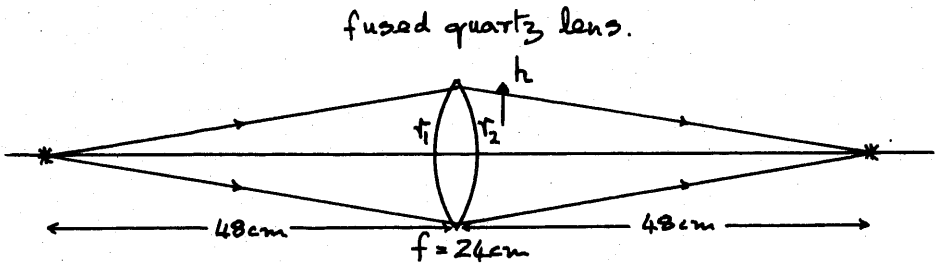

Fig E.16

substituting in (E-12) gives $p = 0$
from (E-14) this leads to $q = 0$ for minimum lateral spherical aberration

i.e. $$\frac{r_2 + r_1}{r_2 - r_1} = 0$$

$$\therefore \quad r_1 = -r_2$$

substituting in equation (E-2) gives the surface radia for paraxial focal length 24cm ; $r_1 = 21{\cdot}2$ cm ; $r_2 = -21{\cdot}2$ cm

$$\text{Lateral S.A.} = \frac{h^2}{8\times 13840} \cdot \frac{1}{1{\cdot}44\times{\cdot}44}\left[\frac{1{\cdot}44^3}{{\cdot}44}\right] = 9{\cdot}6.10^{-5}.h^2$$

Table XVII shows both the lateral and longitudinal spherical aberration arising from rays traversing the lens at different distances from the axis, h.

TABLE XVII

h (cm)	$\frac{1}{v_m} - \frac{1}{v_p}$	$v_p - v_m$
0	0	0
2	$3.84.10^{-4}$	.85
4	$1.54.10^{-3}$	3.3
6	$3.47.10^{-3}$	6.85

E.9. Application to doublet

Consider the second half of the doublet

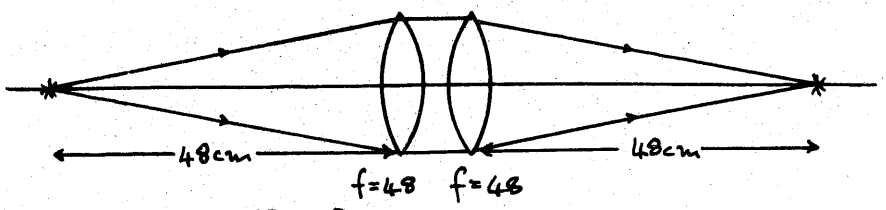

Fig E.17.

substitution in (E-12) gives $p = -1$ and from (E-14) $q = \cdot 622$ } hence

and from (E-2) $\frac{1}{r_1} - \frac{1}{r_2} = \cdot 0472$ } r_1 and r_2

$$\text{Lat. S.A.} = \frac{h^2}{8 \times 110500} \cdot \frac{1}{\cdot 634} \left[\frac{3 \cdot 44}{\cdot 44} (\cdot 622)^2 - 4(2 \cdot 44) \cdot 622 + 6 \cdot 32 \times \cdot 44 + \cdot 68 \right] = 1 \cdot 17 . 10^{-5} h^2$$

Again the table shows the lateral and longitudinal spherical aberration at various values of h.

Table XVIII

h	$\frac{1}{v_m} - \frac{1}{v_p}$	$v_p - v_m$	$2(v_p - v_m)$
0	0	0	0
2	$4.68.10^{-5}$	0.11	0.22
4	$1.87.10^{-4}$	0.42	0.84
6	$4.21.10^{-4}$	0.94	1.88

In practice it is found that a doublet consisting of two plano-convex lenses with convex faces adjacent approaches very nearly the above minimum spherical aberration condition. Such a doublet would be more economical because assuming a sufficiently flat blank is used only one surface requires figuring at each lens.

From these calculations it can be seen that the spherical aberration of the focal isolation system will produce differences in image distance for marginal and paraxial rays, which have the same order of magnitude as the chromatic aberration upon which the system relies for the wavelength separation. This would cause a deterioration in the filtering properties of the system with a subsequent reduction in the sensitivity curve of ratio R against temperature T. The spherical aberration could be reduced or even eliminated by a more complex lens arrangement but the increased cost and absorption of energy becomes a serious disadvantage. These factors combined with the inevitable size of the system led to its rejection for this particular application. The one great advantage of the system lies in the ability to vary the wavelengths and band pass characteristics by adjusting the stop sizes and their distance apart. Thus its use is to be recommended at longer wavelengths.

E.10 References

1. H. Rubens and R.W. Wood. Phil.Mag.,1911,21,p.294

2. F.A. Jenkins and H.E. White. Fundamentals of Optics,2nd Edition. New York,McGraw-Hill,1950,p.62

3. R.W. Wood. Physical Optics. London,MacMillan,1934,

4. A.E. Conrady. Applied Optics and Optical Design.Vol.1.1929

Appendix F - The angular sensitivity of the galvanometer/magnet system

The magnet system normally employed with pencil galvanometers in ultra violet light recorders was considered too bulky for use in the pyrometer optical system. It was decided that sufficient deflection would be attainable using a smaller magnet because the maximum current handling of the galvanometer coil was far in excess of that normally used.

A magnet of convenient size was obtained and three sets of pole pieces were manufactured. To measure the sensitivity a S.E.L. type A900 galvanometer was mounted vertically in the magnet with its stem protruding through a small hole in the back. A pair of pole pieces was attached and the angular sensitivity of the galvanometer was measured with the aid of a lamp and scale. The measurements were made at a frequency of 900cps and the peak to peak amplitude was taken as the distance between points within which an image of the lamp could be seen in the galvanometer mirror.

Sensitivity curves for each set of pole pieces are shown in Fig. F.1 from which it can be seen that the most sensitive performance was obtained from type C. A sensitivity of 53 mA r.m.s/degree (2.8mA peak to peak/degree) was measured in this case.

According to the manufacturers data the A1600 galvanometer is 0.365 times the sensitivity of the A900. Thus in a magnet block with pole pieces as type C above we may expect:-

Galvanometer type	resonant frequency	rms current sensitivity	nominal resistance	peak to peak voltage for 5½° deflection
A 900	900 cps	0.53mA/degree	120	0.99v
A 1600	1600 cps	1.45mA/degree	70	1.58v

It was eventually decided to use a type A1600 galvanometer because of its faster response to a 900cps square wave. Thus a minimum drive voltage of 1.58 volts is required to provide the carrier frequency of 900cps. The channel selection drive waveform at 30cps must be sufficient to provide a deflection of 5.5° in the case of the symmetrical galvanometer drive (Fig. 6.5a) and 11° in the case of the assymmetrical galvanometer drive (Fig. 6.5b). Due to the improvement in response at lower frequencies it may be assumed that a 30cps square wave of peak to peak amplitude 3.6 volts will be more than adequate for each type of drive.

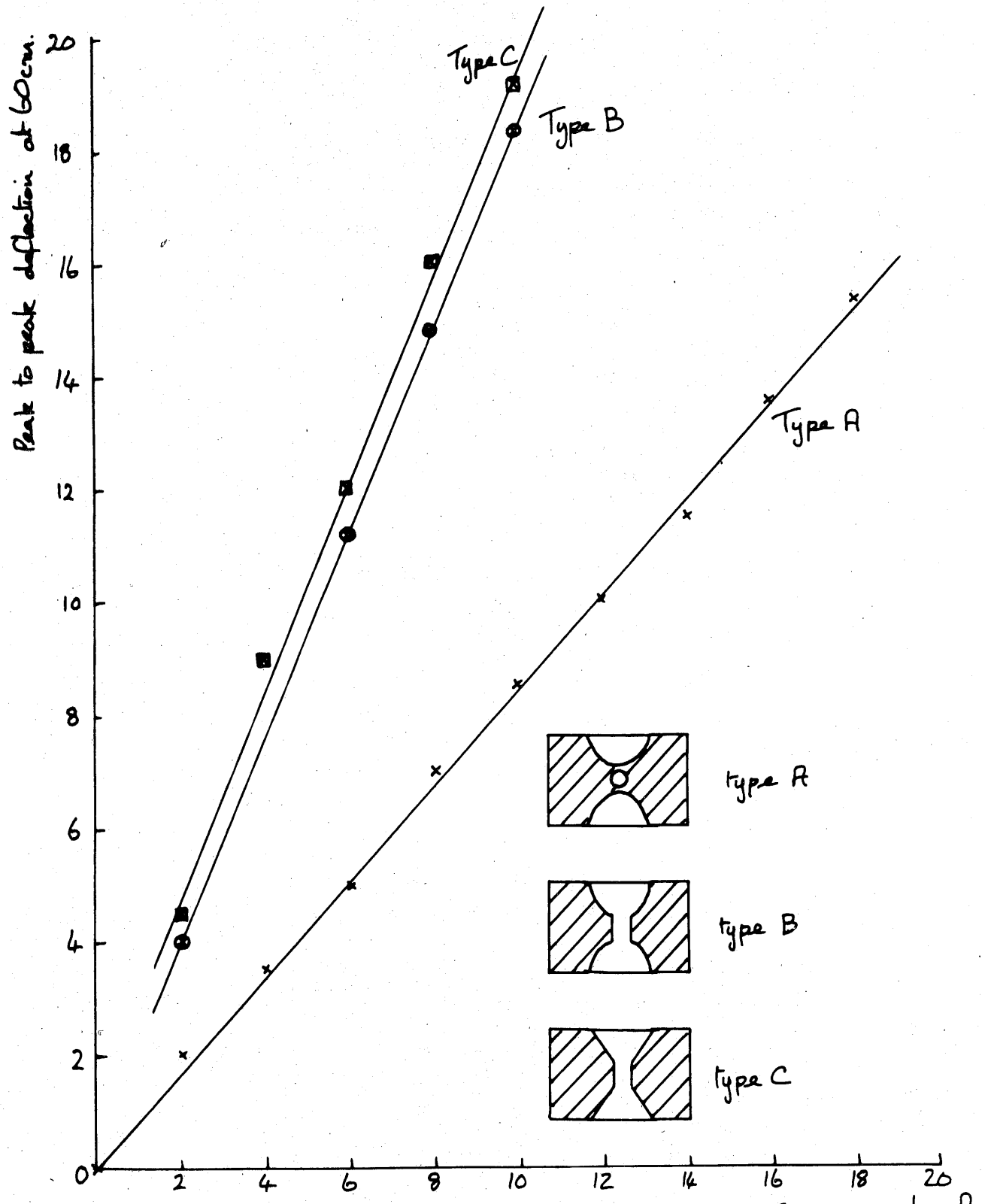

Fig F.1 Sensitivity of A900 pencil galvanometer with various pole pieces.

Appendix G - Spherical aberration in collecting system

G.1. Spherical aberration

If rays of light from a point object are focussed by a spherical mirror, then in general a point image will not be formed. This is due to rays striking the mirror at different distances from the axis being focussed to different points. If the image distance for paraxial rays is v_p and for marginal rays v_m then we have:

longitudinal spherical aberration (long. S.A) = $v_p - v_m$ (G-1)

lateral spherical aberration (lat. S.A) = $\frac{1}{v_m} - \frac{1}{v_p}$ (G-2)

In the following calculations the longitudinal spherical aberration of the optical system of Fig. 4.14 is deduced in three stages. The first stage applies to the image formed by the concave mirror M_1. The image distances for marginal and paraxial rays are then used to obtain object distances for M_2 and in the second stage of the calculation, the longitudinal spherical aberration of the image formed at M_3 is deduced. Finally, the aberration of the final image formed by M_4 is calculated in a similar manner.

G.1.1 Stage 1 - Longitudinal spherical aberration for M_1

The image is located by ray tracing and the parameters used are illustrated in Fig. G.1. The calculation is based on the following two laws:-

angle of incidence = angle of reflection

$$s(2r-s) = h^2 \qquad \text{(G-3)}$$

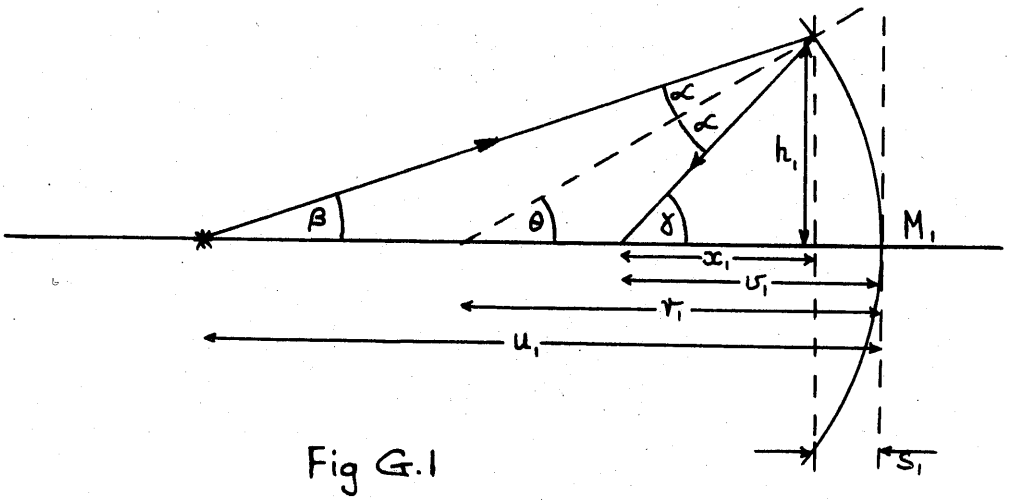

Fig G.1

The calculation is carried out for various object distances and radii of curvature. The only quantity which is constant throughout is the diameter of the primary mirror M_1 which is 15cm. Using this value the calculation takes the following form:-

from (G-3) $S_1 = r_1 - \sqrt{r_1^2 - h_1^2}$

1 Calculate S_1 from above equation
2 Calculate θ using $\tan\theta = \frac{h_1}{r_1 - s_1}$
3 Calculate β using $\tan\beta = \frac{h_1}{u_1 - s_1}$
4 Calculate α using $\alpha = \theta - \beta$
5 Calculate γ using $\gamma = \theta + \alpha$
6 Calculate x_1 using $x_1 = \frac{h_1}{\tan\gamma}$
7 Calculate v_{m_1} using $v_{m_1} = x_1 + s_1$

repeat calculation for $u_1 = 40, 50, 60$ cm
$h_1 = 2.5, 5, 7.5$ cm
$r_1 = 17.5, 22.5, 30$ cm

The image distance for paraxial rays cannot be obtained by the above method since h = 0 in this case.

However we have:-

$$\gamma = \beta + 2\alpha \; ; \quad \gamma = \theta + \alpha \quad \therefore \; \gamma = 2\theta - \beta$$

and if these angles are small

$$\tan\gamma = 2\tan\theta - \tan\beta$$

$$\frac{h}{v_{p_1}} = \frac{2h}{r_1} - \frac{h}{u_1}$$

thus $\frac{1}{v_{p_1}} = \frac{2}{r_1} - \frac{1}{u_1}$ which is exact when the rays are paraxial since (G-4)

$\theta \to \tan\theta$ as $\theta \to 0$
$\beta \to \tan\beta$ $\beta \to 0$
$\gamma \to \tan\gamma$ $\gamma \to 0$

The above formula is used to calculate the paraxial image distances v_{p_1} for various radii of curvature and the spherical aberration at A is then obtained using equation (G-1).

The results of these calculations are given in Fig. G.5 to 7 showing the variation of longitudinal spherical aberration with distance from the axis and radius of curvature for various object distances.

G.1.2 Stage 2 - longitudinal spherical aberration for M_2

The parameters used in this calculation are illustrated in Fig. G.2.

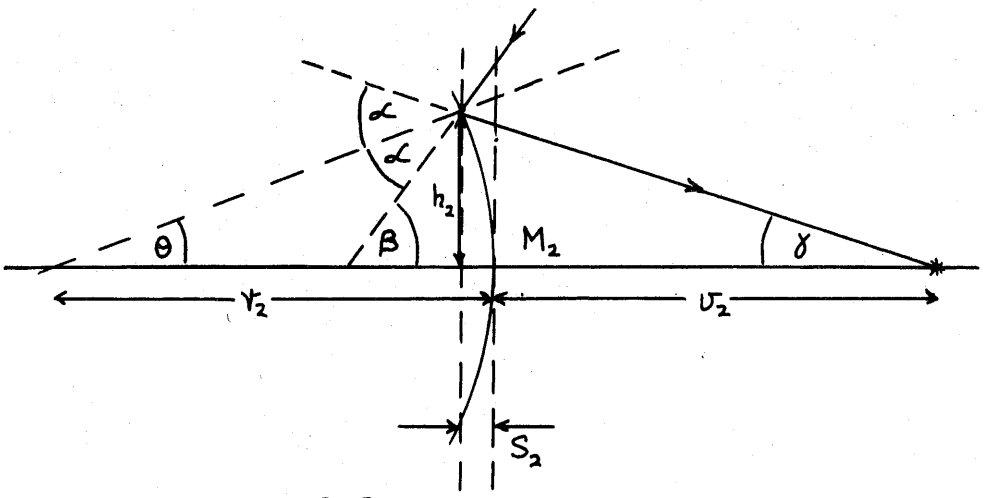

Fig G.2

An image distance for paraxial rays v_{p_2} is now assumed and used to obtain the object distance for M_2. Due to the spherical aberration of M_2 the object distance for paraxial rays is larger than for marginal rays.

Thus the calculation proceeds as follows:-

$$S_2 = r_2 - \sqrt{r_2^2 - h_2^2}$$

1 Calculate S_2 from above equation
2 Calculate θ using $\tan\theta = h_2 / r_2 - S_2$
3 Calculate β using $\tan\beta = h_2 / v_2 + S_2$
4 Calculate α using $\alpha = \theta + \beta$
5 Calculate γ using $\gamma = 2\alpha - \beta$
6 Calculate x_2 using $x_2 = h_2 / \tan\gamma$
7 Calculate u_{m_2} using $u_{m_2} = x_2 + S_2$

repeat calculation for $h_2 = \cdot 835, 1\cdot 67, 2\cdot 5$ cm
$r_2 = 10, 12\cdot 5, 15, 17\cdot 5, 20, 22\cdot 5$ cm
$v_2 = 22\cdot 5, 25, 27\cdot 5, 30$ cm

8 Calculate the object distance for paraxial rays u_{p_2} using equation (G-4) with suitable sign changes
9 Determine longitudinal spherical aberration of object distance using equation (G-1).

The results of these calculations for the particular case $r_2 = 15$ and $v_2 = 22.5, 30$ are given in Fig. G.8 from which it can be seen that the spherical aberration is not sensitive to changes in the image distance v_2.

The calculation now proceeds for particular radii of curvature r_1 and r_2 for which the aberration of the primary image distance $v_{p_1} - v_{m_1}$ is almost the same as that of the secondary object distance $u_{p_2} - u_{m_2}$. When these two quantities are equal exact cancellation is obtained. In the calculation the image distances for M_1 and the object distances for M_2 are used to obtain h for the marginal rays striking M_2. The image distance for marginal rays v_{m_2} is obtained finally as follows:-

1 Calculate $x_2 + S_2 = u_{p_2}$ for paraxial rays using equation (A4-4) with suitable sign changes for given values of v_{p_2}, r_2
2 Calculate u_{m_2} using longitudinal spherical aberration figures for particular u_1 and r_1 chosen
3 Calculate h_2 using $h_2 = 3u_{m_2} / v_{m_1}$
4 Calculate S_2 from equation (G-3)
5 Calculate θ using $\tan\theta = h_2 / r_2 - S_2$
6 Calculate γ using $\tan\gamma = h_2 / u_{m_2} - S_2$
7 Calculate α using $\alpha = \gamma - \theta$
8 Calculate β using $2\alpha - \gamma = \beta$
9 Calculate $v_{m_2} + S_2$ using $v_{m_2} + S_2 = h_2 / \tan\beta$
10 Hence obtain v_{m_2}

This calculation has been carried out for r_1 = 26.25cm, 28.8cm and r_2 = 15, 17.5, 20 and 22.5cm, for object distances u_1 = 40, 50 and 60cm, see Fig. G.10, 11. The longitudinal spherical aberration is seen to be zero at object distances in the region 40 to 45cm and it approaches zero as r_2 increases at larger object distances. The aberration is smallest at the shorter object distances, because the primary mirror, which has the larger contribution to the spherical aberration due its large aperture, is operating with the object near its centre of curvature where the spherical aberration would be zero. The aberration reduces with increasing r_2 because this implies larger values of h_2 for the same image distance and hence larger cancellation of the spherical aberration of M_1. The value of r_2 is eventually limited by the blockage of the incoming energy since the required diameter of M_2 increases as r_2 increases. The values chosen for the optical system are

r_1 = 28.8cm; d_1 = 15cm
u_1 = 60cm (for observation of fin roots, see section 4.4.5)
u_1 = 45cm (for observation of fin tips and other surfaces)
r_2 = 20cm; d_2 = 5cm (20% blockage)

When operating with an object distance of 60cm the circle of least confusion will not be greater than .050cm in diameter. This is illustrated in Fig. G.3 where rays at various distances from the axis are shown. A parabolic variation of spherical aberration with h has been assumed (see Fig. G.8)

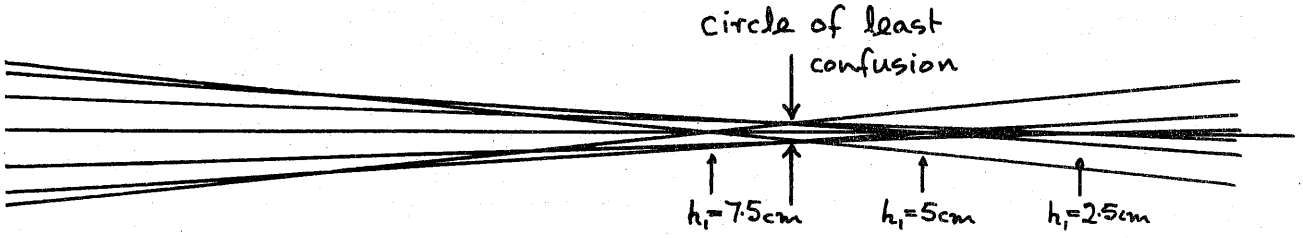

Scale 5:1 Fig. G3.

G.1.3 Stage 3 - longitudinal spherical aberration for M_4

The final stage of the optical system can be considered to consist of two concave mirrors facing each other, between which the energy passes in a parallel beam (see section 4.4.3). If the longitudinal spherical aberration is calculated for the parallel beam forming an image at C, Fig. G.4, and the value doubled, then the aberration produced by the system for a point object at B will be obtained. It should be noted that rays in the horizontal plane, which were paraxial for M_1 and M_2, now become marginal or become paraxial depending on the setting of M_3 at a particular instant. In the vertical plane rays occupying the upper region become marginal due to the permanent inclination of M_3 to the vertical:-

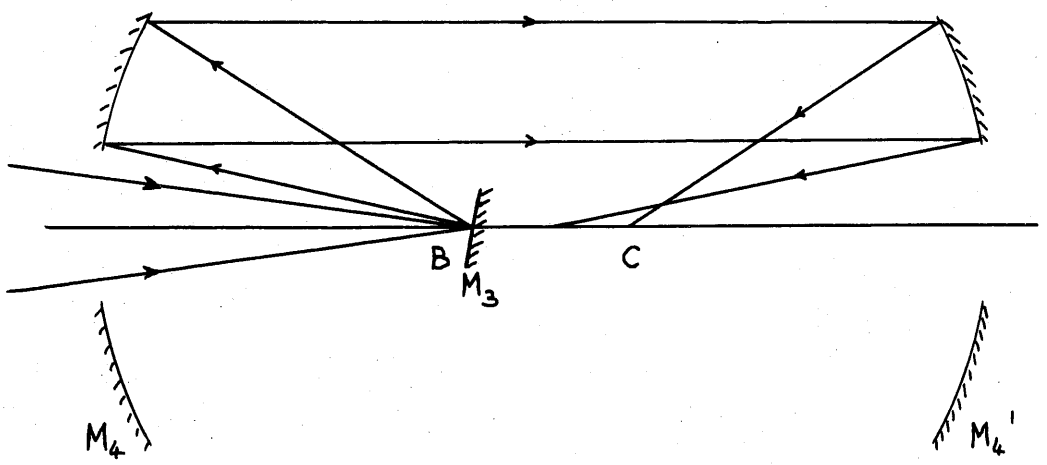

Fig. G.4

The calculation proceeds in the same way as in stage 1. Since the energy incident on M_4 is considered parallel however, the calculation is somewhat simplified. The calculation is carried out for values of h = 1, 1.94 and 2.88cm and the following values are obtained, using r_4 = 21cm.

h	$\upsilon_{p4} - \upsilon_{m4}$	for M_4 & M_4'	referred to original paraxial ray at h_4 = 1.94cm
0	0	0	+ .150
1	.020	.040	+ .110
1.94	.075	.150	0
2.88	.193	.385	-.235

In practice the aberration in this final section of the system is not important if the detector sensitive area is made slightly larger than the mirror M_3. In this case all the energy falling on M_3 will reach the detector in spite of the aberration of M_4. Thus only the aberration of M_1 and M_2 need be considered.

G.2. Accuracy of mirror figures

Each mirror is figured to better than 4 fringes per cm . If it is assumed that the figure on each mirror is no better than this then the distortion will add up for each mirror to produce a maximum deviation of 8×5.10^{-4} radians. This represents .040cm deviation of the final image from the optical axis, which is less than the spherical aberration of the collector system.

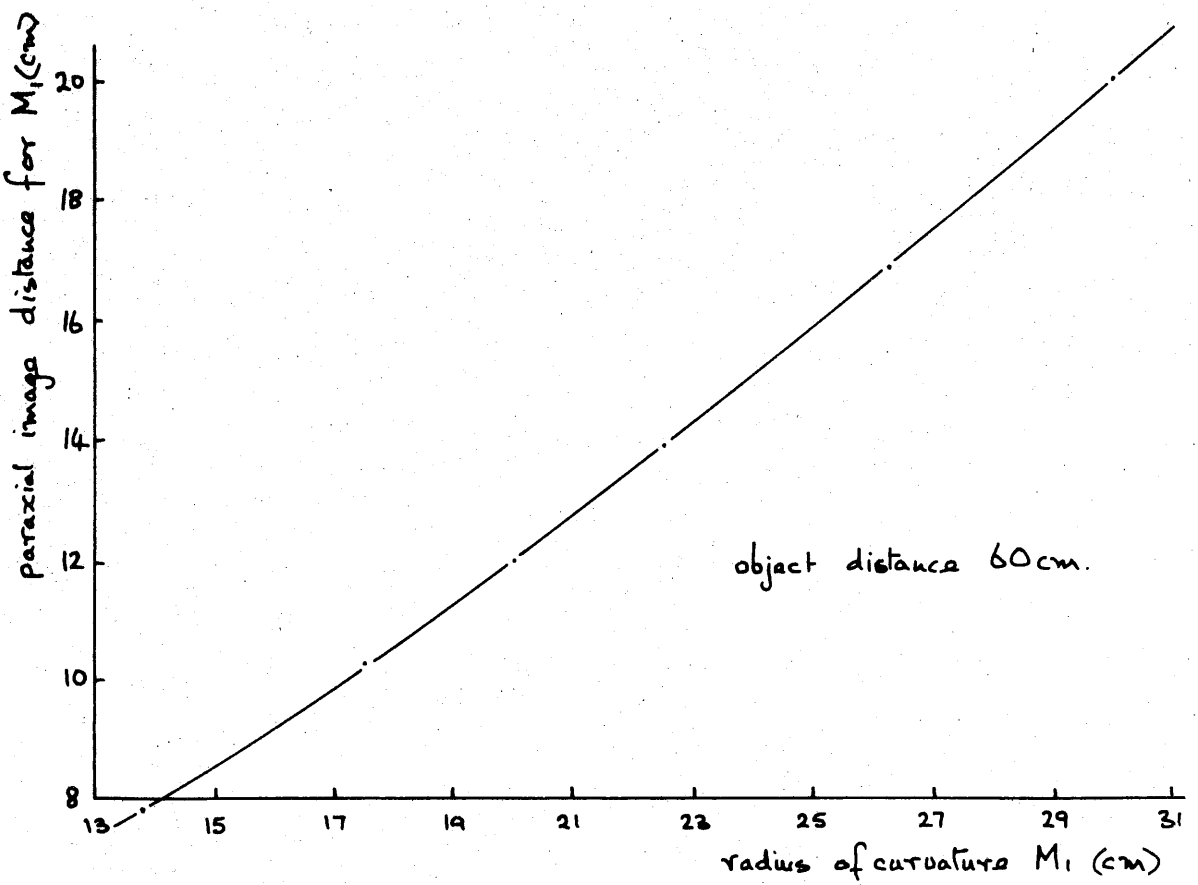

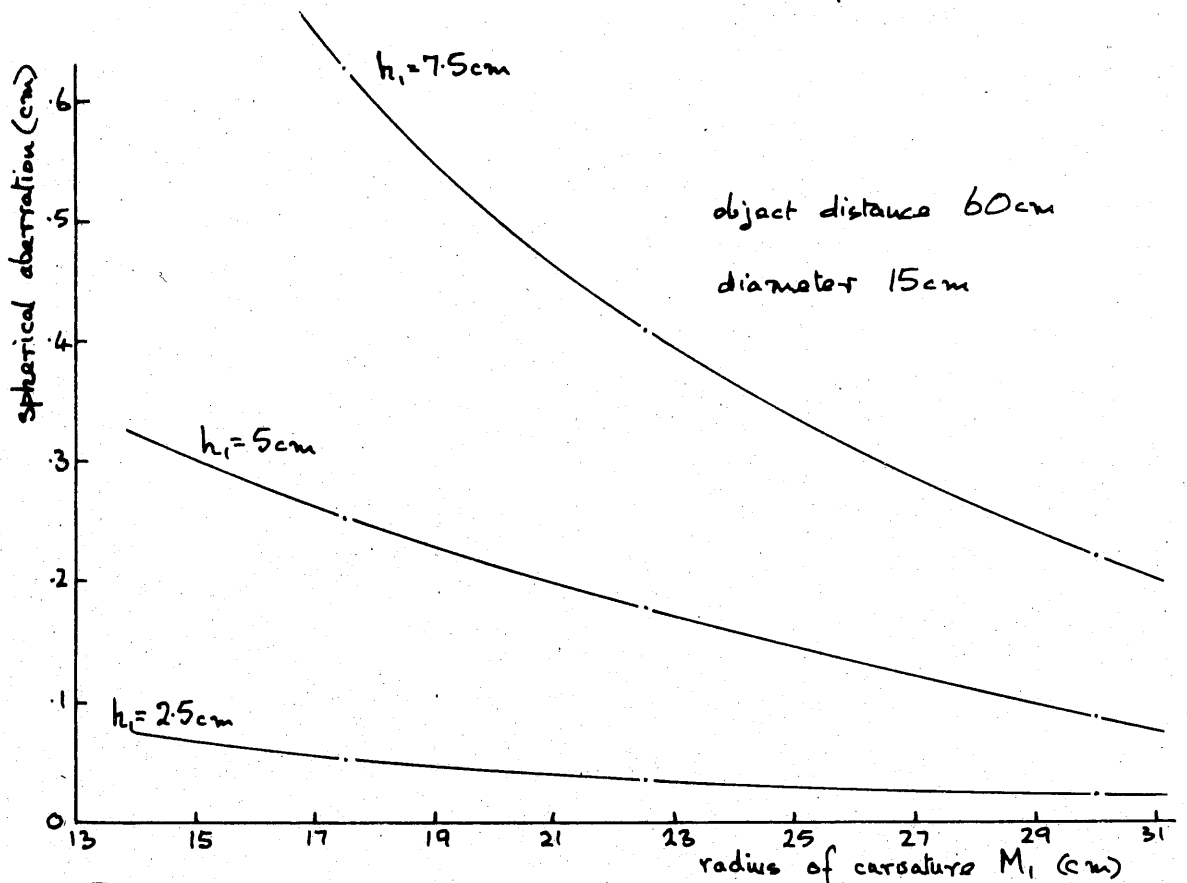

Fig G.5 Spherical aberration due to M_1

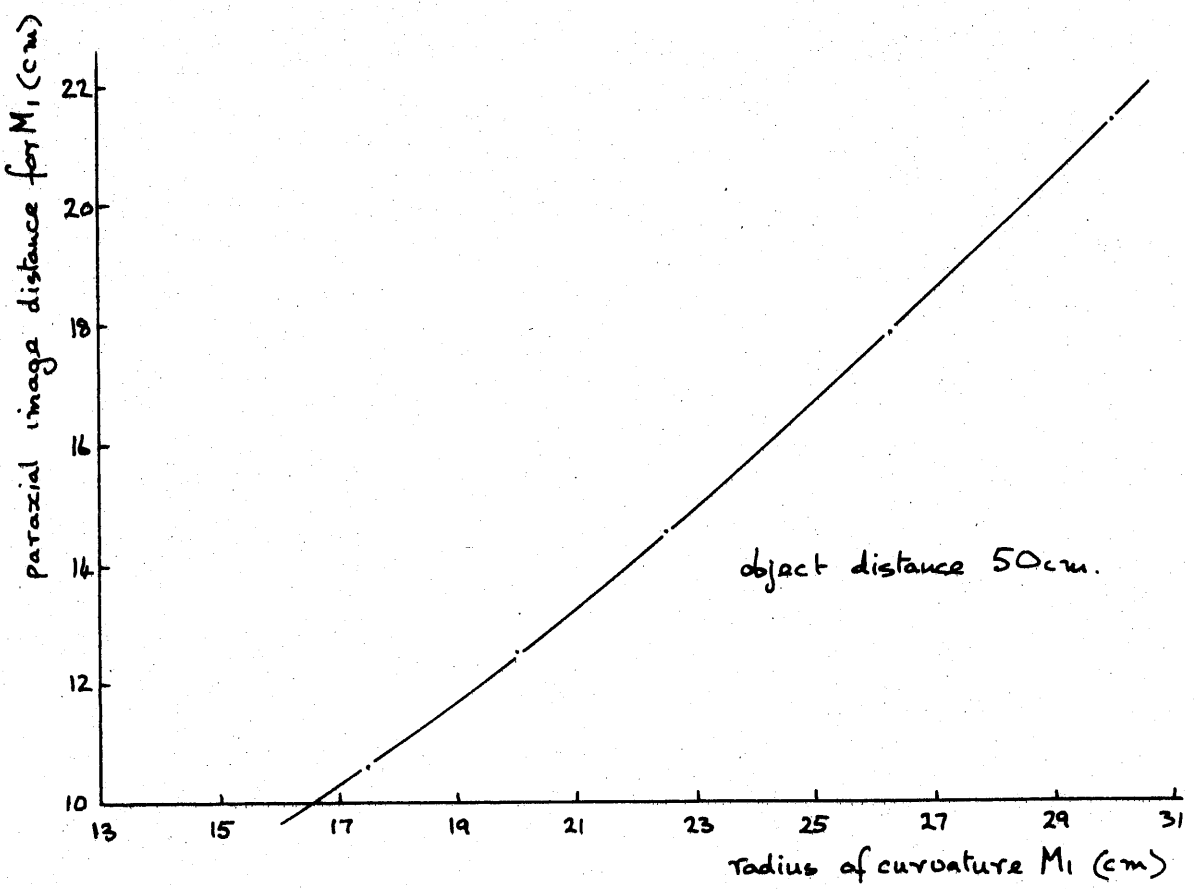

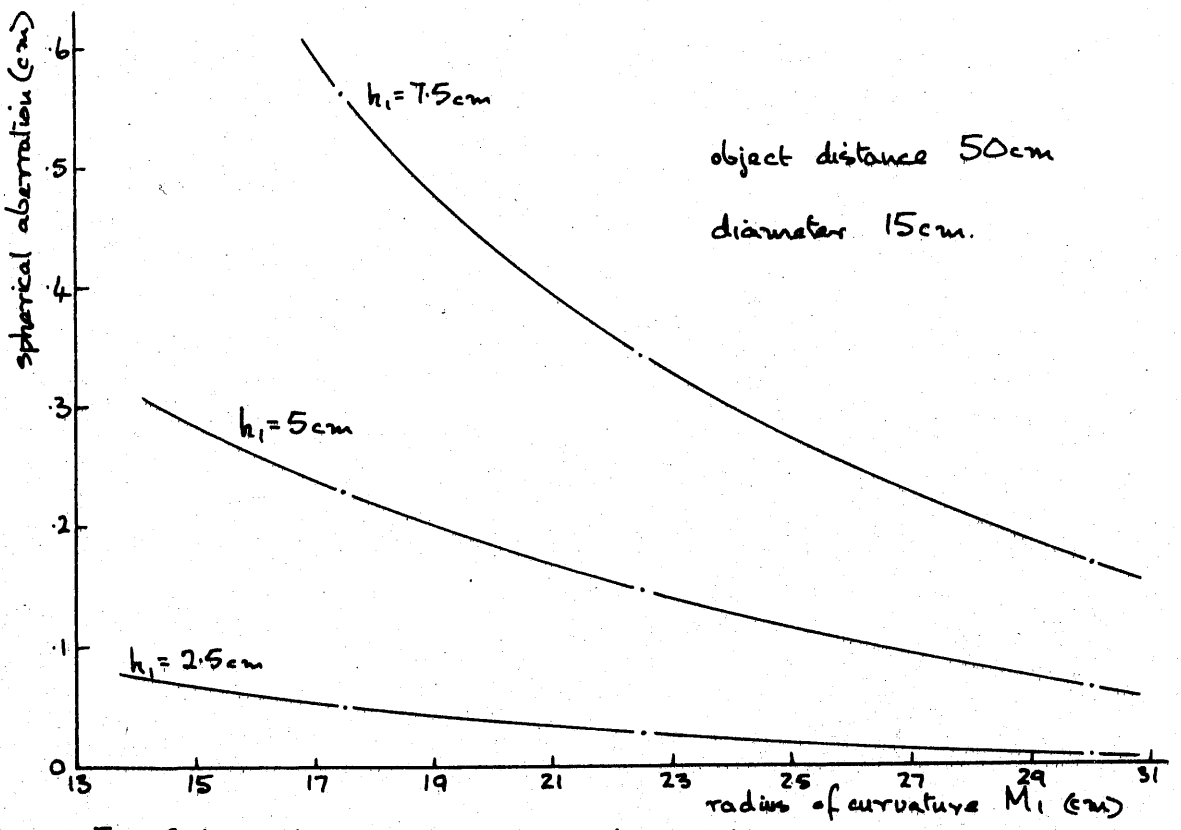

Fig G.6 Spherical aberration due to M_1

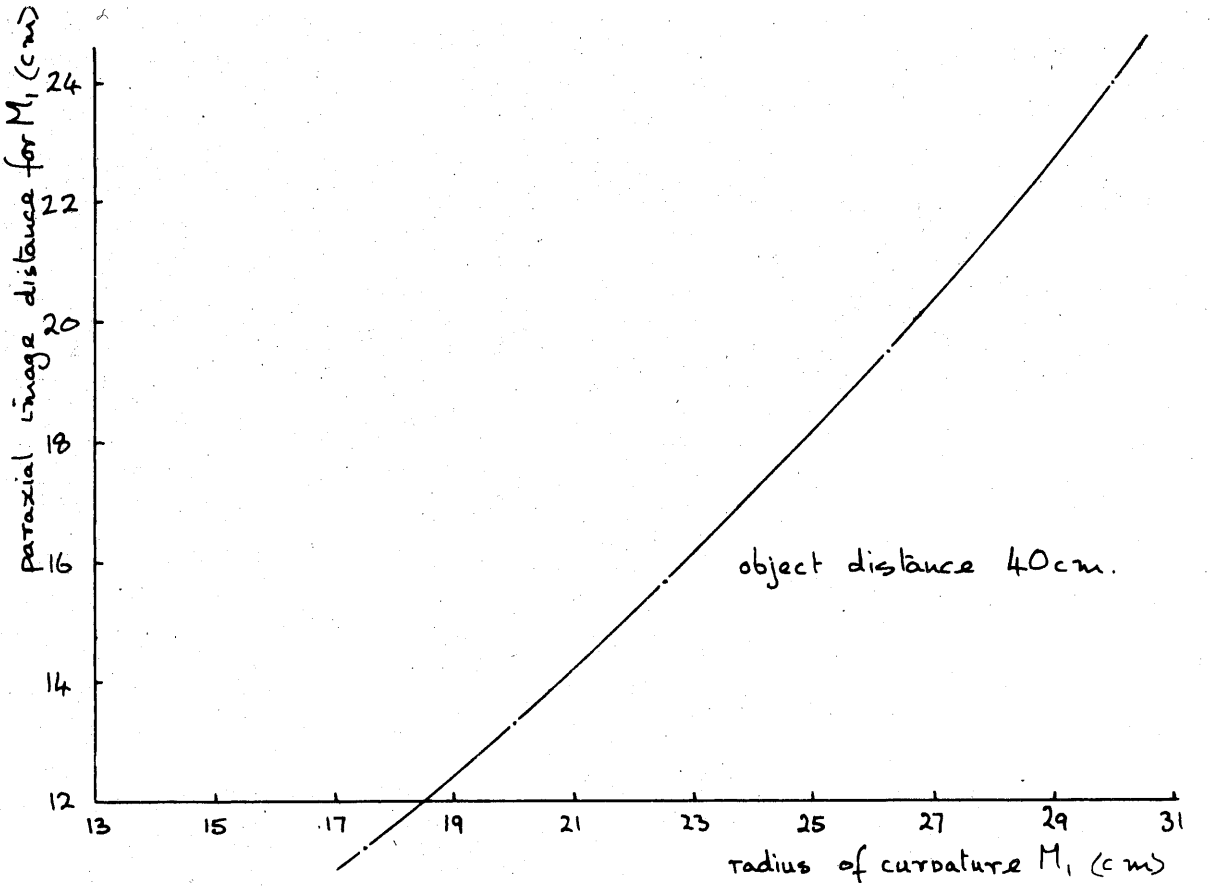

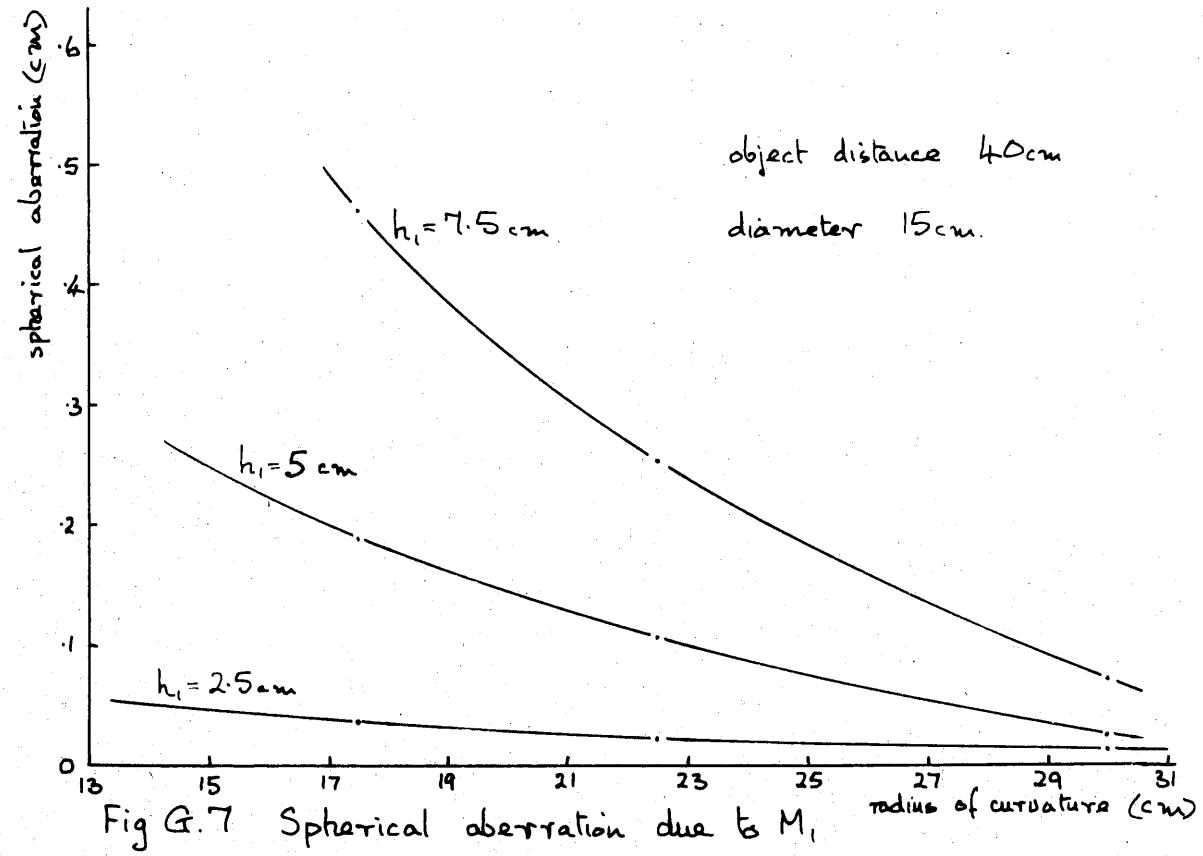

Fig G.7 Spherical aberration due to M_1

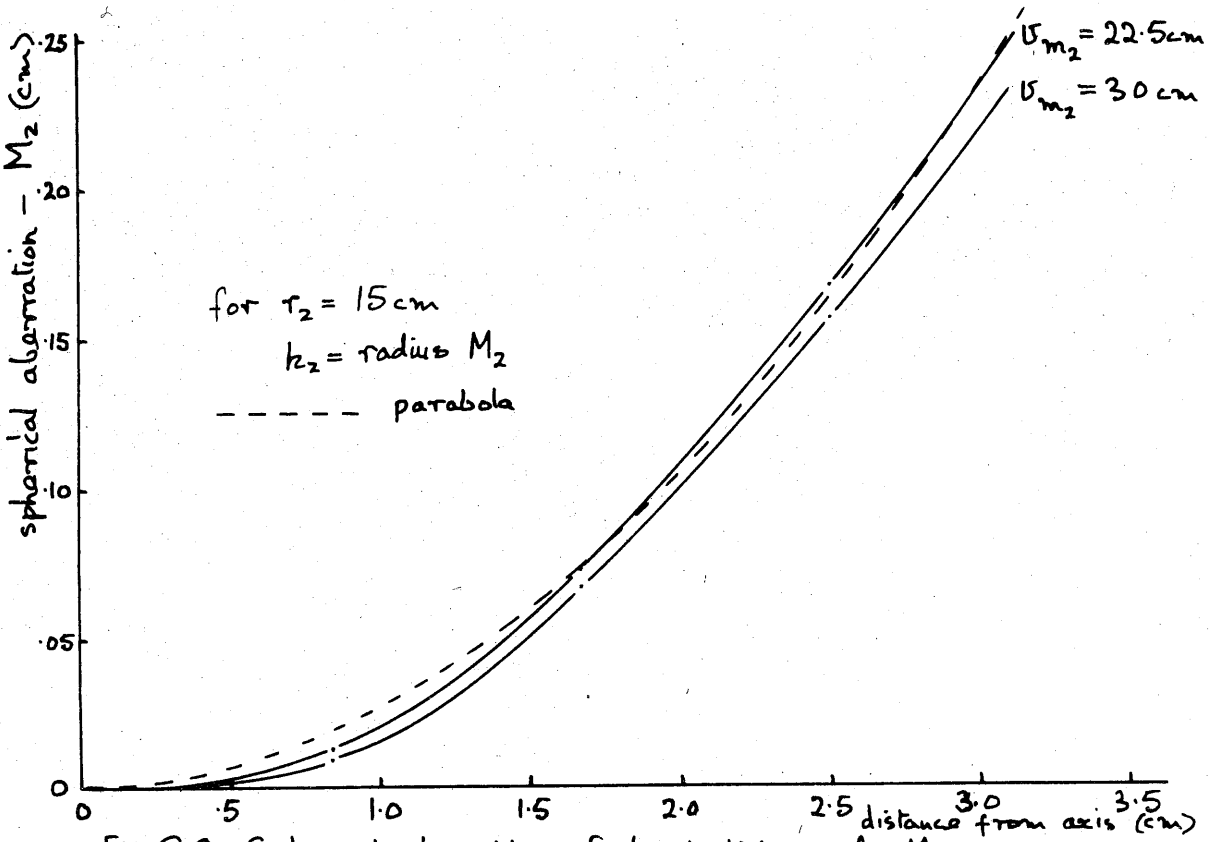

Fig G.8 Spherical aberration of object distance for M_2

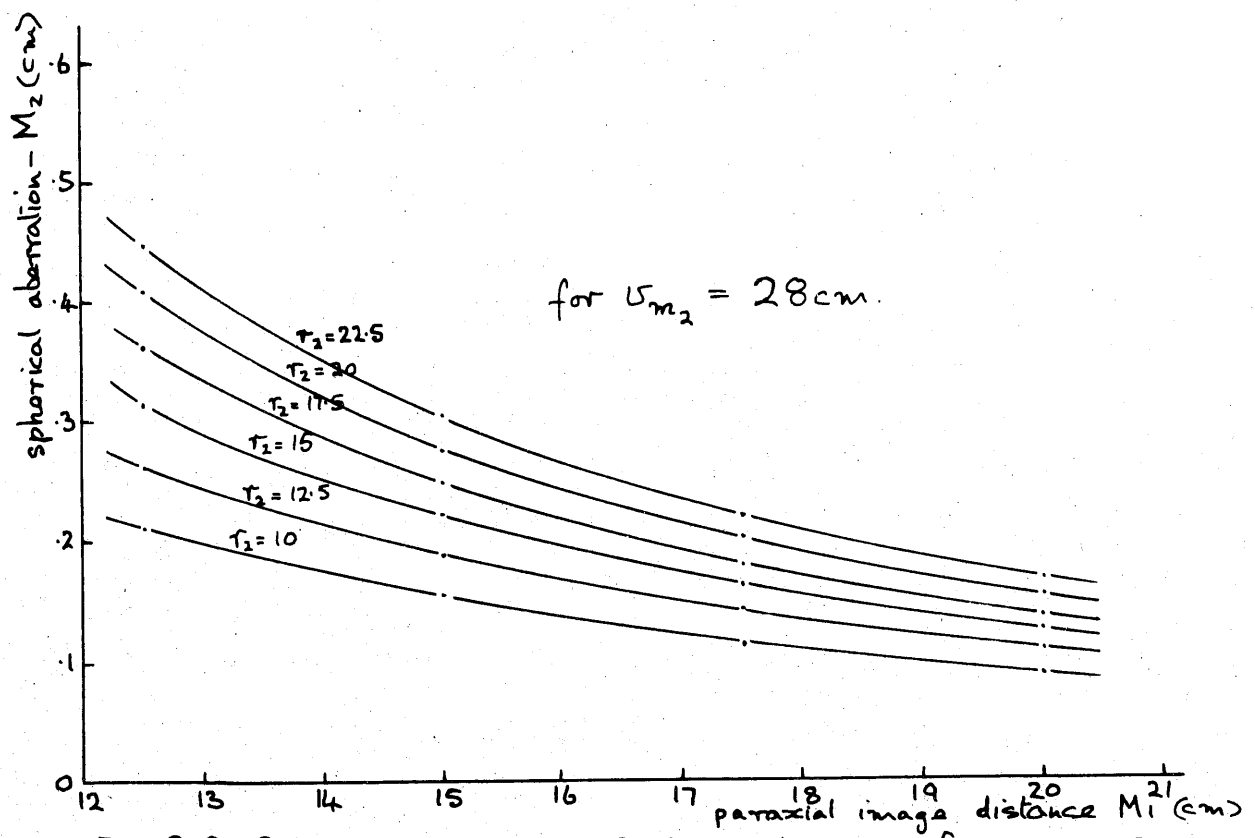

Fig G.9 Spherical aberration of M_2 object distance for various r_2

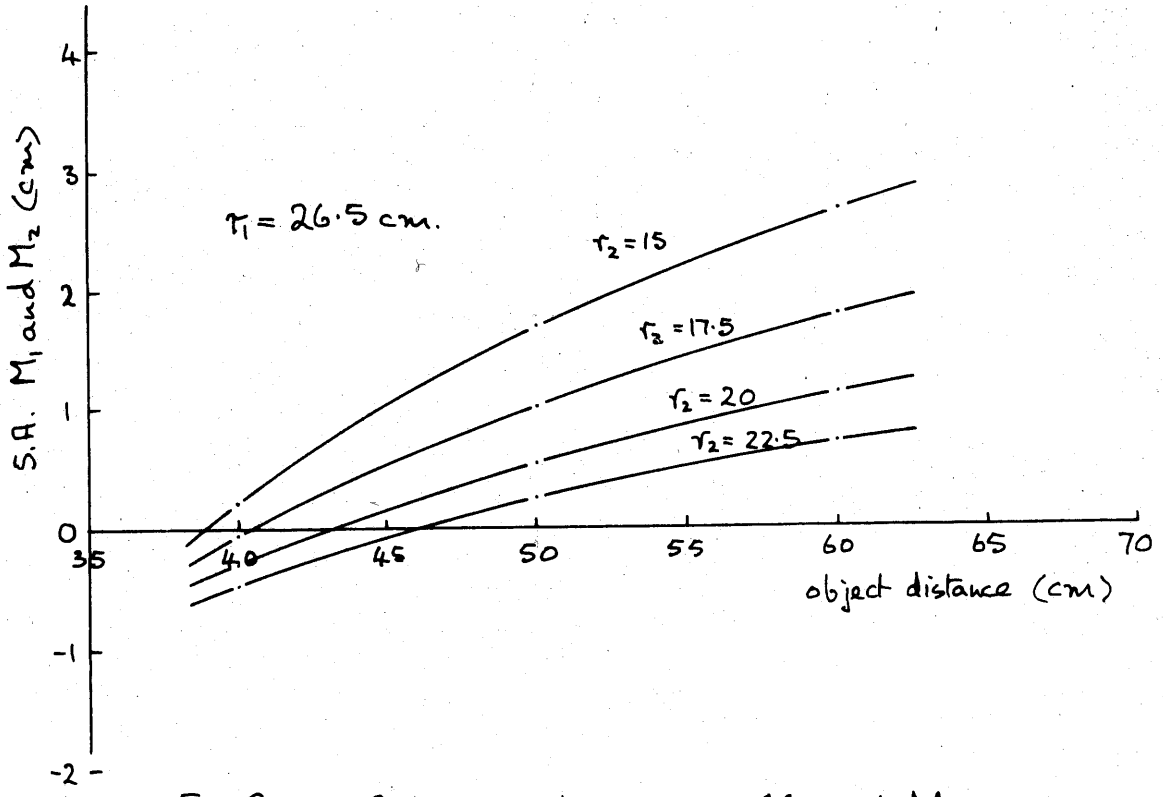

Fig G.10 Spherical aberration M_1 and M_2.

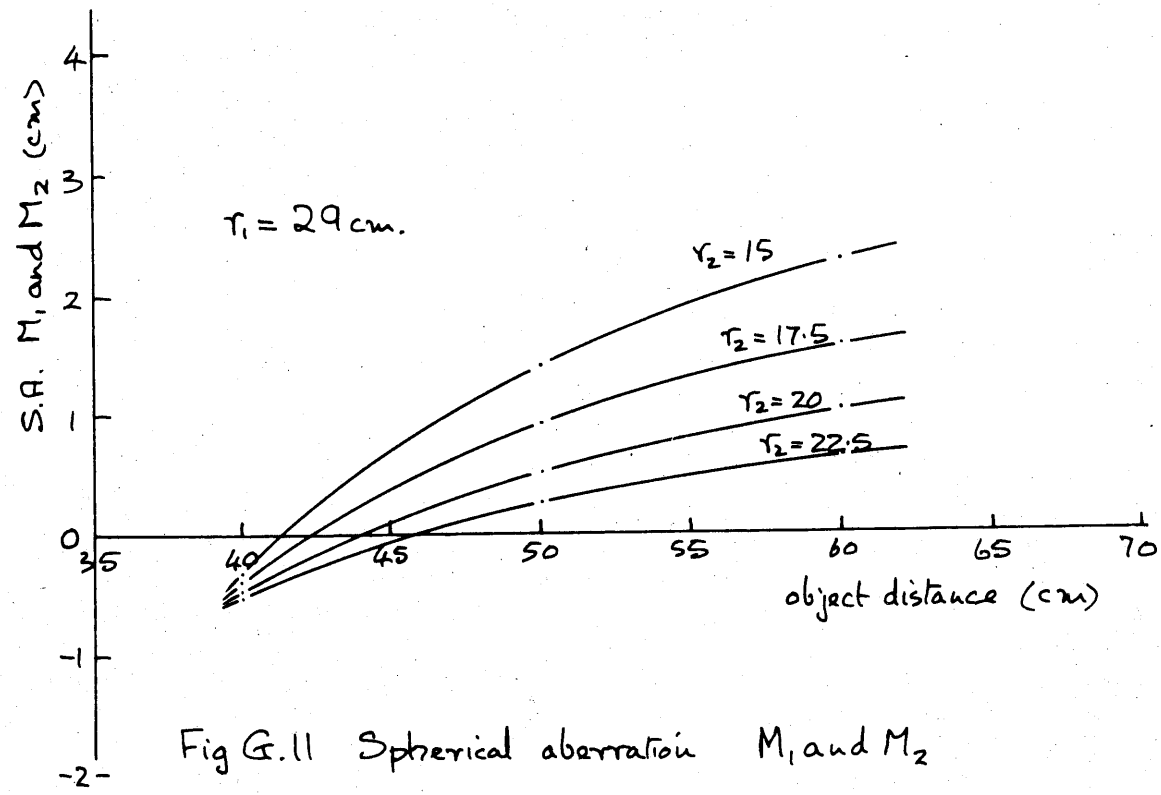

Fig G.11 Spherical aberration M_1 and M_2

Appendix H - Characteristics of the Control Stages

The characteristics of the control stages were measured individually while each was operating in its normal manner. To achieve this the three stages of Fig. H.1 were used and the control voltage was applied from a separate bias battery.

H.1. Characteristics of stage 1

While the characteristics of stage 1 were being measured the correction CD shown by the broken line was dispensed with. This turned T_3 into a normal common emitter amplifier stage biased temporarily by the collector to base resistor (8.2KΩ). The feedback signal to control the gain of T_2 was obtained from the 2v bias battery and could be varied by adjusting R_1. The characteristics of R_d were such that, when the full 2v bias was available, the current limited by R_2 (1 KΩ) was sufficient to reduce R_d to about 50Ω. In this case the gain of the stage approaches $1/R_d$ amps/volt(1). When the bias voltage was reduced until R_d turned off, a gain of $1/R_e$ resulted. The measurements were made with 900cps signal from an oscillator. The input was varied so that the output current in R_3 was maintained constant as the bias was altered. All the voltage measurements were made using a Tektronix oscilloscope type 502.

Table XIX Gain measurements - stage 1

V_1 mV	V_2 mV	i_2 μA	gain = $\frac{i_2}{V_1}$ x 10 ^{3}	V_c volts
.75	1	4.55	6.07	-2.0
.9	"	"	5.05	-1.0
1.1	"	"	4.13	- .66
1.25	"	"	3.64	- .50
1.8	"	"	2.53	- .40
2.2	"	"	2.07	- .30
2.7	"	"	1.69	- .25
3.8	"	"	1.2	- .20
6	"	"	.76	- .15
9	"	"	.51	- .125
12	"	"	.38	- .10
16	"	"	.28	- .075

i.e. voltage range 20:1

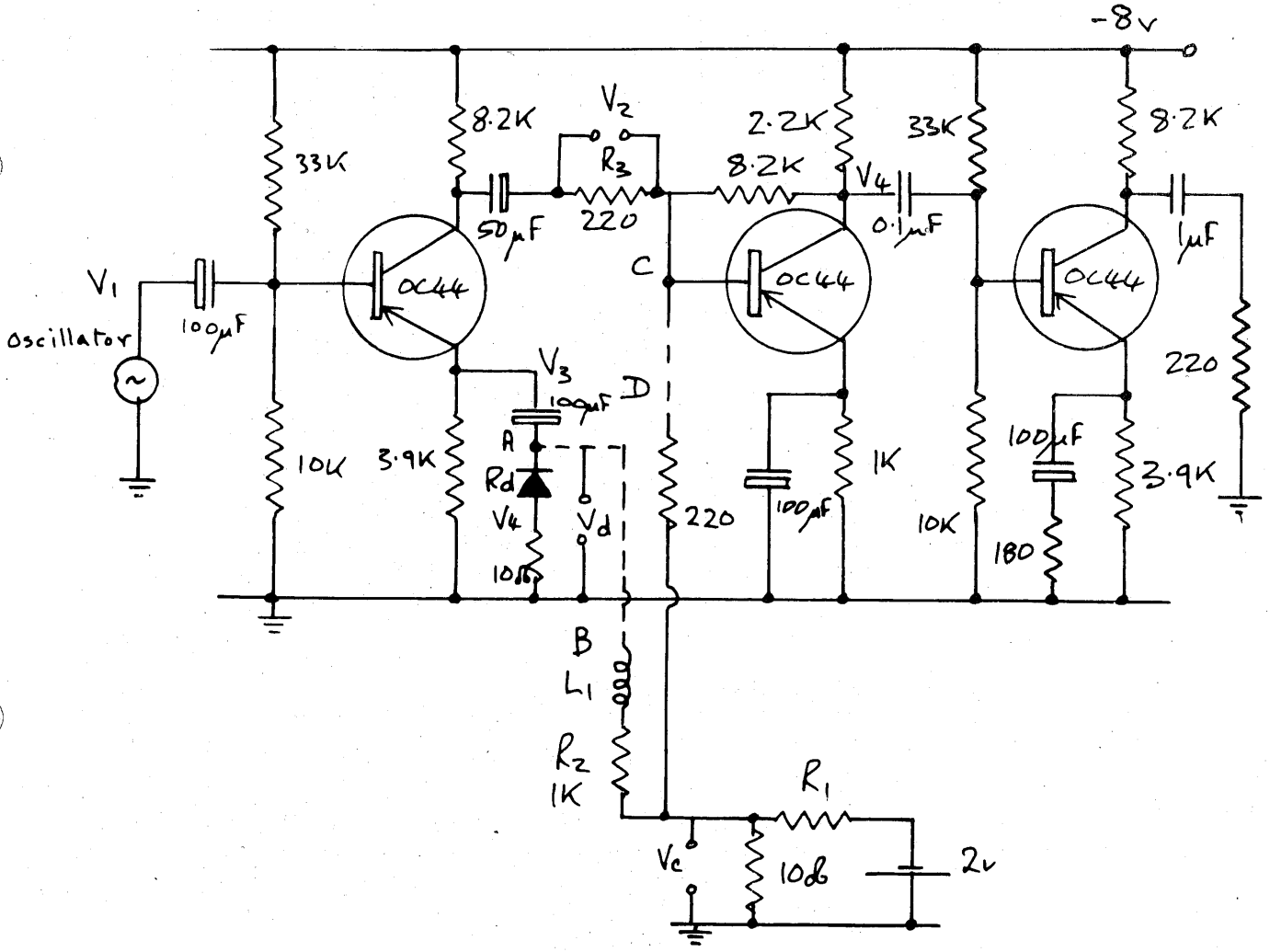

Fig H.1 First three stages of signal amplifier.

A further set of measurements were made to relate the gain with the dynamic resistance of the diode R_d. These measurements show that a knowledge of the characteristics of R_d enables the performance of the stage to be predicted.

Table XX Prediction of gain

V_1 mV	V_3 mV	$r_e = \frac{(10+R_d)(V_1-V_3)}{V_3}$ Ω	V_4 mV	$R_d = \frac{(V_3-V_4)10}{V_4}$ Ω	gain $= \frac{1}{R_d/3900 + r_e} \times 10^3$
2.5	0.8	110	.13	51.5	6.2
3.0	1.8	68	.16	102.5	5.9
3.7	2.5	70	"	146	4.7
4.2	3	71	"	177	4.2
-	4.6	-	"	277	3.0
-	6	-	"	375	2.4
-	9	-	"	552	1.8
-	12.5	-	"	770	1.4
-	21	-	"	1300	.95
-	27	-	"	1670	.81
-	40	-	"	2490	.63
-	59	-	"	3670	.51

H.2. Characteristics of stage 2

The characteristics of stage 2 were measured with the connection AB broken and CD joined and a 330Ω resistor replacing the diode R_d. This caused stage 1 to operate as a normal common emitter amplifier with gain $\frac{1}{330}$ amps/volt. and enabled the gain of T_3 to be varied by adjusting the bias voltage. The input signal was again applied at the base of T_2 and the output was measured at the collector of T_3. The input signal was varied to maintain output constant as the bias was altered. The measurements given in table XXI are for an output of 1.8mV peak to peak.

Table XXI Gain measurements - stage 2

V_1 peak to peak mV	V_4 peak to peak mV	V_c mV	i_{in} peak to peak μA	Gain $\frac{V_4}{i_{in}}$ mV/mA
20	1.8	-10	60.	30
10	"	-45	30.	60
7	"	-45	21.	85.6
4.5	"	-60	13.5	133.3
2	"	-100	6.	300
.65	"	-200	1.95	923
.35	"	-300	1.05	1713
.24	"	-400	.72	2500
.20	"	-506	.60	3000
.16	"	-700	.48	3750
~ .10	"	-1000	.30	6000
~ .08	"	-2000	.24	7500

The signal handling capabilities of these stages amount to 20:1 for T_2 and 250:1 for T_3 under the measuring conditions described above. This amounts to a combined handling range of 5000:1 or 74dB for both stages. When the stages were coupled together it was necessary to introduce the inductance L_1 to maintain the combined control range of the two stages. The inductance prevents signal feedback from stage 2 to stage 1 while allowing the dc control signal through to stage 1.

The gain characteristic for each stage is plotted in Fig. H.2.

H.3. References

1. E.M. Cherry. J.Brit.Inst.Radio Eng.,1963,25,(2),p.129

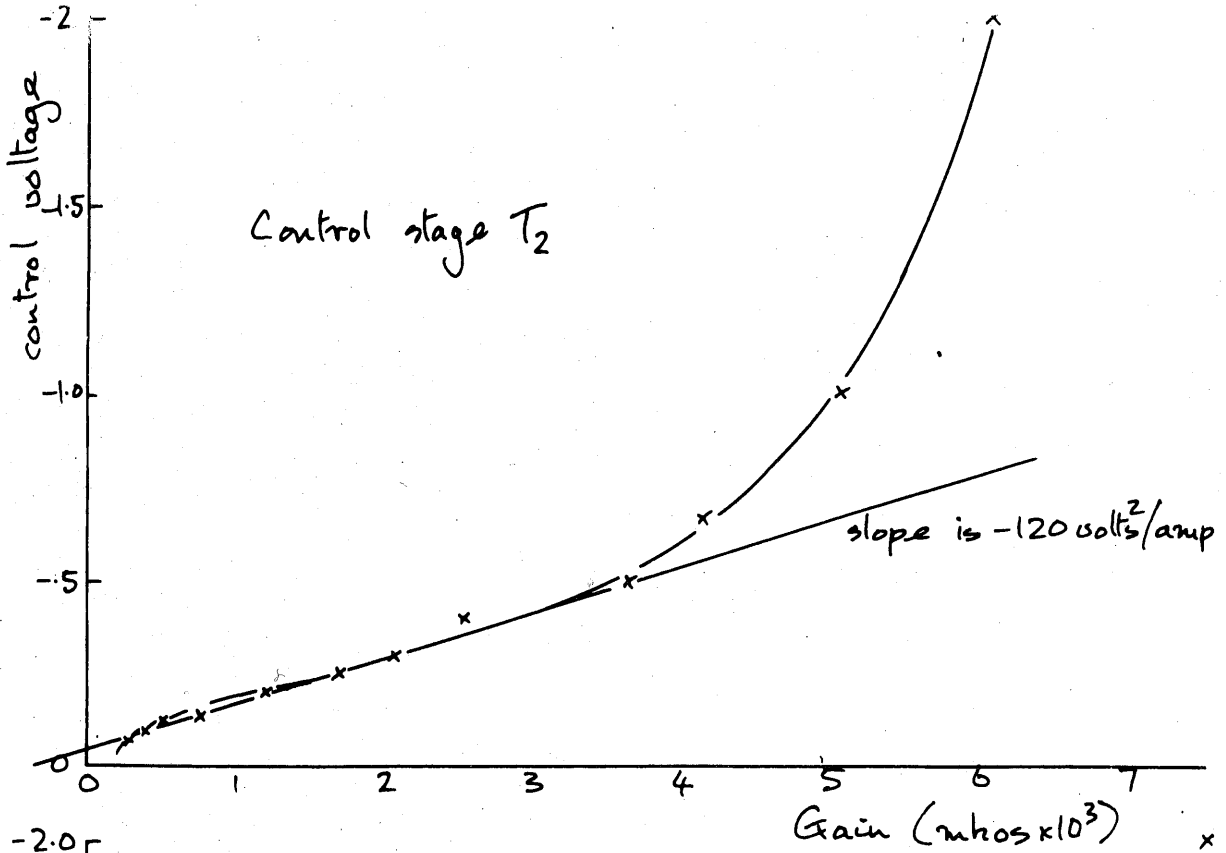

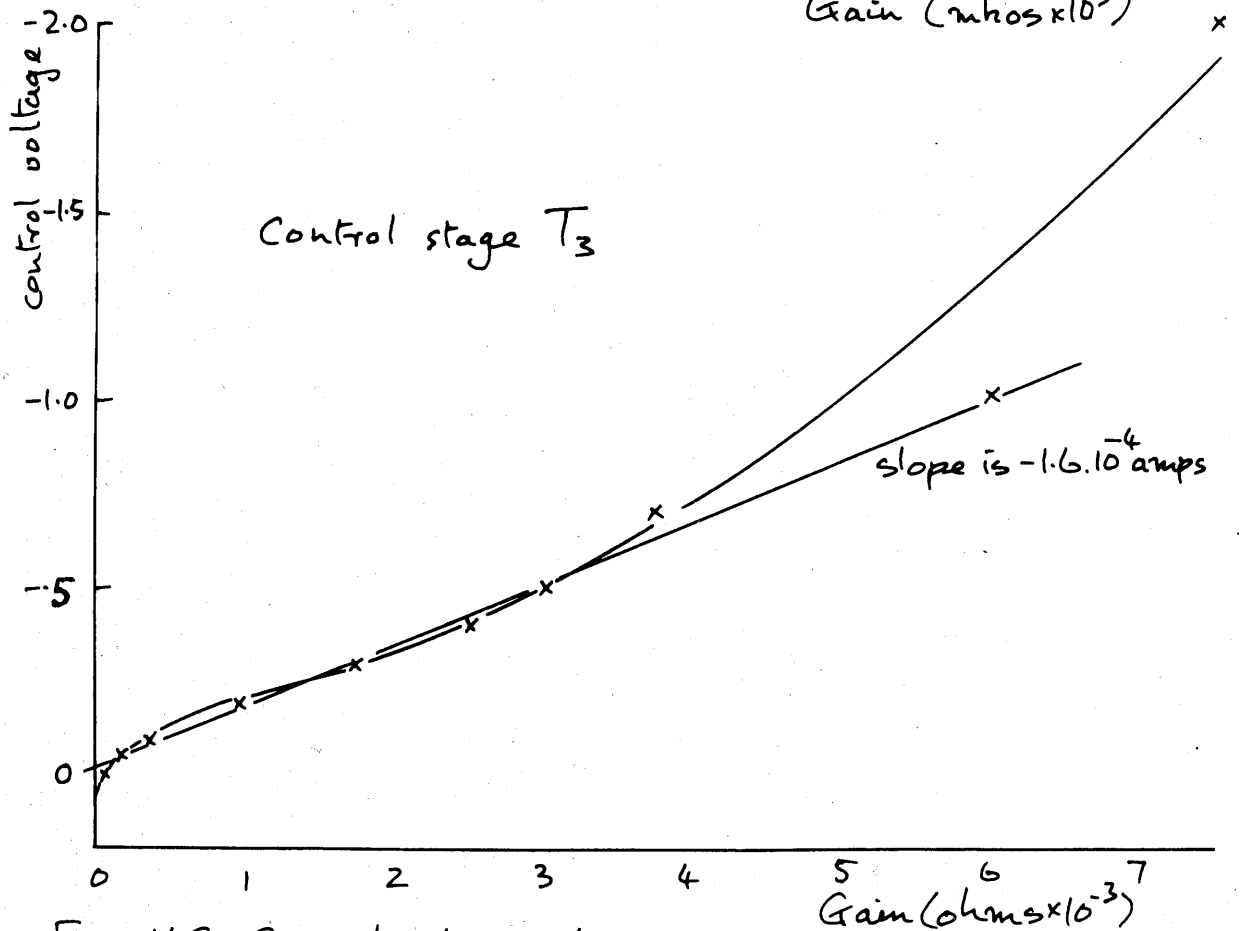

Fig H.2 Control stage characteristics.